Phosphorylation-state dependent modulation of Aβ pathobiology in Alzheimer's disease

Intraneuronal phosphorylated Aβ induced subcellular dysfunction and microglial inflammation

Doctoral thesis

to obtain a doctorate (PhD)

from the Faculty of Medicine

of the University of Bonn

Kapadia, Akshay Bhupendra Leena

from Mumbai, India

2024

Written with authorization of

the Faculty of Medicine of the University of Bonn

Members of the thesis committee:

First reviewer: **Prof. Dr. Jochen Walter** (University of Bonn, Germany)

Second reviewer: **Prof. Dr. Eva Kiermaier** (University of Bonn, Germany)

Prof. Susanne Schoch McGovern (University of Bonn, Germany)

Dr. Anne-Sophie Hafner (Radboud University, Nijmegen, Netherlands)

Day of oral examination:11th July 2024

From the Clinic and Policlinic for Neurology

Director: Prof. Dr. Thomas Klockgether

This Thesis is dedicated to

19-year-old Lorna Anthony Collaco

Table of Contents

List of abbreviations

ACTB	β-actin filaments
AD	Alzheimer disease
AFC	7-Amino-4-trifluoromethylcoumarin
AKT	protein kinase B
Alix	ALG-2-interacting protein X (exosomal marker)
AnnV	annexin V targeting phosphatidylserine
ANOVA	analysis of variance
APOE	apolipoprotein E
APP	amyloid precursor protein
APPSw	amyloid precursor protein expressing Swedish mutation APP K670N-M671L
ASC	apoptosis-associated speck-like protein containing CARD
ATF4	activating transcription factor 4
ATF6	activating transcription factor 6
ATG	autophagy protein
ATPase	proton ATPase
Aβ	amyloid-β
bcl-2	B-cell lymphoma-2
BiP/GRP78	binding immunoglobulin protein/ glucose-regulated protein
CD16/32	cluster of differentiation molecule-antigen CD16/32 (FcγRIII)
CD45	lymphocyte common antigen
CD63 and CD9	member of the tetraspanin superfamily of activation-linked cell surface antigens CD63
CHOP	C/EBP homologous protein
CK1	casein kinase 1
CK1δ	casein kinase 1 isoform delta
Cl. CSP-3	cleaved caspase-3 Asp175
CSP-1	caspase-1
CTFα / β	C-terminal fragment of APP - α / β
CTSD	lysosomal aspartic cathepsin D

CX_3-CR1	C-X3-C motif chemokine receptor 1
DAPI	4’,6-diamidino-2-phenylindole
DAβ	amyloid-β (pseudo-phosphorylated S → D)
DNA	deoxyribose nucleic acid
DRP1	dynamin-related protein 1
EEA1	early endosome antigen 1
eIF2α	eukaryotic initiation factor 2α
ERK1	extracellular-signal regulated serine/threonine-kinases
FA	formic acid
FLOT-1	flotillin-1
GFP	green fluorescent protein
HSP60	heat shock proteins-60
HSP70	heat shock proteins-70
HSP90	heat shock proteins-90
IDE	insulin degradation enzyme
IL-10	interleukin-10
IL-1β	interleukin-1 beta
IL-4	interleukin 4
IRE1α	inositol-requiring enzyme 1 α
LAMP-1/2	lysosome-associated membrane protein-1/2
LDHA	lactate dehydrogenase A
MAP1LC3/LC3	microtubule-associated protein 1 light chain 3
MAP-2	microtubule-associated protein 2
MARCH5	E3 ubiquitin-protein ligase, encoded by the MARCH5 gene
MFN1	mitofusin-1
MLKL	mixed lineage kinase domain like pseudokinase
mTOR	mammalian target of rapamycin
NFκB	nuclear factor kappa-light-chain- B cells
NLRP3	NLR family pyrin domain containing 3
nmAβ	amyloid-β (non-modified)
npAβ	amyloid-β (non-phosphorylated)
OPA-1	optic atrophy 1

p35	Cyclin dependent kinase 5, regulatory subunit 1 (p35)
p53	tumor antigen P35/transformation related protein 53
p62/SQSTM-1	sequestosome-1
p70 S6K	ribosomal protein S6 kinase beta 1/p70S6 kinase
PARK/DJ-1	protein deglycase, encoded by the PARK7 gene
Parkin	E3 ubiquitin ligase, encoded by the PARK2 gene
pAβ	phosphorylated amyloid-β
pAKT	phosphorylated AKT
pbcl-2 S87	phosphorylated bcl-2
pGSKα/β	phosphorylated glycogen synthase kinase 3α/β
PI3K	phosphoinositide 3-kinase
PINK1	PTEN-induced kinase 1
pMLKL	phosphorylated MLKL
pmTOR	phosphorylated mTOR
poly UBQ	ubiquitinylated proteins
PPARγ	peroxisome proliferator-activated receptor γ
pPI3K P85	phosphorylated PI3K
pRIPK1	phosphorylated receptor interacting serine/threonine kinase 1
pS6K (P70)	phosphorylated S6K1
PSEN	presenilin
pSer26Aβ	amyloid-β phosphorylated at serine residue 26
pSer8Aβ	amyloid-β phosphorylated at serine residue 8
PSMB5	proteasome 20S subunit beta 5
pTFEB	phosphorylated TFEB
pUBQ	phosphorylated ubiquitin S65
R110	rhodamine dye
RAB	Ras related in brain
RFP	red fluorescent protein
ROS	reactive oxygen species
S1P1	sphingosine-1-phosphate receptor 1
S26A Aβ	amyloid-β residue 26 (S→A)
S26D Aβ	amyloid-β residue 26 (S→D)

S8A Aβ	amyloid-β residue 8 (S→A)
S8D Aβ	amyloid-β residue 8 (S→D)
sAPPα / β	α / β cleaved soluble forms of amyloid precursor protein -
SDS	sodium dodecyl sulfate
TFEB	transcription factor EB
TfR	transferrin receptor
TGN46	transmembrane glycoprotein localized to the trans-Golgi network
THY1	thymocyte antigen 1
Tim23	mitochondrial import inner membrane translocase subunit TIM23
TNFα	tumor necrosis factor – alpha
Tom70	mitochondrial translocase of outer membrane- 70
TREM2	triggering receptor expressed on myeloid cells 2
UBA1	ubiquitin activating enzyme 1
UBQ	ubiquitin (free form)
UCHL1	ubiquitin C-terminal hydrolase L1
ULK1/atg1	unc-51 like autophagy activating kinase 1
WT Aβ	amyloid-β (wild type/ non-modified)
YFP	yellow fluorescent protein

1. Introduction

Alzheimer's disease (AD) is a progressive neurodegenerative disorder characterized by severe loss of memory and cognition (Selkoe 1991; Scheltens et al. 2021; Sengoku 2020; Lane et al. 2018). Around 45 million people are affected with dementia with around 10 million new cases every year. AD constitutes about 60-70% of dementia cases worldwide (Alzheimer's disease facts and figures 2023). In the past three years, deaths from AD increased by more than 145%, making AD the seventh top cause of death (including deaths from the COVID-19 pandemic). Additionally, AD is a significant contributor to disability and dependency in the elderly population, contributing to the global socio-economic crisis.

AD is a complex and heterogeneous disorder and is characterized by loss of neurons and synapses resulting in atrophy of the affected regions. The complete etiological model remains to be explored, but neuronal degeneration as well as neuropathological hallmark lesions starts much earlier than the onset of symptoms (Yankner 1996; Vickers et al. 2000; Finder 2010). AD brains show presence of two major histopathological hallmarks, deposition of amyloid-β (Aβ) plaques, and neurofibrillary tau tangles (Takashima 2009; Busche and Hyman 2020; Hyman et al. 2012; Jack et al. 2019). The predisposition to the disease is significantly influenced by genetic factors. The amyloid precursor protein (APP), presenilin 1 (PSEN1), or, less commonly, presenilin 2 (PSEN2) genes, are the three genes identified to cause the early onset of AD (EOAD). Mutations in these 3 genes are currently known to cause early-onset familial AD (FAD, <65 years). FAD-causing mutations are very rare (<5%) and the causes of more common late-onset sporadic AD (SAD, >65 years, >95% occurrence), are unknown. Studies indicate genetic contribution of lipid metabolism, protein/lipid trafficking, and inflammation (Andrade-Guerrero et al. 2023). Although the molecular basis of AD pathology is widely investigated, the field of Aβ has been the focus of research for several decades (Murphy and LeVine 2010; Hampel et al. 2021; Ceyzériat et al. 2020; Huang et al. 2020; Rosenblum 2014).

1.1. Amyloid precursor protein (APP)

APP, a transmembrane type I protein plays a role in several cellular processes (Zhang et al. 2012; Zheng and Koo 2006; Haass et al. 2012; Kang et al. 1987). In neurons, APP has

been reported to regulate synaptic function and neuronal plasticity among other functions (Kamenetz et al. 2003; Chow et al. 2010). APP can be cleaved by α-secretase and the resulting soluble APP fragments (sAPP) are secreted into the extracellular milieu and the cerebrospinal fluid (CSF). γ-Secretase cleavage of membrane bound α-CTF (CTF83) results in the generation of P3 as well as the amino-terminal APP intracellular domain (AICD). This is termed as the non-amyloidogenic pathway as α-secretases cleave APP within the amyloid sequence (Fig. **1Ai**). Alternatively, in the amyloidogenic pathway, APP undergoes sequential proteolytic cleavage by β- and γ-secretases on the N- and C-terminal ends of the Aβ domain, resulting in the generation of Aβ peptides of different lengths (Fig. **1Aii**), along with sAPPβ and AICD (Haass and Selkoe 1993). Dysregulation or imbalance (favoring the amyloidogenic pathway) leads to an accumulation of Aβ peptides, promoting Aβ aggregation and formation of amyloid plaque deposits, a hallmark of AD. Several factors can influence the amyloidogenic processing of APP, including genetic mutations, environmental factors, and altered cellular signaling pathways.

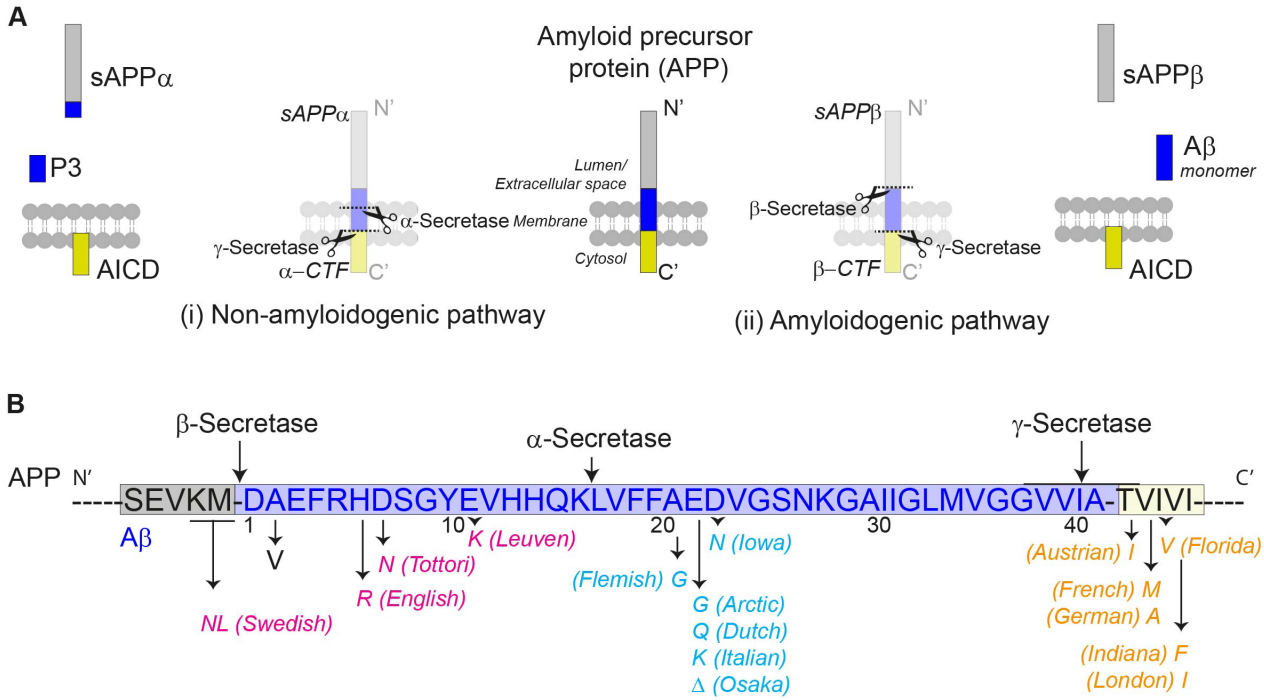

Fig. 1: Schematic representation of APP processing pathways and the localization of FAD associated mutations. A. Proteolytic processing of APP occurs by two distinct pathways. (**i**) Non-amyloidogenic processing is facilitated by α-secretase cleavage within the Aβ region. This cleavage produces a soluble fragment called sAPPα and a membrane-bound C-terminal fragment called α-CTF (CTF83). α-CTF is subsequently processed by γ-secretase, leading to the release of a short peptide called P3, which lacks the

amyloidogenic properties associated with Aβ peptides. (**ii**) Amyloidogenic processing is mainly facilitated by β-secretase (also known as BACE1). APP is first cleaved by β-secretase within the extracellular domain. This cleavage produces a soluble fragment called sAPPβ and a membrane-bound C-terminal fragment called β-CTF (CTF99). γ-Secretase further cleaves β-CTF, resulting in the release of the Aβ peptides of varying lengths ($A\beta_{37-43}$). The balance between amyloidogenic and non-amyloidogenic processing of APP is crucial in determining the levels of Aβ production and the potential for Aβ aggregation and deposition. **B.** FAD-causing mutations identified in APP are localized around N-terminus (*marked in magenta*) and C-terminus (*in orange*) and in the middle region of Aβ (*in cyan*). Aβ peptide sequence within APP has been highlighted in blue. Mutations of the C-terminal region modulate γ -secretase activity and augment production of Aβ peptides. Mutations within the central hydrophobic region of Aβ prevent APP cleavage by α-secretase. Other mutations either facilitate the amyloidogenic pathway of APP proteolysis, increase Aβ production, enhance the Aβ aggregation potential, or hinder Aβ metabolism/degradation. Please see: www.alzforum.org/mutations.

Mutations in the APP gene, accounting for about 10-15% of the FAD cases, have been found to affect the aggregation propensity of Aβ, as well as the turnover via altering of the proteolytic processing of APP. FAD-linked mutations are hereditary and are passed down within generation in affected families. However, it is important to note that mutations within identified AD-risk genes may not be prominent within most sporadic cases of AD (Goldman et al., 2011; Hunter and Brayne, 2018). Sporadic AD (SAD) refers to cases that do not have a dominant genetic cause and are thought to be influenced by a combination of genetic and environmental factors and usually exhibit a later onset of the disease. Numerous studies have been conducted to understand the molecular mechanisms involved in the pathogenesis of AD, both in FAD and SAD cases. These studies have significantly augmented the body of evidence pinpointing the cause of AD pathogenesis. By elucidating the molecular pathways and processes involved in Aβ production, aggregation, and neurotoxicity, researchers have postulated to gain insights into potential therapeutic targets for AD.

1.2. Amyloid-β

Amyloid-β (Aβ), 36–43 amino acid residue peptide, are the primary components of amyloid plaques found AD patient brains (Selkoe 1991). The most common forms of Aβ are $A\beta_{40}$ and $A\beta_{42}$, which consist of 40 and 42 amino acid residues, respectively (Fig. **1B**) (Chow et al. 2010; Selkoe 1994; Murphy and LeVine 2010; Haass and Selkoe 1993). $A\beta_{42}$ is more aggregation-prone and associated with the formation of amyloid plaques (Gouras

et al. 2015; Takahashi et al. 2017). In the brain, Aβ is continuously produced and cleared through various mechanisms. Enzymatic degradation, transport across the blood-brain barrier, and phagocytosis by microglial cells are some of the key mechanisms involved in the clearance of Aβ (Selkoe 1994; Bates et al. 2009; Bell et al. 2007; Kanekiyo et al. 2013; Mandrekar et al. 2009). Enzymes such as neprilysin and insulin-degrading enzyme (IDE) play a role in the enzymatic degradation of Aβ (Malito et al. 2008), while transporters at the blood-brain barrier facilitate the drainage of Aβ from the brain (Zlokovic 2004). According to the amyloid hypothesis postulated in AD, there is an imbalance between Aβ production and clearance, leading to the accumulation of Aβ (Selkoe 1991; Wildsmith et al. 2013; Lee and Landreth 2010; Tarasoff-Conway et al. 2015). This Aβ accumulation ultimately leads to the formation of amyloid plaque deposits alongside the initiation of neurodegenerative processes associated with AD.

1.2.1. Aβ aggregation

Aβ peptides have a propensity to aggregate and can exist in various types of assemblies. Non-aggregated or monomeric peptides likely occur in various forms which include different conformational transitional species. Upon aggregation these could form low molecular weight species (dimers, trimers, tetramers), oligomeric species (>6, both fibrillar and non-fibrillar), protofibrillar assemblies, fibrils, high molecular weight (HMW) oligomeric assemblies, and amyloid plaques (Fig. **2A**) (Aleksis et al. 2017; Finder and Glockshuber 2007). The aggregation process of amyloids is a complex phenomenon that occurs in distinct phases and is influenced by various factors. The Aβ aggregation process can be divided into three distinct phases: lag phase, log phase, and plateau phase (Fig. **2B**). During the lag phase, there is a slow nucleation process where monomeric Aβ peptides undergo conformational changes and form small aggregates. This phase is followed by the log phase, characterized by rapid growth of aggregates through monomer addition. Finally, the aggregation process reaches a plateau or a steady phase *in vitro*. The intramolecular and intermolecular interactions contribute respectively to the folding and aggregation landscape of Aβ, steering towards the formation of amyloid plaques (Aleksis et al. 2017). The folding and aggregation landscape of Aβ peptides is highly complex and heterogeneous (Fig. **2C**). This complexity arises from the involvement of multiple pathways and intermediates in the aggregation process. Many factors, such as pH,

temperature, and organic and inorganic molecules can influence the aggregation kinetics and the types of aggregates formed (Faller et al. 2013; Menon and Sengupta 2019). Genetic factors, including mutations in the APP gene, can also differentially modulate the aggregation propensity of Aβ peptides (Hunter and Brayne 2018). Furthermore, post-translational modifications within Aβ peptide sequence can significantly alter its aggregation process (Kummer and Heneka 2014; Kumar and Walter 2011; Rezaei-Ghaleh et al. 2016b). Additionally, interaction with membrane lipids, molecular chaperones and other proteins, can influence the folding and aggregation of Aβ peptides (Konstantoulea et al. 2022).

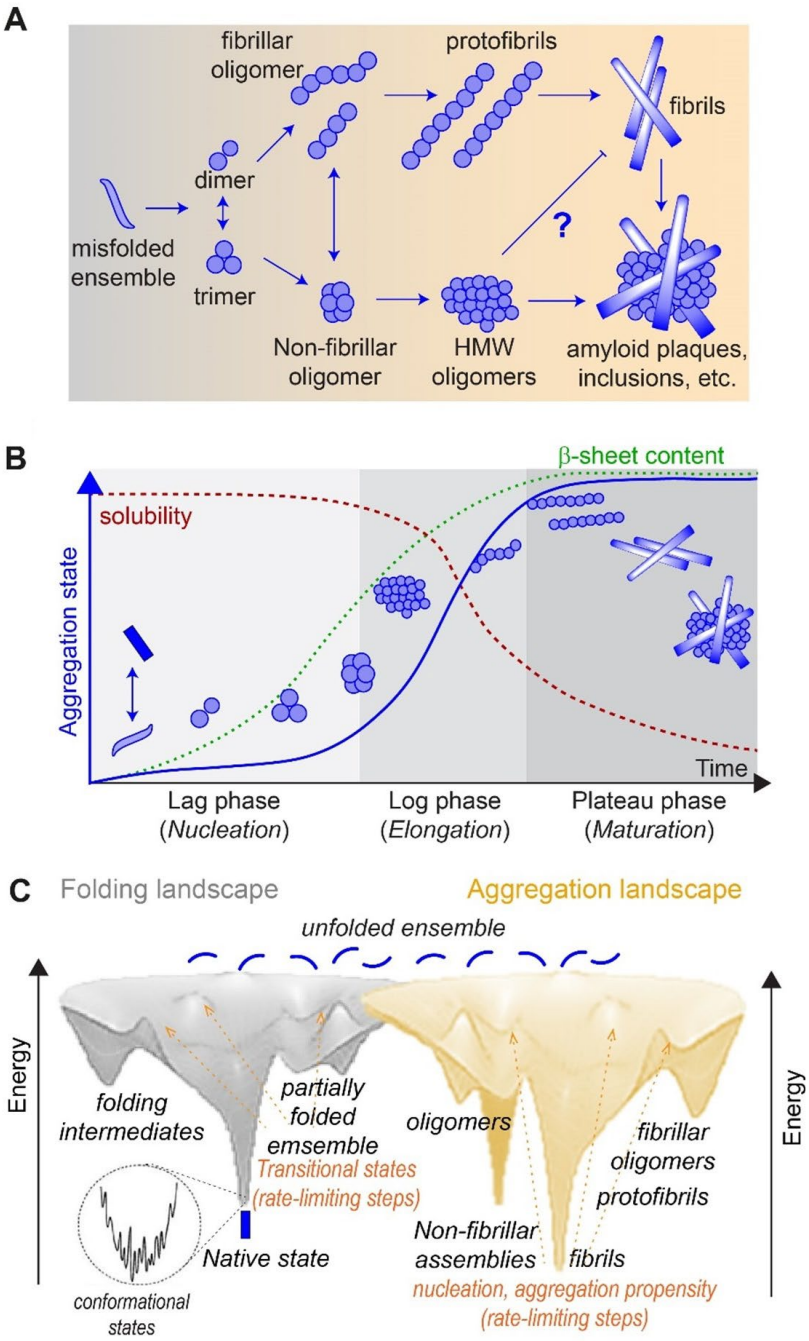

Fig. 2: Overview of the complexity of different states and phases of Aβ aggregation. A. The following are the different states in which Aβ exists: (i) monomeric state; Aβ initially exists as a monomeric peptide soluble in nature, existing in a dynamic equilibrium between disordered or partially structured conformation. (ii) conformational transitional species; monomeric Aβ undergoes conformational transitions, plausibly adopting different secondary structures, including random coil, α-helices, and β-sheets. The transition from a random coil to a β-sheet-rich conformation is considered a critical step triggering Aβ aggregation and amyloid formation. Once unfolded monomeric Aβ transforms into a misfolded ensemble, it acts as a template promoting the process of aggregation. (iii) low

molecular weight species; Aβ monomers have the propensity to self-associate and form small assemblies consisting of a few Aβ peptides. (iv) oligomeric species, which vary in size and structure and are believed to be the most toxic species during Aβ aggregation. These can exist in fibrillar and non-fibrillar oligomers. Mostly, non-fibrillar or globular oligomeric species are known to disrupt neuronal function and induce cellular toxicity. (v) protofibrillar assemblies; fibrillar oligomers can further associate and act as template to assemble into larger structures called protofibrils. Protofibrils are intermediate species on the pathway to fibril formation and may exert considerable cytotoxicity. (vi) fibrils; The ultimate outcome of Aβ aggregation is the formation of amyloid fibrils, which are insoluble, β-sheet-rich structures. Fibrils have a characteristic cross-beta structure representing one of the higher-order assemblies. (vii) High molecular weight (HMW) oligomeric assemblies; are generated from the non-fibrillar oligomeric precursors. Whether these HMW oligomers could aid in formation of fibrils is debatable, but they do substantially contribute to the formation of plaques. (viii) amyloid plaques; as fibrils accumulate, they can further associate with other cellular components, such as proteins, lipids, and extracellular matrix molecules, to form amyloid plaques. Amyloid plaques are dense deposits found in the brains of individuals with AD and are considered pathological hallmarks of the disease. B. Aβ aggregation is usually characterized by three distinct phases: the lag phase, log phase, and plateau phase. The lag phase is the initial stage of amyloid aggregation. During this phase, monomeric peptides undergo conformational changes acting as a template with a β-sheet structure to form oligomeric assemblies. These act as nucleation complexes promoting aggregation to form higher order structure. The duration of the lag phase can vary and is influenced by factors such as protein concentration, temperature, pH, and the presence of cofactors or modulators. The solubility of the aggregating species remains relatively high. The β-sheet content, which is a characteristic secondary structure associated with amyloid fibrils, remains low. Once aggregation promoting conformation templates are formed, the process enters the log phase, wherein, the population of aggregates with β-sheet conformation increases rapidly through monomer addition to the existing aggregates. This leads to the formation of larger oligomers, protofibrils, and eventually mature fibrils. The solubility of the aggregating species decreases gradually as bigger size aggregates begin to form. Oligomers and protofibrils adopt a more structured conformation, characterized by the presence of β-sheet structures. The log phase is characterized by exponential growth of the aggregate population. After the log phase, the aggregation process eventually reaches a plateau phase. In this phase, the rate of aggregation slows down, and a dynamic equilibrium is established between the formation and dissolution of aggregates. The plateau phase is often associated with the presence of mature fibrils *in vitro*. The mature fibrillar structures exhibit a stable and highly ordered β-sheet conformation, resulting in a decreased concentration of soluble species. Ultimately, these deposit *in vivo* in the form of insoluble amyloid plaques in AD patient brains. Aβ peptide exhibits variability and heterogeneity in structure and assembly states during the initiation and elongation phases of aggregation, resulting into a morphological, conformational, and clinical diversity (Aβ pools) within its aggregates and *in vivo* deposits. C. The folding landscape of Aβ refers to the complex journey that the Aβ peptide undergoes in adopting different conformations and structures as it folds and aggregates, wherein the aggregation landscape refers to the complex process by which Aβ peptides self-associate and form various structural entities, leading to the formation of amyloid aggregates, such as oligomers, protofibrils, and fibrils. It’s important to note that, both the

folding and aggregation landscape of Aβ is highly complex, dynamic, and heterogenous, involving a multitude of pathways and complex intermediates.

1.2.2. The biophysical characteristics of Aβ peptide

Aβ peptides are amphiphilic in nature, meaning they have both hydrophilic and hydrophobic regions (Soreghan et al. 1994). This amphiphilicity is attributed to the specific amino acid sequence and structural characteristics of Aβ. The central and C-terminal region of Aβ is characterized by hydrophobic amino acid residues that have a propensity to form β-sheet structures. These hydrophobic domains play a key role in β-sheet formation promoting aggregation of Aβ peptides into amyloid fibrils. (Karran et al. 2011). The central hydrophobic region, particularly residues 25-35, is considered the core amyloidogenic region because it plays a critical role in initiating and stabilizing the aggregation process. The hydrophobic interactions between these residues promote the formation of β-sheet structures, which then serve as templates for the recruitment and alignment of additional Aβ peptides (Fig. **3**). In contrast, the N-terminal region of Aβ, which consists of the first 11 amino acids, is generally considered unstructured and lacks well-defined secondary structures such as α-helices or β-sheets. When considering a misfolded monomer or an aggregated assembly, this region tends to be exposed to the solvent, making it accessible for interactions with other molecules, including receptors, enzymes, and lipids (Konstantoulea et al. 2022; Shi et al. 2022). These interactions can have various effects on Aβ function and aggregation. Aβ interacts with various molecular entities, including proteins, cell surface receptors, enzymes, proteins, lipid entities, and metal ions (Fig. **3**) (Chen et al. 2017). These include low-density lipoprotein receptor-related protein 1 (LRP1) (Bates et al. 2009; Shinohara et al. 2017), apolipoprotein E (ApoE) (Carter 2005), receptor for advanced glycation end products (RAGE) (Leclerc et al. 2009), and N-methyl-D-aspartate (NMDA) and glutaminergic AMPA receptors (Babaei 2021; Fabiani and Antollini 2019), among others. Proteases such as insulin-degrading enzyme and neprilysin, can influence Aβ clearance processes (Malito et al. 2008; Cheignon et al. 2018). Aβ peptides can also interact with lipid entities within the cellular membranes (Niu et al. 2018; Matsuzaki 2007). Specific regions within the Aβ sequence, such as the hydrophobic domain, can associate with lipid bilayers and induce membrane

disruption or alterations in membrane fluidity (Kakio et al. 2004; Ogawa et al. 2011; Hoshino et al. 2013).

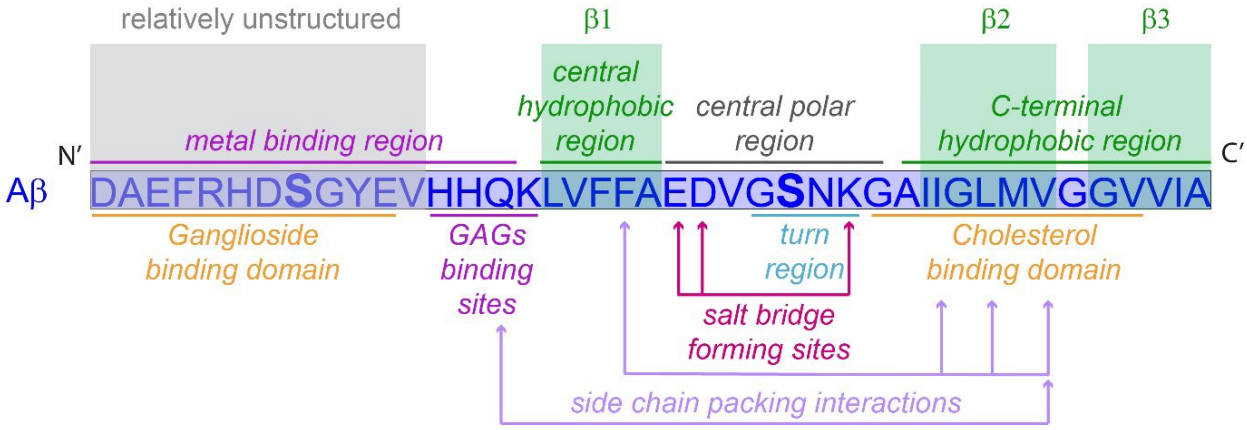

Fig. 3: Structural features and interactions of Aβ peptide. The distinct structural features of the Aβ sequence, including the unstructured N terminus, hydrophobic central region, and hydrophobic C terminus, play a significant role in the aggregation, neurotoxicity, and pathogenesis of AD. The hydrophobic segments promote self-association and the formation of β-sheet-rich structures. Amino acid sequence within the Aβ have been shown to specifically interact with metal ions, proteins, lipids as well as proteoglycans which have been depicted.

Specifically, Aβ has been shown to interact with cholesterol and gangliosides, a major component of cell membranes. Cholesterol can modulate Aβ aggregation and affect its neurotoxic properties (Gibson Wood et al. 2003; Schneider et al. 2006; Sponne et al. 2004). Aβ peptides can interact with metal ions, such as copper and zinc, which promote Aβ aggregation and enhance its neurotoxicity (Pithadia and Lim 2012; Tõugu et al. 2011; Roberts et al. 2012). Aβ has been found to interact with iron (Roberts et al. 2012; Pithadia and Lim 2012), which potentially results in the generation of reactive oxygen species (ROS) through metal-induced oxidative stress (Uranga and Salvador 2018). Overall, the interactions of Aβ with various molecular entities play a significant role in influencing Aβ aggregation, clearance, and neurotoxicity, contributing to the development and progression of the disease.

1.2.3. Post-translational modifications of Aβ

Post-translational modifications (PTMs) of Aβ refer to the chemical changes that occur within the Aβ peptide sequence, generally after it is generated from its precursor protein. (Fig. **4**) (Kummer and Heneka 2014; Roher et al. 2017). Multiple enzymatic and non-

enzymatic reactions result in racemization, isomerization, oxidation, dimerization, or addition of functional groups such as pyroglutamylation, nitration, glycosylation or phosphorylation (Atwood et al. 2002; Kummer and Heneka 2014; Kumar et al. 2011; Kumar et al. 2016). Additionally, N or C-terminal cleavages by several peptidases result in the formation of truncated Aβ species (Mosser et al. 2021; Bayer and Wirths 2014; Kummer and Heneka 2014; Becker-Pauly and Pietrzik 2016). Overall, PTMs have significant effects on the structure, aggregation, and toxicity of Aβ, thereby modulating its pathophysiological properties, in comparison to the non-modified peptide. PTMs of Aβ contribute to the heterogeneity of Aβ pools in the brain and influence their pathogenicity (Konstantoulea et al. 2022; Broncel et al. 2010; Kummer and Heneka 2014). Understanding the impact of PTMs on Aβ is essential for unraveling the mechanisms underlying AD and the specific effects of each PTM and their interactions in the context of Aβ pathology.

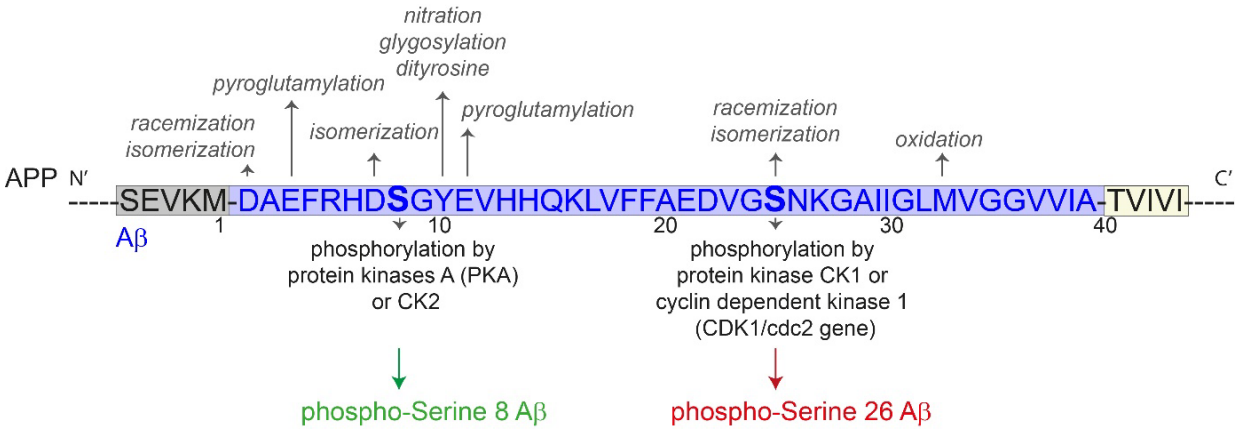

Fig. 4: Post-translational modifications (PTMs) within the Aβ sequence. Schematic representation of key PTMs that can occur within the Aβ sequence (*depicted in blue*). PTMs can alter the biophysical properties, aggregation propensity, and neurotoxicity of Aβ peptides. Putative phosphorylation sites at Serine-8 and Serine-26 within the Aβ sequence have been indicated in bold.

1.2.4. Phosphorylation-state variants of Aβ

Phosphorylation of serine, threonine, and tyrosine residues within proteins is a crucial post-translational modification that plays a significant role in mediating and regulating neuronal function (Nestler and Greengard 1983; Walaas and Greengard 1991). Aberrant protein phosphorylation, characterized by abnormal protein kinase and/or protein phosphatase activity, has been shown to modulate the pathogenesis and progression of AD (Perluigi et al. 2016; Oliveira et al. 2017; Gong et al. 2006). Changes in the patterns of protein phosphorylation not only alter the pathology of Aβ plaques but also affect the formation of tau deposits, which are another hallmark of AD (Braithwaite et al. 2012; Sontag et al. 2014; Saito et al. 2011). Extracellular Aβ can undergo phosphorylation at the two serine residues (Ser-8 and Ser-26) by distinct cell-surface localized or secreted protein kinases (Fig. **4**) (Kumar et al. 2016; Kumar et al. 2011; Milton 2001, 2005). The positioning of the serine residues renders them prone to phosphorylation, Ser-8 is localized within a consensus motif for protein kinase A (PKA) or Casein Kinase 2 (CK2), while Ser-26 residue is localized within a recognition motif for Casein Kinase 1 (CK1), protein kinase C (PKC) and cyclin dependent kinase 1 (CDK1). Phosphorylation of serine residue 8 increases the formation of higher molecular weight assemblies that represent nuclei for fibrillization and promotes aggregation (Kumar et al. 2011; Rezaei-Ghaleh et al. 2016b; Rezaei-Ghaleh et al. 2016a). On the other hand, pSer26Aβ preferentially forms intermediate oligomeric assemblies as compared to pSer8Aβ or non-phosphorylated Aβ (npAβ) peptides which form higher molecular weight assemblies, respectively (Kumar et al. 2016). These phosphorylated Aβ species, pSer8Aβ and pSer26Aβ, exhibit differential aggregation behavior and increased cytotoxic potentials compared to non-phosphorylated Aβ peptides (Kumar et al. 2016; Kumar and Walter 2011; Kumar et al. 2011). Using phosphorylation state- and site-specific antibodies generated in the lab, the presence and deposition of these phosphorylated Aβ (pAβ) species in transgenic animal models as well as human AD cases were previously reported (Kumar et al. 2011; Kumar et al. 2012; Kumar et al. 2016; Kumar et al. 2020b; Kumar et al. 2020a; Kumar et al. 2013). The overall levels of phosphorylated Aβ species are estimated to be no more than 20-30% of the total Aβ pools, but accumulation of pAβ could be a key contributor to the development and progression of AD. Further research is needed to fully understand the mechanisms and implications of phosphorylated Aβ in AD pathobiology.

1.3. Postulated hypotheses in the field of AD

Despite extensive research, the exact cause of AD remains elusive. However, researchers have proposed several hypotheses for the underlying mechanisms of the disease. These hypotheses provide frameworks for investigating the complex etiology of AD and guide ongoing research efforts to validate and refine these theories, as well as explore other potential factors involved. Understanding the intricacies of these underlying mechanisms is crucial for the development of effective treatments and interventions to improve the lives of those affected by this debilitating condition.

1.3.1. Amyloid cascade hypothesis

The amyloid cascade hypothesis postulates that accumulation of Aβ peptides in the brain is the primary cause which triggers a series of events leading to the pathogenesis of AD (Hardy and Higgins 1992). According to this hypothesis, the build-up of amyloid plaques initiates a cascade of pathological processes, including the formation of neurofibrillary tangles and ultimately neuronal death. Numerous studies have supported the amyloid cascade hypothesis in both familial and sporadic AD cases. This is one of the most well-known and influential hypotheses guiding AD research for several decades and influencing drug development efforts targeting Aβ (Bayer and Wirths 2014; Dong et al. 2012; Wu et al. 2022; Karran et al. 2011; Selkoe and Hardy 2016). Conversely, the hypothesis has also faced challenges and criticism (Karran and Strooper 2016; Herrup 2015; Pimplikar 2009; Hardy and Selkoe 2002; Haass and Selkoe 2022).

1.3.2. Amyloid-β oligomer hypothesis

According to the amyloid-β oligomer hypothesis, the primary cause of AD is the malfunctioning of the processes involved in the production, accumulation, or disposal of oligomeric Aβ species (Cline et al. 2018; Lambert et al. 1998; Klein 2001; Klein 2006). The hypothesis proposes that soluble forms of Aβ oligomers (abbreviated as AβO) or the amyloid-derived diffusible ligands (abbreviated as ADDLs, (Klein 2006)); rather than higher molecular weight amyloid aggregates/plaques, are the primary culprits in AD. AβOs disrupt the normal functioning of neurons, leading to neuronal death and ultimately cognitive impairment and neurodegeneration (Selkoe 2008b; Klein 2006). Experiments using animal models have shown that the injection of Aβ oligomers into the brain impairs

synaptic plasticity and memory. Additionally, post-mortem analyses of AD brains has revealed the presence of Aβ oligomers in regions associated with cognitive decline (Tomic et al. 2009). Unlike amyloid plaques, which are insoluble and can be detected using imaging techniques, AβOs or ADDLs are generally difficult to detect and to isolate due to their transient and heterogeneous assembling-disassembling nature (Walsh and Selkoe 2007; Klein 2006; Klein 2001; Shea and Daggett 2022; Rosenblum 2014). Studies have provided evidence that Aβ oligomers present in AD brains, rather than amyloid plaques, correlate with cognitive decline and neurodegeneration (Lacor et al. 2004; Cleary et al. 2005; Selkoe 2008a; Jongbloed et al. 2015). Thus, AβOs have been the subject of much research on AD pathogenesis and are now considered an important target for the development of potential therapeutic interventions (Walsh and Selkoe 2020; Guerrero-Muñoz et al. 2014). Despite considerable debate surrounding the hypothesis in recent decades, it remains one of the most highly regarded explanations for AD (Cline et al. 2018; Rosenblum 2014; Viola and Klein 2015).

Aim: The first part of this study was to understand how phosphorylation-state dependent differences in Aβ aggregation alter its solubility and oligomerization propensity.

1.3.3. Oxidative Stress and mitochondrial dysfunction hypothesis

The oxidative stress hypothesis proposes that an imbalance between the production of reactive oxygen species (ROS) and the brain's antioxidant defense mechanisms initiates AD pathogenesis (Picone et al. 2014; Moreira et al. 2010; Hirai et al. 2001). This hypothesis suggests that increased oxidative damage to neurons leads to cellular dysfunction and neuronal death (Wang et al. 2020; Markesbery 1997; Praticò 2008). On similar lines, mitochondria, which are regarded as the powerhouse of the cell, play a significant role in AD. (Wang et al. 2020). Mitochondrial dysfunction can lead to increased oxidative stress, impaired energy production, and the release of toxic redox species (Fig. **5**), ultimately contributing to neurodegeneration and cognitive decline.

1.3.4. Glial cell dysfunction and the neuroinflammation hypothesis

The involvement of glial cells, particularly microglia and astrocytes, in AD has been a topic of interest in recent research (Rostami et al. 2021; Streit et al. 2004). The glial cell dysfunction hypothesis suggests that dysfunctional glial cells fail to properly clear toxic

substances, leading to an accumulation of these substances and subsequent inflammation. This inflammation disrupts neuronal function, ultimately resulting in neuroinflammation, neuronal damage, and cognitive decline (Fig. **5**) (Heneka et al. 2015). The chronic neuroinflammation observed in AD is believed to play a significant role in the pathogenesis of the disease. The immune response plays a role in the development and progression of AD, with literature highlighting the significance of neuroinflammation, microglial activation, glial cell dysfunction, as well as the involvement of the complement system; underscoring the importance of additional research in this field. (Shah et al. 2021; Leng and Edison 2021; Nagele et al. 2004). Understanding the mechanisms underlying glial cell dysfunction and neuroinflammation may provide insights into the development of therapeutic strategies for AD.

1.3.5. Miscellaneous hypotheses

Various other hypotheses have also been proposed addressing the complex mechanisms underlying AD pathophysiology. One such hypothesis is the tau hypothesis, which suggests that abnormal phosphorylation and aggregation of tau protein within neurons are central drivers of neurodegeneration (Mohandas et al. 2009; Maccioni et al. 2010). This hypothesis is also in conjugation or in part with the amyloid hypothesis discussed earlier. Although the amyloid cascade and AβO hypothesis have been the mainstream concepts driving most of the AD research globally for the past decades, most of the clinicals trails have ended up in failures. The tau hypothesis postulates that tau, and not Aβ, is the main factor underlying the progression of AD (Kametani and Hasegawa 2018; Savelieff et al. 2013). This has led to a polarization of beliefs among researchers (Mudher and Lovestone 2002; Benjamin Yang 2009; Frisoni 2023; Trojanowski 2002).

Other hypotheses focus on different aspects of AD pathogenesis. Synaptic failure and the cholinergic hypothesis emphasize synaptic dysfunction (Sheng et al. 2012; Marcello et al. 2012) and the degeneration of cholinergic neurons (Francis et al. 1999; Majdi et al. 2020), respectively, contributing to cognitive deficits. The network hypothesis posits that disrupted connectivity and communication between brain regions, especially those involved in memory and cognition, contribute to cognitive impairments in AD (Brier et al. 2014; Frere and Slutsky 2018). The vascular hypothesis links vascular dysfunction, such as impaired blood flow and compromised blood-brain barrier integrity, to AD development,

particularly in the context of vascular risk factors (La Torre 2010). Genetic factors also play a significant role in AD. APP, PSEN1, and PSEN2, as well as APOE identified as AD-risk genes associated with early-onset familial (as well as late-onset AD, to certain extent); are the subject of extensive research (Lambert and Amouyel 2011). The epigenetic hypothesis suggests that modifications in gene expression patterns play a role in AD pathogenesis (Bellenguez et al. 2020). These diverse hypotheses collectively contribute to the understanding of the multifaceted nature of AD. These hypotheses are not to be deemed mutually exclusive, and they may contribute factorially to alterations in Aβ metabolism, but the cause-consequence relationship remains unclear. It is very likely that a combination of multiple factors contributes to the development and progression of AD.

1.4. Membrane interaction and intracellular occurrence of Aβ

Along with progressive accumulation in extracellular deposits, Aβ species is also detected intracellularly (Cuello 2005; Glabe 2001; Oddo et al. 2006). Numerous reports in the literature suggest and argue that along with extracellular Aβ, intracellular Aβ, is linked to compromised cellular homeostasis, ultimately leading to neuronal death (Oddo et al. 2006; Glabe 2001; Cuello and Canneva 2008; Bayer and Wirths 2010; Zheng et al. 2012; Roos et al. 2021). Aβ fibrils accumulate outside of neurons and form plaques, wherein the soluble or other smaller aggregated assemblies exist both extracellularly and intracellularly (Cuello 2005; Finder and Glockshuber 2007). These intracellular Aβ species can take various forms, including lower and higher molecular weight oligomeric assemblies. Aβ species inside cells are believed to contribute to cellular dysfunction, potentially interfering with intracellular processes, disrupting protein homeostasis, impairment of organelle function, and triggering cellular stress responses (Fig. **5**). The presence of intracellular Aβ has been associated with neuronal dysfunction, synaptic loss, and ultimately, neurodegeneration (Okazawa 2021; LaFerla et al. 2007; Glabe 2001; Cuello and Canneva 2008; Bayer and Wirths 2010).

The plasma membrane poses as the primary barrier preventing the entry of any foreign material into the cell. For Aβ to induce neurotoxicity its interaction with cellular membranes is pertinent (Gibson Wood et al. 2003; Niu et al. 2018) and Aβ-membrane interactions are being widely studied (Stefani 2010; Niu et al. 2018). Aβ peptides can directly interact with

lipid molecules in the cellular membrane (Williams and Serpell 2011). Aβ peptides are amphipathic, meaning they have both hydrophobic and hydrophilic regions (Fig. **3**). The positively charged amino acid residues of Aβ (lysine and arginine) can interact with negatively charged phospholipids present in the cellular membrane, such as phosphatidylserine or gangliosides (Teixeira et al. 2012). These electrostatic interactions can facilitate the binding of Aβ to the membrane surface (Williams and Serpell 2011; Niu et al. 2018). The hydrophobic region of Aβ, containing mainly nonpolar amino acid residues, can interact with the hydrophobic core of the lipid bilayer in the cellular membrane (Fig. **3**). These hydrophobic interactions can promote the insertion of Aβ into the membrane, leading to the formation of membrane associated Aβ aggregates (Williams and Serpell 2011; Matsuzaki 2020). Lipid rafts are specialized microdomains within the cellular membrane that are enriched in specific lipids, including cholesterol and sphingolipids (Cordy et al. 2006). Aβ peptides have been found to associate with lipid rafts, which may facilitate their interactions with other proteins and signaling molecules. This association with lipid rafts could affect Aβ aggregation and cellular responses to Aβ toxicity (Fabiani and Antollini 2019; Lai and McLaurin 2010).

Aβ peptides have been shown to interact with and disrupt the lipid bilayer structure of the cellular membrane (Matsuzaki 2007, 2020; Williams and Serpell 2011). The insertion of Aβ into the membrane can disturb the integrity and fluidity of the lipid bilayer, leading to membrane destabilization/permeabilization, resulting in leakage of cytosolic subcellular material. This disruption of membrane integrity can occur through the formation of ion channels or pores by Aβ species (Lin et al. 2001; Shirwany et al. 2007). Several reports have also indicated that Aβ peptides could induce changes in the curvature of the cellular membrane (Terakawa et al. 2018). This can occur through interactions with specific regions of the membrane, causing local deformations. The induction of membrane curvature by Aβ may influence its aggregation propensity and the subsequent formation of amyloid fibrils. Also, Aβ impacts fluidity and dynamics of the cellular membrane. They can affect the movement and organization of lipids within the membrane, influencing their physical properties. Aβ peptides have been shown to interact with specific membrane receptors, such as neuronal receptors or immune receptors, along with various membrane proteins, including receptors and ion channels, thereby modulating intracellular signaling pathways (Verdier et al. 2004; Nagele et al. 2002). These interactions modulate the

activity and function of these proteins, affecting cellular processes, signaling pathways, and can also trigger cellular responses, including inflammation, oxidative stress, and apoptosis, which are associated with AD pathogenesis (Williams and Serpell 2011).

There have been multiple proposals postulated for the presence of Aβ intracellularly. One of the widely believed and proven mechanisms is that Aβ peptides can be internalized by cells through endocytosis (Cirrito et al. 2008; Wu and Yao 2009; Zadka et al. 2023; Mohamed and Posse de Chaves 2011). Additionally, multiple mechanisms of Aβ internalization described in literature, these include receptor-mediated uptake processes, interaction with lipids (lipid rafts) and ion channels as well as formation of amyloid-like ion channels (Mohamed and Posse de Chaves 2011; Bharadwaj et al. 2018; Kayed and Lasagna-Reeves 2013; Glabe 2001; Oddo et al. 2006; Lai and McLaurin 2010). It is important to note that apart from interactions of extracellular Aβ pools with lipids and receptors at the membrane, facilitating its internalization, Aβ can also be generated by APP processing intracellularly within subcellular vesicles (Oddo et al. 2006; LaFerla et al. 2007; Glabe 2001; Cataldo et al. 2004). This intraneuronal processing of APP further adds to the pool of intracellular Aβ. The quantitative division of Aβ species resulting from sub-cellular/vesicular processing of APP or re-uptake of Aβ from extracellular space via different internalization mechanisms has not yet been elucidated and has been in debate in the past decades. Along with extracellular deposition, pAβ peptides were also detected intracellularly, in the early stages in animal AD models (Kumar et al. 2013; Kumar et al. 2016; Kumar et al. 2011; Kumar et al. 2020a; Joshi et al. 2021a) as well as human AD cases (Kumar et al. 2020b).

Aim: The next objective of this study was to link the differences in solubility and oligomerization properties of pAβ peptides to their intracellular accumulation and subsequent cytotoxicity.

Intracellular Aβ accumulation can also result from impaired clearance mechanisms (Tarasoff-Conway et al. 2015; Wildsmith et al. 2013). Cellular degradation pathways, such as autophagy, lysosomal or proteasomal function, serve as primary cellular mechanisms responsible for clearing Aβ. These processes are disrupted in AD, augmenting intracellular accumulation of Aβ (Bates et al. 2009; Kanekiyo et al. 2013; Tarasoff-Conway et al. 2015; Vilchez et al. 2014). As a result, intracellular Aβ levels may increase over time.

Recent studies have also suggested that intracellular Aβ may interact with other proteins within the cell, impairing cellular processes leading to further toxicity and cellular damage (Wildsmith et al. 2013; Marshall et al. 2020; Cuello and Canneva 2008). Multiple reports have shown the presence of intracellular Aβ to affect autophagy and lysosomal degradation or ubiquitin proteasomal function (Cao et al. 2019; Zhang et al. 2017; Cataldo et al. 2004), facilitating the vicious cycle of intracellularly retaining Aβ. It is still under debate whether age dependent or Aβ induced impaired clearance mechanisms cause or effect of intracellular presence of Aβ (Tarasoff-Conway et al. 2015). Furthermore, intracellular Aβ has also been implicated in the spreading of Aβ pathology from one cell to another (Eisele and Duyckaerts 2016; Sengupta et al. 2016). It is hypothesized that intracellular Aβ species can be released from cells and taken up by neighboring cells, contributing to the propagation of Aβ within different regions of the diseased brain.

1.5. Intraneuronal Aβ alters subcellular organelle function

Intraneuronal Aβ can alter subcellular organelle function, leading to neuronal dysfunction and cell death (Penke et al. 2012; Langui et al. 2004; Harris and Fahrenholz 2005; Gouras et al. 2005; Gouras et al. 2010; Omtri et al. 2018; Umeda et al. 2011; Wirths and Bayer 2012; Takahashi et al. 2002; Takahashi et al. 2017; Roos et al. 2021; Gouras et al. 2000). The differential impact of intraneuronal Aβ on subcellular organelles highlights the complex and multifaceted nature of Aβ-induced cellular dysfunction in AD. The precise mechanisms by which intraneuronal Aβ alters intracellular organelle function ultimately disrupting fundamental cellular processes (Fig. **5**) are complex and not fully understood. Their contribution to neurodegeneration and cognitive decline is being widely investigated.

1.5.1. Autophagy and endo-lysosomal dysfunction in AD

Autophagy is a process by which cells degrade and recycle damaged or dysfunctional proteins and organelles, while the endo-lysosomal system is responsible for the degradation of extracellular proteins and the recycling of cellular membrane components (Finkbeiner 2020). Neuronal autophagy, and the endo-lysosomal pathway play an important role in the intracellular trafficking and accumulation of Aβ (Nixon 2007; Nixon and Yang 2011; Colacurcio et al. 2018; Orr and Oddo 2013). In AD, the accumulation of Aβ peptides can interfere with both autophagy and endo-lysosomal function, leading to

the build-up of toxic protein aggregates and contributing to neurodegeneration (Capetillo-Zarate et al. 2012; Gouras et al. 2005; Malik et al. 2019; Nixon et al. 2001; Wang et al. 2018). Aβ has been shown to impair autophagy by inhibiting the formation of autophagosomes (Nixon 2007; Nixon and Yang 2011) or by blocking the fusion of autophagosomes with lysosomes (Ntsapi et al. 2018; Wen et al. 2018), where the degradation of cargo occurs. Literature reports showed that Aβ can also interfere with endo-lysosomal function by disrupting lysosomal acidification and impairing the activity of lysosomal enzymes (Marshall et al. 2020; Umeda et al. 2011; Yang et al. 1998; Zheng et al. 2012). As the process of degradation is impaired, Aβ species remain compartmentalized within these dysfunctional organelles (Kimpe et al. 2013; Brewer et al. 2020; Pacheco-Quinto and Eckman 2013), impacting cellular homeostasis. Examination of Aβ plaque pathology in AD brains showed the presence of dystrophic neurites (Dickson et al. 1999; Sharoar et al. 2019; Shoji et al. 1990), enlarged autophagic vesicles (Nilsson et al. 2013; Nixon et al. 2005; Nixon and Yang 2011; Nixon 2007) as well as endo-lysosomal structures (Colacurcio et al. 2018; Gowrishankar et al. 2015; Takahashi et al. 2002; Roos et al. 2021; Cataldo and Nixon 1990) within or around the Aβ plaque core. Thus, the impact of Aβ on autophagy and endo-lysosomal system may play a role in contributing to AD pathology.

1.5.2. Effects of Aβ on the ubiquitin proteasomal system

The ubiquitin-proteasome system (UPS) is a cellular mechanism responsible for the degradation of damaged or misfolded cytosolic proteins as well as for constitutive protein turn-over (Nandi et al. 2006; Upadhya and Hegde 2007). The system involves the tagging of proteins with ubiquitin molecules for targeted degradation by the proteasome. Multiple reports have shown that Aβ can cause permeabilization of endo-lysosomal membranes and escape into cytosolic space (Yang et al. 1998; Zaretsky et al. 2022; Kayed et al. 2004). In AD the intracellular accumulation of Aβ peptides has been shown to interfere with the UPS, leading to the buildup of toxic protein aggregates within the cytosol, contributing to neurodegeneration (Hong et al. 2014). Literature reports have shown that Aβ induced UPS dysfunction occurs by impairing the function of ubiquitin ligases, which are responsible for adding ubiquitin to target proteins (Wolfe and Cyr 2011; Hong et al. 2014). Aβ species have also been shown to inhibit the activity of the proteasome, thereby

leading to accumulation of proteasomal machinery associated compartments (Lopez Salon et al. 2003; Oh et al. 2005; Tseng et al. 2008; Upadhya and Hegde 2007; Zhang et al. 2017). Interestingly, Aβ plaques also show accumulation of ubiquitin and proteasomal markers indicating potential contribution of UPS to plaque pathology (Zhang et al. 2017; Nandi et al. 2006; Hong et al. 2014).

1.5.3. Aβ induced ER stress response and mitochondrial dysfunction

Endoplasmic reticulum (ER) stress response and mitochondrial function are two cellular processes that have been shown to be disrupted by the accumulation of Aβ species intracellularly (Butterfield and Boyd-Kimball 2020; Onyango and Khan 2006; Praticò 2008; Umeda et al. 2011). The ER is responsible for the synthesis, folding and processing of membrane-associated and secretory proteins. Aβ has been shown to initiate ER stress response by causing the accumulation of misfolded proteins in the ER lumen, thereby interfering with ER protein folding functions (Penke et al. 2012; Penke et al. 2017; Pande and Srivastava 2019). This can activate the unfolded protein response (UPR), a cellular mechanism that attempts to restore ER homeostasis by reducing protein synthesis and increasing the degradation of misfolded proteins (Pande and Srivastava 2019; Gerakis and Hetz 2018). Chronic activation of the UPR has been involved in neuronal death in AD pathogenesis (Chen et al. 2015).

Mitochondria which play a crucial role in cellular energy production and are also involved in regulating cell death, also represent a potential target for Aβ induced toxicity (Calvo-Rodriguez and Bacskai 2021; Butterfield and Boyd-Kimball 2020; Hirai et al. 2001). Aβ has been shown to interfere with the normal functioning of mitochondria (Moreira et al. 2010; Picone et al. 2014). Aβ can disrupt the mitochondrial homeostasis by affecting mitochondrial fragmentation, fission-fusion cycles, thereby perturbing mitochondrial structure, integrity, and function. Aβ-induced mitochondrial dysfunction has been associated with alterations in the electron transport chain, which is responsible for the production of ATP, leading to decreased energy production and increased oxidative stress and neuronal death, ultimately resulting in synaptic damage and cognitive decline (Picone et al. 2014; Santos et al. 2010; Zhang et al. 2016; Mecocci et al. 1994).

Aim: Thus, one of the goals was to elucidate phosphorylation-state dependent effects of Aβ on subcellular organelle function and neuronal homeostasis.

1.6. Cell death associated pathways in response to Aβ

The effect of Aβ induced dysfunction in cellular homeostasis is instigated by impairing the function of essential organelles, which ultimately results in cytotoxicity (Bayer and Wirths 2010; Cuello and Canneva 2008; Glabe 2001; Kimpe et al. 2013; LaFerla et al. 2007; Nagele et al. 2002; Okazawa 2021; Zheng et al. 2012). It is important to note that dysfunction of subcellular compartments can trigger specific cell death-associated pathways (Denton et al. 2015; González-Polo et al. 2005; Kroemer and Jäättelä 2005; LaFerla et al. 1997; Umeda et al. 2011; Guérin et al. 2008).

Apoptosis is a highly regulated form of programmed cell death, which has been connected to neuronal loss in AD (Behl 2000; Majd et al. 2015; Li et al. 2007). Aβ induced activation of apoptotic pathways could include and result in the activation of caspases, a family of proteases involved in apoptosis (Eimer and Vassar 2013; Fossati et al. 2012; Hyman 2011). Aβ-induced apoptosis can be mediated through the intrinsic mitochondrial pathway, or the extrinsic death receptor pathway (Leong et al. 2020; Fossati et al. 2012). Aβ accumulation can generate oxidative stress, which is characterized by an imbalance between the production of reactive oxygen species (ROS) and the antioxidant defense system (Butterfield and Boyd-Kimball 2020; Markesbery 1997; Mecocci et al. 1994; Onyango and Khan 2006; Picone et al. 2014). Excessive ROS can cause damage to cellular components, including lipids, proteins, and DNA. Oxidative stress can lead to cellular dysfunction, activation of pro-apoptotic signaling pathways, and ultimately neuronal death. Aβ induced prolonged or severe ER stress can initiate apoptotic pathways and contribute to neuronal death (Praticò 2008; Gerakis and Hetz 2018; Onyango and Khan 2006). Activation of these pathways can result in the cleavage of cellular proteins, DNA fragmentation, and ultimately the dismantling of the neuron (Mecocci et al. 1994).

On the other hand, necrosis is a form of cell death characterized by rapid cell swelling, membrane rupture, and inflammation. Necrotic cell death has also been suggested as a potential mechanism for Aβ-induced cytotoxicity in neurons (Okazawa 2021; Tanaka et al. 2020). The excessive accumulation of Aβ peptides and the subsequent disruption of

cellular membranes or dysregulation of cellular homeostasis can trigger necrotic cell death mechanisms (Leong et al. 2020; Zaretsky et al. 2022; Zaretsky and Zaretskaia 2021b). Additionally, Aβ induced activation of cell death pathways directly or indirectly triggers multiple inflammatory responses, involving the activation of glial cells (Nagele et al. 2004; Verdier et al. 2004). The release of pro-inflammatory molecules by microglia, such as cytokines and chemokines, contribute to localized neuroinflammation affecting neighboring cells. Aβ induced chronic neuroinflammation further aggravates neuronal death, leading to neuronal loss (Heneka et al. 2015; Leng and Edison 2021; Rostami et al. 2021; Streit et al. 2004).

Aim: The next aspect of this study was to understand the role of intraneuronal pAβ in activation/regulation of cell death associated pathways.

1.7. Interactions between neurons, microglia, and Aβ

Neurons are responsible for producing and secreting Aβ peptides through sequential cleavage of APP by β-secretase and γ-secretase enzymes (Chow et al. 2010). Along with neuronal autophagy-lysosomal and proteasomal cargo degradation machinery, microglia also play a key role in the clearance of Aβ (Mandrekar et al. 2009; Rostami et al. 2021; Frigerio et al. 2021).

1.7.1. Cell-to-cell spreading of Aβ species

In the progression of AD pathology, the interneuronal spreading or neuron-to-glial transfer of Aβ species is being investigated by many research groups (Eisele and Duyckaerts 2016; Esler et al. 2000; Jucker and Walker 2013; Li et al. 2022; Sardar Sinha et al. 2018; Sengupta et al. 2016). There have been multiple pathways postulated which involve the synaptic transmission, wherein Aβ can be released from neurons into the synaptic cleft during synaptic exocytosis. Aβ can undergo trans-synaptic transfer, where it is passed from one neuron to another across synapses and endocytosis (Eisele and Duyckaerts 2016; Li et al. 2022; Spires-Jones and Hyman 2014). Also, extracellular Aβ can interact with neighboring neurons and could be potentially internalized via endocytic mechanisms previously described (Mohamed and Posse de Chaves 2011). A phenomenon that has also been described is the transcytosis of Aβ, wherein Aβ is internalized by one part of a neuron, transported through the neuron, and then released at a different location,

potentially allowing Aβ to propagate from one region of the brain to another (Zhao et al. 2015; Domínguez-Prieto et al. 2018; Pflanzner et al. 2011).

Aβ can also be released from neurons via exocytosis (Liu and Hong 2005), allowing it to potentially affect neighboring cells. In this scenario, Aβ can be packaged into small membrane-bound vesicles secreted by cells such as exosomes and other extracellular vesicles (Rajendran et al. 2006; Sardar Sinha et al. 2018). Exosomes and other extracellular vesicles play a significant role in the cell-to-cell specific communication within the brain and have been shown to contribute to the spread of Aβ pathology in AD (Sharma et al. 2013). These small membranous structures released by various cell types, including neurons or glial cells, contain a cargo of proteins, lipids, nucleic acids, and other molecules, including Aβ (Malm et al. 2016). Exosomes are generated through the process of inward budding of endosomal membranes, forming intraluminal vesicles within multivesicular bodies (MVBs). Subsequently, MVBs fuse with the plasma membrane, releasing the intraluminal vesicles as exosomes into the extracellular space (Edgar et al. 2015; Verbeek et al. 2002). The released vesicles positive with Aβ species can be taken up by neighboring neurons or glial cells, resulting in the transfer of Aβ between cells (Rajendran et al. 2006; Sardar Sinha et al. 2018; Sharma et al. 2013; Asher et al. 2020). Several mechanisms proposing exosome-mediated transfer of Aβ pathology have been discussed in literature and is also widely under critical investigation (Sardar Sinha et al. 2018; Esler et al. 2000; Eisele and Duyckaerts 2016).

1.7.2. Microglial clearance of Aβ

Microglia have the ability to phagocytose and remove Aβ species from the brain (Block et al. 2007). As discussed earlier, Aβ species exist in the brain both in soluble and in fibrillar forms, and microglia have been shown to interact with these two forms of Aβ in different ways. They recognize and bind to soluble Aβ through various receptors, internalizing Aβ through endocytosis or via micropinocytosis (Bell et al. 2007; Zlokovic et al. 1996). The interaction between insoluble forms of Aβ and innate immune system initiates intracellular signaling cascades that stimulate glial phagocytosis (D'Andrea et al. 2004). Inflammatory responses influence the activation status of microglia and regulate their ability to take up and degrade Aβ. ApoE, one of the major genetic AD risk factors, plays a critical role in regulating microglial activation and Aβ clearance (Carter 2005; Wolfe et al. 2018). ApoE4,

an isoform of ApoE, impairs microglial Aβ phagocytosis compared to ApoE3 (Lefterov et al. 2023). Moreover, the receptors for ApoE, such as the low-density lipoprotein receptor-related protein-1 (LRP1) and the triggering receptor expressed on myeloid cells 2 (TREM2), have also been implicated in modulating microglial function and Aβ clearance (Wolfe et al. 2018; Joshi et al. 2021b; Joshi et al. 2021a).

Microglia can also interact with neurons through direct cell-to-cell contact and signaling, thereby modulating synaptic function and plasticity. Studies have shown that Aβ peptides can directly activate microglia, triggering morphological and functional changes (Morgan et al. 2005; Leng and Edison 2021; Joshi et al. 2021b). A significant correlation between plaque size and the number of associated microglia has been shown, suggesting that the extent of microglial activation is influenced by the size of amyloid plaques (Wegiel et al. 2003; Wegiel et al. 2001). However, in the process of clearing Aβ species, microglia can become dysfunctional and less efficient in clearing Aβ, contributing further to AD pathology (Boon et al. 2018; Heneka et al. 2015; Streit et al. 2004). The interactions between neurons, microglia, and Aβ are intricate and dynamic, wherein the physiological balance between neuronal Aβ production, neuronal/glial-associated clearance, and neuroinflammation is crucial in AD pathophysiology.

Aim: An additional goal was to assess the neuronal exosome-mediated transfer of pAβ species to microglial cells and its subsequent effect on microglial homeostasis.

1.7.3. Aβ induced microglial inflammation

ASC (Apoptosis-associated Speck-like protein containing a CARD) is a key component of the inflammasome, which is a multiprotein complex involved in the regulation of inflammation and immune responses. In response to various stimuli, including Aβ, the inflammasome can be activated in microglial cells (Leng and Edison 2021; Morgan et al. 2005). Cytosolic ASC proteins undergo oligomerization resulting in the formation of a ‘speck’ termed as an ‘ASC speck’, observed with activated microglia (Fig. **5**) (Heneka et al. 2015; Hulse and Bhaskar 2022; Venegas et al. 2017; Friker et al. 2020). This process is tightly linked particularly to the activation of NLRP3 inflammasome. Additionally, ASC have been reported to have an intrinsic property to co-aggregate with cytosolic proteins (including Aβ) through non-specific hydrophobic interactions (Venegas et al. 2017; Friker

et al. 2020; Hulse and Bhaskar 2022). These aggregated ASC protein specks serve as a platform to recruit and activate caspase-1, an inflammatory caspase involved in the processing and secretion of pro-inflammatory cytokines, particularly interleukin-1β (IL-1β) and interleukin-18 (IL-18) (Hulse and Bhaskar 2022; Salminen et al. 2008; Franklin et al. 2014). These cytokines are potent mediators of inflammation and can contribute to neuroinflammation in the brain (Heneka et al. 2015; Boon et al. 2018; Barczuk et al. 2022; Leng and Edison 2021; Streit et al. 2004). Literature reports have shown that release of IL-1β and IL-18 from microglia initiates and amplifies the inflammatory response in the presence of Aβ. Thus, neuroinflammation can further exacerbate Aβ-induced neurotoxicity and contribute to the progression of AD. The formation of ASC specks in microglia in response to Aβ accumulation highlights the involvement of the inflammasome pathway in AD pathogenesis (Barczuk et al. 2022; Hulse and Bhaskar 2022; Hanslik and Ulland 2020).

Aim: The final goal of this thesis was to understand the contribution of pAβ to microglial dyshomeostasis and neuroinflammation in AD.

In summary, this thesis aims to

- *(i) elucidate the effects of phosphorylation in Aβ aggregation, solubility, and oligomerization propensity*
- *(ii) understand phosphorylation-state specific effects of Aβ on intracellular accumulation, subcellular organelle function and neuronal homeostasis*
- *(iii) characterize the involvement of intraneuronal pAβ in exosome-mediated transfer and their contribution to microglial activation.*

The culmination of this research would shed light on the contribution of pAβ to neuronal (dys)function and microglia-associated neuroinflammation in AD.

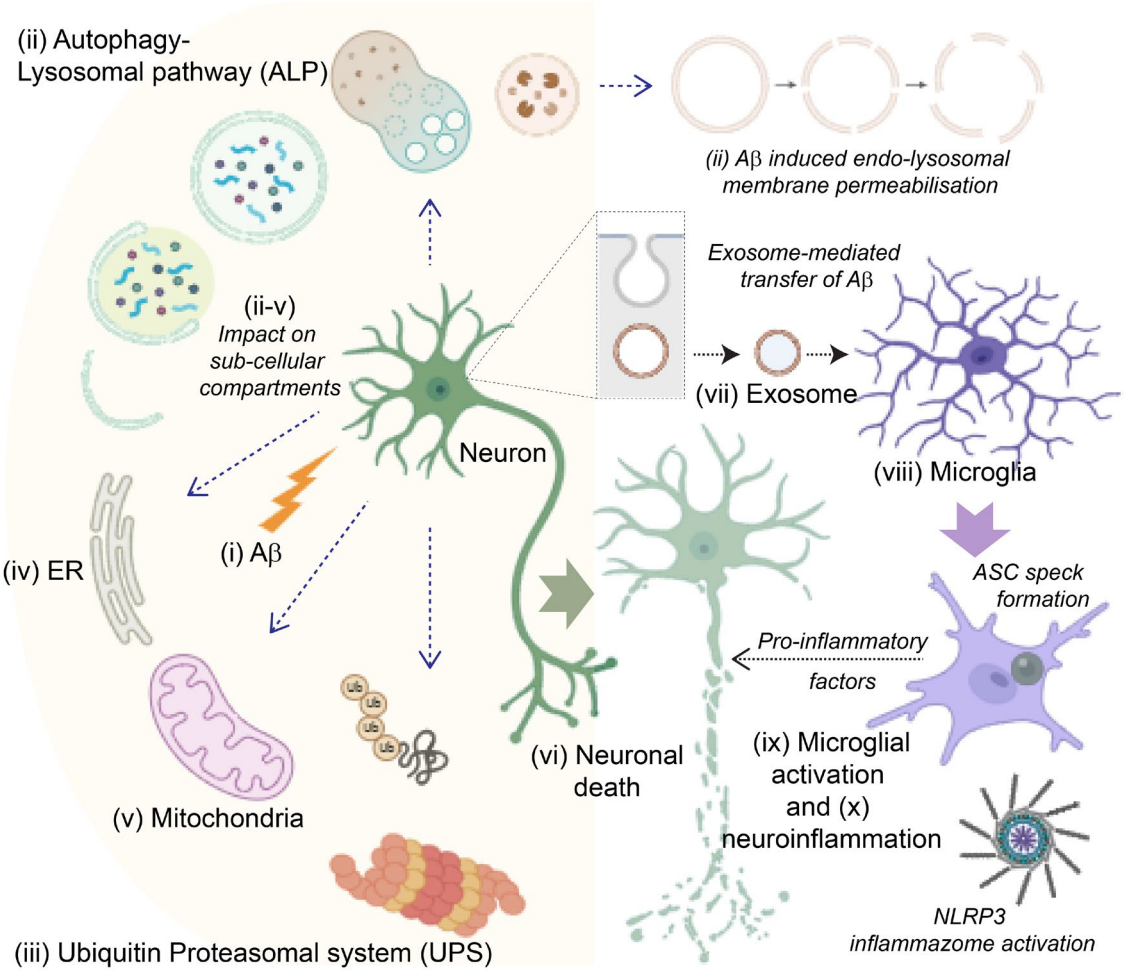

Fig. 5: The pathophysiological impact of Aβ in AD. The impact of Aβ in AD is multifaceted and involves various cellular processes. Literature reports have demonstrated intracellular uptake (i) and accumulation of Aβ within subcellular autophagic vesicles and endosomal or lysosomal compartments (ALP). Also, dysfunction within the autophagy and endo-lysosomal pathway could promote the intracellular production of Aβ peptides (ii). There are also reports postulating Aβ induced permeabilization of vesicular and cellular membranes. Furthermore, the ubiquitin-proteasome system (UPS), another cellular pathway involved in protein degradation, is also affected by Aβ (iii). Additionally, impaired autophagy and proteasomal regulation leads to the accumulation of damaged organelles and proteins, contributing to neuronal dysfunction and neurodegeneration. Intraneuronal Aβ can induce endoplasmic reticulum (ER) stress, leading to the activation of the unfolded protein response (iv). Subsequently Aβ has also been implicated in mitochondrial dysfunction and oxidative stress (v). These cellular dysfunctions can ultimately contribute to initiating and/or promotion of cell death pathways in AD (vi). The exosome-associated transfer of Aβ (vii) has been reported as a mechanism for neurons to microglia Aβ crosstalk (viii). In AD pathophysiology, Aβ is involved in microglial activation, which plays a key role in the neuroinflammatory response (ix). Aβ-induced microglial activation has also been shown to lead to the formation of ASC specks and the activation of the inflammasome, further exacerbating the inflammatory response. The effect of phosphorylation-state of Aβ in these discussed scenarios remains unelucidated. Figure was created using ChemDRAW and BioRender tools.

2. Materials and Methods

All chemicals and reagents were purchased from Sigma-Aldrich, Merck Millipore, or Carl Roth, and used without purification unless otherwise indicated. Source of procurement of specific chemicals, reagents and instrument make have been mentioned in the protocols/procedures, respectively. List of antibodies and reagents used in western immunoblotting (WB), immunocytochemistry (ICC), immunohistochemistry (IHC) and enzyme linked immunosorbent assay (ELISA) are indicated in the following table.

Tab. 1: List of antibodies and reagents used in the experiments.

Target of interest	Antibody clone / specificity; Compound	Make (Cat. No.)	WB dilution	IHC/ICC dilution
Amyloid β (Aβ)	82E1 ($Aβ_{1-x}$)	IBL International (JP10323)	1:500	1:200
	82E1-Biotin	IBL International (JP10326)		ELISA: 1:1000
	4G8	Biolegend (800709)	1:500	1:250
	4G8-Biotin	Biolegend (800704)		ELISA: 1:1000
	Aβ-Aggregate specific (OC)	Merck Millipore (AB2286)		ELISA: 1:500
	Aβ-Oligomer specific (A11)	TFS (AHB0052)		ELISA: 1:500
	7H3D6 (nmAβ)	In-house (Kumar et al. 2013)		1:100
	1E4E11 (pSer8Aβ)	In-house (Kumar et al. 2013)	1:250	1:100
	5H11C10 (pSer26Aβ)	In-house (Kumar et al. 2020a)	1:250	1:100
	SA6192 (pSer26Aβ)	In-house (Kumar et al. 2016)	1:250	1:100
	BAP-29 ($Aβ_{x-40}$)‡	(Brockhaus et al. 1998)		ELISA: 1:250
	BAP-15 ($Aβ_{x-42}$)‡	(Brockhaus et al. 1998)		ELISA: 1:100
Amyloid precursor protein (APP)	140 (C-terminal specific)	In-house (Wahle et al, 2006)	1:500	1:100

APP and Aβ	6E10	Covance (SIG-39340)		1:250
Soluble APP	sAPPα	Covance (SIG-39139)		ELISA: 1:250
	sAPPβ	Covance (SIG-39138)		ELISA: 1:250
Transferrin receptor	Anti-TfR	IHB (G1-221-12)		1:200
EEA1 (early endosome antigen 1)	Anti-EEA1	MBL (PM062) Abcam (ab206860)	1:1000	 1:200
RAB7 (late endosomal protein)	Anti-Rab7	Abcam (ab50533)		
LC3B (autophagy protein)	Anti-LC3	MBL (PM036)	1:1000	1:200
	Anti-LC3B	CST (2775)		1:200
SQSTM1/p62	Anti-p62/SQSTM-1	Sigma Aldrich (P0067)	1:1000	1:200
LAMP2 (lysosomal protein)	Anti-LAMP-2, H4B4	IHB (H4B4)	1:1000	1:200
	Anti-LAMP-2, ABL-93c	IHB (ABL-93c)	1:1000	1:200
	Anti-LAMP-2A	Abcam (ab25068)	1:1000	1:200
	Anti-LAMP-1, 1D4B	Abcam (ab25245)	1:1000	1:200
CTSD (lysosomal aspartic endopeptidase)	Anti-CTSD	Abcam (ab75852)	1:1000	
Proton ATPase	Anti-ATPase	Synaptic Systems (109 002)	1:500	
Ubiquitin (free form)	Anti-Ubiquitin	Sigma Aldrich (U5379)	1:1000	
ATG14 (autophagy related 14)	Anti-ATG14[#]	MBL (PD-026)	1:1000	
ULK1/atg1 (unc-51 like autophagy activating kinase 1)	Anti- ULK1/atg1	Sigma Aldrich (87841)	1:1000	
ATG5 (autophagy related 5)	Anti-ATG5	Abcam (ab108327)	1:1000	
ATG12 (autophagy related 12)	Anti-ATG12	CST (2010)	1:1000	
ATG3 (autophagy related 3)	Anti-ATG3	CST (3415S)	1:1000	

Rab5 (Early endosome protein 5)	Anti-Rab5	BDB (610724)	1:1000	
Rab11 (Recycling endosomal protein)	Anti-Rab11	CST (3539)	1:1000	
PI3K (phosphoinositide 3-kinase)	Anti-PI3K	TFS (710400)	1:1000	
Phosphorylated PI3K	Anti-phospho PI3K (P85)	TFS (PA5-38905)	1:1000	
AKT (protein kinase B)	Anti-AKT	CST (9272)	1:1000	
Phosphorylated AKT	Anti-phospho AKT	Sigma Aldrich (05-802R)	1:1000	
mTOR (Mammalian target of rapamycin)	Anti-mTOR	CST (2983)	1:1000	
Phosphorylated-mTOR	Anti-phospho mTOR	CST (5536)	1:1000	
S6K1 (ribosomal protein S6 kinase beta 1/p70S6 kinase)	Anti-p70 S6K	CST (9202)	1:1000	
Phosphorylated S6K1	Anti-phospho p70 S6K	CST (9204)	1:1000	
TFEB (Transcription factor EB)	Anti-TFEB	Abcam (ab264421)	1:1000	
Phosphorylated TFEB	Anti-phospho-TFEB	Merck Millipore (ABE1971)	1:1000	
Ubiquitinylated proteins	Anti-poly UBQ, clone FK2	Merck Millipore (04-263)	1:1000	1:250
Phospho-Ubiquitin (S65)	Anti-phospho UBQ	Merck Millipore (ABS1513-I)	1:1000	
UBA1 (Ubiquitin Activating Enzyme 1)	Anti-UBA1	Abcam (ab180125)	1:1000	
UCHL1 (Ubiquitin C-terminal hydrolase L1)	Anti-UCHL1	CST (3524S)	1:1000	
MARCH5 (E3 ubiquitin-protein ligase)	Anti-MARCH5	CST (19168)	1:1000	
PSMB5 (proteasome 20S subunit beta 5)	Anti-PSMB5	TFS (PA1-977)	1:1000	
Calnexin	Anti-Calnexin	Merck Millipore (AB2301)	1:10000	
BiP/GRP78 (binding immunoglobulin protein/ glucose-regulated protein)	Anti-BiP/GRP78	BDB (610978 - 610979)	1:1000	
Hsp70 (Heat shock proteins-70)	Anti-HSP70	SCB (sc-32239)	1:5000	
Hsp90 (Heat shock proteins-90)	Anti-HSP90	SCB (sc-101494)	1:1000	

IRE1α (Serine/threonine-protein kinase/endoribonuclease inositol-requiring enzyme 1 α)	Anti-IRE1α	CST (3294)	1:1000	
ATF6 (activating transcription factor 6)	Anti-ATF6	CST (65880)	1:1000	
S1P1 (sphingosine-1-phosphate receptor 1)	Anti-S1P1	SCB (sc-48356)	1:500	
eIF2α (Eukaryotic Initiation Factor 2)	Anti-eIF2α	CST (9722)	1:1000	
ATF4 (activating transcription factor 4)	Anti-ATF4	CST (11815)	1:1000	
CHOP (C/EBP homologous protein)	Anti-CHOP	CST (2895)	1:1000	
ERK1 (extracellular-signal regulated Serin/Threonin-kinases)	Anti-ERK1	SCB (SC-93G)	1:1000	
TGN46 (transmembrane glycoprotein predominantly localized to trans-Golgi network)	Anti-TGN46	AbD Serotec (AHP500G)	1:1000	
Golgin-97	Anti-Golgin	Invitrogen (PA5-30048)	1:1000	
PINK1 (PTEN-induced kinase 1)	Anti-PINK1	NB (BC100-494)	1:1000	1:200
OPA-1 (optic atrophy-1)	Anti-OPA-1	Abcam (ab80471)	1:500	
MFN1 (mitofusin-1)	Anti-MFN1	TFS (PA5-79665)	1:1000	
Dynamin-related protein	Anti-DRP1	NB (NB110-55288)	1:1000	
DJ-1 (protein deglycase)	Anti-PARK/DJ-1	NB (NB300-270)	1:1000	
Parkin (E3 ubiquitin ligase, encoded by the PARK2 gene)	Anti-Parkin	TFS (702785)	1:1000	1:200
Tim23 (mitochondrial import translocase subunit)	Anti-Tim23*	BDB (611222)	1:1000	
TOM70 (mitochondrial import receptor subunit)	Anti-Tom70*	SCB (sc-390545)	1:1000	
HSP60 (Heat shock proteins-60)	Anti-HSP60*	SCB (sc-59567)	1:1000	
PS (phosphatidylserine)	Anti-PS (Annexin V)	Alexis (ALX-209-002)		1:500

MLKL (mixed lineage kinase domain like pseudokinase)	Anti-MLKL	Abcam (ab243142)	1:1000	
Phosphorylated MLKL	Anti-phospho MLKL	Abcam (ab187091)	1:1000	1:200
CK1δ (casein kinase 1 isoform delta)	Anti-CK1δ	Abcam (ab48031)	1:1000	1:200
RIPK1 (Phosphorylated receptor interacting serine/threonine kinase 1)	Anti-phospho RIPK1	SCB (sc-133102)	1:1000	1:200
P53 (tumor protein P53)	Anti-p53	SCB (sc-126)	1:1000	
P35 (tumor protein P35)	Anti-p35	SCB (sc-820)	1:1000	
bcl-2 (B-cell lymphoma-2)	Anti-bcl-2	Abcam (ab692)	1:1000	
Phosphorylated bcl-2	Anti-phospho bcl-2 (S87)	Abcam (ab73985)	1:1000	
CSP1 (caspase 1)	Anti-Caspase-1	TFS (MA5-32909)	1:1000	
Cleaved Caspase-3 (Asp175)	Anti-cleaved caspase 3	CST (9661)	1:1000	
IL-1β (interleukin-1 beta)	Anti-IL-1β	Abcam (ab9722)	1:1000	ELISA: 1:100
		TFS (14-7012-85)		
TNFα (tumor necrosis factor – alpha)	Anti-TNFα	TFS (13-7341-81)	1:1000	ELISA: 1:100
Vimentin (fibroblast intermediate filament)	Anti-Vimentin	CST (5741/11843)	1:1000	
GSKα/β (phosphorylated glycogen synthase kinase 3α/β)	Anti-phospho-GSKα/β	CST (9331)	1:1000	
PPARγ (peroxisome proliferator-activated receptor γ)	Anti-PPARγ	Abcam (ab272718)	1:1000	
NFκB (nuclear factor kappa-light-chain- B cells)	Anti-NFκB	CST (3034)	1:1000	
CK1 (Casein kinase 1)	Anti-CK1	CST (2655)	1:1000	
LDHA (Lactate Dehydrogenase A)	Anti-LDHA	Abcam (ab47010)	1:1000	
Alix (exosomal marker)	Anti-Alix	TFS (MA1-83977)	1:1000	1:200
	Anti- Alix (1A12)	SCB (Sc53540)		1:250
Flotillin-1	Anti-Flotillin-1	BDB (610820)	1:1000	1:250
CD9 (tetraspanin-CD9)	Anti-CD9	SCB (sc-9148)	1:1000	1:200
CD63 (tetraspanin-CD63)	Anti-CD63	IHB (H5C6)	1:1000	

IDE (insulin degradation enzyme)	Anti-IDE	Abcam (ab63137)	1:1000	
IL-10 (interleukin-10)	Anti-IL-10	R and D systems (1064-ILB)		ELISA: 1:100
		TFS (13-7102-85)		
IL-4 (interleukin-4)	Anti-IL-4	R and D systems (404-ML)		ELISA: 1:100
		Abcam (ab225638)		
		Abcam (ab11524)		
ASC (apoptosis-associated Speck-like Protein Containing CARD)	Anti-ASC (AL177)[#]	AdipoGen Life Sciences (AG-25B-0006)		1:250
Actin	Anti-β-actin	CST (4967)	1:5000	
	Cell Light Actin-RFP	TFS (C10583)		1:10000
	Phalloidin-Alexa555	TFS (A34055)		1:10000
GAPDH	Anti-GAPDH	SCB (sc-32233)	1:5000	
Microtubule protein	Anti-MAP-2	Synaptic Systems (188004)		1:500
Nuclei/DNA	Hoechst 33342[$]	TFS (H1399)		1:1000
	4′,6-diamidino-2-phenylindole (DAPI)	TFS (D1306)		1:1000
	DRAQ5	TFS (62251)		1:500
Oxidative stress marker	8-Hydroxy-2'-deoxyguanosine (8-OHdG)	Abcam (ab48508)		1:250
Mitochondrial membrane potential	Tetramethyl rhodamine, ethyl ester (TMRE)*	TFS (T669)		FACS: 1:250
Dead cells	Trypan Blue Solution	TFS (15250061)		1:100
	7-Aminoactinomycin D (7-AAD)[$]	TFS (A1310)		1:1000
	Propidium Iodide (PI)	TFS (BMS500PI)[$]		1:500

Alexa405/488/546/647 dye conjugated secondary antibody	Donkey/goat – mouse/rabbit IgG	TFS	1:2500
Streptavidin-HRP conjugate		Biolegend (1474)	ELISA: 1:2500/ 5000

CST, Cell signaling technology; TFS, ThermoFischer Scientific; SCB, SantaCruz Biotechnology; IHB, Iowa Hybridoma bank; MBL, MBL international, BDB, BD Biosciences, NB, Novous Biologicals. ‡*Gift from Novartis;* #*Gift from Thomas Bajaj and Dr. N. Gassen;* $ *Gift from Dr. Cira Dansokho and Prof. M. Heneka; *Antibodies used by Daniel Puchta-Schomberg and Prof. W. Voos.*

2.1. Aβ aggregation experiments

2.1.1. Preparation of non-aggregated and pre-aggregated Aβ

Synthetic $Aβ_{1-40}$ peptides - non-phosphorylated Aβ (npAβ), phosphorylated Aβ- pSer8Aβ and pSer26Aβ, pseudo-phosphorylated DAβ -S8D Aβ and S26D Aβ (1 mg) were procured from Peptide Specialty Laboratories GmbH. Synthetic Tide Fluor-conjugated $Aβ_{1-40}$ variants: Cys (succinimido-Tide Fluor2)- linked non-phosphorylated Aβ (TF-npAβ), pseudo-phosphorylated TF-S8D Aβ and TF-S26D Aβ were purchased from BACHEM (1 mg). Lyophilized peptides were dissolved in 10 mM NaOH buffer to a stock concentration of ~230 µM, sonicated for 10 min, flash frozen and stored at -20^{o}C. Aβ stock solutions (~230 µM) were respectively diluted to 50 µM in phosphate buffered saline (PBS) and were allowed to aggregate in a glass vial with a magnetic stirrer (200 rpm) at 37^{o}C. Aliquots were drawn at indicated time points, flash frozen and stored at -20^{o}C until further use.

2.1.2. Thioflavin-T Fluorescence assay

Sample aliquots from Aβ aggregation assay collected at different time points were mixed with 10 µM Thioflavin-T dye (ThT, Sigma Aldrich, #T3516-256) in PBS (1.92 µM of Aβ and 9.61 µM of ThT) and incubated for 10 min at room temperature (RT). After incubation, the fluorescence was measured on a spectrophotometer (Tecan Inc., Switzerland) at RT. ($λ_{Ex}$ 446 nm and $λ_{Em}$ 482 nm, slit width 10 nm)

2.1.3. Solubility fractionation of Aβ species (*Scheme **1A***)

Sample aliquots from Aβ aggregation assay collected at different time points were ultracentrifuged at 100,000 *g* for 60 min, maximum acceleration, minimum deceleration

(Beckman Coulter Optima X-series Ultracentrifuge; Germany). Supernatant was collected as the *soluble fraction* and flash frozen. Pellet was resuspended in HEPES buffer (ThermoFischer Scientific, #15630080) on an Eppendorf Thermomixer (Germany) at 37°C for 1 h, after which the samples were flash frozen.

2.1.4. Sucrose density gradient (*Scheme **1B***)

Equal amounts of Aβ samples (15 µl) were loaded on a discontinuous gradient [(OptiPrep™, Sigma Aldrich #92339-11-2) - 50, 40, 30, 25, 20, 15, 10, and 5%; 1.2 ml each]; tubes stored on ice and kept refrigerated. Samples were ultracentrifuged at 120,000 *g* at 4°C for 8 h, maximum acceleration and without using the brake. Next day, single fractions were collected at a volume of 1 ml each. 300 µl of each fraction was precipitated using 30% trichloroacetic acid (TCA) for 30 min at RT. The resultant pellet was washed with acetone twice and resuspended in 10mM TRIS and 1% SDS buffer along with Laemelli sample buffer (50 µl) for western blot analyses.

2.2. Cell culture

2.2.1. Human neuroblastoma SH-SY5Y cells

SH-SY5Y cells (ATCC, CTR-2266) were cultured in DMEM/F-12 (Life Technologies, USA, #10565018) supplemented with 10% fetal calf serum (FCS; PAN-Biotech, #P30-3306), 1% penicillin-streptomycin solution (PS; 50 U/ml penicillin, 50 µg/ml Streptomycin; Life Technologies, #15140122), 2 mM L-glutamine (Life Technologies, #25030081), 1% sodium pyruvate (Life Technologies, #11360039) and 1% non-essential amino acids (NEAA, Life Technologies, #11140050). Cells were maintained at 37°C in a 5% CO_2 humidified atmosphere with a media change every alternate day. Cells were used within passage number 8-13 and were split with 0.05% Trypsin-EDTA (Life Technologies, #25300104) in a 1:10 ratio.

2.2.2. SH-SY5Y cells with reporter constructs

SH-SY5Y cells were transfected with either GFP-LC3-LC3Δ-RFP (*C1*, Addgene, plasmid #117413) or mCherry-GFP-LC3B (*C2*, Addgene, plasmid #123230) tandem constructs, or pEGFP-N1-TFEB (*C3*, Addgene, plasmid #38119) reporter construct (0.5 µg/well + 1uL transfection reagent – 24-well plate) with Lipofectamine 2000 (Life Technologies,

#11668019) in OptiMEM (Life Technologies, #11058021) in DMEM/F-12, FCS$^-$PS$^-$ media. After 8 h, FCS$^-$PS$^-$media was changed to normal culture media respectively. Transfection efficiency was around more than 60% in all the analyzed coverslips. *Plasmids C1 and C3 were received from Mr. T Bajaj and Dr. N Gassen. Plasmid C2 was received from Drs. S. Höning and J. Höhfeld.*

2.2.3. SH-SY5Y-APP$_{Sw}$ transgenic cell lines

SH-SY5Y cells were transfected with wild type (*C4*, WT-APP$_{Sw}$/Aβ), and pseudo-phosphorylated or non-phosphorylated versions (*C5-6*, S8D/S8A- APP$_{Sw}$/Aβ and *C7-8*, S26D/S26A- APP$_{Sw}$/Aβ) of APP695 with a Swedish mutation, 0.5 µg/well plasmid DNA + 1 µL transfection reagent – 24-well plate) with Lipofectamine 2000 in OptiMEM in DMEM/F-12, FCS$^-$PS$^-$ media. After 8 h, FCS$^-$PS$^-$ media was changed to normal culture media overnight. Next day onwards, cells were cultured in normal growth media supplemented with 2 µg/ml of Geneticin™ Selective Antibiotic (G418 sulphate) (Life Technologies, #10131027), to ensure stable expression of APP. Non-transfected cells received only transfection reagent without any plasmid DNA, were processed similarly to APP$_{Sw}$ stable cells, and were cultured in media containing 0.2 µg/ml of G418. DMEM/F-12, FCS$^-$PS$^-$ media was conditioned for 24 h in presence of SH-SY5Y-APP$_{Sw}$ cells. Media was collected, centrifuged at 1000 g, 3 min, to get rid of cell debris, flash frozen and stored at -20^{o}C until further use. *All APP$_{Sw}$/Aβ DNA plasmids (C4-C8) were generated and characterised by Ms. S. Theil and Dr. S. Kumar.*

2.2.4. Mouse primary cortical neurons

Mouse primary cortical neurons were obtained from wildtype C57BL/6 mouse pups (E13-E18). Brain tissue was dissected, and the cortical region was dissociated in trypsin (Life Technologies, 25300104). Post-trypsinization, cells were seeded in Basal Medium Eagle (BME) (Life Technologies, #41010026) supplemented with 1x B-27 nutrient supplement (Life Technologies, #A1486701), 1% FCS, 2 mM L-glutamine. Next day, media was discarded to remove unattached cells and fresh Neurobasal media (Life Technologies, #21103049) supplemented with 1% FCS, 1% PS, 2 mM L-glutamine) was added. Cells were then maintained at 37^{o}C in a 5% CO_2 humidified atmosphere with until D14. *Ms. S. Opitz assisted with the preparation of mouse primary cortical neurons.*

2.2.5. Microglial SIMA9 cells

Spontaneously immortalized mouse primary microglial (SIMA9) cells were cultured in DMEM/F-12 supplemented with 10% FCS, 1% horse serum (New Zealand origin, Life Technologies, #16050122) 1% PS, 2 mM L-glutamine, 1% sodium pyruvate and 1% NEAA. Cells were maintained at 37°C in a 5% CO_2 humidified atmosphere. Cells were used within passage number 12-16 and were split with 0.05% Trypsin-EDTA in a 1:25/50 ratio.

2.2.6. GFP expressing SIMA9 cell line

SIMA9 cells were transfected with pcDNA3-EGFP (*C9*, Addgene, plasmid #13031) (2 µg/well plasmid DNA + 4 µL Lipofectamine 2000 transfection reagent – 6 cm dish) in OptiMEM in DMEM/F-12, FCS^-PS^- media. After 8 h, FCS^-PS^- media was changed to normal culture media overnight. Next day onwards, cells were cultured in growth media supplemented with 2 µg/ml of G418, to ensure stable expression of cytoplasmic GFP. *Plasmid C9 was received from Mr. T Bajaj and Dr. N Gassen.*

2.2.6.1. SH-SY5Y and GFP expressing SIMA9 co-culture experiments

SH-SY5Y cells cultured in 96-well plate (Ibidi, #89626) were treated with Aβ peptides (1 µM, 6 h) in DMEM/F-12, FCS-/PS- media. Washing steps were performed as mentioned, and GFP expressing SIMA9 cells (1:2 ratio) were co-cultured in DMEM/F-12 with 10% FCS, 1% horse serum, 1% PS, 2 mM L-glutamine, 1% sodium pyruvate and 1% NEAA. Plates were then maintained at 37°C in a 5% CO_2 humidified atmosphere for 18 h. After incubation, washing steps were repeated and cells were fixed and analyzed via immunocytochemistry.

2.2.7. ASC-Cerulean expressing SIMA9 cell line

SIMA9 cells stably expressing ASC-Cerulean reporter construct were cultured in DMEM/F-12 supplemented with 10% FCS, 1% PS, 2 mM L-glutamine, 1% sodium pyruvate and 1% NEAA along with 2 µg/ml of G418. *Cells were provided by Mr. T Bajaj and Dr. N Gassen.*

2.3. Mice

Transgenic AD, APP-PSEN1delE9xThy1-YFP, APP-PSEN1delE9xCX3CR1-GFP and respective wild type, WTxThy1-YFP, WTxCX3CR1-GFP mice were maintained and handled according to the Declaration of Helsinki and approved by the local ethical committees (LANUV NRW 84–02.04. 2017.A226). Mice details are indicated in Tab. 2. *Dr. Nadia Villacampa from Prof. M Heneka's group, DZNE; provided, and assisted in sacrificing mice and isolating mouse brains.*

Tab. 2: Details of the mice analyzed in this study.

Animal	Genotype	Age (m)	Sex	Background
1	Thy-YFP wt/ins	7.3	m	C57Bl6
2	Thy-YFP wt/ins	11.4	f	C57Bl6
3	Thy-YFP wt/ins	13.4	m	C57Bl6
4	Thy-YFP wt/ins	13.4	f	C57Bl6
5	Thy-YFP wt/ins, APP-PSEN1 wt/tg	7.4	m	C57Bl6
6	Thy-YFP wt/ins, APP-PSEN1 wt/tg	7.4	f	C57Bl6
7	Thy-YFP wt/ins, APP-PSEN1 wt/tg	7.3	f	C57Bl6
8	Thy-YFP wt/ins, APP-PSEN1 wt/tg	7.3	f	C57Bl6
9	CX3-GFP wt/ins	13.5	f	C57Bl6
10	CX3-GFP wt/ins	13.5	f	C57Bl6
11	CX3-GFP wt/ins	13.5	m	C57Bl6
12	CX3-GFP wt/ins, APP-PSEN1 wt/tg	13.4	f	C57Bl6
13	CX3-GFP wt/ins, APP-PSEN1 wt/tg	15.7	m	C57Bl6
14	CX3-GFP wt/ins, APP-PSEN1 wt/tg	15.7	m	C57Bl6

Whole-brain homogenates from mice hemibrains were prepared as described previously (Kumar et al. 2020a; Kumar et al. 2016; Joshi et al. 2021a). Briefly, brain tissue was homogenized with a douncer followed by sonication in sucrose buffer (30% in PBS) containing Complete® protease and PhosSTOP® phosphatase inhibitors (Roche, #4906837001 and #04693124001); to isolate soluble protein fraction. Homogenates were cleared by centrifugation at 14,000 *g* for 30 min at 4°C. After centrifugation, the resulting supernatant containing respective protein fractions were aliquoted, flash frozen and stored at −80°C until further usage. Pellet was re-homogenized in 2% SDS in water (pH 7.3) supplemented with protease & phosphatase inhibitors, following ultrasonication and centrifugation steps as described above. The resultant supernatant (SDS soluble fractions) was aliquoted and stored at −80°C. The SDS insoluble pellet was further

resolved in 70% formic acid overnight at 4°C with constant agitation. The supernatants after centrifugation at 14,000 *g* for 30 min at 4°C, were aliquoted and stored at −80°C. For further examination via WB or ELISA, FA soluble fractions were neutralized with 1-5 mM NaOH in 1% Tris buffer. Samples were boiled in Laemmli sample buffer and used for WB analyses or diluted in respective buffers and used for ELISA analyses.

2.4. Cell biochemistry

2.4.1. Aβ treatment

SH-SY5Y or SIMA9 cells seeded on D1, were treated with respective Aβ peptides on D3 in serum free culture media for mentioned time points, respectively. Control condition included treatment with equal volume of 10 mM NaOH solution used for preparing the Aβ stock solutions. Primary cortical neurons (DIV14) were treated with 500 nM of non-aggregated Aβ peptides in neurobasal, $FCS^{-}PS^{-}$ media. After treatment, cells were washed twice with PBS and with 0.005% trypsin-EDTA in PBS to get rid of cell bound Aβ, followed by subsequent washings with PBS again. Cells were either fixed with 4% PFA-PBS for 15 min at RT, for further immunocytochemical experiments; or collected by scraping using a cell-scraper in respective buffers, for analyses of cellular proteins. Collected treatment media was centrifuged at 1000 *g* for 5 min, pellet discarded and supernatant frozen at -20°C until further usage.

2.4.2. Cellular fractionation (*Scheme **1C***)

Cells were collected by scraping and mechanically homogenized in hypotonic D buffer (10 mM Tris-HCl, pH 7.4, 10 mM NaCl, 0.1 mM EGTA, 25 mM glycerol 2-phosphate, 1 mM DTT) containing protease and phosphatase inhibitors for preparation of post-nuclear supernatant (PNS), membrane crude cytosolic, soluble, and insoluble cytosolic (Scheme **1C**). Cell membranes were disrupted by mechanical sheer force by repeated suspension through a 23G x 1” needle. Post-nuclear supernatant (*PNS*) was collected by centrifugation of the mechanically homogenized cellular material at 2,000 *g* for 5 min. The pellet containing nuclear material was resuspended in Buffer C (5 mM HEPES, 1.5 mM $MgCl_2$, 0.2 mM EDTA, 0.5 mM DTT, 0.05% IGEPAL CA-630 (NP-40 substitute), 30% v/v glycerol, pH 7.9) containing protease and phosphatase inhibitors. Resuspended nuclear material was ultrasonicated at minimum voltage, 3 currents in four cycles, followed by

repetitive cooling of samples on ice. *Nuclear fraction* was the supernatant collected post centrifugation at 16,100 *g* for 15 min. The PNS from the first step collected was centrifuged at 16,100 *g* for 60 min, and supernatant was used as the *crude cytosolic fraction*. The pellet containing membrane associated material were re-homogenized in hypotonic D buffer and centrifugation at 16,100 *g* for 60 min was repeated. The supernatant was discarded, and pellet was resuspended in STEN lysis buffer (20 mM Tris (pH 7.5), 150 mM NaCl, 1 mM EDTA, 1 mM EGTA, 1% Triton X-100, 2.5 mM sodium pyrophosphate, 1 mM β-glycerophosphate) containing protease and phosphatase inhibitors. *Membrane fraction* was the supernatant collected after centrifugation at 16,100 *g* for 15 min. Additionally, the crude cytosolic fraction was further subjected to ultracentrifugation at 100,000 *g* for 70 min at 4^{o}C under vacuum (maximum acceleration, partial deceleration). The supernatant was the *soluble cytosolic fraction*. Pellet containing insoluble material was further resuspended in STEN lysis buffer and *insoluble cytosolic fraction* was the supernatant collected post-centrifugation at 16,100 *g* for 15 min.

2.4.3. Preparation of cell lysates (*Scheme **1F***)

Cells collected by scraping were mechanically homogenized in STEN lysis buffer containing protease & phosphatase inhibitors, and subjected to ultrasonication at minimum voltage, 3 currents in four cycles, followed by repetitive cooling of samples on ice. Samples were left standing on ice for 15 min and centrifuged at 16,100 *g* for 10 min, pellet discarded, and *cell lysates* (supernatant) was used for further WB analyses or functional assays.

2.4.4. Subcellular fractionation by density gradient centrifugation

A similar procedure as described before was followed (Tien et al. 2016; Li and Donowitz 2014). Briefly, post- nuclear fractions from Aβ treated SH-SY5Y cells were collected. Protein concentrations were determined using Pierce BCA protein assay kit (ThermoFischer Scientific #23227). Equal amounts of protein (500-600 µg) were then loaded on a discontinuous gradient (OptiPrep - 40, 30, 25, 20, 15, 12.5, 10, and 5 %; 1.2 ml each) while tubes were stored on ice or kept refrigerated. Samples were ultracentrifuged at 120,000 *g* at 4°C for 8 h, maximum acceleration and without using the brake. Next day, 1 ml fractions were collected, and protein concentration determined using

Pierce™ BCA Protein Assay Kit (ThermoFischer Scientific, #23225). Since the total protein content in individual fractions was lower, fractions were precipitated using 30% trichloroacetic acid for 1 h at RT. The resultant pellet was washed with acetone twice and resuspended in 10 mM TRIS and 1% SDS buffer along with Laemelli sample buffer for WB analyses.

2.4.5. Enrichment of lysosomes (*Scheme **1D***)

Cells collected by scraping were homogenized in isotonic buffer (10 mM Tris-HCl, pH 7.4, 1 mM $MgCl_2$, 0.1 mM EGTA, 0.25 M sucrose) containing protease & phosphatase inhibitors, by repeated suspension through a 23G x 1" needle. Cell homogenate was centrifuged at 2,000 *g* for 5 min and pellet (*nuclear material*) was discarded. Procedure previously described (Graham 2001), was slightly modified. The homogenate was centrifuged at 16,100 *g* for 15 min, wherein the pellet was resuspended in STEN lysis buffer and the lysosome enriched fraction was the supernatant collected after centrifugation at 16,100 *g* for 15 min. Supernatant from earlier step (*crude lysosome material*) was further centrifuged at 16,100 *g* for 60 min, pellet contained lysosome depleted material and supernatant was the remaining *cytosol*. The pellet was re-homogenized in STEN lysis buffer and *lysosome depleted fraction* was the supernatant was the collected post-centrifugation at 16,100 *g* for 15 min.

2.4.6. Immunoprecipitation (*Scheme **1E***)

Equal concentrations of protein in cell homogenate/PNS fraction (prepared as described earlier) was estimated by BCA protein estimation kit and used for IP experiments. Sepharose G beads (ThermoFischer Scientific, #101242) were incubated with homogenate/PNS for 1 h at RT, beads were further pelleted down and boiled in 1% SDS and 50 mM TRIS + sample buffer were used as *bead control*. The homogenate/PNS exposed to beads only were devoid of non-specific binding substrates and was used further as loading control. New set of beads were precoated with respective primary antibodies for 1 h and then incubated with homogenate/ PNS overnight at 4^{o}C, facilitated with agitation. Beads containing immunoisolated material were pelleted down and boiled with 1% SDS and 50 mM TRIS and Laemelli buffer as the *IP eluate*, wherein the remaining homogenate/ PNS was used as the *supernatant*.

2.4.7. Enrichment of exosomes

Exosomes from SH-SY5Y-APP$_{Sw}$ cell conditioned media (10 x 10 cm dishes containing 5 ml media each) were enriched as described earlier (Tamboli et al. 2010; Glebov et al. 2015). 50 ml conditioned media were subjected to sequential centrifugation steps (10 min at 300 *g*, two times for 10 min at 2,000 *g*, 30 min at 10,000 *g*, and 1 h at 100,000 *g*). 1.3 ml of supernatant at each step were collected in fresh tubes and subjected to TCA precipitation. Pellet fractions were resuspended in 100 µl of PBS. A part of supernatant media and PBS resolved pellet fractions were aliquoted for cell viability assays. Pellet-PBS and TCA pellets were further resuspended with STEN lysis buffer along with Laemelli sample buffer and analyzed via WB.

2.5. Biochemical analyses

2.5.1. Protein gel electrophoresis and Western immunoblotting

For NATIVE-PAGE, 5 µl of Aβ samples comprising of Aβ (~1 µg) were mixed with 5 µl of native sample buffer, loaded on Native PAGE™ 4-16% Bis-Tris protein gels (ThermoFischer Scientific, #BN1004BOX) and separated using Novex™ Tris-Glycine running anode and cathode buffers respectively (ThermoFischer Scientific, Native PAGE™ Running Buffer Kit, #BN2007), with an approximate run time of 90 min at 150 V and 300 mA. The separated proteins were electro-transferred onto a methanol preactivated 0.45 µm polyvinylidene difluoride (PVDF) membrane (Amersham Hybond, #10600023) using a blotting buffer (30 mM Tris, 48 mM glycine, 10% methanol, pH 9.0) at 300 V and 400 mA for 2 h. Activation of PVDF membrane was done by dipping the membrane in methanol for 1 min. Similarly, for SDS-PAGE, 5 µl of Aβ samples were mixed with 5 µl LDS sample buffer without boiling. For different cellular fractions or cell lysates prepared as described earlier, the protein content was estimated using the standard Pierce™ BCA protein assay kit (ThermoFischer Scientific, 23225). For direct comparison between the samples, equal amount of protein was loaded. Samples were dissolved in Laemmli buffer and boiled at 95^{o}C for 5 min. Samples were loaded on a 4-12% gradient gel (NuPage® Bis-Tris gels, Life technologies, #NP0335-6, #WG1402-3) using 1x MES SDS running buffer (Life technologies, USA, #NP0002) with an approximate run time of 60 min at 150 V and 300 mA. Prestained protein molecular weight markers for SDS-PAGE

(ThermoFischer scientific, #26616/19, #LC5925) or NATIVE-PAGE (ThermoFischer Scientific, NativeMark™ Unstained Protein Standard, # LC0725) were purchased from Life Technologies. The separated proteins were electro-transferred onto a 0.2 µm nitrocellulose (NT) membrane (Amersham Protran, #10600001) using a blotting buffer (30 mM Tris, 48 mM glycine, 10% methanol/ isopropanol, pH 9.0) at 300 V and 400 mA for 1 h 45 min or 2 h. After blotting, the PVDF or NT membranes were boiled in PBS for 10 min. Ponceau staining was done to monitor protein load. The blots were then incubated in 5% skim milk in TBS-T (TBS [50 mM Tris-HCl, pH 7.5, 150 mM NaCl] containing 0.1% Tween 20 [Sigma Aldrich, P1379]) for 1 h at RT. Blots were incubated overnight at 4°C in the primary antibody solution (respective dilutions in TBS-T) with constant rotation. Next day, blots were washed with TBS-T and incubated with respective secondary antibody (HRP, 1:5000; IR-dyes, 1:5000 dilutions in TBS-T, Tab. **1**) for 1 h at RT. Blots were developed either by chemiluminescence (ECL) or fluorescence imaging. For ECL detection, blots were incubated with equivalent mixtures of solution A (0.1 M Tris, 0.4 mM coumaric acid, 2.5 mM luminol, pH 8.5) and B (0.1 M Tris, 0.018% H_2O_2), and imaged with an ECL imager (Bio-Rad, Germany). For fluorescence detection, blots were imaged on a Li-COR imaging station (Li-COR Biosciences, Germany). Blots were presented as is or with minimal linear contrast enhancement. Quantification of band signals was done using ImageJ – Gel processing module or Image Studio processing software (LiCOR Biosciences, Germany). All samples were analyzed in biological duplicates in two or three independent experiments as indicated in the respective figure legends. Values from each sample were normalized to the values from the control cells in that experiment and expressed as fold-change as indicated in the respective graphs.

2.5.2. TAE gel electrophoresis

Aβ treated SH-SY5Y cells (2 x 6 cm dishes) were lysed with 150 µl STEN lysis buffer containing phosphatase and protease inhibitors along with Proteinase K (Sigma Aldrich, #P4850-5ml). Mixture was subjected to vortex pulsing 3 times for 15 sec and left on ice for 15 min and 300 µl of 1:1 mixture of chloroform: phenol was added and again allowed to stand for 10 min on ice. Aqueous phase was collected in a separate tube along with 2 additional washes of 75 µl organic phase. 200 µl of chloroform wash of the aqueous phase was performed and organic layer was discarded. 100 µL of 5M NaCl and 800 µl of ethanol,

was added to the aqueous phase and stored at -20°C for 48 h to facilitate DNA precipitation. DNA pellet was separated by centrifugation at maximum speed, 2 min; and allowed to dry at 37°C for 15-20 min. Pellet was resuspended in 100 µl of DNase/RNase free water and concentration was measured using Nanodrop spectrophotometer. Isolated DNA (8-10 µg) and 3-5 µg of Gel red DNA stain (Biotium #41008) was loaded on a 2% agarose gel (10 cm long/ ~3 mm thick). LAB running buffer (10 mM lithium acetate and 10 mM boric acid) was used to separate DNA material at 100 V, 108 mA current for a run time of ~2h. DNA separated in the gel was analyzed by observing Gel Red and ladder migration patterns. Gel was later stained with ethidium bromide (MP Biomedicals, #802511) and visualised on a Bio-Rad gel imager system.

2.5.3. ELISA

Nunc-Immuno™ 96 microwell plates (ThermoFischer Scientific, #44-2404-21) were used for in-house generated ELISA systems. For indirect ELISA, antigen solution was directly added to the wells and incubated at 4°C for 16 h, with subsequent dilutions in blocking buffer (1 mg/ml BSA in PBS). For sandwich ELISA, wells were initially coated with capture primary antibodies for 2 h at RT, also respectively diluted in blocking buffer. Standard Aβ dilution curve or inflammation marker controls were optimised and maintained in each plate to avoid plate-to-plate variation. Wells were rinsed with PBS thrice, residual liquid was removed by gently tapping the plates, blocking buffer (1 mg/ml BSA, 200 µL) was added per well and incubated for 2 h at RT. This was followed by subsequent washing and incubation with respective HRP conjugated secondary antibody/streptavidin (1:2500-5000) for an additional 2 h at RT. Wells were then washed thoroughly four times and filled with 100 µL of 3,3′,5,5′-tetramethylbenzidine substrate (TMB; ThermoFischer scientific, #N301) and incubated at RT until sufficient blue colour developed. Time of incubation ranged from 2-15 min depending on the different capture /detection antibodies and was kept constant in subsequent experiments. 100 µL of stop solution (4 M H_2SO_4) was added to each well and optical density (OD) was measured on a spectrophotometer (measurement 450 nm / background 620 nm). Multiple readings were recorded for a single well, averaged, and computed with respect to the standard controls in the experiment. In each experiment, reading for a single sample was recorded in technical duplicates/triplicates/quadruplets, as indicated in respective experimental legend.

2.5.3.1. Indirect ELISA of Aβ in aggregation assay

Aβ ELISA analyses in aggregation assays, wells were incubated overnight with respective Aβ fractions at 4ºC as antigen, subsequently diluted in blocking buffer. Anti-Aβ (82E1, A11, OC) antibodies (0.1 mg/well) were used as detection antibodies, respectively.

2.5.3.2. Sandwich ELISA of Aβ in mouse brain and cell fractions

Anti-Aβ (82E1, 4G8), anti-nmAβ (7H3D6) or anti-pAβ (pSer8Aβ - 1E4E11 and pSer26Aβ – 5H11C10 (0.1 µg/ well) were used as capture antibodies coated on the wells for 2 h at RT followed by blocking. Protein material in mouse brain or cellular fractions were diluted respectively; and equal protein amounts were then added as antigen solutions and incubated at 4°C for 16 h. Biotin conjugated anti-Aβ 82E1-Biotin or 4G8-Biotin antibodies (0.1 mg/well) were used as detection antibodies, respectively.

2.5.3.3. Aβ ELISA analyses in SH-SY5Y-APP_{Sw} cell conditioned media

Anti-Aβ - 4G8, $Aβ_{1-x}$ – 82E1 (0.1 µg/ well) or $Aβ_{x-40}$ – BAP-29, and $Aβ_{x-42}$ – BAP-15 (0.1 µg/ well) antibodies were used as capture antibodies and biotin conjugated anti-Aβ 82E1-biotin or 4G8-biotin antibodies were used as detection antibodies, respectively. 200 µl of conditioned media from transgenic cells were used as antigen solutions. sAPPα/β species in conditioned media was analyzed via indirect ELISA using in house generated sAPPα/β specific antibodies (0.2 µg/ well), respectively.

2.5.3.4. Cytokine ELISA assay

Sandwich ELISA technique was used for the analyses of cytokines, primary antibodies specific to IL-1β, TNFα, IL-10 and IL-4, were used as capture antibodies (0.01-0.02 µg/ well) and biotin conjugated antibodies were respectively used as detection antibodies.

2.5.4. Immunocytochemistry

Cells cultured on glass coverslips (procured from DECKGLÄSER, Germany) were treated and washed as previously indicated. Cells were fixed with 4% paraformaldehyde (PFA) in PBS for 15 min on ice, followed by multiple washings with PBS. Cells were then permeabilized with 0.25% Triton X-100 in PBS for 1 min followed by blocking with 2.5% BSA, 0.125% Triton-X 100 in PBS with or without 1-2% normal horse serum (NHS) for 1 h at RT. Incubation with primary antibodies (respective dilutions in blocking buffer) was

performed overnight at 4^{o}C in a humidified chamber. Next day, coverslips were washed and incubated with respective secondary antibodies (respective dilutions in blocking buffer) for 1 h at RT. Following multiple washes of PBS and lastly distilled water, coverslips were inverted and mounted on the glass slides using ImmuMount (ThermoFischer Scientific -Shandon Epredia™ 9990412). For surface staining without permeabilization, Triton X-100 was not used in any solutions, during the staining procedure.

2.5.5. Immunohistochemistry

Immunofluorescence staining of mouse brains was performed on 30 µm coronal brain sections fixed in 4% PFA in PBS, as described previously (Kumar et al. 2020a; Joshi et al. 2021a). Brain tissue sections were washed twice with PBS and then subjected to antigen retrieval methods using reveal decloaker (Biocare Medical, #RV1000M) followed by permeabilization by using 0.25% Triton X-100 in PBS for 10 min. Prior to permeabilization, multiple PBS and water washes were done to get rid of acidic content that plausibly quench YFP/GFP fluorescence. Sections were stained with X-34 (Sigma Aldrich #SML1954; 0.5 µg/mL) in 60% isopropanol (ISP) in PBS for 10 min. Sections were then washed thrice with 60% ISP-PBS solution. Non-specific binding sites were blocked by treatment with 5% NHS and 2.5% BSA in PBS, before addition of the primary antibodies. Mouse on Mouse (M.O.M) blocking reagent (Vector Laboratories, #MKB-2213-1) was used for primary antibodies generated in mouse or rat (dilutions: 1 drop/10 ml). Sections were incubated overnight in a humidified chamber at 4°C with the respective dilutions of primary antibodies followed by subsequent washing steps with PBS thrice and blocking buffer twice. Sections were then incubated with an appropriate fluorescently tagged secondary antibody solutions in blocking buffer for 2 h at RT. After incubation, tissue sections were washed in PBS thrice, and mounted onto slides by using VECTASHIELD Antifade mounting medium (Vector laboratories, #H-1000-10) with DAPI.

2.6. Cell viability assay

Cells were seeded in a corning transparent 96-well plate, and Aβ/ conditioned media treatment was done (100 µl of serum free media). After treatment, cells were washed twice with 100 µl PBS and replaced with 90 µl phenol red free cell culture media. Wells treated with 10% methanol or 50% DMSO in culture media for 10 min, were used as dead cell

control. Untreated controls were maintained in growth media and considered 100% viable (positive control) and readings were calculated as a ratio of the relative fluorescence units with respect to untreated cells.

2.6.1. Presto Blue® cell viability assay

Viability of the cells was determined by Presto Blue® cell viability assay as per manufactures protocol. In brief, 10 µL Presto Blue reagent (Life Technologies, #A13261) was added to make the final volume to 100 µL/well. Plate was incubated at 37°C in a 5% CO_2 humidified atmosphere for 30 min. Fluorescence (λ_{Ex} 555 nm / λ_{Em} 600 nm) and absorbance (OD measurement 525 nm / background 600 nm) were recorded after incubation with the reagent.

2.6.2. Apoptotic and necrotic dead cell assays

SH-SY5Y cells seeded in imaging 96-well plates were treated with Aβ peptides (1 µM, 24 h) and stained with 7AAD (Miltenyi Biotec #130-111-568; 1:1000) or extracellular phosphatidyl serine (Alexa Fluor® 647 Annexin V, Biolegend, #640911; 1: 1000) conjugated to Alexa 647 or propidium iodide dye (Sigma Aldrich, #537059; 1:500) for 15 min. Cells were further co-stained with Hoechst 33342 (Invitrogen, #H3570) to visualize and compute total cell count. 150 µL PBS was added in each well and image acquisition and analyses were performed on Keyence BZ-X800 fluorescence microscope (20x and 40x objective).

2.6.3. Cell size analyses using cell-counter

SH-SY5Y cells seeded in 24-well plates were treated with Aβ peptides (1 µM, 24 h). Cells in treatment media or adhered to plates (collected by trypsinization in PBS) were pelleted by centrifugation at 3000 g, 3 min; and resuspended in 100 µL of culture media on ice. 10 µl of 0.4% Trypan Blue solution (ThermoFischer Scientific, #15250061; 1:10000 dilution) was added to each tube and analyzed via Corning® Cell Counter (Germany), using default software settings.

2.6.4. Trypan blue dead cell assay

After treatment and subsequent washing steps, 10 µl of Trypan Blue solution (1:10000 dilution) was added to each well and plate was incubated at 37ºC in for 10 min. Fluorescence (λ_{Ex} 488 nm / λ_{Em} 660 nm) were recorded on a spectrophotometer.

2.6.5. MTT cell viability assay

Procedure previously described was followed (Glebov et al. 2015). After treatment and subsequent washing steps, 10 µL MTT (3-(4,5-Dimethylthiazol-2-yl) solution (Sigma Aldrich, # M2003, 5.5 mg/ml in PBS) was added into each well and incubated at 37ºC in a 5% CO_2 humidified atmosphere for 2 h. After incubation, MTT solution was discarded followed with two PBS washes and 100 µL of DMSO was added in each well, and plate was allowed to shake on an orbital shaker for 15 min. OD at 560 nm was measured.

2.6.6. MultiTox-Fluor multiplex cytotoxicity assay

Analyses of percent live and dead SH-SY5Y cells post Aβ treatment (imaging 96-well plate) was determined by MultiTox-Fluor multiplex cytotoxicity assay® from Promega as per manufactures protocol. In brief, GF-AFC and bis-AAF-R110 substrate solution (1:5 dilution, 10 µL) was added to each well. Plate was incubated at 37ºC in a 5% CO_2 humidified atmosphere for 30 min. Live-cell fluorescence (λ_{Ex} 400 nm / λ_{Em} 505 nm) and dead-cell fluorescence (λ_{Ex} 485 nm / λ_{Em} 520 nm) was measured, respectively.

2.7. Cell function assays

2.7.1. Live-cell calcium assay

SH-SY5Y cells seeded on Ibidi 8-well plate, glass bottom, on D1. On D3 pre-treatment was done with Ca2+ minus media for 30 min followed by incubation with Rhod-3 dye according to manufacturer's protocol for 25 min. After incubation, cells were washed with multiple washes of PBS to remove the excess dye. Live cells were imaged on Carl Zeiss Axio Imager 2 ApoTome fluorescence microscope (20x objective). After initial three baseline recordings of intracellular Ca2+ levels, cells were treated with non-aggregated or pre-aggregated 1 µM Aβ variants and recording were resumed for a time span of 2 h and interval of 5 min each.

2.7.2. SH-SY5Y reporter cell-based assessment of autophagic flux and TFEB nuclear localization

SH-SY5Y cells seeded on 24-well plates and transfected with either GFP-LC3-LC3Δ-RFP (Kaizuka et al. 2016) or mCherry-GFP-LC3B (Tien et al. 2016) tandem, or GFP-TFEB (Zhang et al. 2018) reporter constructs. 16 h post transfection media change, SH-SY5Y cells, were treated with different Aβ peptides (1 μM, 24 h), or autophagy modulator substrates 10 μM rapamycin, 100 nM Bafilomycin A1 (BAF A1), 1 μM 3MA or with respective controls for the mentioned time points. RFP/GFP ratiometric images were created by using the image calculator module. Fluorescence signal intensities of respective channels were calculated for the ROI (manually selected) and RFP/GFP or mCherry/GFP ratios of the individual values were computed. Cell outline was drawn manually and number of mCherry+ GFP± vesicles per cell were counted.

2.7.3. Lysosomal acidification assay using Lysosensor

Cells were cultured on coverslips and treated with Aβ variants (primary cortical neurons, 500 nM, 4 h; SH-SY5Y cells, 1 μM, 24 h) in presence of 50 μM Lysosensor-dextran probe (ThermoFischer Scientific, L7545) in $FCS^{-}PS^{-}$ media for the indicated time points. Post incubation, cells were washed thrice with PBS to remove the excess probe, fixed, and stained as indicated. Lysosensor green/blue ratiometric images were created by using the image calculator module. The number of perinuclear and peripheral LAMP-2 positive lysosomes or percentage of LAMP-2 compartments containing Aβ was computed using the concentric circle processing module. For fluorescence assessment, cells were cultured and treated in a black wall 96-well plate for the indicated time points. Fluorescence intensity analyses of blue and green channel was done using a spectrophotometer, RFU (λ_{Ex} 340 nm / λ_{Em} 450 nm (*blue channel*) and λ_{Ex} 340 nm / λ_{Em} 535 nm (*green channel*)) and the emission intensity ratio was computed. Values normalized to absorbance OD at 340 nm and protein content per well and represented as change of lysosensor acidification with respect to control cells. pH values were computed by preparing a standard curve, wherein cells treated with 1 μM Nigericin and 1 μM Monensin were incubated with media of pH 4.5, 7.5 and 9.2. 100 nM BAF A1, 1 mM NH_4Cl and 10 μM rapamycin treated cells were also used as independent controls to check the

validity of the experiment. Change in lysosensor pH (ΔpH_l) for Aβ treated cells was quantified using the formula $\Delta pH_l = pH_{final}$ (control/Aβ, t = 24 h) − $pH_{initial}$ (control, t = 0 h).

2.7.4. Cathepsin D & E assay

Cells were seeded in a 96-well plate and treated with different Aβ variants (primary cortical neurons, 500 nM, 4 h; SH-SY5Y cells, 1 μM, 24 h) in $FCS^{-}PS^{-}$ media. After treatment, supernatant was discarded, and cells were washed as described earlier. Procedure previous described (Dana et al. 2019), was followed with slight modifications. Cells were further lysed by solubilizing the plasma membrane and intracellular membranes by adding 50 μL of 200 μg/mL digitonin in acetate buffer followed by incubation on ice for 15 min. Additionally, 50 μL of the Omnicathepsin D & E fluorogenic substrate (Enzo Life sciences, BML-P145) in sodium acetate buffer was added to the lysates in the wells for a final concentration of 30 μM of substrate and 10 mM DTT. Plate was incubated for 25 min at RT and the reaction was stopped by addition of 10 μl of ethanol. Fluorescence values (λ_{Ex} 380 nm / λ_{Em} 460 nm) were recorded on a spectrophotometer and the relative amount of substrate cleavage in each well was computed, respectively.

2.7.5. Proteasomal and proteolytic activity assay

Procedure previous described was followed with minor modifications. Briefly, cells seeded in 96-well plate, treated with different Aβ variants (1 μM, indicated time points) were lysed in digitonin-acetate lysis buffer and incubated on ice for 15 min. Proteasomal sensitive fluorogenic substrates were added to each well respectively. Fluorogenic substrate for proteasome - Ac-Nle-Pro-Nle-Asp-AMC (trifluoroacetate salt) (Cayman chemicals, #21639); 26S proteasome - Ac-RLR-AMC (trifluoroacetate salt) (Cayman chemicals, #26643); 20S proteasome and calpain - Suc-Leu-Leu-Val-Tyr-AMC (Cayman chemicals, #10008119); caspase-like post-glutamate peptide hydrolase of the 26S proteasome or 20S proteolytic core - Z-LLE-AMC (Cayman chemicals, #10008117); and colorimetric caspase substrate - Ac-DEVD-pNA (Cayman chemicals, #14460) or a commercial Proteasome 20S assay kit (ENZO life sciences, #BML-PW8720) was used to measure proteasomal activities. Standard curve for the fluorogenic, or colorimetric response was done using 7-Amino-4-methylcoumarin dye (AMC, Sigma Aldrich, #257370) or 4-Nitroaniline (pNA, Sigma Aldrich, #185310). Proteasomal assay buffer (50 mM Tris-HCl,

pH 7.5, 40 mM KCl, 5 mM $MgCl_2$, 0.5 mM ATP, 1 mM DTT and 10% glycerol) was used for subsequent dilution of substrates or cell lysates. Addition of ATP prevented dissociation of the 26S proteasome. Pilot experiments were conducted to optimise the amount of fluorogenic substrates. Depending on the fluorophore in each experiment, a standard AMC dye fluorescence or pNA absorbance curve was prepared in each plate to avoid plate to plate variation. Plates were incubated for 30-45 min at RT and the reaction was stopped by addition of 10-25 µl of ethanol. Fluorescence values of AMC (λ_{Ex} 400 nm / λ_{Em} 505 nm) or absorbance of pNA OD at 380 nm were recorded on a spectrophotometer and the relative amount of substrate cleavage in each well was computed, respectively.

2.7.6. Mitochondrial susceptibility and viability assay

SH-SY5Y cells were seeded in a 96-well plate, were treated with 10-1.11 µM serial dilution of Aβ or mitochondrial substrates for 24 h, supplemented with growth media either containing glucose or galactose. Serial dilution curve of valinomycin (Sigma Aldrich, #V0627) was used as negative control, respectively. Mitochondrial susceptibility and viability were measured using a Mitochondrial ToxGlo™ assay kit from Promega (#G8000), according to manufactures protocol. Briefly, after treatment, cytotoxicity reagent (bis-AAR-R110) was added to each well, plates were incubated at 37°C for 30 min; and fluorescence (measurement λ_{Ex} 485 nm / background λ_{Em} 525 nm) was measured using a spectrophotometer. Next, ATP detection reagent (1:2 dilution) was added to each well and luminescence was recorded on a spectrophotometer.

2.7.7. Mitochondrial membrane potential measurement

Experiments were performed by Mr. Daniel Puchta-Stromberg from the laboratory of Prof. Wolfgang Voos. Mitochondrial membrane potential ($\Delta\psi_{mt}$) was analyzed by the potential-sensitive fluorescent dye TMRE (ThermoFischer Scientific, #T669), using a previously reported protocol (Cenini et al. 2016). After incubation with Aβ peptides, isolated mitochondria were resuspended in potential buffer (0.6 M sorbitol, 0.1% BSA, 10 mM $MgCl_2$, 20 mM KP_i, pH 7.2, 5 mM malate, 10 mM glutamate) and incubated with 1 µM TMRE for 30 min at 30°C on ice. After washing away of excess of TMRE, the TMRE fluorescence was measured in a spectrophotometer (λ_{Ex} 540 nm / λ_{Em} 585 nm) on an Infinite M200ProTecan spectrophotometer (Männedorf, Switzerland).

2.7.8. Oxidative stress assay

Literature reported protocol (Li et al. 2018) was followed with slight modifications. Briefly, cells seeded in a black imaging 96-well plates, treated with Aβ peptides, were stained with anti-Aβ and 8-OHdG antibody (Abcam, #ab48508), respectively. Post-staining with respective secondary antibodies, cells were imaged on Keyence fluorescence microscope automated imaging module. Percent cells positive for Aβ and 8-OHdG signals were quantified and normalised to the number of total cell count (DAPI) per frame using the processing module of Keyence software.

2.7.9. pH measurements

For intracellular pH (pH_i) measurements, cells seeded in a 96-well plate and initially loaded with pHrodo red dye (pHrodo™ AM Variety Pack, ThermoFischer Scientific, #P35380) along with 1x of powerload® concentrate component (50 nM, 20 min, 37^{o}C). Multiple washing with PBS was done to ensure complete removal of pHrodo dye and treatment media containing Aβ of standard pH controls were added. For a pH standard curve, cells were treated with 1 µM nigericin and 1 µM monensin and incubated with media of pH 4.5, 7.5 and 9.2, respectively. 100 nM BAF A1, 1 mM NH_4Cl and 10 µM rapamycin treated cells were also used as independent controls. Plates were then incubated in a spectrophotometer equipped with temperature and CO_2 controlled conditions. Fluorescence readings (λ_{Ex} 560 nm / λ_{Em} 585 nm) were recorded for 26 h at regular intervals of 15 min. Values were then computed and readings were normalised to that of control conditions and standard pH controls. Fluorescence imaging of cells plated in Ibidi-8-well dishes and treated with Aβ (1 µM, 24 h) was done on Carl Zeiss Axio Imager 2 ApoTome fluorescence microscope. 6 random images per condition were acquired and representative image from two independent experiment has been represented. Since Phenol red present in culture media is a pH indicator, extracellular pH of the cells was analyzed by plating 200 µl of treatment media from Aβ treated SH-SY5Y cells (1 µM, 24 h) in 96-well plates. Absorbance of each well at 427 nm was measured and compared to standard pH modulators in cell culture media.

2.7.10. LDHA measurements

TCA precipitated supernatant and cell lysates of Aβ treated SH-SY5Y cells (6 cm dish) were analyzed via WB. 0.1% TRT-X100 treated cells were used as positive control. LDHA activity was computed by analysing the ratio of LDHA secreted in the supernatant with respect to cell lysates, respectively.

2.7.11. β-galactosidase activity assay

Literature published protocol (Schaefer et al. 2016) was followed with certain modifications. Briefly, supernatant of cells (seeded in 24-well plate) treated with Aβ peptides were plated in technical duplicates in a 96-well plate and 100 µl β-galactosidase assay buffer (60 mM Na_2HPO_4, 40 mM NaH_2PO_4, 10 mM KCl, 1 mM $MgSO_4$, 36 mM β-mercaptoethanol and 0.3% NP40) containing 1.1 mg/ml *o*-nitrophenyl-beta-D-galactopyranoside (ONPG) substrate was added in each well and incubated for 60 min at 37^oC. OD of each well at 420 nm with a background subtraction at 600 nm, was done on a spectrophotometer.

2.7.12. Caspase-1 and Caspase3/7 fluorescence assay

Procedure similar to literature published protocol were followed (Hieronymus et al. 2000; Nicholson et al. 1995). SIMA9 cells seeded in a 96-well plate, were treated with SH-SH5Y-APP_{Sw} cell conditioned media or Aβ peptides (1 µM) for 18 h. After treatment, cells were washed as described earlier and incubated with Caspase-1 (Ac-WEHD-AMC, Enzo Lifesciences, ALX-260-057-M001) or Caspase-3/7 (Ac-DEVD-AFC, Enzo Lifesciences, ALX-260-032) fluorogenic peptides for 25-30 min. Post incubation with peptides, cells were fixed and counterstained with CD16/32 or CD45 antibodies respectively. Plates were then imaged using Keyence BZ-X800 fluorescence microscope.

2.7.13. Caspase-1, 4, 5 activity assay

Procedure previous described was followed (O'Brien et al. 2017). SH-SH5Y-APP_{Sw} cell conditioned media or Aβ treated SIMA9 cells (96-well plate) were lysed in 50 µL of 200 µg/mL digitonin in acetate buffer to the wells containing the cells and incubating on ice for 15 min. Additionally, 50 µL of the Ac-WEHD-pNA substrate (Enzo Lifesciences, ALX-260-082) in caspase activity buffer (100 mM HEPES pH 7.2, 0.1% NP-40, 10 mM DTT, 0.2%

CHAPs) was added to the lysates in the wells for a final concentration of 25 µM of caspase sensitive substrate. Plate was incubated for 45 min at RT and the reaction was stopped by addition of 10 µl of ethanol. OD of each well at 420 nm with a background subtraction at 600 nm was measured on a spectrophotometer and the relative amount of substrate cleavage in each well was computed.

2.7.14. ASC speck formation assay

Procedure similar to literature published protocol was followed (Stutz et al. 2013). SIMA9 cells stably expressing ASC-cerulean construct were seeded in a 96-well plate and treated with SH-SH5Y-APP_{Sw} cell conditioned media or Aβ peptides (1 µM) in presence or absence of lipopolysaccharides (LPS, 2.5 ng/mL) for 18 h. After treatment, cells were stained with DRAQ5 (ThermoFischer Scientific, #62254) to visualise the nuclei, and imaged post fixation. Images were acquired on VisiScope spinning disk confocal microscope, whereas formation of ASC specks were computed on Keyence fluorescence microscope automated imaging module and quantified using the processing module of Keyence software.

2.8. Microscopy

2.8.1. Fluorescence microscopy

Immunocytochemical analyses of SH-SY5Y or SH-SY5Y-APP_{Sw} cells were performed either on Carl Zeiss Axio Imager 2 ApoTome (63× oil immersion objective) or Keyence BZ-X800 fluorescence microscope (20× or 40× air objective). Image acquisition and parameter settings were kept constant for the acquisition of each set. Each immunostaining was performed with cross-combination of secondary antibodies to rule out non-specific reactivity. Analyses of acquired images were performed using the processing module of Keyence software.

2.8.2. Confocal microscopy

Confocal images of primary cortical neurons and mouse brain sections were acquired on VisiScope CSU-W1 spinning disk confocal microscope using VisiView Software (Visitron Systems GmbH, Germany). Laser power, detector gain, and other parameter settings were kept constant for the acquisition of each set. Images were acquired using either 5×

(for complete frame) or 20×, 40× water or 63× water objective (higher magnification), 2048 × 2048 pixels, 1 x 1 binning. *z*-stacks were obtained at 2,048 × 2,048 resolution, steps = 16, and step size = 0.33-1 µm.

2.8.3. Electron microscopy (EM)

SH-SY5Y cells were seeded and treated on glass coverslips as mentioned earlier. After treatment cells were washed and fixed with 4% EM grade PFA (methanol free) and 2.5% glutaraldehyde in ddH_2O overnight at 4°C. Cells immunofluorescence analyses were processed as previously described. For EM analyses, fixed cells were washed in 0.1 M cacodylate buffer (pH 7.4), and incubated in 1% osmium tetroxide, 0.8% potassium ferricyanide in 0.1 M cacodylate buffer (pH 7.4) for 2 h at RT, followed by washing for 10 min in 0.1 M cacodylate buffer (pH 7.4) thrice. Osmified cells were then dehydrated in a series of increasing ethanol solutions (30, 50, 70% for 10 min each; 0.5% uranyl acetate in 70% ethanol for 60 min; 90, 95, and 100% ethanol, 10 min each) at RT. Further, cells were infiltrated with a 1:1 ratio of ethanol and propylene oxide for 10 min at RT and finally 10 min incubation in 100% propylene oxide twice. Cells were then infiltrated with Epon epoxy resin (Sigma-Aldrich, #45359-1EA-F) in increasing ratios of propylene oxide: Epon (1:1 for 1 h, 1:2 overnight at RT), and finally 2x 100% Epon for 1 h at RT and embedded using beem capsules (Plano, #G360-1). Epon was polymerized by curing for 48 h at 60°C. After polymerization, beem capsules were trimmed away with a razor blade and the coverslips were removed using freeze-thaw cycles of liquid nitrogen and a heating plate set to 60°C. Once the coverslips were removed, the block face was trimmed to fit on an EM grid (formvar and copper-coated copper slot grid; Science Services, #EFCF2010-Cu-50) and ultra-thin sections 50 nm-thick were collected. Sections were counterstained with 1% aqueous uranyl acetate for 25 min and lead citrate Ultrastain solution (Leica, #16707235) for 7 min with thorough washing and drying in between. Sections were imaged with a Zeiss Crossbeam 550 (acceleration voltage: 30 keV, probe current: 150 pA) using a STEM detector. For all examined samples, multiple cells were imaged (>4) with resolution between 24 nm and 2.4 nm per pixel, across each EM grid. This ensured classification of different cellular morphology and avoided inadvertent production of a biased/subjective data selection. Images were processed using Fiji ImageJ software and best representative images from three independent experiments have been illustrated.

Quantification of the number of autophagic compartments was done manually using a 10 μm^2 ROI grids, placed in the cytosolic region of the individual cells using the 'rule of L' counting method. Results are representative of values computed from three independent experiment (n ~30 cells).

2.9. Image analyses and processing

In all experiments, per coverslip or brain section, randomly selected 6-10 images were captured, which were further used for quantification or colocalization analyses. All images depicted herewith were minimally processed using Fiji ImageJ software (version 1.53t). Due to slight variability in transfection efficiency or the number of cells in different experimental set-ups, the readings from each experiment were averaged and normalized to the control cells from that particular set. Average values from each experiment were normalized to the respective controls (or standard positive/negative control conditions) in the same set. Values from independent experiments were then compared together and values are represented as independent data points, as respectively mentioned in the figure legends.

2.10. Statistical analyses

All graphical illustrations have been prepared using GraphPad Prism 9.5.1.733, Serial number: GPS-1692665-T, Machine ID: 1CFB4E038FE. Statistical analyses for a particular graph have been mentioned in the respective figure legends. All tests have been performed using the in-built default settings of the module in the software, without modifications, until mentioned otherwise; not significant (ns) $p > 0.05$; * $p = 0.05$; ** $p = 0.01$; *** $p = 0.001$; **** $p = 0.0001$.

3. Results

3.1. Differential aggregation behavior, solubility characteristics and intracellular uptake of phosphorylated Aβ

3.1.1. Site-specific phosphorylation affects Aβ oligomerization and cytotoxicity

The effect of site-specific phosphorylation on Aβ oligomerization was examined using synthetic Aβ peptides - non-phosphorylated (npAβ), phosphorylated (pSer8Aβ and pSer26Aβ; pAβ) or pseudo-phosphorylated peptides (Serine → Aspartic acid; S8D Aβ and S26D Aβ; DAβ). Aβ peptides aggregated for indicated time points were analyzed by Native-PAGE (Fig. **6A**), SDS-PAGE (Fig. **6B**, Ext. Fig. **1**) and Thioflavin-T (ThT) fluorescence assays (Fig. **6C**). In line with previously published reports (Kumar and Walter 2011; Kumar et al. 2013; Kumar et al. 2016), phosphorylation of the Aβ peptide altered the aggregation behavior of Aβ, in a phosphorylation site-specific manner. 96 h incubated npAβ forms aggregates, which do hardly migrate in the gels and are detected near the wells (*asterisks*, Fig. **6A-B**). Similar aggregates were also detected for the Aβ peptide phosphorylated at serine residue 8 (pSer8Aβ) (Fig. **6A-B**). However, pSer8Aβ showed augmented aggregation propensity, wherein aggregated Aβ species are already detected at 8 h of incubation, in contrast to npAβ (Ext. Fig. **1A, B**). On the other hand, Aβ phosphorylated at serine residue 26 (pSer26Aβ) preferentially forms intermediate weight oligomeric species and very little if any signals are detected in the upper regions of the gel (Fig. **6A**, **B**, Ext. Fig. **1C**). The pseudo-phosphorylated DAβ peptides, S8D Aβ and S26D Aβ, showed comparable aggregation behaviour as the corresponding phosphorylated variants (Ext. Fig. **1D**, **E**). Assessment of β-sheet content within these aggregates species was evaluated using ThT fluorescence assay (Fig. **6C**). pSer8Aβ aggregates showed the highest ThT fluorescence indicative of higher β-sheet content as compared to other two peptides. Although, oligomeric pSer26Aβ showed lower ThT fluorescence in comparison to aggregated npAβ or pSer8Aβ species, a modest but significant elevation in ThT fluorescence post-aggregation, is indicative of β-sheet structures present in intermediate weight pSer26Aβ oligomers.

Next, the effects of non-aggregated or pre-aggregated Aβ peptides on viability of human neuroblastoma SH-SY5Y cells (Fig. **6D**), was examined. β-Sheet rich fibrillar aggregates

of npAβ species were slightly less cytotoxic than non-aggregated npAβ, in line with previous reports (Vadukul et al. 2020; Cecchi and Stefani 2013; Stefani 2012). Phosphorylated Aβ peptides in (pre)aggregated and non-aggregated state exerted higher cytotoxicity, as compared to npAβ, respectively. The two phosphorylated Aβ variants, exerted similar effects on cell viability.

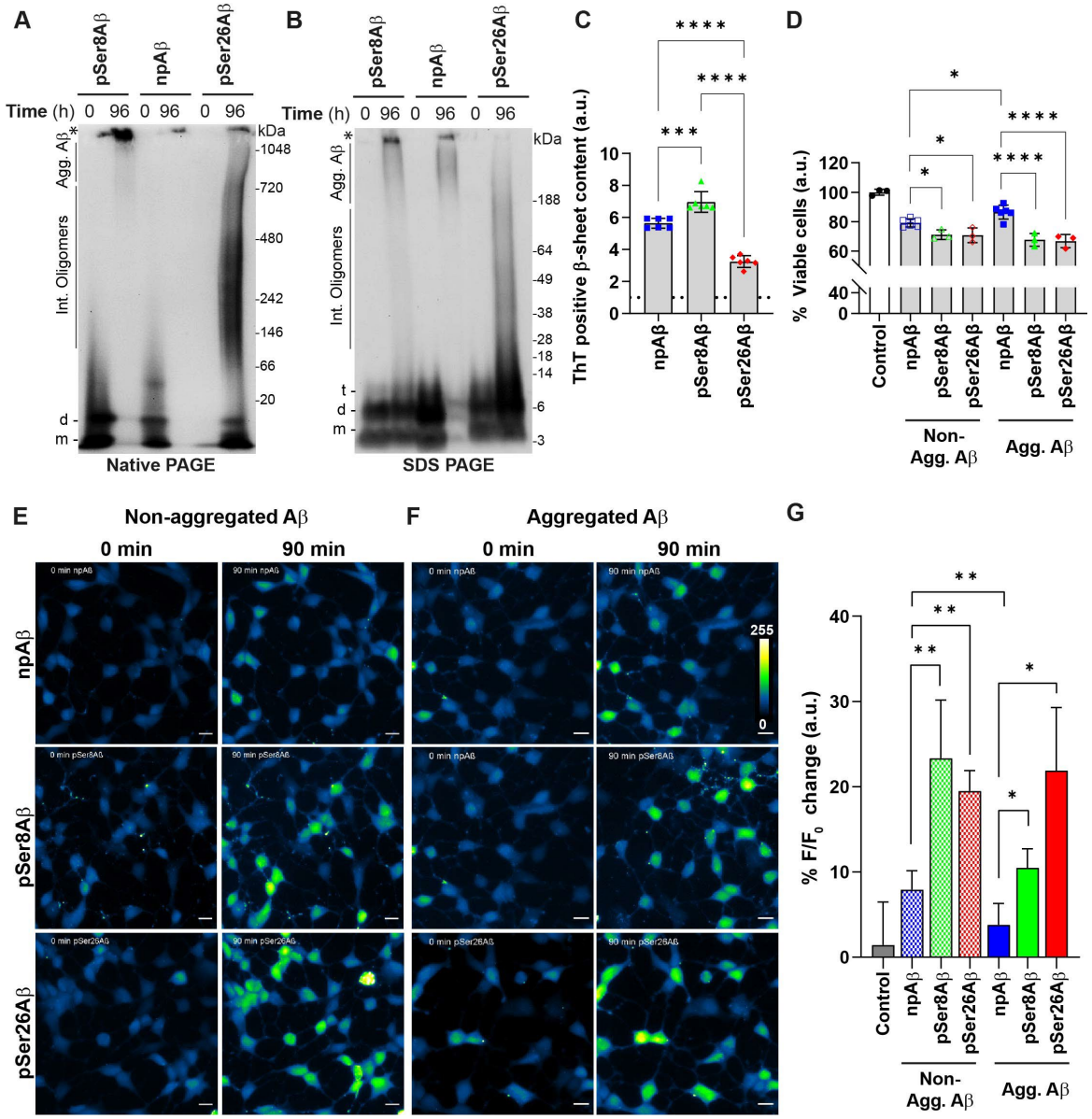

Fig. 6: Site- and aggregation- specific effects of phosphorylated Aβ on cell viability and intracellular calcium flux. A, B. Western immunoblotting (WB) showing differential aggregation behaviour of phosphorylated Aβ variants (pSer8Aβ, pSer26Aβ) to non-phosphorylated npAβ peptide at 0 h and 96 h of incubation, analyzed via Native PAGE (**A**) and SDS-PAGE (**B**). Aβ species were detected with anti-Aβ antibody 82E1; *m,* monomer*; d,* dimer*; t,* trimer*; Agg.,* aggregated*; Int. oligomers,* Intermediate-weight

oligomers*; ** fibrils*.* Data is representative of two independent experiments. **C.** Thioflavin-T measurements representing the relative amounts of β-sheet positive structures after 96 h of incubation, expressed as fold increase in the ThT fluorescence intensity with normalised to 0 h readings of the individual peptides (*dotted line*). Values represent mean ± S.D; n = 6, N = 2. **D.** SH-SY5Y cells were treated without (control, *white bar*) or with 0 h non-aggregated or 96 h aggregated Aβ peptides (1 μM, 60 min). Cell viability was determined by Presto Blue assay, depicted as percentage of untreated/control cells. Values represent the mean ± S.D; n = 9, N = 3. **E-G.** SH-SY5Y cells loaded with Rhod-3 dye were treated without or with the indicated Aβ variants (1 μM, 90 min) and readings were recorded in the intervals of every 5 min. Time snap images depict change in intracellular calcium flux in presence of non-aggregated (**E**) or non-aggregated (**F**) Aβ variants at 0 and 90 min respectively. Pseudo colour 3D intensity bar indicates relative change of intracellular Ca^{2+} flux. Scale bar = 10 μm. Data is representative of four independent experiments. Bar plot (**G**) comparing the rate of calcium flux (F/F_0) in SH-SY5Y cells treated with respective non-aggregated and pre-aggregated Aβ variants (90 min). Change in fluorescence intensities were computed and normalised to readings prior to treatment (t = 0 min). Values represent mean ± S.D; n = 200 cells, N = 4. * $p < 0.05$; ** $p < 0.01$; *** $p < 0.001$; **** $p < 0.0001$; n.s. $p \geq 0.05$, not significant (One-way ANOVA, GraphPad Prism). Time-dependent Aβ aggregation experiments are provided in Ext. Fig. **1**.

SH-SY5Y cells initially starved of Ca^{2+} and loaded with Rhod-3 dye, were treated with either non-aggregated or pre-aggregated Aβ species to monitor the changes in intracellular Ca^{2+} levels. Physiological calcium levels were restored in treatment media and changes in Rhod-3 fluorescence signals were recorded as an indicative of changes in the intracellular Ca^{2+} concentration. As seen in Fig. **6E-G**, non-aggregated npAβ significantly increased intracellular Ca^{2+} concentration, compared to its aggregated form. Notably, both pAβ peptides in non-aggregated or pre-aggregated states showed a significant increase in intracellular Ca^{2+} signals, as compared to npAβ (Fig. **6E-G**). Although the individual phosphorylated variants in non-aggregated (pSer8Aβ > pSer26Aβ) or aggregated states (pSer26Aβ > pSer8Aβ) tended evoke differential Ca^{2+} response, the differences were not statistically significant. Together, these findings demonstrate phosphorylation-state specific effect on Aβ aggregation behavior associated with Ca^{2+} dyshomeostasis and cytotoxicity.

3.1.2. Phosphorylation promotes the generation of soluble oligomeric species that are distinctly toxic

We further examined if there is a phosphorylation-state specific effect on the solubility of Aβ species. Aβ aggregated for the indicated time periods were fractionated by

ultracentrifugation, as depicted in scheme **1A** (Esparza et al. 2016) and the soluble (*supernatant*) and insoluble (*pellet*) fractions were analyzed by western immunoblotting (WB, Fig. **7A-F** and Ext. Fig. **2A-D**). Additionally, their effect on cell viability was examined (Fig. **7G-I** and Ext. Fig. **2E-F**). Non-aggregated Aβ species were almost completely detected in the supernatant. Aggregates of npAβ formed during incubation are progressively detected in the pellet fractions indicating a decrease in solubility of these aggregates (Fig. **7A-D**). An inverse relationship was seen between the duration of npAβ aggregation and its solubility characteristics. 24 h npAβ (insoluble) species showed significantly higher cytotoxicity as compared to non-aggregated soluble species and insoluble 96 h aggregated fibrillar species (Fig. **7G**). Analyzing pAβ peptides, pSer8Aβ was readily detected in soluble fractions until 48 h and showed an Aβ concentration dependent effect on cell viability. However, aggregated pSer8Aβ species in the insoluble fraction induced higher cytotoxicity as compared to the aggregated npAβ species. (Fig. **7B, E, H**). On the other hand, assemblies formed by pSer26Aβ peptides during the aggregation period are mostly detected in the soluble fraction (Fig. **7C, F, I**). Soluble oligomeric pSer26Aβ species tended to show an aggregation-time dependent effect on cell viability, but the differences are not statistically significant. Also, pseudo-phosphorylated peptides were analysed in a similar experimental set-up (Ext. Fig. **2**). Substitution of the serine residue with aspartic acid augmented the solubility of the aggregated S8D Aβ substantially, which is also reflected in its effect on cell viability, as compared to the phosphorylated Aβ peptide (Ext. Fig. **2A, C, E**). S26D Aβ and pSer26Aβ showed comparable behavior. Overall, soluble oligomeric pAβ (and DAβ) assemblies showed a stronger detrimental effect on cell viability as compared to the npAβ peptide.

Non-aggregated and pre-aggregated Aβ peptides were loaded on a sucrose gradient and subjected to rate zonal ultracentrifugation (Scheme **1B**) to separate the species based on differences in both size and density. Fractions were analyzed by SDS-PAGE (WB, Fig. **8A-F**) and indirect enzyme linked immunosorbent assay (ELISA, Fig. **8G-K**). 96 h aggregates of npAβ are mostly detected in fraction 6-8, densely in fraction 7, wherein non-aggregated npAβ species are detected in the earlier fractions 1-4, predominantly in fractions 1 and 2 (Fig. **8A, D, G**).

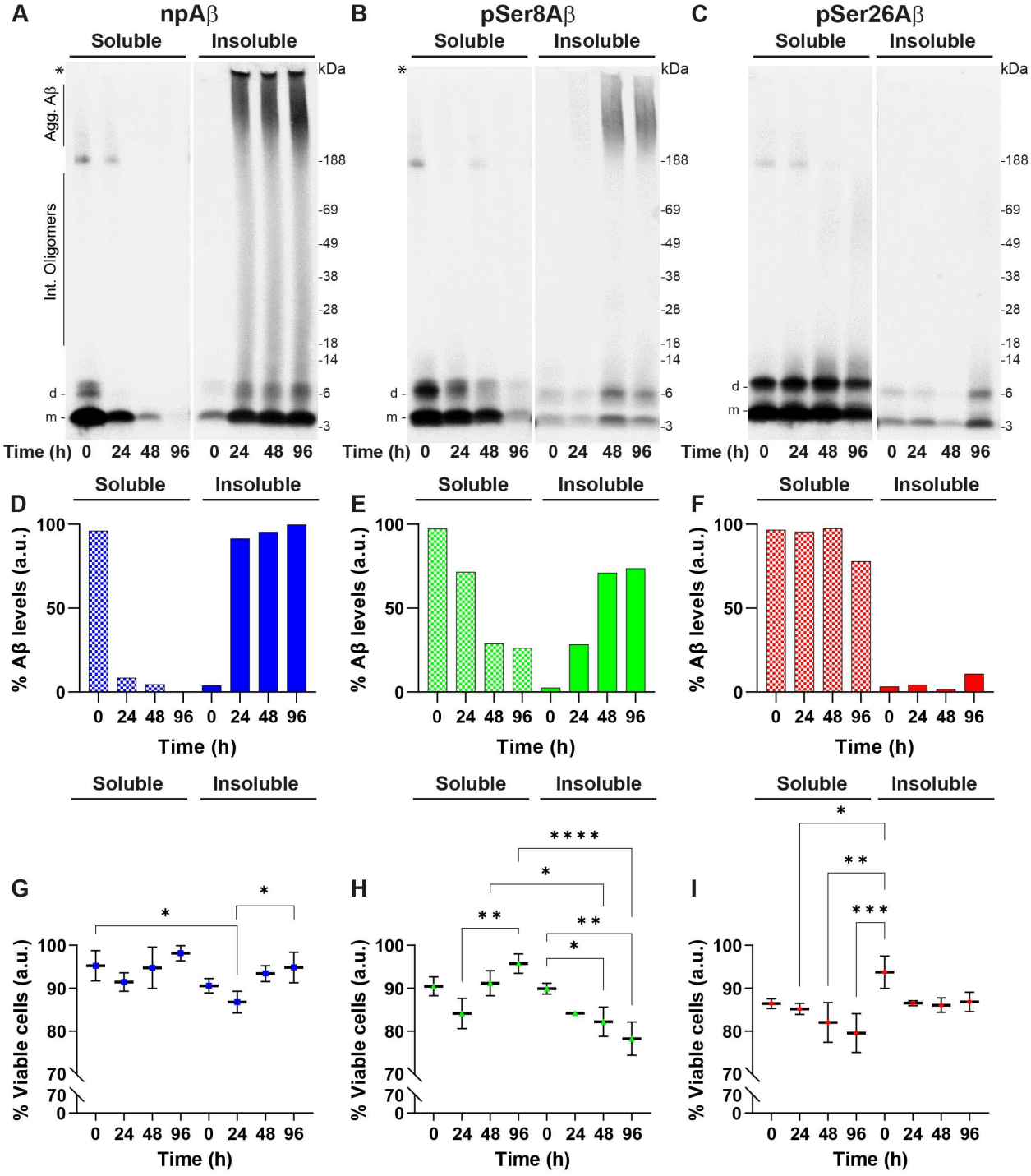

Fig. 7: Phosphorylation and aggregation-state dependent soluble-Aβ-oligomer-induced cytotoxicity of pAβ peptides. A-C. Non-aggregated (0 h) and aggregated Aβ for different time points (24, 48 and 96 h) were subjected to fractionation into soluble (*supernatant*) and insoluble (*pellet*) fractions and were analyzed by SDS-PAGE. Immunoblots depicting soluble and insoluble fractionated pre-aggregated species of npAβ (**A**), pSer8Aβ (**B**), and pSer26Aβ (**C**). Aβ species were detected with anti-Aβ antibody 82E1. *m,* monomer*; d,* dimer*; t,* trimer*; Agg.,* aggregated*; Int. oligomers,* Intermediate-weight oligomers*;* * fibrils **D-F.** Bar plots showing densitometric quantification of the Aβ

signal intensities in the soluble and insoluble fractions of npAβ (**D**), pSer8Aβ (**E**) and pSer26Aβ (**F**) variants, at indicated time points, respectively. Soluble: transparent, insoluble: opaque colours, respectively. Values were computed using ImageJ gel quantification module. Values were normalised to total signals in both soluble and insoluble fraction and depicted as percent Aβ levels in respective fractions. Data depicted herewith is representative of two independent experiments. **G-I.** Scatter plots showing the percentage viability of SH-SY5Y cells treated with the soluble and insoluble fractions of npAβ (**G**), pSer8Aβ (**H**) and pSer26Aβ (**I**) variants, at indicated time points, respectively. Cell viability is evaluated using Presto-Blue assay. Readings were normalised to control untreated cells and presented as percent change in viable cells *wrt* control. Values represent mean ± S.D; n = 3, N = 3. * $p < 0.05$; ** $p < 0.01$; *** $p < 0.001$; **** $p < 0.0001$; n.s. $p \geq 0.05$, not significant (One-way ANOVA, GraphPad Prism). Additional control experiments with pseudo-phosphorylated S8D and S26D Aβ variants are provided in Ext. Fig. **2**.

pSer8Aβ aggregates are detected primarily in fractions 5-7, densely in fraction 6 (Fig. **8B, E, H**). A significant shift of pSer8Aβ assemblies to the earlier fractions is suggestive of their smaller size and/or density in comparison to the fibrillar npAβ species. The non-aggregated pSer8Aβ peptide is predominantly detected in fractions 1 and 2. Low intensity signals detected in fractions 4-6 could be attributed to the increased aggregation propensity of pSer8Aβ peptide. Since pSer26Aβ peptides do not form higher molecular weight assemblies, they are only detected in the earlier fraction, in either aggregation states. Non-aggregated pSer26Aβ peptides are seen predominantly in fraction 1, and little in fraction 3. Oligomeric pSer26Aβ peptides showed differential segregation in fractions 1-4 (monomers, fraction 1 and dimers/trimers/oligomers in fraction 2-4) (Fig. **8C, F, I**). ELISA analyses using fibrillar (OC. Fig. **3J**) or oligomer (A11, Fig. **8K**) conformation specific antibodies, showed significant differences within the aggregation assemblies of the analyzed peptides. The OC antibody recognizes the specific "β-turn conformation" within Aβ oligomers/fibrils which are mostly linear in nature. On the other hand, A11 antibody recognizes compact, globular oligomeric Aβ assemblies which are more soluble in nature. Differences in A11 and OC signals for npAβ and pSer8Aβ, in fractions 5-8 (OC:pSer8Aβ - maxima in fraction 6; A11:npAβ – maxima in fractions 7-8) indicated that pSer8Aβ aggregates are rich in soluble oligomeric assemblies rather than β-sheet rich npAβ fibrils. Similarly, soluble oligomeric pSer26Aβ species are detected in fractions 1-2 by A11 antibody as compared to the OC antibody, being rather smaller in size and density when compared to oligomeric pSer8Aβ assemblies or npAβ fibrils. These observations indicate that phosphorylation at either site of the Aβ peptide increases the oligomerization

propensity (pSer8Aβ – high molecular weight oligomers, pSer26Aβ – low and intermediate weight oligomers), irrespective of their differential aggregation behavior.

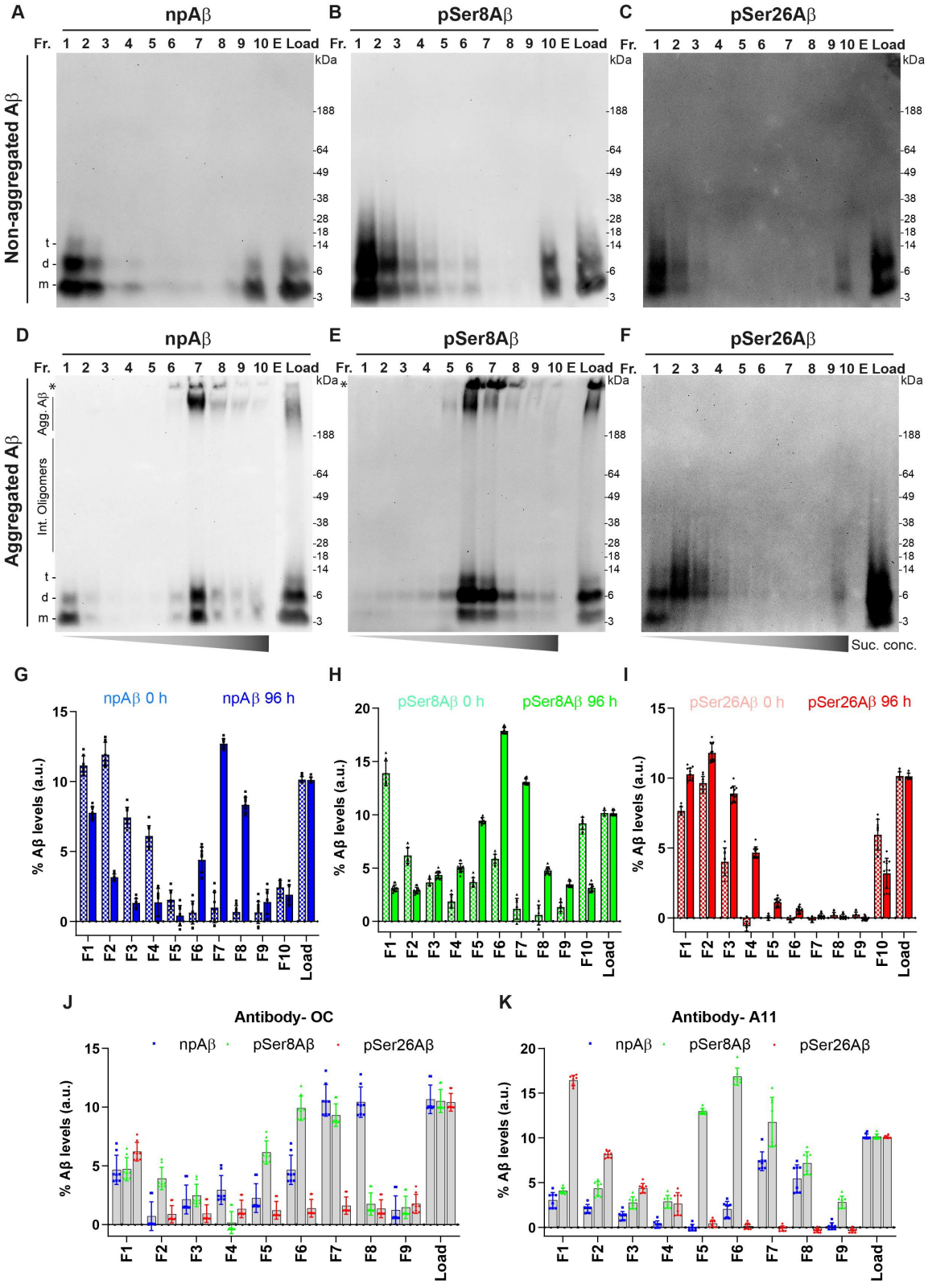

Fig. 8: Phosphorylation of Aβ alters density dependent fractionation of Aβ peptides. A-F. Non-aggregated (0 h, **A-C**) and pre-aggregated (96 h, **D-F**) Aβ samples were subjected to sucrose-gradient dependent centrifugation. Post fractionation, samples were analyzed by SDS-PAGE and WB showing differential distribution of Aβ species in different fractions. Load represents 1/10th of the total load of Aβ samples. *m,* monomer*; d,* dimer*; t,* trimer*; Agg.,* aggregated*; Int. oligomers,* Intermediate-weight oligomers*;* * fibrils Data is representative of three independent experiments. **G-K.** Percent Aβ content in each fraction was analyzed by indirect ELISA. Bar plots showing densitometric quantification of npAβ (**G**), pSer8Aβ (**H**) and pSer26Aβ (**I**) levels in each respective fraction. Aβ species were detected with a generic Aβ antibody - 82E1. Values represent mean ± S.D; n = 12, N = 4. Additionally, bar plots showing densitometric quantification of aggregated Aβ species (96 h) in each respective fraction, detected with Aβ aggregate-specific antibody-OC (**J**) and Aβ oligomer-specific antibody – A11 (**K**). Values represent mean ± S.D; n = 8, N = 2.

3.1.3. Phosphorylated Aβ species are constitutively internalized via endocytosis with different efficiencies

Pseudo-phosphorylated DAβ variants (S8D and S26D) were used in the next set of experiments to avoid influences of cellular kinases and phosphatases. SH-SY5Y cells were treated with non-aggregated or pre-aggregated (96 h) Tide Fluor-labelled variants of npAβ, S8D Aβ and S26D Aβ peptides for 60 min. After the treatment, cells were fixed, counterstained with Actin-RFP (actin microfilaments, *red*) along with Hoechst (nuclei, *blue*) and imaged (Fig. **9A-B**). Intracellular Aβ fluorescence signals in the green channel were quantified (Fig. **9C**). Treatment with non-aggregated npAβ species led to significantly increased intracellular Aβ signals as compared to the pre-aggregated npAβ. In either aggregation state, both DAβ variant showed higher intracellular accumulation as compared to npAβ (Fig. **9C**). In particular, pre-aggregated S26D Aβ species accumulated most within cells. Pre-aggregated npAβ and S8D Aβ assemblies are also attached to the cell surface (Fig. **9B**, *asterisks*). Interestingly, apart from the cell-surface associated/adhered aggregates in npAβ and S8D Aβ species, only S8D Aβ signals are detected juxtanuclearly (Fig. **9B**, *arrowheads*). Increased intracellular signals indicate more efficient uptake of the pre-aggregated DAβ species as compared to pre-aggregated npAβ.

Since endocytosis is one potential pathway of Aβ uptake (Yamazaki et al. 1996), cells were treated with TF-Aβ variants for 60 min (Fig. **9D-F**), without or with methyl-β-cyclodextrin (β-MCD, 5 µM, 30 min) treatment before incubation with the Aβ species. β-

MCD has been reported to modulate cholesterol levels in cell membranes thereby inhibiting endocytosis (Rodal et al. 1999). Cells were co-stained for Transferrin receptor (TfR, *red*) along with Hoechst (nuclei, *blue*) and imaged (Fig. **9D-E**). All Aβ peptides (*green channel*) were found to localise with distinct TfR (*red channel*) positive puncta, indicative of the uptake of fluorescent Aβ species via clathrin dependent endocytosis. Cells more efficiently endocytose non-aggregated npAβ peptides as compared to pre-aggregated fibrils. However, the uptake is lower when compared with DAβ species in either aggregation state. The colocalization of intracellular S8D Aβ signals with TfR (*arrows*) indicated the endocytic uptake of S8D Aβ species, plausibly the soluble oligomeric assemblies, as compared to insoluble pre-aggregated npAβ fibrils. Pre-treatment with β-MCD tended to decrease intracellular Aβ signals, wherein the strongest effect was only observed in the case of npAβ peptide in both aggregation state (Fig. **9F-G**). Pre-aggregated DAβ peptides showed slight but significant depreciation in the presence of β-MCD (Fig. **9G**). Non-aggregated DAβ variants on the other hand showed very little if any change (Fig. **9F**), indicating the possible contribution of other membrane associated components facilitating their internalization, which were not examined in this study. Additionally, to understand the link between intracellular DAβ accumulation and cytotoxicity, the viability of cells treated with non-aggregated or pre-aggregated Aβ peptides without or with β-MCD pre-treatment were examined (Fig. **9H**). β-MCD pre-treatment partially alleviated the cells of Aβ induced cytotoxicity. A significant increment of viable cells was seen in the case of non-aggregated npAβ peptides, whereas the viability remained unaffected with aggregated npAβ with β-MCD pre-treatment. Non-aggregated/ aggregated S8D Aβ induced toxicity was significantly alleviated in presence of β-MCD. A similar trend was also seen for S26D Aβ, but the difference with non-aggregated peptide was not statistically significant. These observations indicate that cholesterol facilitates the uptake of npAβ species, ultimately altering cell viability. On the other hand, the uptake of DAβ peptides might involve membrane components other than cholesterol, that facilitate their internalization within cells. Taken together, these results demonstrate interaction of DAβ species with cell membrane lipids like cholesterol facilitates its intracellular uptake contributing to phosphorylated Aβ-induced cytotoxicity. Oligomeric and soluble species formed by DAβ peptides are efficiently taken up via endocytosis and exert higher cytotoxicity.

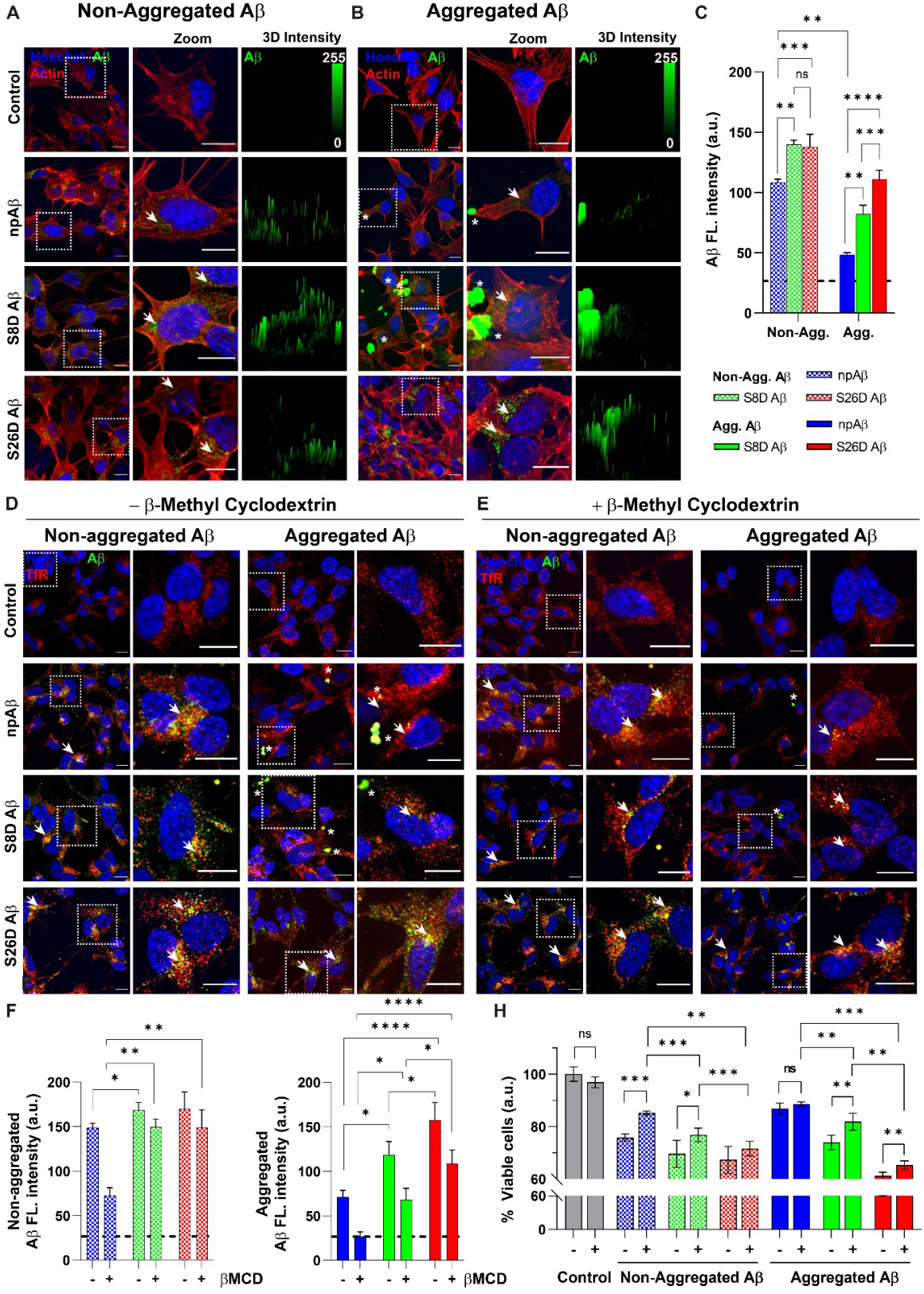

Fig. 9: Intracellular endocytic uptake of Aβ peptides is altered by its phosphorylation state. A-C. Microscopy images of SH-SY5Y cells treated with 1 μM of non-aggregated (**A**) or aggregated (**B**) Tide Fluor (TF)-DAβ variants (npAβ, S8D Aβ and

S26D Aβ) for 60 min respectively (*green channel*). Cells were fixed and counterstained with Actin-RFP (*red channel*) to visualise the cells periphery and Hoechst to visualise the nuclei (*blue channel*). Scale bar: 10 µm. Asterisks indicate TF-Aβ aggregates and arrow indicates intracellular Aβ signals. White dotted boxes indicate the region of interest in the depicted in the zoomed panel. Scale bar = 10 µm. **C.** Bar plots depicting the quantification of the absolute Aβ fluorescence intensities (*green channel*) depicting intracellular accumulation of non-aggregated and aggregated npAβ, S8D Aβ and S26D Aβ variants in SH-SY5Y cells. Dotted line indicated the average baseline fluorescent intensity recorded for untreated control cells. Values represent mean ± S.E.M.; n ~ 100 cells, N = 2. **D-G.** Microscopy images of SH-SY5Y cells pre-treated without (**D**) or with (**E**) 5 mM Methyl-β-cyclodextrin (30 min) and incubated with either 1 µM non-aggregated or pre-aggregated TF-Aβ variants for additional 30 min respectively (*green channel*). Cells were fixed and counterstained with anti-TfR antibody (*red channel*) to visualise clathrin mediated endocytosis along with Hoechst (*blue channel*, nuclei). Asterisks indicate TF-Aβ aggregates and arrows indicate puncta colocalizing in both green (Aβ) and red (TfR) channels, depicting the internalisation of Aβ through the process of endocytosis. White dotted boxes indicate the region of interest in the depicted in the zoomed panel. Scale bar = 10 µm. Bar plots depicting the quantification of the absolute Aβ fluorescence intensities (*green channel*) depicting intracellular accumulation of non-aggregated (**F**) and aggregated (**G**) npAβ, S8D Aβ and S26D Aβ variants in the presence (+) or absence (-) of MβCD. Dotted line indicated the average baseline fluorescent intensity recorded for untreated control cells. Values represent mean ± S.E.M.; n ~ 100 cells, N = 2. **H.** Bar plot depicting percent cell viability of SH-SY5Y cells, pre-treated in absence (-) or presence (+) of 5 mM Methyl-β-cyclodextrin for 30 min, followed by the treatment with either 1 µM non-aggregated or pre-aggregated TF-Aβ variants for 30 min respectively. Viability of the cells was determined by PrestoBlue® cell viability assay. Readings were normalised to untreated cell controls and represented as percent viable cells *wrt* untreated controls, values represent the mean ± S.D; n = 3, N = 3. * $p < 0.05$; ** $p < 0.01$; *** $p < 0.001$; **** $p < 0.0001$; n.s. $p \geq 0.05$, not significant (Two-way ANOVA, GraphPad Prism).

3.2. Intracellular localization and effects of phosphorylation-state Aβ variants

3.2.1. Phosphorylation-state dependent accumulation of pAβ in neurons

We detected phosphorylated Aβ variants (pSer8Aβ or pSer26Aβ) as well as N-terminal non-modified Aβ (nmAβ) species in the APP-PSEN1 transgenic mouse model that was crossed with Thy1-YFP transgenic mice to specifically label forebrain neurons (Tab. **1**, Ext. Fig. **3A-E** and Fig. **10A**). Consistent with previous reports (Kumar et al. 2020b; Kumar et al. 2020a; Kumar and Walter 2011; Kumar et al. 2016; Joshi et al. 2021a), the individual phosphorylated Aβ species *(red channels*, Fig. **10A**) showed differential deposition when compared to nmAβ (*gray channels*, Fig. **10A**) or to total fibrillar Aβ detected by X-34 (*blue channels*, Fig. **10A**, Kapadia et al. 2024).

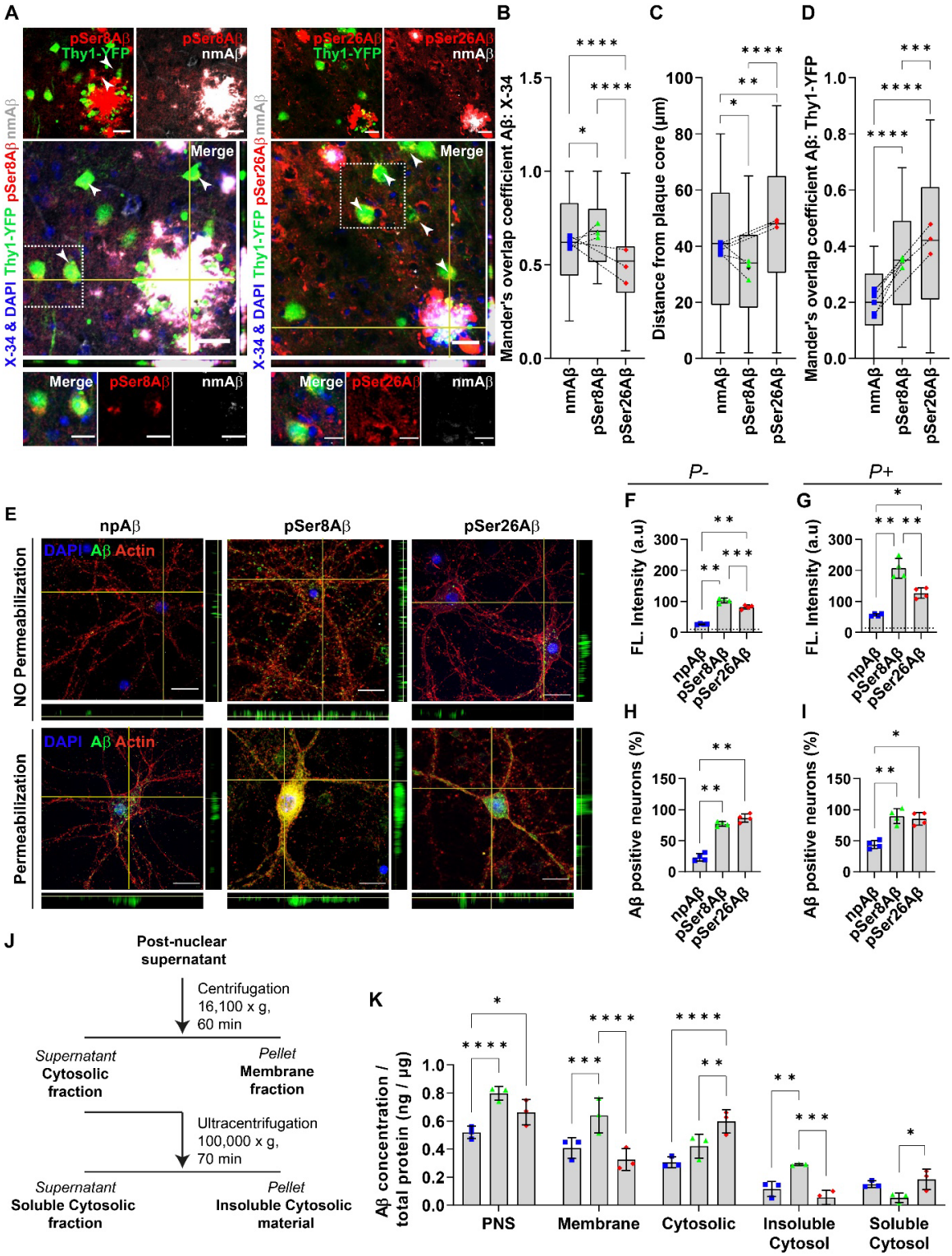

Fig. 10: Differential intraneuronal accumulation of pAβ species in APP-PSEN1 transgenic mice and primary cortical neurons. A-D. Immunohistochemistry (**A**) depicting differential intraneuronal and extracellular deposition of pSer8Aβ (stained with antibody 1E4E11, *red*) and pSer26Aβ (stained with antibody 5H11C10, *red*) compared to non-modified Aβ (nmAβ, stained with antibody 7H3D6, *gray*) in brain sections of APP-

PSEN1delE9xThy1-YFP transgenic mouse cortex (7.4 m, female). Scale bar: 50 µm; zoomed panels, 10 µm. White arrowheads indicate colocalized punctate staining between red and gray channels in Thy1-YFP positive neurons. Box plot (**B**) showing Mander's coefficient of overlap between nmAβ (*A, gray channel*; *B, blue data points*), pSer8Aβ (*A, red channel*; *B, green data points*) and pSer26Aβ (*A, red channel*; *B, red data points*) with X-34 (plaque core, *blue channel*). Box plot quantification (**C**) depicting plaque association of nmAβ, pSer8Aβ and pSer26Aβ species. Distance from the plaque core was measured using Fiji ImageJ concentric circle processing module. Box plot (**D**) depicting Mander's coefficient of overlap between nmAβ (*blue data points*), pSer8Aβ (*green data points*) and pSer26Aβ (*red data points*) with respect to Thy1-YFP positive neurons (*green channel*), respectively; computed using Fiji ImageJ Coloc processing module. Box plots depict the overall distribution of data, and each data point represents average values from an individual mouse, (B, C, n = ~100 cortical plaques), N = 3 transgenic mice, (One-way ANOVA, GraphPad Prism). **E-I.** Immunocytochemistry (**E**) depicting Aβ accumulation in primary cortical neurons treated with the indicated Aβ variants (500 nM, 4 h). Cells were processed without permeabilization or with permeabilization to detect surface associated Aβ and internalized Aβ, respectively, by staining with anti-Aβ antibody 82E1 (*green*). Cells were co-stained with Alexa555-conjugated phalloidin (actin*, red*) and DAPI (nuclei*, blue*). Scale bar, 10 µm. Bar plots depicting average values of absolute fluorescence intensities in the green channel (Aβ signals) in non-permeabilized cells (*P*-, **F**) and permeabilized cells (*P*+, **G**), analyzed by immunocytochemistry. Dotted line depicts the fluorescence signals in cells treated without Aβ (control). Bar plots depicting the quantification of neurons with surface bound Aβ (*P*-, **H**) and internalized Aβ (*P*+, **I**). Images were acquired and analyzed using Keyence automated image acquisition and processing modules. Values represent mean ± S.D.; n = ~200 neurons, N = 4, (One-way ANOVA, GraphPad Prism). **J-K.** Workflow representation (**J**) for fractionation of cellular protein based on differential centrifugation. Densitometric quantification (**K**) of absolute Aβ levels in different cellular fractions by ELISA (PNS, post nuclear supernatant) using anti-Aβ antibody 82E1. Readings were normalised to the total protein content in each fraction, respectively. Values represent mean ± S.D.; n = 6, N = 3, (Two-way ANOVA, GraphPad Prism). * $p < 0.05$; ** $p < 0.01$; *** $p < 0.001$; **** $p < 0.0001$; n.s. $p \geq 0.05$, not significant. Characterization of wild type (WT) and APP-PSEN1delE9xThy1-YFP transgenic mouse brain lysates, Aβ ELISA analyses in sucrose, SDS and FA fractions along with antibody control staining are provided in Ext. Fig. **3**. Additional quantification of Aβ levels in different cellular fractions by ELISA and SDS-WB have been provided in Ext. Fig. **4**. Figure adapted from Kapadia et al. 2024.

pSer8Aβ and nmAβ species prominently localize within the core of extracellular plaques that contain X-34 positive fibrillar Aβ (Fig. **10B**). In contrast, colocalization of pSer26Aβ with X-34 was significantly lower, wherein, pSer26Aβ species are also detected around the plaque core. The differential distribution of the Aβ phosphorylation-state variants within the plaque area was also confirmed by quantifying the distance of signals from the centre of the X-34 positive plaque core (Fig. **10C**). pSer8Aβ is present within the compact core of the plaque, whereas pSer26Aβ is detected rather diffused from the core.

Immunohistochemical analyses further revealed increased accumulation of both pAβ species within YFP positive neurons (Fig. **10D**). Together, these data indicate that the phosphorylation state of Aβ not only affects its deposition in extracellular plaques, but also their accumulation inside of neurons (Kapadia et al. 2024).

Mouse brains were also subjected to differential extraction and individual Aβ species detected by ELISA (Tab. **3a** and Ext. Fig. **3F**). Highest levels of total Aβ ($Aβ_{1-x}$) were detected in the formic acid (FA) fraction that contains plaque associated fibrillar material. Consistent with the accumulation of pSer8Aβ in the plaque core, this species was also abundant in the FA fraction (Tab. **3a** and Ext. Fig. **3F**). Levels of Ser26Aβ were overall lower as compared to pSer8Aβ and showed no pronounced enrichment in the FA fraction, in line with the previously described effect of Ser26 phosphorylation to form soluble oligomeric assemblies, rather than fibrillar assemblies (Kumar et al. 2016; Kumar et al. 2020a). Aβ species were also detected in sucrose and SDS extracted fractions that predominantly contain soluble, and membrane/cell associated Aβ, respectively. Comparing the individual pAβ peptides within different fractions, pSer8Aβ showed ~1.9-fold enrichment in SDS verses sucrose soluble fraction, whereas pSer26Aβ species were enriched in sucrose soluble fractions (1.5-fold) compared to the SDS fractions, respectively (Kapadia et al. 2024).

To specifically analyse the interaction, uptake and intraneuronal accumulation of Aβ phosphorylation-state variants, cultured mouse primary cortical neurons were used as an *in vitro* model. Neurons were exposed to synthetic npAβ, pSer8Aβ or pSer26Aβ peptides, respectively. Immunocytochemical detection of the different Aβ variants in neuronal cultures with or without plasma membrane permeabilization revealed significantly higher association of both phosphorylated Aβ species with the neuronal membrane surface, and increased accumulation in the cytoplasm (Fig. **10E-I**), further supporting the results seen earlier with SH-SY5Y cells (Fig. **9A, C**). Here, highest fluorescence intensities were detected for pSer8Aβ in both unpermeablized and permeabilized cells, indicating most efficient binding to neuronal membranes and intraneuronal accumulation, followed by pSer26Aβ and least for npAβ peptides (Fig. **10F-G**). Additional quantitative analyses further supported increased interaction of neurons with pAβ species. Here, the number of neurons with membrane bound Aβ (Fig. **10H**) and internalized Aβ (Fig. **10I**) is significantly

higher after exposure to the pAβ species as compared to npAβ. To complement these microscopic analyses, primary cortical neurons treated with different Aβ variants were fractionated by differential centrifugation to separate cellular membranes and cytosolic components (Fig. **10J** and Scheme **1C**). Aβ levels in each fraction were then analyzed by ELISA (Fig. **10K**, Ext Fig. **4A-D**) and WB (Ext Fig. **4E**). The post nuclear supernatant (PNS) that comprises cellular membranes and total cytosolic content, contained increased levels of both pAβ species, indicating increased cell association and/or accumulation as compared to npAβ (Fig. **10K**, Ext Fig. **4A-B**). Consistent with the increased fluorescence intensities for pSer8Aβ in microscopic analyses, this species also showed highest levels in the isolated membrane fraction (16,100 *g* pellet), while levels of npAβ and pSer26Aβ were significantly lower in this fraction. The total cytosolic fraction (supernatant after 16,100 *g* spin) showed highest levels for pSer26Aβ, followed by that of pSer8Aβ and npAβ. These data are consistent with increased binding and uptake of both phosphorylated Aβ species by neurons. Further separation of the cytosolic fraction by centrifugation at 100,000 *g* also revealed differential distribution of the phosphorylated Aβ species in soluble and insoluble fractions (Fig. **10K**, Ext Fig. **4A-B**). Levels of pSer8Aβ were significantly higher in the 100,000 *g* pellet as compared to npAβ and pSer26Aβ species, but significantly lower in the 100,000 *g* supernatant as compared to pSer26Aβ. The differences between pSer8Aβ and npAβ levels in the 100,000 *g* supernatant was not statistically significant. WB analyses further revealed partial aggregation of Aβ species during the incubation with neurons, wherein pSer8Aβ form more SDS resistant aggregates that npAβ or pSer26Aβ peptide (Ext Fig. **4E**, Kapadia et al. 2024).

We also analyzed the levels of Aβ in the treatment media by ELISA (Ext Fig. **4C**). Levels of npAβ and pSer26Aβ were significantly decreased after 4 hours incubation with primary neurons. Levels of pSer8Aβ showed modest decrease but were not significantly different to the amount before incubation. Since, pSer8Aβ also showed the highest association with cultured neurons and intraneuronal accumulation, these data could indicate higher metabolic stability. Indeed, phosphorylation of Aβ at Ser8 strongly decreases its degradation by Aβ degrading proteases, was previously reported (Kumar et al. 2012). This effect could also further contribute to the increased association of pSer8Aβ with neurons described above. Very similar results described above for primary mouse neurons, were

also obtained in another set of experiments with SY-SY5Y cells (Ext Fig. **4B, D**). These results indicated that phosphorylation of Aβ enhances membrane interaction and intraneuronal accumulation of the individual pAβ peptides. Alterations in aggregation states during these experiments could potentially contribute to the observed differences between the individual Aβ species and would reflect intrinsic effects caused by phosphorylation at the respective serine residues of Aβ. Together, these data strongly support a differential subcellular distribution of phosphorylated Aβ in cultured neurons (Kapadia et al. 2024).

3.2.2. Site-specific phosphorylation of Aβ modulates its vesicular localization

Once internalized into neurons via endocytosis, Aβ can be sorted to autophagy-related and endo-lysosomal compartments (LaFerla et al. 2007; Nixon 2017; Marshall et al. 2020; Pasternak et al. 2004). Localization of Aβ species with several marker proteins within distinct endosomal (Fig. **11** and Ext Fig. **5**), autophagy (Fig. **12** and Ext Fig. **5**) and lysosomal (Fig. **13** and Ext Fig. **5**) related marker proteins in YFP positive neurons of APP-PSEN1delE9xThy1-YFP transgenic mice or primary cortical neurons from wild-type mouse pups; using immunohisto(cyto)chemical analyses was examined. Mander's coefficient of overlap was computed to analyse the colocalization of intraneuronal Aβ species with respect to vesicular marker proteins, respectively. Depending on the phosphorylation-state or -site of Aβ, the internalized pAβ peptides showed differential association with autophagy and lysosome related compartments. Intraneuronal pAβ species were detected in association with early endosomal (EEA1 positive) compartments (Fig. **11A-B, D-E**), wherein colocalization with EEA1 was significantly higher for pSer8Aβ in comparison to pSer26Aβ and nmAβ. Interestingly, pSer26Aβ showed highest colocalization with RAB7, a marker for late endosomes, followed by pSer8Aβ and nmAβ species (Fig. **11C, F** and Ext Fig. **5A, J**). pAβ species were also co-detected with LC3 positive autophagic compartments (Fig. **12A-B, D-E**) in neurons. As compared to nmAβ and pSer26Aβ, pSer8Aβ showed significantly higher colocalization with LC3 as well as sequesterome-1 (p62/SQSTM-1, Fig. **12C, F**). In primary cortical neurons, nmAβ and pSer26Aβ showed comparable ratios of colocalization with both LC3 and p62/SQSTM-1.

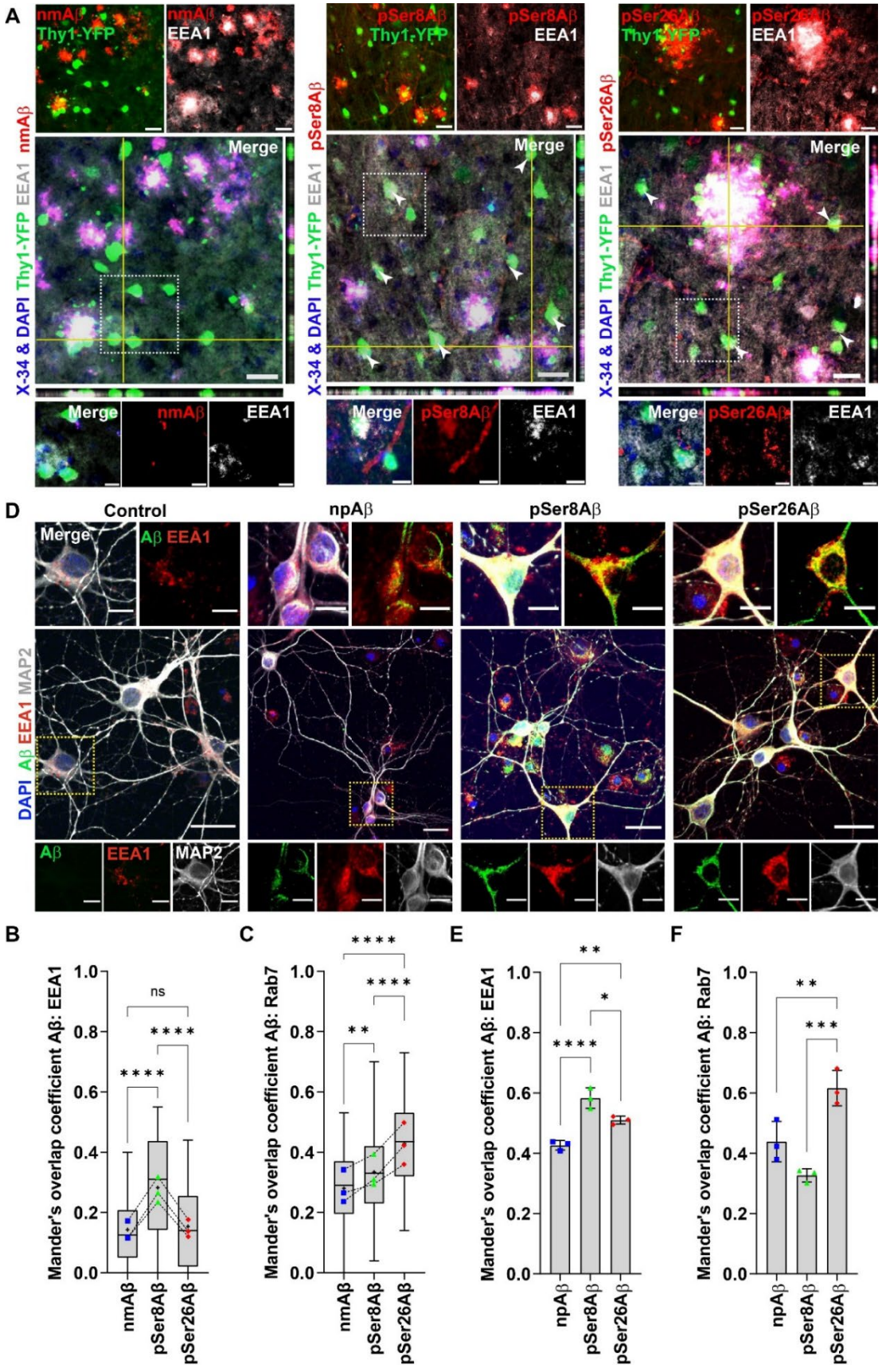
A
nmAβ
Thy1-YFP
EEA1
Merge
X-34 & DAPI Thy1-YFP EEA1 nmAβ
pSer8Aβ
pSer26Aβ
D
Control
npAβ
pSer8Aβ
pSer26Aβ
Aβ EEA1
DAPI Aβ EEA1 MAP2
MAP2
B
Mander's overlap coefficient Aβ: EEA1
nmAβ
pSer8Aβ
pSer26Aβ
ns
****
C
Mander's overlap coefficient Aβ: Rab7
**
E
npAβ
*
F
***

Fig. 11: Intraneuronal colocalization of pAβ with endosomal proteins in APP-PSEN1 transgenic mice and primary cortical neurons. A-C. Immunohistochemical staining (**A**) depicting differential intraneuronal colocalization of Aβ species in brain sections of APP-PSEN1delE9xThy1-YFP transgenic mouse cortex (7.3 m, female) stained with different phosphorylation state specific Aβ antibodies (nmAβ- 7H3D6, pSer8Aβ- 1E4E11 and pSer26Aβ- 5H11C10; *red channels respectively*) along with antibodies against early endosomes, EEA1 (*gray*) and DAPI + X-34 (nuclei and plaque core, *blue*). Scale bar: 50 µm; zoomed panels, 10 µm. White arrowheads indicate colocalized punctate staining between red and gray channels in Thy1-YFP positive neurons. Box plot summarizing Mander's coefficient of overlap between red channels (npAβ, *blue*; pSer8Aβ, *green* and pSer26Aβ, *red data points*) with respect to gray channels (EEA1, **B** and late endosomes, RAB7, **C**), quantified within Thy1-YFP positive neurons respectively. Box plot depicts the overall distribution of data, and each data point represents average values from an individual mouse, N = 3 transgenic mice. **D-F.** Immunocytochemical staining (**D**) of primary cortical neurons were incubated without (control) or with the indicated Aβ variants (500 nM, 4 h) and co-stained with antibodies against the microtubule-associated protein 2 (MAP2, *gray*), Aβ (82E1, *green*) and EEA1 (*red*). Nuclei were stained with DAPI (*blue*). Scale bar, 10 µm. Dotted boxes indicate the regions zoomed in the merged panels (*above*) and individual channels (*below*). Mander's overlap coefficients between Aβ (*green channel*) with EEA1 (**E**) and RAB7 (**F**) (*respective red channels*), are presented as bar plots, respectively. Values represent mean ± S.D.; n = 6, N = 3. * $p < 0.05$; ** $p < 0.01$; *** $p < 0.001$; **** $p < 0.0001$; n.s. $p \geq 0.05$, not significant (One-way ANOVA, GraphPad Prism). Additional staining experiments and WB analyses of endosomal proteins in wild type (WT) and APP-PSEN1delE9xThy1-YFP transgenic mouse brain lysates are provided in Ext. Fig. **5A, J, C-E**, respectively. Figure adapted from Kapadia et al. 2024.

To analyse the association of Aβ species with lysosomal proteins, lysosomal membrane associated (LAMP-2, Fig. **13A-B, D-E**) and luminal protease cathepsin D (CTSD, Fig. **13C, F** and Ext Fig. **5B, K**) specific markers were used, respectively. Intraneuronal pSer26Aβ showed significantly higher colocalization with LAMP-2 as compared to that of nmAβ. On the other hand, pSer8Aβ peptides showed the lowest colocalization with LAMP-2 as well as CTSD (Fig. **13C, F** and Ext Fig. **5B, K**). Together, these results indicate differential intraneuronal accumulation of Aβ phosphorylation-state variants in endo-lysosomal and autophagy related pathways as well as a differential routing of pAβ within endo-lysosomal and autophagy-related compartments, depending on the site of phosphorylation (Kapadia et al. 2024).

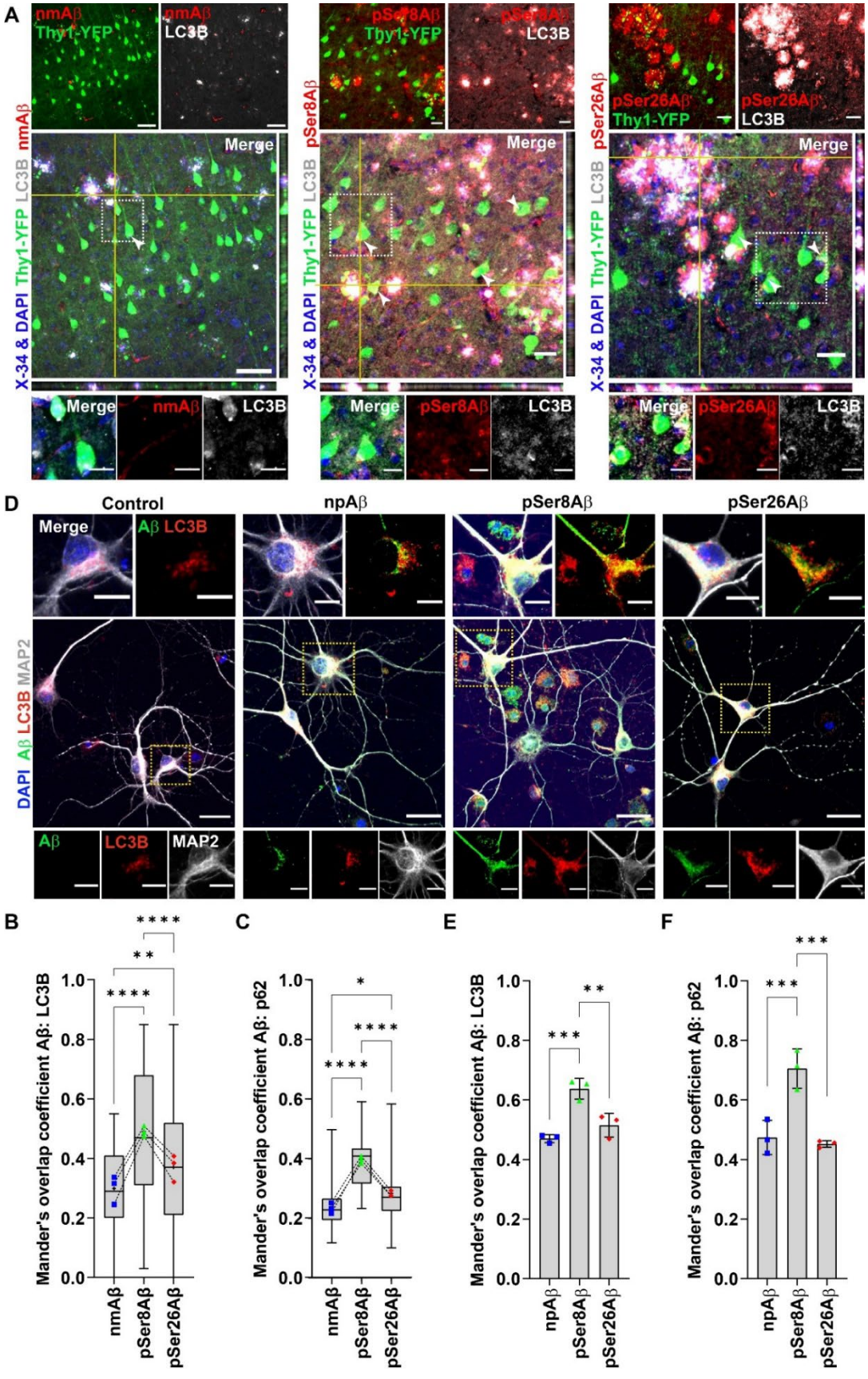
A
nmAβ
Thy1-YFP
LC3B
Merge
X-34 & DAPI
pSer8Aβ
pSer26Aβ
D
Control
npAβ
pSer8Aβ
pSer26Aβ
Aβ
MAP2
DAPI
B
C
E
F
Mander's overlap coefficient Aβ: LC3B
Mander's overlap coefficient Aβ: p62
npAβ
pSer8Aβ
pSer26Aβ

Fig. 12: Intraneuronal colocalization of pAβ with autophagic vesicle markers in APP-PSEN1 transgenic mice and primary cortical neurons. A-C. Immunohistochemistry (**A**) depicting differential intraneuronal colocalization of Aβ species in brain sections of APP-PSEN1delE9xThy1-YFP transgenic mouse cortex (7.3 m, female) stained with different phosphorylation state specific Aβ antibodies (nmAβ- 7H3D6, pSer8Aβ- 1E4E11 and pSer26Aβ- 5H11C10; *red channels respectively*) along with antibodies against autophagic vesicle marker protein, LC3B (*gray*) and DAPI + X-34 (nuclei and plaque core, *blue*). Scale bar: 50 µm; zoomed panels, 10 µm. White arrowheads indicate colocalized punctate staining between red and gray channels in Thy1-YFP positive neurons. Box plot summarizing Mander's coefficient of overlap between red channels (npAβ, *blue*; pSer8Aβ, *green* and pSer26Aβ, *red data points*) with respect to gray channels (LC3B, **B** and sequesterome-1, p62/SQSTM-1, **C**), quantified within Thy1-YFP positive neurons respectively. Box plot depicts the overall distribution of data, and each data point represents average values from an individual mouse, N = 3 transgenic mice. **D-F.** Immunocytochemical staining (**D**) of primary cortical neurons were incubated without (control) or with the indicated Aβ variants (500 nM, 4 h) and co-stained with antibodies against the microtubule-associated protein 2 (MAP2, *gray*), Aβ (82E1, *green*) and LC3B (*red*). Nuclei were stained with DAPI (*blue*). Scale bar, 10 µm. Dotted boxes indicate the regions zoomed in the merged panels (*above*) and individual channels (*below*). Mander's overlap coefficients between Aβ (*green channel*) with LC3B (**E**) and p62/SQSTM-1 (**F**) (*respective red channels*), are presented as bar plots, respectively. Values represent mean ± S.D.; n = 6, N = 3. * $p < 0.05$; ** $p < 0.01$; *** $p < 0.001$; **** $p < 0.0001$; n.s. $p \geq 0.05$, not significant (One-way ANOVA, GraphPad Prism). WB analyses of LC3B and p62/SQSTM-1 in wild type (WT) and APP-PSEN1delE9xThy1-YFP transgenic mouse brain lysates are provided in Ext. Fig. **5C, F, G**, respectively. Figure adapted from Kapadia et al. 2024.

To complement these microscopic analyses, subcellular fractionation (Ext Fig. **6**) of SH-SY5Y cells treated with different Aβ variants (1 µM, 24 h) was performed. Autophagy-associated proteins LC3 and p62/SQSTM-1 were highest in fractions 6 and 7, respectively, indicating the presence of autophagosomal compartments (Ext. Fig. **6C-F**). LAMP-2 and the mature form CTSD are mainly detected in fractions 5 and 6, indicating enrichment of lysosomes (Ext. Fig. **6G-J**). However, there is considerable overlap of these marker proteins. The different Aβ peptides are also distributed to these fractions (Ext. Fig. **6A-B**), indicating sorting of internalized Aβ peptides to autophagic and lysosomal compartments (Kapadia et al. 2024).

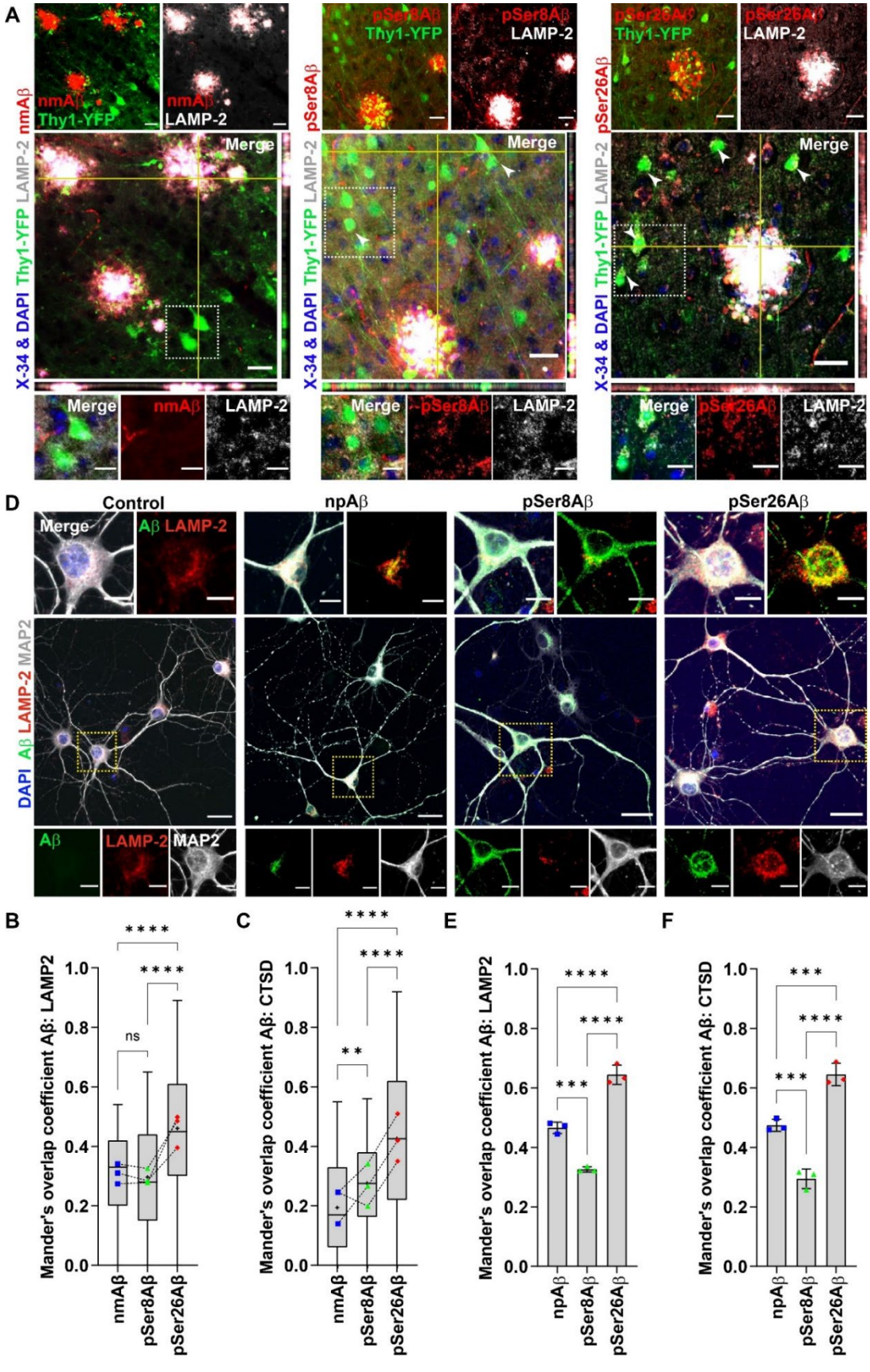
A
nmAβ
Thy1-YFP
LAMP-2
Merge
X-34 & DAPI Thy1-YFP LAMP-2
pSer8Aβ
pSer26Aβ
D
Control
npAβ
pSer8Aβ
pSer26Aβ
Aβ LAMP-2
DAPI Aβ LAMP-2 MAP2
B
C
E
F
Mander's overlap coefficient Aβ: LAMP2
Mander's overlap coefficient Aβ: CTSD
ns
nmAβ
pSer8Aβ
pSer26Aβ
npAβ

Fig. 13: Intraneuronal colocalization of pAβ with lysosomal associated proteins in APP-PSEN1 transgenic mice and primary cortical neurons. A-C. Immunohistochemical staining (**A**) depicting differential intraneuronal colocalization of Aβ species in brain sections of APP-PSEN1delE9xThy1-YFP transgenic mouse cortex (7.3 m, female) stained with different phosphorylation state specific Aβ antibodies (nmAβ-7H3D6, pSer8Aβ- 1E4E11 and pSer26Aβ- 5H11C10; *red channels respectively*) along with antibodies against lysosome associated membrane protein-2, LAMP-2 (*gray*) and DAPI + X-34 (nuclei and plaque core, *blue*). Scale bar: 50 µm; zoomed panels, 10 µm. White arrowheads indicate colocalized punctate staining between red and gray channels in Thy1-YFP positive neurons. Box plot summarizing Mander's coefficient of overlap between red channels (npAβ, *blue*; pSer8Aβ, *green* and pSer26Aβ, *red data points*) with respect to gray channels (LAMP-2, **B.** and lysosomal luminal protease cathepsin-D, CTSD, **C**), quantified within Thy1-YFP positive neurons respectively. Box plot depicts the overall distribution of data, and each data point represents average values from an individual mouse, N = 3 transgenic mice. **D-F.** Immunocytochemistry (**D**) of primary cortical neurons were incubated without (control) or with the indicated Aβ variants (500 nM, 4 h) and co-stained with antibodies against the microtubule-associated protein 2 (MAP2, *gray*), Aβ (82E1, *green*) and LAMP-2 (*red*). Nuclei were stained with DAPI (*blue*). Scale bar, 10 µm. Dotted boxes indicate the regions zoomed in the merged panels (*above*) and individual channels (*below*). Mander's overlap coefficients between Aβ (*green channel*) with LAMP-2 (**E**) and CTSD (**F**) (*respective red channels*), are presented as bar plots, respectively. Values represent mean ± S.D.; n = 6, N = 3. * $p < 0.05$; ** $p < 0.01$; *** $p < 0.001$; **** $p < 0.0001$; n.s. $p \geq 0.05$, not significant (One-way ANOVA, GraphPad Prism). Additional staining experiments and WB analyses of lysosome associated proteins in wild type (WT) and APP-PSEN1delE9xThy1-YFP transgenic mouse brain lysates are provided in Ext. Fig. **5B, K, C, H, I**, respectively. Figure adapted from Kapadia et al. 2024.

To further assess the sorting of phosphorylation-state Aβ variants to lysosomal compartments, an additional cell fractionation protocol was employed (Fig. **14A** and scheme **1D**). Here, LAMP-2, CTSD, and RAB7 were preferentially detected in the 16,000 *g* pellet, indicating high enrichment of lysosomal/late endosomal compartments in this fraction (Fig. **14B**). Importantly, this fraction contains high levels of pSer26Aβ and moderate levels of npAβ, but only marginal levels of pSer8Aβ. Instead, pSer8Aβ is mainly found in the lysosome depleted fraction containing early endosomal (EEA1 positive) and autophagic (p62/SQSTM-1 and LC3-II positive) compartments (Fig. **14B**). The final supernatant (*cytosol*) contains mainly pSer26Aβ and npAβ, but very little if any pSer8Aβ (Kapadia et al. 2024).

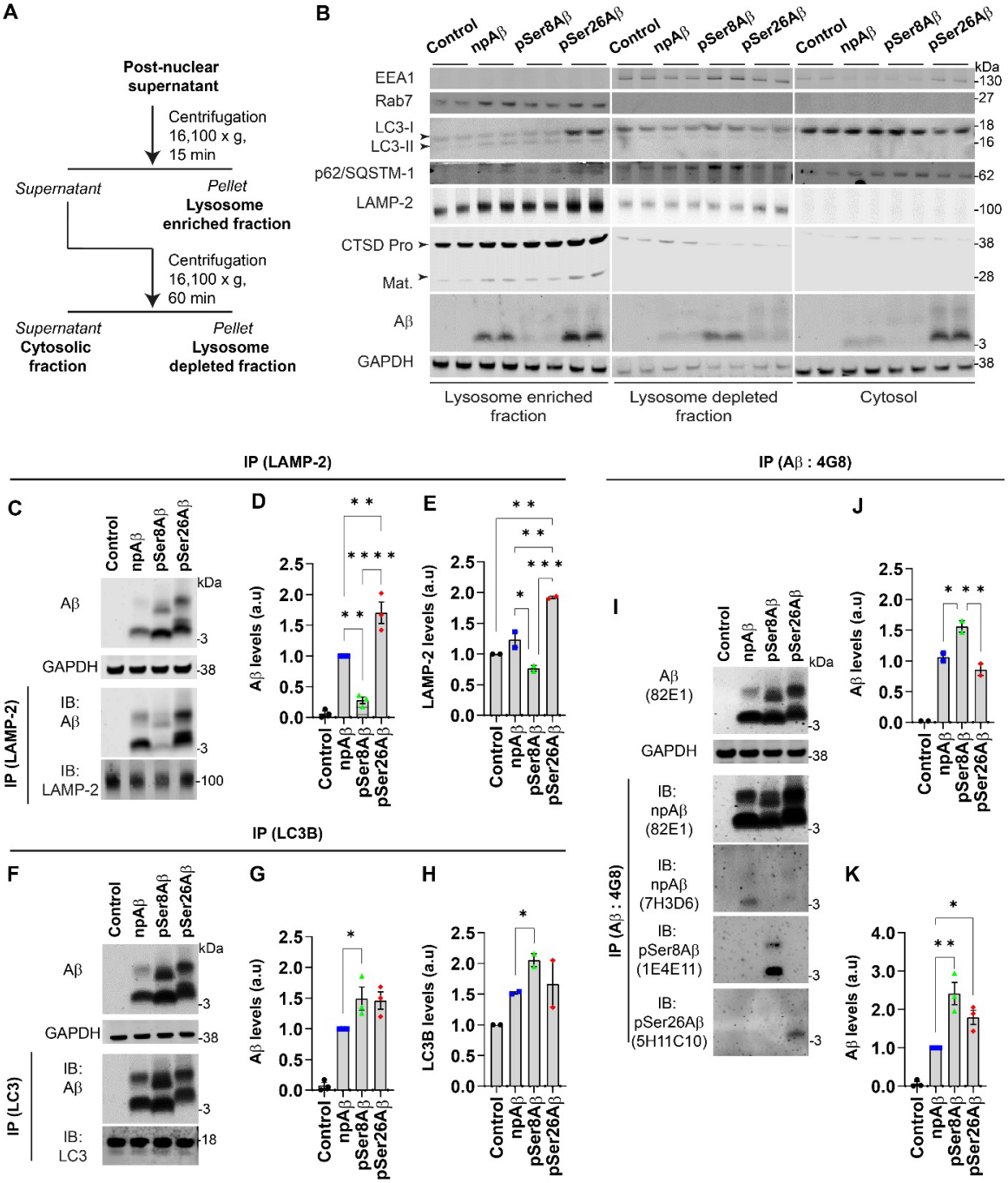

Fig. 14: Phosphorylation-state dependent vesicular localization of Aβ. Primary cortical neurons treated with Aβ variants (500 nM, 4 h) were subjected to lysosome enrichment (**A-B**) or immunoisolation of LAMP-2 (**C**) or LC3 (**F**) positive compartments or immunoprecipitation of total intracellular Aβ content (**I**). **A-B.** Workflow representation (**A**) for lysosome enrichment based on differential centrifugation. Immunoblot analyses (**B**) of lysosome-enriched, lysosome-depleted, and cytosolic fractions depicting the differential separation of Aβ with the indicated endo-lysosomal and autophagy associated proteins. **C-H.** Intact lysosomes using LAMP-2 (**C-E**) or autophagic vesicles using LC3 (**F-H**) specific antibodies were immunoisolated from cellular homogenate of primary cortical neurons treated with Aβ variants (500 nM, 4 h). Aβ in the isolated vesicles was detected

with anti-Aβ antibody 82E1, along with the indicated proteins via western immunoblotting (**C, F**). GAPDH and Aβ (82E1) were used as loading/starting controls. Results are representative of two independent experiments. IP, immunoprecipitation; IB, immunoblot. Bar plots depicting the relative Aβ levels in the IP eluates (**D, G**) detected with Aβ antibody 82E1. Values represent mean ± S.E.M.; n = 9, N = 3. Levels of LAMP-2 (**E**) and LC3B (**H**) respective IP eluates were also quantified. Values represent mean ± S.E.M.; n = 6, N = 2. **J-L.** Primary cortical neurons treated with Aβ variants (500 nM, 4 h) were homogenized in hypotonic buffer and Aβ from the PNS was immunoprecipitated with anti-Aβ antibody 4G8. Aβ in the individual fractions was then detected using anti-Aβ antibody 82E1 or the indicated phosphorylation-state specific antibodies via Western immunoblotting (**J**). GAPDH and Aβ (82E1) were used as loading/starting controls. Bar plots depicting the relative Aβ levels in the IP eluates detected with phosphorylation state specific antibodies (**K**) or Aβ antibody 82E1 (**L**), respectively. Values represent mean ± S.E.M.; K, n = 6, N = 6; L, n = 9, N = 3. All results and analyses are representative of two independent experiments. * $p < 0.05$; ** $p < 0.01$; *** $p < 0.001$; **** $p < 0.0001$; n.s. $p \geq 0.05$, not significant (One-way ANOVA, GraphPad Prism). Results of subcellular fractionation experiments have been provided in Ext. Fig. **6**. Figure adapted from Kapadia et al. 2024.

Further, lysosomes from Aβ treated primary cortical neurons were immunoisolated using a LAMP-2 specific antibody (Scheme **1E**, Fig. **14C-E**). Again, pSer26Aβ and npAβ peptides are strongly enriched in immunoisolated lysosomes as compared to pSer8Aβ. A similar experimental set-up was used to immunoisolate autophagosomal components using a LC3 specific antibody (Fig. **14F-H**). Here, all Aβ variants were immunoisolated with LC3-positive autophagosomal compartments. In contrast to LAMP-2 immunoisolated vesicles, the LC3 immunoisolated vesicles contain high levels of pSer8Aβ, indicative of differential sorting of pAβ peptides in autophagic and lysosomal compartments, respectively. As a control, cells were homogenized in hypotonic buffer to extract all Aβ associated with cellular membranes and intracellular organelles/vesicles. Total Aβ pools were then immunoisolated by a generic Aβ specific antibody (4G8, Scheme **1E**, Fig. **14I-K**), which showed the differential accumulation of intraneuronal Aβ peptides (pSer8Aβ > pSer26Aβ > npAβ, Fig. **14J-K**), respectively (Kapadia et al. 2024).

We also performed scanning transmission electron microscopy (STEM) along with complementary immunocytochemistry on SH-SY5Y cells treated with different Aβ variants (1 μM, 24 h), to further assess the subcellular localization of Aβ and potential effects on autophagy related vesicles. As seen in Fig. **15A**, cells treated with Aβ showed accumulation of electron dense material within autophagic compartments, probably representing accumulated Aβ. Notably, the pSer8Aβ treated cells showed accumulated autophagosomes still containing cargo material. On the other hand, pSer26Aβ as well as

npAβ treated cells present with compartments containing less cargo material, indicative for autolysosomes wherein the cargo is already degraded. Parallel immunocytochemical experiments support a preferential accumulation of pSer8Aβ in LC3 positive autophagosomal structures (Fig. **15C, D**). In contrast, pSer26Aβ showed predominant colocalization with LAMP-2 (Fig. **15E, F**). Quantification of autophagic compartments from STEM images (Fig. **15B**) suggest phosphorylation-state dependent effects of Aβ on autophagosome and/or lysosome accumulation. Taken together, these results depict phosphorylation-state specific trafficking and sorting of Aβ variants within autophagic and endo-lysosomal compartments and indicate potential effects on autophagic flux and/or lysosomal function (Kapadia et al. 2024).

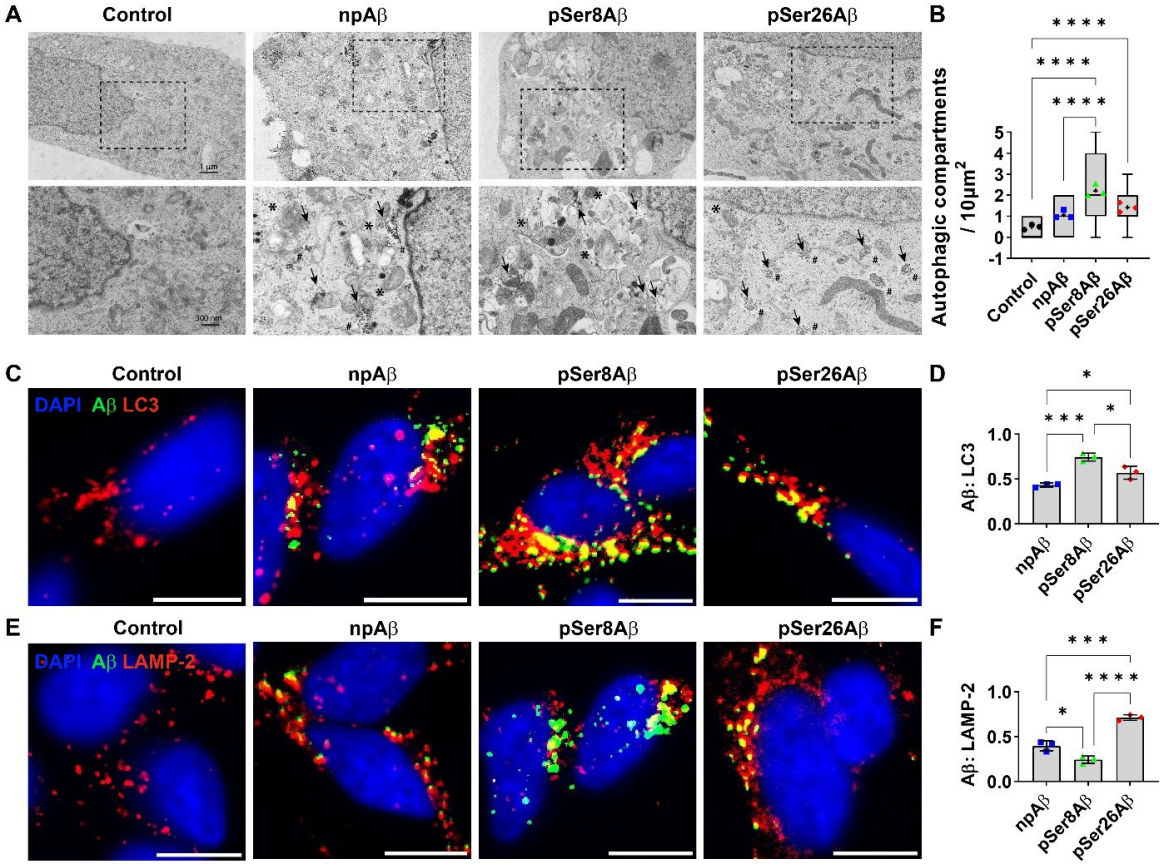

Fig. 15: Compartmentalization of Aβ in autophagic or lysosomal vesicles is modulated by the phosphorylation state of Aβ. A-B. Scanning transmission electron microscopy (STEM, **A**) of SH-SY5Y cells treated without (control) or with Aβ variants (1 mM, 24 h); scale bar, 1 µm. Dotted rectangles indicate the region zoomed in the panels (*below*). Scale bar, 300 nm. Arrows indicate electron dense structures; asterisks ~ autophagosomes; hashtags ~ autolysosomes. Results are representative of three independent experiments. Box plot (**B**) depicting quantification of autophagic components in the ROI (10 µm^2) within the cytoplasm of SH-SY5Y cells treated with Aβ variants (1 mM,

24 h). Box plot depicts the overall distribution of data, and each data point represents average values from independent experiments; n ~ 30 cells, N = 3. **C-F.** Immunocytochemical staining of LC3 (**C**) and LAMP-2 (**E**), in SH-SY5Y cells upon incubation without (control) or with the indicated Aβ variants (1 μM, 24 h). Cells were stained with anti-Aβ (82E1, *green*) and respective vesicular markers (*red*) along with DAPI (nuclei, *blue*). Scale bar, 5 μm. Mander's overlap coefficients between Aβ (*green channel*) with autophagic vesicles, LC3 (**D**) and lysosomes, LAMP-2 (**F**), red channels respectively; analyzed by the FiJi ImageJ colocalization processing module. Values represent mean ± S.D.; n = 6, N = 3. * $p < 0.05$; ** $p < 0.01$; *** $p < 0.001$; **** $p < 0.0001$; n.s. $p \geq 0.05$, not significant (One-way ANOVA, GraphPad Prism). Figure adapted from Kapadia et al. 2024.

3.2.3. pSer8Aβ and pSer26Aβ differentially modulate autophagic flux

To further investigate functional effects of phosphorylated and non-phosphorylated Aβ species on autophagosome formation and maturation (Fig. **16A-B**), a tandem reporter construct GFP-LC3-RFP-LC3Δ (Kaizuka et al. 2016); was employed primarily. Induction of autophagy results in the cleavage of the tandem reporter into two separate entities, GFP-LC3 that can be incorporated into autophagosomal membranes, and RFP-LC3Δ serve as an internal control for expression of the construct. Fusion of autophagosomes with acidic lysosomes results in quenching of the fluorescence signals from the GFP. Thus, the ratio of RFP to GFP fluorescence intensity provides a measure for autophagic flux. As shown in Fig. **16A-B**, cell treatment with pSer26Aβ significantly increased the RFP/GFP ratio, indicating augmented autophagic flux as compared to control cells. Cell treatment with npAβ tended to increase, while treatment with pSer8Aβ tended to decrease the RFP/GFP ratio compared to that of control cells, but these effects were not statistically significant. The slightly lower RFP/GFP ratio in pSer8Aβ treated cells could indicate an increase in autophagic activation and/or inefficient fusion to lysosomes, as compared to pSer26Aβ or npAβ treated cells (Kapadia et al. 2024).

Next, an alternative tandem reporter construct mCherry-GFP-LC3B (Fig. **16C-E**) (N'Diaye et al. 2009; Tien et al. 2016), was also used. Here, the LC3 is fused with both fluorescent proteins, mCherry and GFP. Thus, LC3-positive compartments with neutral or weakly acidic pH showed mCherry and GFP fluorescence simultaneously. Upon acidification of autophagosomes by fusion with lysosomes, the fluorescence of GFP, but not that of mCherry is quenched resulting in an increased ratio of mCherry/GFP positive vesicles, and increased ratio of mCherry/GFP fluorescence intensity (Klionsky et al. 2021). The

ratio of mCherry/GFP fluorescence intensity was strongly elevated in pSer26Aβ treated cells, but not significantly altered in pSer8Aβ and npAβ treated cells when compared to control cells (Kapadia et al. 2024).

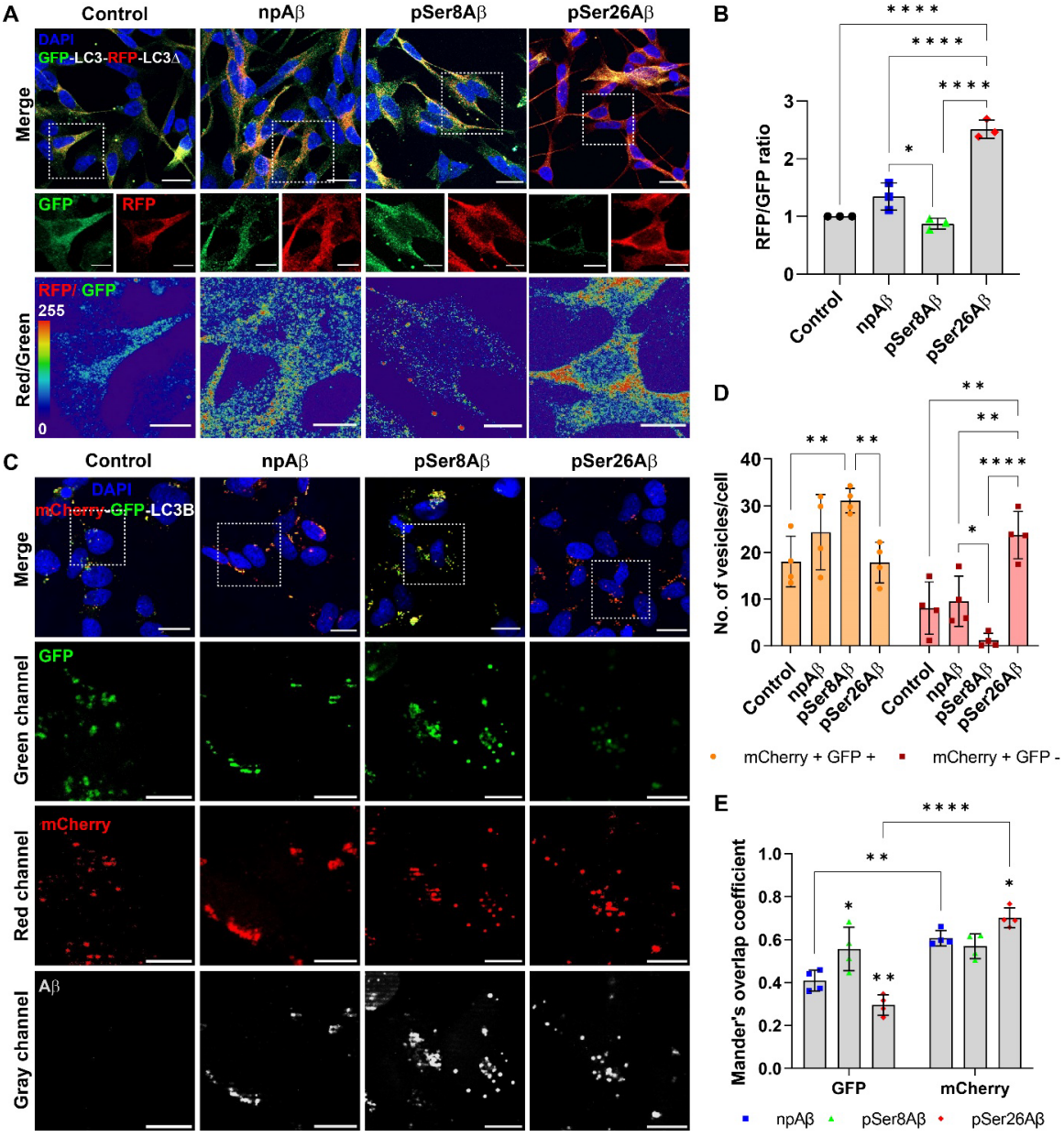

Fig. 16: Phosphorylation-state specific effects of Aβ on autophagic vesicles. Immunocytochemical analyses of SH-SY5Y cells expressing tandem reporter constructs GFP-LC3-RFP-LC3Δ (**A-B**) or mCherry-GFP-LC3B (**C-E**) upon treatment with different Aβ variants (1 µM, 24 h). Cells were co-stained with DAPI (nuclei, *blue*). Scale bar, 10 µm. Dotted boxes indicate the region zoomed in the panels below. **A-B.** Microscopy images (**A,** *merge*) showing GFP (*green*) and RFP (*red*) signals along with DAPI (nuclei, *blue,* upper row). Single channel images and RFP/GFP ratiometric images are shown in the middle and lower row, respectively. Bar plot (**B**) showing the ratio of RFP/GFP

fluorescence intensities, respectively. Readings were normalized to cells incubated without Aβ (control). Values represent mean ± S.D.; n = 6, N = 3, (One-way ANOVA, GraphPad Prism). **C-E.** Microscopy images (**C,** *merge*) depict GFP (*green*) and mCherry (*red*) signals along with DAPI (nuclei, *blue*). Independent zoom regions below depict GFP (*green*), mCherry (*red*) and Aβ (*gray*) channels, respectively. Quantification (**D**) of the number of dual fluorescent (mCherry+/GFP+) and only mCherry positive (mCherry+/GFP-) vesicles per cell representing differential autophagic flux. Values represent mean ± S.D.; n = 8, N = 4. (Two-way ANOVA, GraphPad Prism). Bar plot (**E**) showing Mander's overlap coefficient analyses of Aβ (*gray channel*) with GFP (*green channel*) and mCherry (*red channel*) positive vesicles analyzed using the Fiji ImageJ colocalization processing module. Values represent mean ± S.D.; n = 8, N = 4, (Two-way ANOVA, GraphPad Prism). * $p < 0.05$; ** $p < 0.01$; *** $p < 0.001$; **** $p < 0.0001$; n.s. $p \geq 0.05$, not significant. Figure adapted from Kapadia et al. 2024.

The number of mCherry and GFP dual-fluorescent positive ($mCherry^{+}GFP^{+}$) vesicles per cell is significantly higher in pSer8Aβ treated cells, compared to control and to pSer26Aβ treated cells (Fig. **16D**). However, the number of mCherry positive/GFP negative ($mCherry^{+}GFP^{-}$) vesicles per cell is significantly least in pSer8Aβ treated cells, indicating inefficient transport to and/or impaired fusion with lysosomes. In contrast, cells treated with pSer26Aβ showed a significantly higher number of $mCherry^{+}GFP^{-}$ vesicles (Fig. **16D**), indicating increased autophagic flux and/or inefficient protein degradation in lysosomes. Analyses of the Mander's overlap coefficient of the Aβ signals with GFP or mCherry channels depict the similar association of pSer8Aβ with both channels, supporting an accumulation of pSer8Aβ in non-acidic autophagic vesicles. In contrast, npAβ and particularly pSer26Aβ showed higher colocalization with mCherry than with GFP (Fig. **16E**). Mander's overlap coefficient with GFP positive vesicles was the highest for pSer8Aβ, followed by npAβ and lowest for pSer26Aβ. On the other hand, pSer26Aβ showed highest colocalization with mCherry positive vesicles as compared to the other peptides. Based on these observations, it could be inferred that site-specific phosphorylation of Aβ differently modulates autophagic flux with pSer8Aβ impairing autophagosome maturation and/or fusion to lysosomes, and npAβ and particularly pSer26Aβ rather affecting lysosomal function and/or acidification (Kapadia et al. 2024).

3.2.4. Phosphorylation state specific effects of Aβ on lysosomal function

The results with both reporter constructs indicated differential effects of the Aβ phosphorylation-state variants on the quenching of GFP fluorescence. Thus, lysosomal

acidification using a lysosensor-dextran ratiometric probe by microscopy (Fig. **17A-D**) or time-dependent fluorescence analyses in multi-well plates (Fig. **17B-C**), was assessed. The fluorescence emission of the probe changes from the blue to the green channel (*red shifted*) upon vesicle acidification, and the ratio of the green to blue fluorescence intensity provides a measure for acidification of the lysosensor (Fig. **17A**, *lowermost panel*). Cell treatment with pSer26Aβ and to a lesser extent npAβ increased lysosensor signals indicative for increased acidification of lysosomes, while pSer8Aβ had no comparable effect, as compared to control (Fig. **17A-B**). Using standard pH modulators within cells, the changes in lysosensor pH was quantified (ΔpH_l, Fig. **17D**). The data indicated that pSer26Aβ decreased the pH_l by 0.17 ± 0.12 units within 24 h of incubation. A similar decrease in the pH_l by 0.13 ± 0.11 units was also seen in npAβ treated cells. Contrastingly, pSer8Aβ did not alter pH_l with respect to control cells, deferring significantly compared to npAβ and pSer26Aβ treatment (Fig. **17D**). Similar results were also seen in primary cortical neurons treated with Aβ variants (Ext. Fig. **7A-B**, Kapadia et al. 2024).

Co-staining with an anti-LAMP-2 antibody (Fig. **17A**, *red channel*) revealed a significant increase in the ratio of perinuclear lysosomes to peripheral lysosomes (Johnson et al. 2016) upon treatment with Aβ variants in comparison to control cells (Fig. **17E-F**). The extent of increase was highest in cells treated with pSer26Aβ (~2.5 fold), followed by npAβ (~1.8 fold) and pSer8Aβ peptides (~1.6 fold), respectively. Additional analyses depict a significant increase in the perinuclear localisation of Aβ positive lysosomes in pSer26Aβ treated cells as compared to npAβ and pSer8Aβ treated cells. pSer8Aβ showing overall lower colocalization with lysosomal compartments, also showed a decrease in perinuclear localisation with respect to pSer26Aβ and npAβ treated cells, respectively. To examine effects of Aβ species on the activity of lysosomal hydrolases, a cathepsin D and E cleavable fluorogenic substrate assay was employed (Yasuda et al. 1999). In both, SH-SY5Y cells, (Fig. **17J**) and primary cortical neurons (Ext. Fig. **7C**), The increase in the number of lysosomes in pSer26Aβ treated cells was associated with increased activity of lysosomal CTS D and E enzymes. A similar increasing trend was also seen with npAβ. pSer8Aβ treated cells, on the other hand showed no significant effect compared to control cells (Kapadia et al. 2024).

These results demonstrate that pSer26Aβ augments autophagic flux, resulting in increased intracellular accumulation of acidified lysosomes. On the other hand, pSer8Aβ has negligible or modest effect, indicating phosphorylation-state and site- specific effect of Aβ on lysosomal functioning (Kapadia et al. 2024).

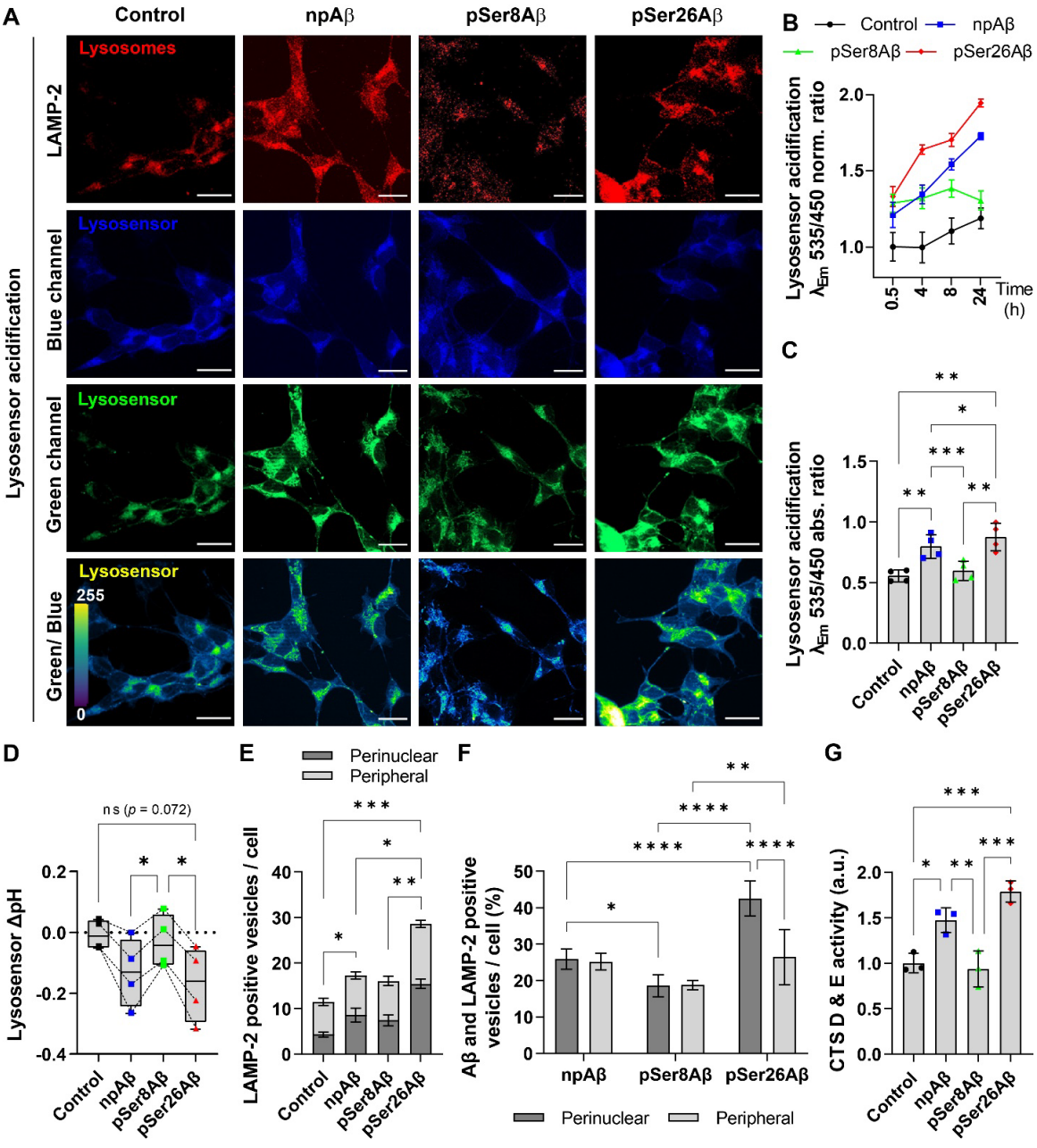

Fig. 17: Differential effects of phosphorylated Aβ species on lysosomes. A-D. SH-SY5Y cells loaded with lysosensor-dextran complex (50 μM) were treated without or with the indicated Aβ variants (1 μM, 24 h). After incubation, cells were co-stained with anti-LAMP-2 antibody to visualise lysosomes (*red*, **A**). Green/blue channel ratiometric images (*lower panel*, scale 0-255) indicate acidification of the lysosensor. Scale bar, 10 μm. Line

plots (**B**) represent time-dependent lysosomal acidification from the cell lysates. SH-SY5Y cells (50 µM lysosensor + 1 µM Aβ variants) were analyzed in a multi-well plate reader at the mentioned time points. Readings were normalized to cells incubated only with the lysosensor. Fluorescence emission intensities were measured at λ_{Ex} 380 nm and ratio at λ_{Em} 535, and 450 nm was computed. Values were normalized to control cells and presented as mean ± S.E.M.; n = 9, N = 3, (One-way ANOVA, GraphPad Prism). Bar plot (**C**) depict the absolute ratios of fluorescence emission intensities (λ_{Em} 535 and 450 nm) measured at λ_{Ex} 380 nm were computed to determine the ratiometric response of lysosensor acidification in SH-SY5Y cells treated with different Aβ variants (1 µM, 24 h). Values represent mean ± S.E.M.; n = 12, N = 4, (One-way ANOVA, GraphPad Prism). Change in lysosensor pH ($\Delta pH_{l,}$ **D**) was quantified using the formula $\Delta pH_l = pH_{final}$ (control/Aβ, t = 24 h) − $pH_{initial}$ (control, t = 0 h). Box plot depicts the overall distribution of data, and each data point represents average values from an independent experiment; n = 12, N = 4, (Repeated measures one-way ANOVA, GraphPad Prism). **E-F.** Quantification of the number of LAMP-2 positive compartments within the perinuclear (< 2 µm from nucleus) or peripheral space (> 2 µm from nucleus until cell periphery) per cell (**E**). Quantification of the percentage of perinuclear or peripheral LAMP-2 compartments positive for Aβ, per cell (**F**). Readings were manually computed using Fiji ImageJ image processing module. Values represent mean ± S.E.M.; n = 12, N = 3, (Two-way ANOVA, GraphPad Prism). **G.** SH-SY5Y cells treated with Aβ variants (1 µM, 24 h) or without (control) were examined for cathepsin-D & E activity (per µg of total cellular protein) using a CTS D & E cleavable fluorogenic substrate. Readings were normalized to control cells; values represent mean ± S.D.; n = 6, N = 3, (One-way ANOVA, GraphPad Prism). * p < 0.05; ** p < 0.01; *** p < 0.001; **** p < 0.0001; n.s. $p \geq 0.05$, not significant. Similar experiments (B, D, J) with primary cortical neurons are provided in Ext. Fig. **7**. Figure adapted from Kapadia et al. 2024.

3.2.5. Phosphorylated Aβ variants differentially modulate autophagic and endocytic pathways

The results described so far indicate a phosphorylation-state dependent sorting and functional effects of Aβ on different autophagic and endo-lysosomal compartments. Thus, the effects of the different Aβ species on individual proteins functionally involved in macroautophagy and endocytic trafficking (Fig. **18A**) by quantitative WB, was analysed next. The combined results obtained with SH-SY5Y cells and primary neurons cells are shown in Fig. **18B-F** and Tab. **3**, respectively. Early endosomal proteins EEA1 and RAB5 were increased by cell treatment with pSer8Aβ. pSer26Aβ also increased RAB5 but had no significant effect on EEA1. pSer26Aβ had the strongest effects on RAB7 and RAB11 that mediate trafficking and function of late and recycling endosomal compartments, respectively. npAβ had no significant (EEA1, RAB5, RAB7) or smallest effect (Rab11) on

levels of these endosomal proteins (Fig. **18B**). Notably, lysosomal proteins LAMP-2 and CTSD were selectively increased in the presence of pSer26Aβ (Fig. **18C**).

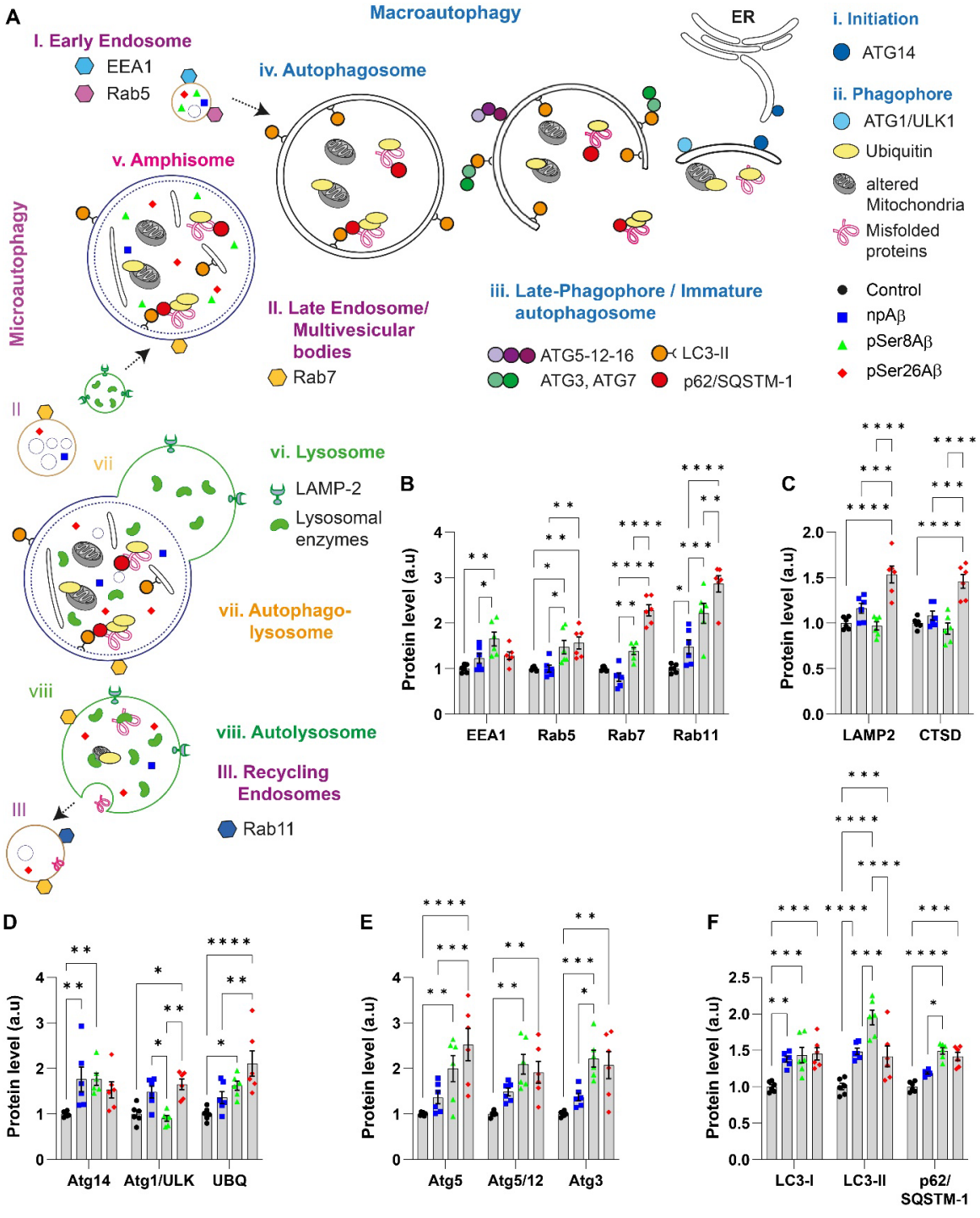

Fig. 18: Dysregulation of autophagy-endo-lysosomal pathway by pAβ species. A. Schematic depicting the major components in the different phases of the autophagy-endo-lysosomal pathway. Respective symbols indicate the localisation of pSer8Aβ (*green triangles*) and pSer26Aβ (*red diamonds*) in comparison to npAβ (*blue squares*) peptide.

B-F. Quantification of western immunoblot data of proteins involved in the individual phases of autophagy and endo-lysosomal function from SH-SY5Y cells upon treatment without (control) or with the indicated Aβ variants (1 µM, 24 h). Values represent mean ± S.E.M.; n = 6, N = 3. * $p < 0.05$; ** $p < 0.01$; *** $p < 0.001$; **** $p < 0.0001$; n.s. $p \geq 0.05$, not significant (Two-way ANOVA, GraphPad Prism). Figure adapted from Kapadia et al. 2024.

It is also interesting to note that all Aβ species caused elevated levels of ATG14L (Fig. **18D**) that is required for the initiation of autophagy (Noda and Fujioka 2015). npAβ and pSer26Aβ, but not pSer8Aβ, also increased the ULK1/atg1 kinase complex that is also involved autophagosome-lysosome fusion (Noda and Fujioka 2015; Wong et al. 2013; Ganley et al. 2009). Analyses of additional proteins involved in phagophore and autophagosome formation revealed that treatment with either pAβ species leads to an increase in ATG5 and the ATG5-12 complex (Fig. **18E**). Similarly, both phosphorylated Aβ species, but not npAβ, significantly increased levels of ATG3. Cell treatment with the individual Aβ variants resulted in significantly increased levels of LC3-I and II as compared to control cells. Treatment with pSer8Aβ peptide significantly increased levels of LC3-II as compared to the pSer26Aβ and npAβ treated cells (Fig. **13F**). This indicates an increase in autophagosome formation or impaired autophagic flux for cells treated with pSer8Aβ compared to pSer26Aβ and npAβ treatment. Treatment with both pAβ variants significantly increased the levels of p62/SQSTM-1, a receptor for autophagic substrates that is itself degraded during completion of autophagy (Fig. **18F**). Increased LC3-II levels and accumulation of p62/SQSTM-1 upon treatment with pSer8Aβ indicate decreased fusion of autophagosomes with lysosomes resulting in impaired autophagic flux (Klionsky et al. 2021). Overall, similar data were obtained with primary cortical neurons (Tab. **3**, Kapadia et al. 2024).

Several studies have indicated that Aβ can directly impact the PI3K-AKT-mTOR pathway (Oddo, 2012). Moreover, increasing evidence suggests that this signalling pathway is directly impacted by Aβ exposure and is altered in AD brains (Heras-Sandoval et al. 2014; Razani et al. 2021). Thus, the effects of Aβ phosphorylation-state variants on tightly regulated PI3K-AKT-mTOR-TFEB pathway was further examined (Fig. **19A**). Treatment of SH-SY5Y cells with Aβ species modulated the expression of individual proteins involved in this pathway (Fig. **19B-E**). pSer8Aβ significantly increased the levels of PI3K, pAKT, mTOR and phospho-p70 S6K. Notably, PI3K, phospho-mTOR and phospho-p70 S6K

were selectively increased by pSer26Aβ as compared to npAβ and control cells. Observations from pAβ-induced alteration of the PI3K-AKT-mTOR pathway corelates with the phosphorylation-state dependent effects on the autophagic flux, demonstrated in previous experiments (Fig. **16**, **18**). It is also important to note that the relationship between Aβ and the PI3K-AKT-mTOR pathway in altering autophagic flux is complex and bidirectional. Here, it is quite difficult to state if the effect on one has a consequence on the other. Further studies are necessary to fully understand the intricate molecular mechanisms.

Activation of transcription factor EB (TFEB) has been shown to upregulate lysosomal biosynthesis as well as enhance lysosomal stress response (Willett et al., 2017). The increase in number of perinuclear/total lysosomal vesicles in case of pSer26Aβ treated cells (Fig. **17E**) is also further supported by the increase in levels of TFEB in the nuclear fraction (Fig. **19F-G**), as nuclear TFEB stimulates lysosome biogenesis (Xiao et al. 2015). The modest increase in nuclear TFEB and phosphorylated TFEB in the cytosol, also corroborate the observed differences in the ratio of perinuclear to peripheral lysosomes in npAβ and pSer8Aβ treated cells (Fig. **17E**). The expression of V_oA1 subunit of ATPase (Mauvezin and Neufeld 2015), which regulates lysosomal pH, is significantly increased in the lysates of cells treated with pSer26Aβ as compared to the other conditions (Fig. **19H**). A further analyses of the nuclear localisation of TFEB was visualised using the GFP-TFEB (Fig. **19I-J**) (Napolitano et al. 2018). Here, the localisation of GFP fluorescence in the nuclear and cytosolic compartments was quantified, respectively (Fig. **19J**). Significantly, npAβ, and pSer26Aβ treated cells, showed an increase GFP-TFEB fluorescence signals in the nucleus as compared to pSer8Aβ treatment. A significant increase in the levels of p-TFEB (Fig. **19G**) and GFP-TFEB (Fig. **19J**) in the cytosol in the case of npAβ treated cells was detected. The increased cytosolic TFEB-GFP pool is/can be phosphorylated or not, was not specifically examined in this study; but the specific observed effect of npAβ in this scenario would need to be examined further. The nuclear translocation of TFEB is also influenced by multiple signalling pathways, including mTORC1, calcineurin, and JNK, which play crucial roles in regulating TFEB subcellular localization (Medina et al., 2015; Martina & Puertollano, 2018; Liu et al., 2018; Kim et al., 2017).

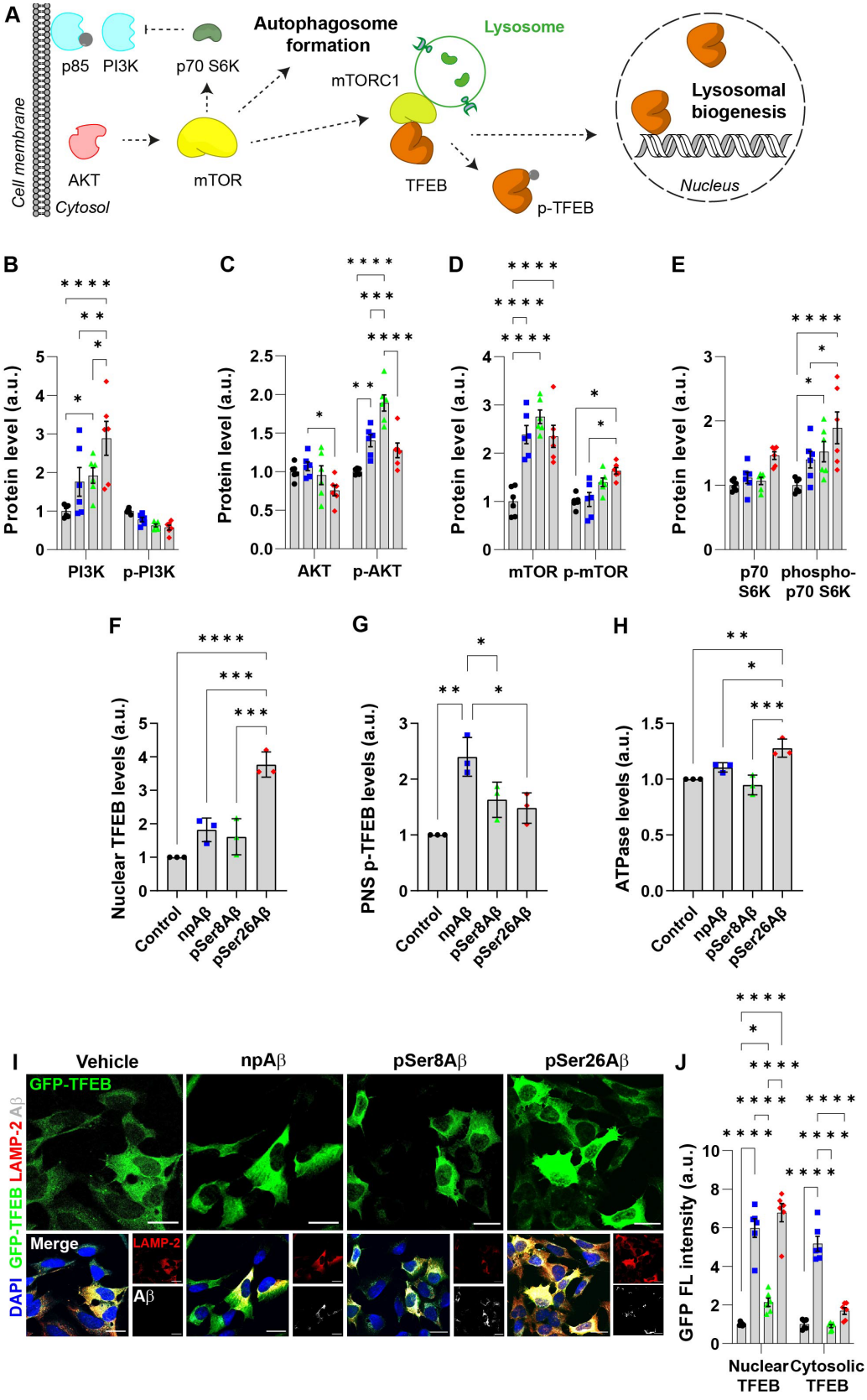

Fig. 19: Effect of pAβ species on PI3K-AKT-mTOR-TFEB pathway. A. Scheme depicting the major components involved in PI3K-AKT-mTOR-TFEB pathway. **B-H**.

Quantification of western immunoblot data of different proteins involved in the individual phases of PI3K-AKT-mTOR-TFEB pathway from SH-SY5Y cells upon treatment without (control) or with the indicated Aβ variants (1 µM, 24 h). Values represent mean ± S.E.M.; n = 6, N = 3. **I-J.** Immunocytochemical analyses (**I**) of SH-SY5Y cells expressing GFP-TFEB reporter construct treated with different Aβ variants (1 µM, 24 h). Control represents untreated cells. After treatment, cells were co-stained to visualize the nucleus (DAPI, *blue*), lysosomes (LAMP2, *red*) and Aβ (82E1, *gray*). Scale bar, 10 µm. GFP fluorescence intensities localized to the nucleus or cytosolic compartment of cells were quantified using FiJi ImageJ image processing module and depicted as bar graphs (**J**). Readings were normalized and depicted as fold change *wrt* control untreated cells, respectively. Values represent mean ± S.E.M.; n = 6, N = 3. * $p < 0.05$; ** $p < 0.01$; *** $p < 0.001$; **** $p < 0.0001$; n.s. $p \geq 0.05$, not significant (Two-way ANOVA, GraphPad Prism).

These observed differences in the altered expression of these proteins in one specific or interconnecting pathways could either be caused by the respective Aβ species or result from the either direct or indirect downstream effect of sub-cellular trafficking, which would also need to be additionally examined in future studies. This comprehensive analyses of autophagy and endo-lysosomal pathway related proteins revealed complex and differential effects of Aβ phosphorylation-state variants at specific phases during autophagy that could result in impaired protein homeostasis.

3.2.6. Phosphorylated Aβ alters the ubiquitin proteasomal system

The interplay between ubiquitin proteasomal system (UPS) and autophagy is pivotal in maintaining protein homeostasis (Zhang et al. 2017; Upadhya and Hegde 2007; Korolchuk et al. 2010; Ding et al. 2007; Ji and Kwon 2017). UPS-mediated proteolysis involves the ubiquitination of a protein substrate, the recognition of ubiquitinated proteins and their delivery to the proteasome by ubiquitin receptors, and finally proteasomal degradation of these substrates (Ciechanover and Schwartz 1998). As seen in Fig. **18D**, both phosphorylated Aβ species resulted in a significant increase in the amount of free ubiquitin, indicating an effect on UPS. Thus, the colocalization of Aβ species with poly-ubiquitinylated proteins in APP-PSEN1delE9xThy1-YFP transgenic mice (Fig. **20A-B**) as well as mouse primary cortical neurons (Fig. **20C-D**) using immunohistochemical/immunocytochemical analyses was examined. Both phosphorylated peptides showed increased intraneuronal colocalization with poly-UBQ within mouse brains as well as in cultured neurons indicating their association with ubiquitinylated proteins (*Mander's overlap coefficients*, Fig. **20B, D**). An increase in

intracellular accumulation of ubiquitinylated proteins could indicate an pAβ-induced impairment in protein turnover.

Analyses of different proteins/factors associated within the UPS showed that treatment of SH-SY5Y cells with pAβ variants significantly increased the levels of ubiquitin-like modifier activating enzyme-1 (UBA1, Fig. **20E**), which sits at the apex of ubiquitin pathways and plays a critical role in regulating protein homeostasis (Ciechanover and Schwartz 1998). pSer8Aβ, and more significantly pSer26Aβ treatment, increases ubiquitin C-terminal hydrolase L1 (UCHL1, Fig. **20F**) as well as E3 ubiquitin-protein ligase (MARCH5, Fig. **20G**) expression. An increase in levels of free UBQ was also detected within neurons upon treatment with pAβ variants (Fig. **18D**). Increased E3 ligase, when combined with an ample supply of free ubiquitin could promote ubiquitinoylation of proteins, indicating more proteins being tagged for degradation. This could indicate that the cell might attempt to clear damaged or misfolded proteins to efficiently maintain homeostasis. In addition, both pAβ species increase the levels of proteasome 20S subunit beta 5 (PSMB5, Fig. **20H**) along with poly-ubiquitinylated (Fig. **20I**) and phospho-ubiquitinylated proteins (Fig. **20J**) suggesting an increase in the assembly of 20S proteasome complex. npAβ treated cells only showed a significant increase in the levels of poly-ubiquitinylated proteins, and no significant effect on others, as compared to control cells. An increase in the expression of these proteins/factors (Zhang et al. 2017; Upadhya and Hegde 2007), is a potential indicator of pAβ induced impairment of ubiquitin dependent protein metabolism.

Evaluation of the UPS function was done by incubation of small fluorogenic peptide substrates with lysates of SH-SY5Y cells treated with different Aβ variants (Kisselev and Goldberg 2005; Moravec et al. 2009). The fluorescence emission of the fluorogenic dye is enhanced when the conjugated substrate undergoes proteasomal degradation, in turn giving a measure of the proteasomal activity of the lysate (Fig. **21**). pSer26Aβ, and to a smaller extent pSer8Aβ significantly increased proteasomal activity, whereas npAβ had only a small, non-significant effect (Fig. **21A-B**). Although, lysates from pSer8Aβ treated cells showed swift change in fluorescence response over time, as compared to control, the values were comparable to that of npAβ and pSer26Aβ conditions. The mean proteasomal activity was highest in the case of pSer26Aβ, followed by pSer8Aβ and least by npAβ treatment for 24 h, wherein these differences lie beyond the set limit of statistical significance (Fig. **21C**).

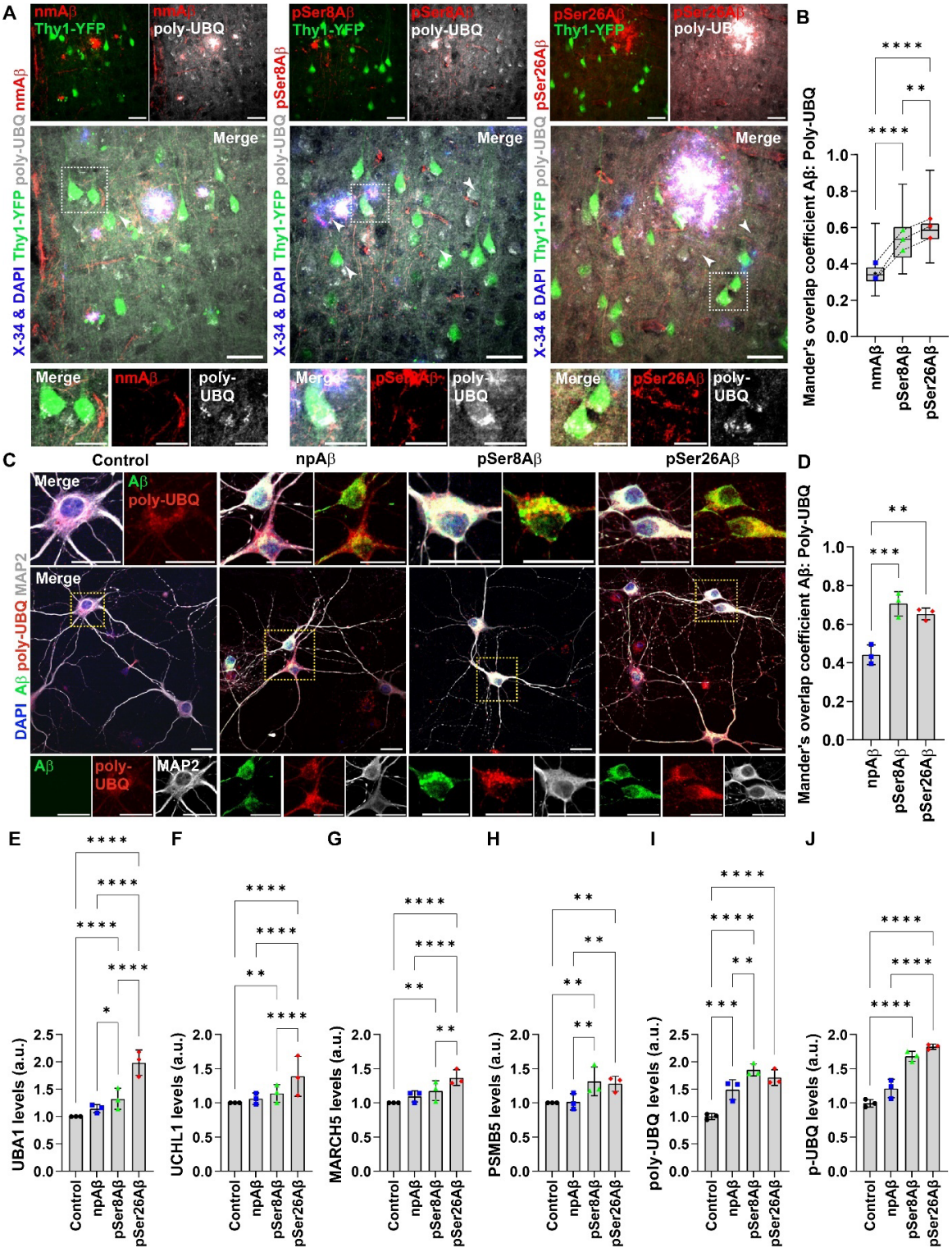

Fig. 20: Intraneuronal pAβ associates with poly-ubiquitinylated proteins in APP-PSEN1 transgenic mice and primary cortical neurons affecting the ubiquitin proteasomal system (UPS). A-B. Immunohistochemical staining (**A**) depicting intraneuronal colocalization of Aβ species in brain sections of APP-PSEN1delE9xThy1-YFP transgenic mouse cortex (7.3 m, female) stained with different phosphorylation state specific Aβ antibodies (nmAβ- 7H3D6, pSer8Aβ- 1E4E11 and pSer26Aβ- 5H11C10; *red*

channels respectively) along with antibody against mitochondrial marker protein, poly-ubiquitinylated proteins (poly-UBQ) (*gray*) and DAPI + X-34 (nuclei and plaque core, *blue*). Scale bar: 50 µm; zoomed panels, 10 µm. White arrowheads indicate colocalized punctate staining between red and gray channels in Thy1-YFP positive neurons. Box plot (**B**) depicting Mander's coefficient of overlap between red channels (npAβ, *blue*; pSer8Aβ, *green* and pSer26Aβ, *red data points*) with respect to gray channels (poly-UBQ), quantified within Thy1-YFP positive neurons respectively. Box plot depicts the overall distribution of data, and each data point represents average values from an individual mouse, N = 3 transgenic mice. **C-D.** Immunocytochemical staining (**C**) of primary cortical neurons were incubated without (control) or with the indicated Aβ variants (500 nM, 4 h) and co-stained with antibodies against the microtubule-associated protein 2 (MAP2, *gray*), Aβ (82E1, *green*) and poly-UBQ (*red*). Nuclei were stained with DAPI (*blue*). Scale bar, 10 µm. Dotted boxes indicate the regions zoomed in the merged panels (*above*) and individual channels (*below*). Bar plot (**D**) depicting Mander's overlap coefficients between Aβ (*green channel*) with poly-UBQ (*respective red channels*). Values represent mean ± S.D.; n = 6, N = 3. **E-J**. Quantification of western immunoblot data of different proteins involved in the ubiquitin proteasomal system from SH-SY5Y cells treated without (control) or with indicated Aβ variants (1 µM, 24 h). Values represent mean ± S.E.M.; n = 6, N = 3. * $p < 0.05$; ** $p < 0.01$; *** $p < 0.001$; **** $p < 0.0001$; n.s. $p \geq 0.05$, not significant (One-way ANOVA, GraphPad Prism).

Each proteasome contains two chymotrypsin-like, two trypsin-like, and two caspase-like proteolytic sites, conjugated in a complex network of allosteric interactions between these catalytic and regulatory sites. The mean changes in proteasome dependent proteolytic activity were further studied by examining the activity using different classes of proteolytic substrates, i.e., caspase-like, trypsin-like, chymotrypsin-like, or post-glutamyl peptide hydrolase, respectively (Fig. **21D-M**). Thus, lysates from SH-SY5Y cells pretreated with respective Aβ variants (24 h) were used to examine time-dependent modulation of proteolytic activities (30 min – 24 h, Fig. **21I-M**). End-point change in proteolytic activity has been presented in the form of bar blots (Fig. **21D-H**).

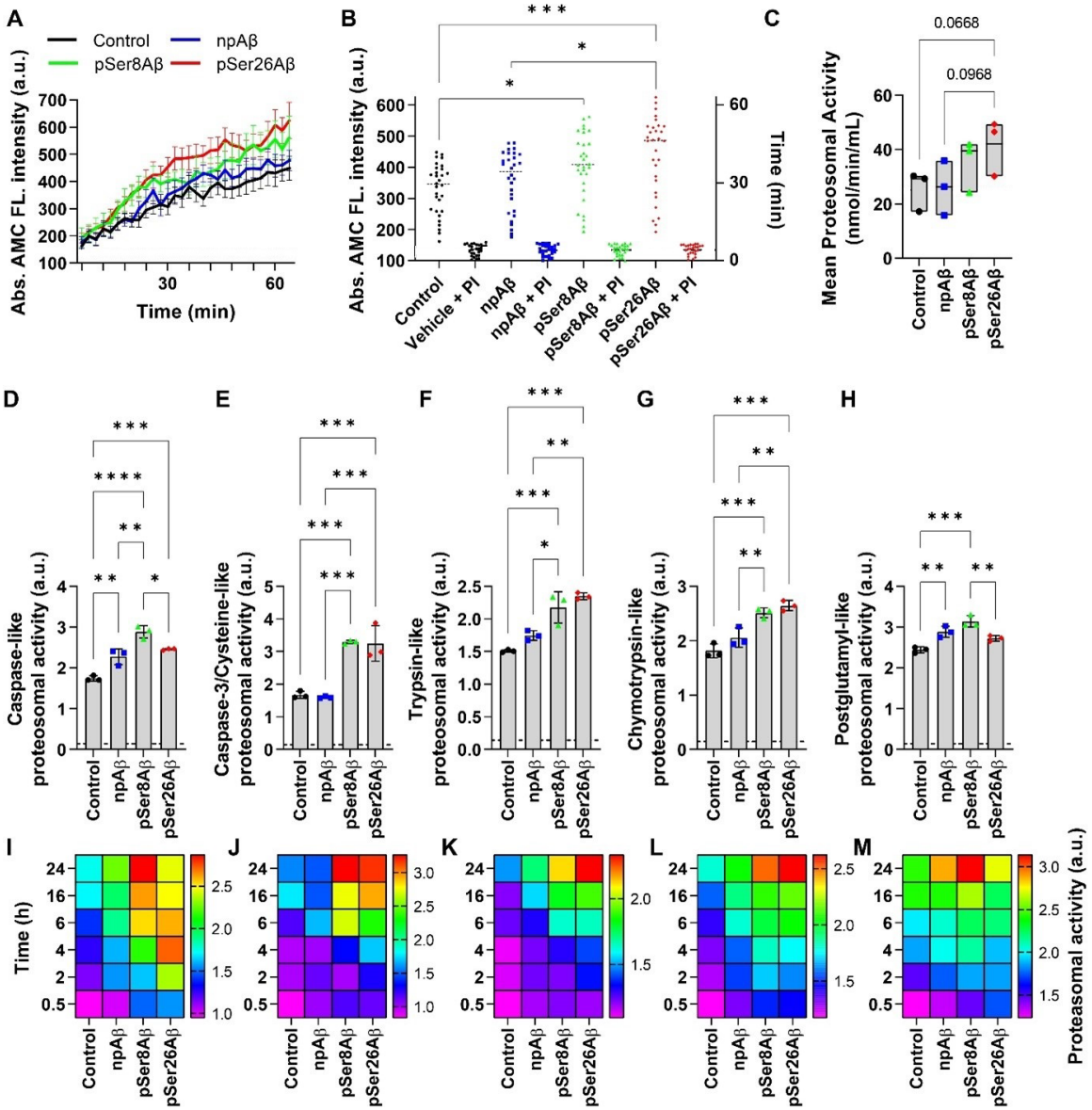

Fig. 21: pAβ differentially impairs proteasomal function. A-C. SH-SY5Y cells were treated without (control) or with Aβ variants (1 µM) for 24 h, were lysed and total proteasomal activity was measured using a proteasome Assay kit. Line plot (**A**) depicts time dependent increase in absolute fluorescence intensity of AMC dye indicating change in total proteasomal activity in presence of respective cell lysates. Dotted line represents values from untreated cells. Values represent mean ± S.E.M.; n = 9, N = 3. Comparative scatter plot (**B**) showing the distribution of abs. fluorescence intensities of AMC dye over a time span of 65 min measured by cell lysates of SH-SY5Y cells treated without (control) or with Aβ variants (1 µM) for 24 h, in presence or absence of proteasomal inhibitors (10µM MG132 and 1µM vYAD). Assay readings in presence or absence of proteasomal inhibitors showed significant differences (p = 0.0001), respectively. Values represent mean ± S.E.M.; n = 9, N = 3, without inhibitors; n = 6, N = 3, with inhibitors, (Two-way ANOVA, GraphPad Prism). Box plot (**C**) depicting the mean proteasomal activity (nmol/min/mL) computed from the raw data depicted in graphs A-B. Individual points depict the average values from each individual experiment; n = 9, N = 3, (Repeated

measures one-way ANOVA, GraphPad Prism). **D-M.** SH-SY5Y cells were treated without (control) or with Aβ variants (1 µM) for different time points until 24 h, were lysed in respective proteasomal assay buffers and were treated with different fluorogenic substrates to measure the substrate specific-proteasomal activity, respectively. Bar plots (**D-H**) depict mean proteasomal activity of cell lysates from SH-SY5Y cells were treated without (control) or with Aβ variants (1 µM, 24 h). Readings were normalized to untreated cells (growth medium) and represented as fold change. Values of blank wells (without cells) have been indicated as a dotted line. Values represent mean ± S.E.M.; n = 6, N = 3, (One-way ANOVA, GraphPad Prism). Heat maps (**I-M**) depict the fold change in proteasomal activity measured from cells lysates of SH-SY5Y cells treated for different time points until 24 h, as indicated. Readings were normalized to untreated cells (growth medium) and represented as fold change. Values of blank wells (without cells) have been indicated as a dotted line. Values represent geometric mean.; n = 6, N = 3. * $p < 0.05$; ** $p < 0.01$; *** $p < 0.001$; **** $p < 0.0001$; n.s. $p \geq 0.05$, not significant.

Treatment with either pAβ peptides upregulated proteasome function as compared to npAβ treated or control cells, even at shorter treatment times. npAβ peptide only induced significant increment in total caspase- and postglutamyl like- proteolytic activity, whereas pSer8Aβ, shows enhanced caspase- and postglutamyl like- hydrolase activities. On the other hand, pSer26Aβ showed highest increment in trypsin- and chymotrypsin-like proteasomal activity. The effects were quite comparable to that of pSer8Aβ treatment. Both phosphorylated Aβ peptides showed stronger differences when compared to npAβ treated, as well as control cell lysates. These data suggest that phosphorylated Aβ variants differentially alter proteasome function as compared to npAβ, by modulating proteolytic activity. Also, the increase in proteasomal function could be a compensatory response to increased proteotoxic stress induced by intracellular accumulation of Aβ, in particular of pAβ species.

3.2.7. Phosphorylation of Aβ alters ER stress response

The UPS is also involved in the degradation of endoplasmic reticulum (ER)-associated protein degradation (ERAD) targets, which are misfolded or unassembled proteins selected by a quality control system within the ER lumen (Hwang and Qi 2018; Meusser et al. 2005). Alteration of UPS could thereby affect unfolded protein response (UPR) and interfere with normal physiological functions of the cell resulting in ER stress (Fig. **22A**) (Nishikawa et al. 2005; Hwang and Qi 2018). Phosphorylation state of Aβ alters the expression of different proteins/factors involved in the ERAD degradation pathway (Fig.

22). Notably, calnexin, an ER chaperone involved in quality control of protein folding (Guérin et al. 2008), is significantly increased in cells treated with pSer26Aβ as compared to npAβ and control cells. pSer8Aβ also tended to increase calnexin levels, but the effect was not statistically significant. Another important ER chaperone, BiP/GRP78, a direct ER stress sensor leading to UPR activation (Wang et al. 2009), is significantly upregulated upon treatment with both pAβ peptides (pSer26Aβ > pSer8Aβ). Heat shock proteins 70 and 90 (HSP70 and HSP90) functioning as molecular chaperones and folding catalysts (Albakova et al. 2022), showed altered expression depending the phosphorylation state of the Aβ peptide. There are three key UPR signal activator proteins (Fig. **22A**) (Adams et al. 2019), inositol requiring enzyme 1α/β (IRE1), PKR-like ER kinase (PERK), and activating transcription factor 6α/β (ATF6). Treatment with either pSer8Aβ, and more potently pSer26Aβ increases the expression of IRE1α and ATF6, as compared to npAβ and control cells. Aβ treatment influenced the downstream factors associated with these pathways. C/EBP homologous protein (CHOP) plays an important role in ER stress-induced apoptosis which is significantly increased in the case of pSer26Aβ treated cells as compared to the other conditions. This increase in expression of CHOP could be a result of the downstream UPR signal activator proteins (Hu et al. 2018). Also, as UPR modulates MAPK signalling (Shah et al. 2017), a significant increase in the expression of extracellular signal-regulated kinases (ERK) was seen upon pSer26Aβ treatment. This could indicate a ‘pro-survival response’ to increased cellular stress, particularly activated by pSer26Aβ. Crosstalk between the ER and Golgi apparatus maintains cellular homeostasis, especially through the regulation of proteostasis. Alterations in the ERAD, UPR and augmented ER stress could contribute to Golgi stress (Benyair et al. 2022). The levels of the trans-Golgi network (TGN), a major secretory pathway sorting station, showed elevation only in case of cells treated with pSer26Aβ. Expression of Golgi matrix associated protein - golgin seem to be slightly altered in case of pAβ treated cells, although these differences were not statistically significant. In conclusion, the data herewith indicate that intracellular pAβ could potentially induce ER stress, which in turn could activate UPR, as an adaptive cellular response.

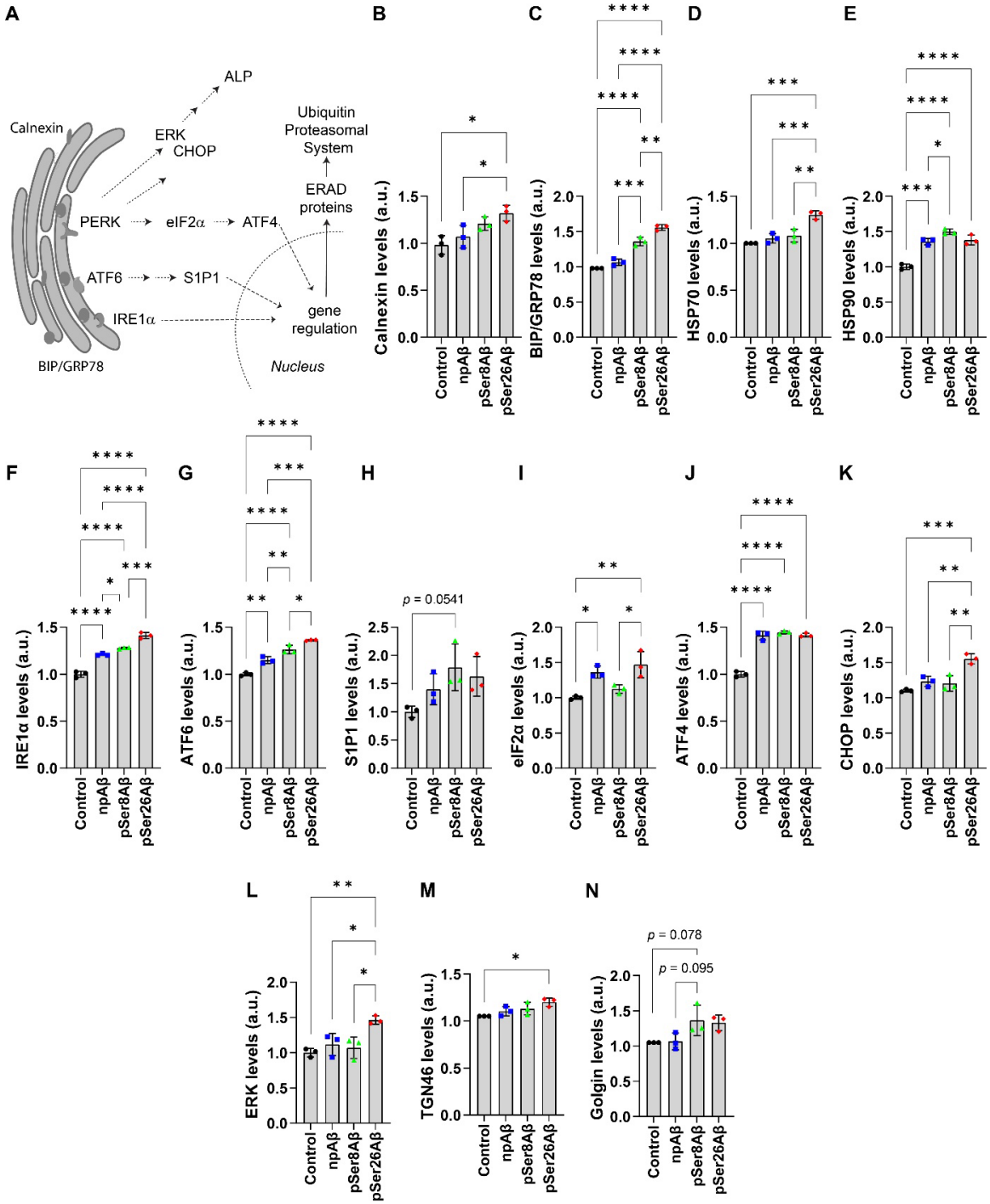

Fig. 22: Alteration of ER associated proteins by pAβ species. A. Schematic depicting the major proteins/factors involved in ER-associated degradation (ERAD) response. **B-N**. Quantification of western immunoblot data of different proteins/factors involved in the ERAD function from SH-SY5Y cells treated without (control) or with the indicated Aβ variants (1 μM, 24 h). Values represent mean ± S.E.M.; n = 6, N = 3. * $p < 0.05$; ** $p < 0.01$; *** $p < 0.001$; **** $p < 0.0001$; n.s. $p \geq 0.05$, not significant (One-way ANOVA, GraphPad Prism).

3.2.8. Phosphorylated Aβ differentially triggers mitochondrial dyshomeostasis and oxidative stress

Mitochondrial dysfunction in AD has been previously reported (Cardoso et al. 2004; Du et al. 2010; Wang et al. 2020). The PINK1-Parkin pathway plays an important role in mitochondrial damage (Fig. **23C**) and increase in PINK1/Parkin levels is a potential indicator of mitochondrial dysfunction and is associated with the rate of cognitive decline (Goudarzi et al. 2021; Wang et al. 2020). Immunohistochemical analyses of APP-PSEN1delE9xThy1-YFP transgenic mice (Fig. **23, A-B**; Ext. Fig. **8A-B**) as well as immunocytochemical examination of mouse primary cortical neurons (Ext. Fig. **8C-F**) showed differential colocalization of Aβ species with PTEN-induced kinase 1 (PINK1) and the ubiquitin E3 ligase Parkin (Goudarzi et al. 2021). Both phosphorylated peptides showed increased colocalization with both markers indicating their association with dysfunctional mitochondria, both intraneuronal as well as within extracellular plaque pathology (Fig. **23A-B**, Ext. Fig. **8**).

Mitochondrial fission and fusion cycles (mitochondrial dynamics) play critical roles in maintaining functional mitochondria (Fig. **23C**). During mitochondrial stress events, especially in AD, partially damaged mitochondria are fused which further facilitate apoptosis (Santos et al. 2010; Zhang et al. 2016). Aβ has been associated with the downregulation of fusion-related proteins such as optic atrophy 1 (OPA-1) and mitofusins 1 and 2 (MFN1, MFN2), while upregulating fission proteins including dynamin-related protein 1 (DRP1) and fission 1 (FIS1) (Wong et al. 2020; Batista et al., 2021; Han et al. 2017; Kaur et al. 2014; Müller et al. 2010). Aβ significantly altered the expression of different proteins involved in fusion and fission cycles of mitochondrial homeostasis, in a phosphorylation-state specific manner (Fig. **23D-I**). As seen in Fig, **23D**, both pAβ variants showed stronger effect on decreasing the expression OPA-1 as compared to npAβ or control conditions. Contrary to published literature, MFN1 levels are slightly upregulated in the presence of npAβ and pSer26Aβ. An increase in the levels of dynamin-related protein (DRP1) and protein deglycase (PARK/DJ-1) with respective Aβ peptides, could further indicate a cellular response towards fusion events to target degradation of damaged/dysfunctional mitochondria. These data suggest that there is a phosphorylation-state dependent impact of Aβ on mitochondrial homeostasis. Additionally, treatment with

pAβ variants strongly increase the expression of both PINK1 and Parkin levels, as compared to npAβ or control treated cells, indicative of differential effect of phosphorylation-state Aβ variants on mitochondria function (Fig. **23H-I**).

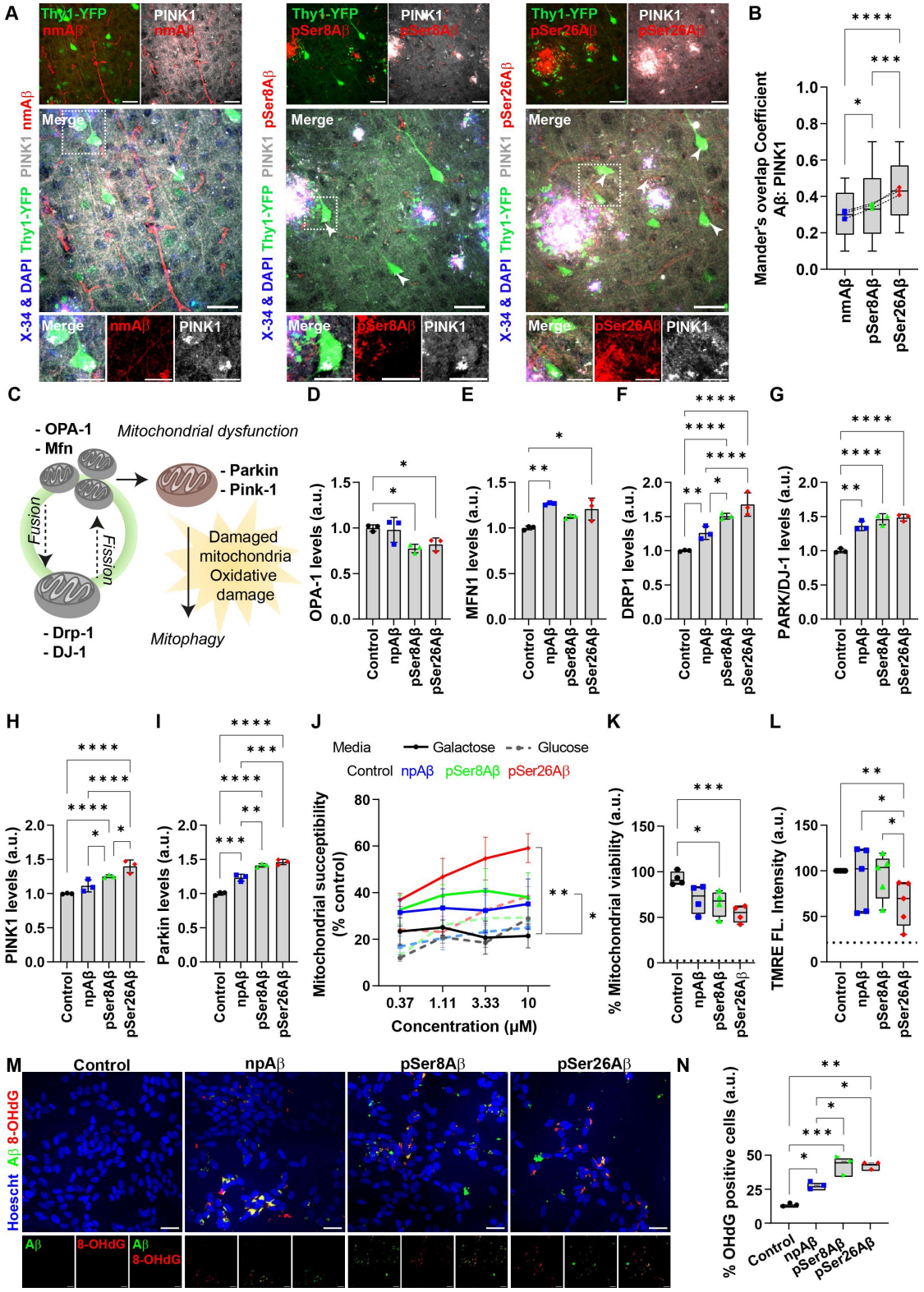

Fig. 23: Effect of pAβ species on mitochondrial homeostasis and oxidative stress. A-B. Immunohistochemical staining (**A**) depicting intraneuronal colocalization of Aβ species in brain sections of APP-PSEN1delE9xThy1-YFP transgenic mouse cortex (7.3 m, female) stained with different phosphorylation state specific Aβ antibodies (nmAβ- 7H3D6, pSer8Aβ- 1E4E11 and pSer26Aβ- 5H11C10; *red channels respectively*) along with antibody against mitochondrial marker protein, PINK1 (*gray*) and DAPI + X-34 (nuclei and plaque core, *blue*). Scale bar: 50 µm; zoomed panels, 10 µm. White arrowheads indicate colocalized punctate staining between red and gray channels in Thy1-YFP positive neurons. Box plot (**B**) depicting Mander's coefficient of overlap between red channels (npAβ, *blue*; pSer8Aβ, *green* and pSer26Aβ, *red data points*) with respect to gray channels (PINK1), quantified within Thy1-YFP positive neurons respectively. Box plot depicts the overall distribution of data, and each data point represents average values from an individual mouse, N = 3 transgenic mice. **C.** Scheme depicting the major components in the different phases of the mitochondrial homeostasis and dysfunction. **D-I**. Quantification of western immunoblot data from SH-SY5Y cells for mitochondrial proteins treated without (control) or with the indicated Aβ variants (1 µM, 24 h). Values represent mean ± S.E.M.; n = 6, N = 3. **J.** Aβ concentration dependent mitochondrial susceptibility of SH-SY5Y cells treated with different Aβ variants (24 h) or without (control) in presence of galactose (*bold line*s) or glucose containing (*dotted line*s) media, examined using a Mitochondrial ToxGlo™ assay kit. Readings were normalized to untreated cells (growth medium) and represented as percent control; values represent mean ± S.D.; n = 8, N = 4. **K.** Box plot depicting percent mitochondrial viability of SH-SY5Y cells treated with Aβ variants (1.11 µM, 24 h) or without (control) in presence of galactose containing media, examined using a Mitochondrial ToxGlo™ assay kit. Readings were normalized to untreated cells (growth medium) and represented as percent control; individual points depict the average values from each individual experiment; n = 8, N = 4. **L.** Mitochondrial membrane potential was examined using TMRE fluorescence measurements after 24 h treatment with Aβ variants (1 µM). The control cells were untreated. Individual points depict the average values from each individual experiment, normalized to control from that particular experiment; n = 5, N = 5, (Repeated measures one-way ANOVA, GraphPad Prism). **M-N.** Fluorescence analyses (**M**) of SH-SY5Y cells treated with different Aβ variants (24 h) or without (control) were co-stained with 8-hydroxy-2' -deoxyguanosine (8-OHdG) as a marker for oxidative stress/DNA damage, Aβ antibody 82E1 and DAPI to visualize the nuclei. Data is representative of three independent experiments. Box plot (**N**) depicting the percent cells prone to oxidative damage quantified by analyzing cells positive for 8-OHdG. Readings were normalized to untreated cells (growth medium) and represented as percent control; individual points depict the average values from each individual experiment; n ~120 cells, N = 3. * $p < 0.05$; ** $p < 0.01$; *** $p < 0.001$; **** $p < 0.0001$; n.s. $p \geq 0.05$, not significant (One-way ANOVA, GraphPad Prism). Additional staining experiments in mouse brain sections, primary cortical neurons and control experiments are provided in Ext. Fig. **8**.

Damaged mitochondria function less-efficiently and are more susceptible to oxidative stress (Mecocci et al. 1994). Examination of mitochondrial susceptibility upon exposure to Aβ (Fig. **23J**) shows that both phosphorylated Aβ variants induced a concentration

dependent effect in SH-SY5Y cells further leading to decreased mitochondrial viability (Fig. **23K** and Ext. Fig. **8K**). Another indication of mitochondrial dysfunction is their failure to sequester the fluorescent dye TMRE as an indicative for lower mitochondrial membrane potential. pSer26Aβ significantly decreased mitochondrial membrane potential, as compared to pSer8Aβ, npAβ treated or control cells (Fig. **23L**). Mitochondrial dysfunction could also affect mitochondrial Ca^{2+} homeostasis and influence reactive oxygen species (ROS) production. Microscopic examination of 8-OHdG, a biomarker of oxidative stress, in cells treated with Aβ variants (Fig. **23M-N**), showed that intracellularly accumulated Aβ induced oxidative stress. Although all variants induced significant changes, both pAβ induced a higher increase in mitochondrial associated oxidative stress in cells, as compared to npAβ treated or control cells (Fig. **23N**). Inter-relationship between mitochondrial function and the susceptibility to oxidative stress has been previously implicated in AD (Butterfield and Boyd-Kimball 2020; Hirai et al. 2001; Mecocci et al. 1994; Santos et al. 2010; Zhang et al. 2016; Wang et al. 2020). These data indicate that pAβ peptides, impair mitochondrial function, eventually contributing to the observed neurotoxicity.

3.3. Site specific effect of Aβ phosphorylation on cell death associated pathways

Impaired autophagy, UPR and oxidative stress can initiate regulated cell death (RCD) mechanisms, such as apoptosis or necroptosis (Behl 2000; LaFerla et al. 1997; Cotman and Su 1996). Employing immunohistochemistry the association of intracellular Aβ species localized in Thy1-YFP positive neurons with different marker proteins for necrotic cell death, i.e. casein kinase I isoform delta (CK1δ, Fig. **24A-B**), phosphorylated receptor-interacting serine/threonine-protein kinase 1 (p-RIPK1, Fig. **24C-D**) and phosphorylated-mixed lineage kinase domain-like protein (p-MLKL, Ext. Fig. **9A-B**) or for the apoptotic cell death marker Annexin V (Ann V, Ext. Fig. **9C-D**) in APP-PSEN1delE9xThy1-YFP transgenic mice, was examined. pSer26Aβ showed highest colocalization with CK1δ, pMLKL, and pRIPK1 within Thy1 labeled neurons as compared to npAβ and pSer8Aβ. On the other hand, pSer8Aβ showed highest colocalization with AnnV as analyzed by the Mander's overlap coefficients (Ext. Fig. **9C-D**).

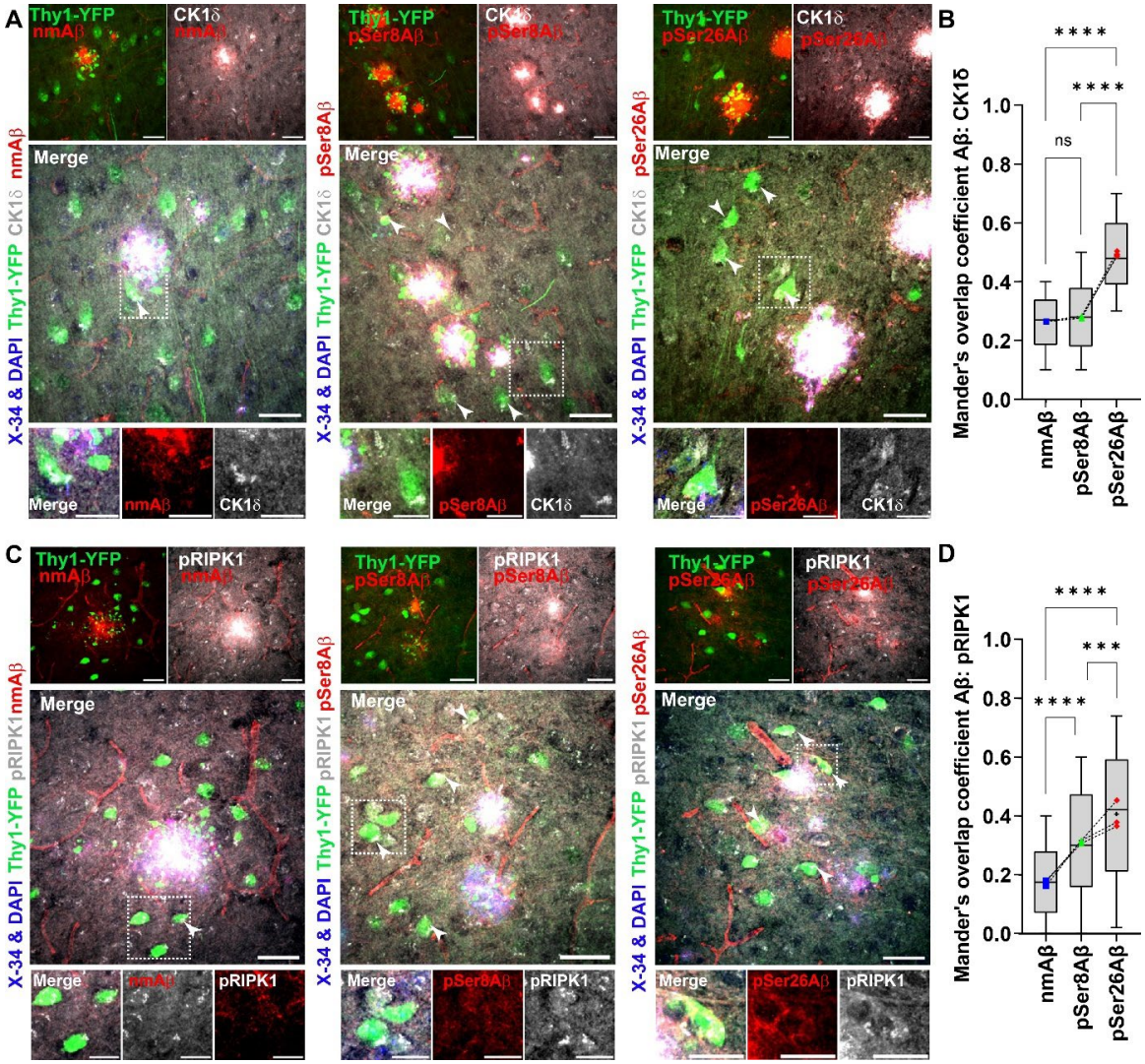

Fig. 24: Intraneuronal pAβ differentially directs neuronal cell fate in APP-PSEN1 transgenic mice. A-D. Immunohistochemical staining (**A, C**) depicting intraneuronal colocalization of Aβ species in brain sections of APP-PSEN1delE9xThy1-YFP transgenic mouse cortex (7.3 m, female) stained with different phosphorylation state specific Aβ antibodies (nmAβ- 7H3D6, pSer8Aβ- 1E4E11 and pSer26Aβ- 5H11C10; *red channels respectively*) along with antibody against Casein kinase I isoform delta, CK1δ (*gray,* **A**) and phosphorylated-receptor-interacting serine/threonine-protein kinase 1, p-RIPK1 (*gray,* **C**). DAPI + X-34 were used to stain nuclei and plaque core (*blue*), respectively. Scale bar: 50 µm; zoomed panels, 10 µm. White arrowheads indicate colocalized punctate staining between red and gray channels in Thy1-YFP positive neurons. Box plot (**B, D**) depicting Mander's coefficient of overlap between red channels (npAβ, *blue*; pSer8Aβ, *green* and pSer26Aβ, *red data points*) with respect to gray channels (CK1δ, **B** and p-RIPK1, **D**), quantified within Thy1-YFP positive neurons respectively. Box plot depicts the overall distribution of data, and each data point represents average values from an individual mouse, N = 3 transgenic mice. Values represent mean ± S.E.M. * $p < 0.05$; ** $p < 0.01$; *** $p < 0.001$; **** $p < 0.0001$; n.s. $p \geq 0.05$, not significant (One-way ANOVA, GraphPad Prism). Additional staining experiments (p-MLKL and AnnV) in mouse brain sections are provided in Ext. Fig. **9**.

To further examine site-specific effect of Aβ phosphorylation on RCD, Aβ treated SH-SY5Y cells were stained with 7AAD, AnnV and propidium Iodine (PI) (Fig. **25A-C**). Furthermore, analyses of percent $AnnV^+$ and PI^+ cells were quantified indicating cells prone to apoptotic or necrotic cell death (Fig. **25D**). Here, npAβ treatment significantly increased the number of both $AnnV^+$ and PI^+ cells. pAβ also significantly increased the number of $AnnV^+$ and PI^+ cells indicating cell death via apoptosis and necrosis. In particular, $AnnV^+$ cells were significantly higher following pSer8Aβ treatment, wherein the values were still comparable to pSer26Aβ treatment. pSer26Aβ treatment led to highest percentage of PI^+ cells. npAβ and pSer8Aβ also increased in the number of PI^+ cells, although the effect was significantly lower than that of pSer26Aβ. Additional analysis of time dependent accumulation of intracellular Aβ contributing to differential RCD mechanisms have been summarized in Ext. Fig. **10**. pAβ species induced a time-dependent apoptosis (AnnV positivity) to a very similar extent, but the effects were stronger than that induced by npAβ. Necrosis (PI positivity) induced by all Aβ species, in particular pSer26Aβ showed a stronger response.

During these experiments, significant decrease in the number of cells attached to the plates following pAβ treatment, in particular pSer26Aβ, was observed. Therefore, Aβ treated SH-SY5Y cells adhered to the culture plate as well as floating in the treatment media were stained with Trypan Blue dead cell stain and analyzed via cell counter. A significant decrease in adhered viable cells and with a subsequent increase in dead cells (either adhered or floating) was seen with pSer8Aβ, in particular pSer26Aβ treatment (Fig. **25E**). Additional analyses of the cell diameter (Fig. **25F-G**) revealed that pSer26Aβ treated cells, either live or dead, are larger as compared to npAβ or control cells, further supporting increased necrotic cell in presence of pSer26Aβ. Contrastingly, pSer8Aβ treated cells rather induced shrinkage of cells as a classic indicator of apoptotic cell death. Analysis of the DNA from Aβ treated SH-SY5Y cells showed ‘laddering’ of DNA specifically with pSer8Aβ peptide, as well as pSer26Aβ to some extent. Treatment with npAβ, or specifically pSer26Aβ shows smearing of the DNA, a characteristic indicator of necrotic cell death.

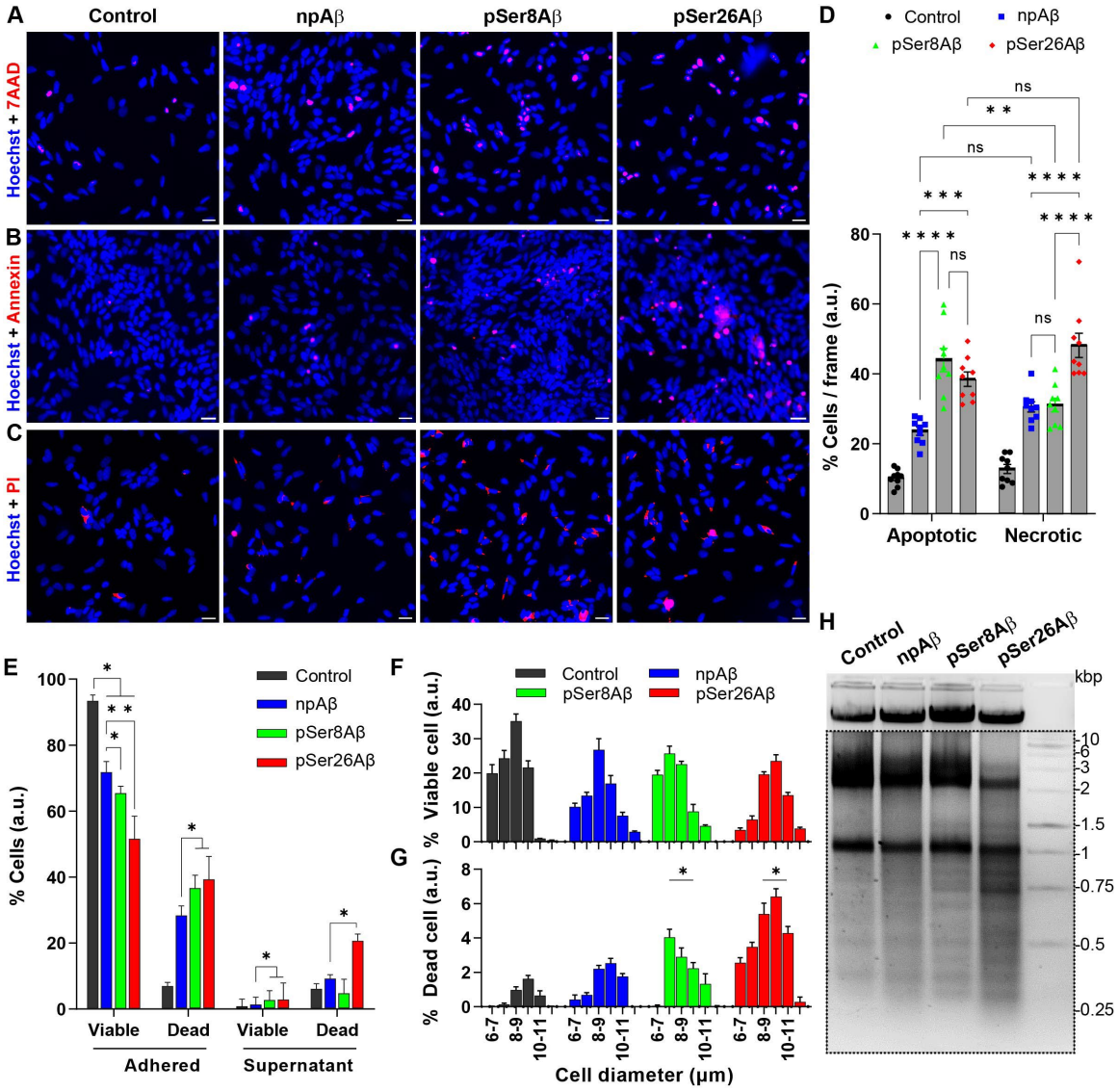

Fig. 25: Phosphorylation state of Aβ differentially dictates cell fate via apoptotic or necrotic cell death pathways. A-D. SH-SY5Y cells treated cells treated without (control) or with Aβ variants (1 μM, 24 h), were stained with 7AAD (A, *red*), AnnV (**B**, *red*) of Propidium Iodide (**C**, *red*) along with Hoechst (nucleus, *blue*). Scale bar, 10μM. Scatter plot (**D**) showing percent apoptotic (AnnV positive) or percent necrotic (PI positive) dead cells per frame, respectively. Values represent mean ± S.E.M. n = 9, N = 3, (Two-way ANOVA, GraphPad Prism). **E-G**. SH-SY5Y cells treated without (control) or with Aβ variants (1μM, 24 h) were subjected to Trypan Blue staining and analyzed using cell counter. **E.** Viable and dead cells adhered to the plate or detached in the culture media were quantified. Values were normalized to untreated control cells (growth medium) and presented as mean ± S.E.M.; n = 4, N = 2, (One-way ANOVA, GraphPad Prism). Histogram (**F, G**) depicts the percent cell population and distribution of cell diameters of adhered viable (**F**) and detached damaged cells (**G**), respectively. Readings of each experiment were averaged and presented as mean ± S.E.M.; n = 4, N = 2. **H**. Analyses of DNA isolated from SH-SY5Y cells treated without (control) or with Aβ variants (1μM, 24 h), analyzed via agarose TAE gel electrophoresis. Region of interest in dotted box is

shown in higher exposure time. * $p < 0.05$; ** $p < 0.01$; *** $p < 0.001$; **** $p < 0.0001$; n.s. $p \geq 0.05$, not significant. Time dependent analyses of intracellular Aβ accumulation and its effect on different cell death pathways has been provided in Ext. Fig. **10**.

Treatment of cells with Aβ peptides depicted that phosphorylation state of Aβ alters the expression of different proteins/factors involved in differential phases of the cell death-associated pathway (Fig. **26**). Aβ has been implicated in the upregulation and induction of wnt–PCP–JNK pathway, resulting in p53-dependent apoptosis (Killick et al., 2012). Apoptotic cell death associated p53 protein (also called TP53) is significantly increased in cells treated with all Aβ variants, but pSer8Aβ showed the maximum effect (Fig. **26A**). On the other hand, anti-apoptotic p35 protein is decreased in pSer26Aβ and npAβ treated cells (Fig. **26B**), wherein pSer8Aβ induced changes in p35 were not significantly different to that of the control of npAβ treated cells. These results suggest the role of Aβ phosphorylation-state in differentially regulating the intricate interplay between Aβ, p53, and p35/Cdk5 in the contributing to AD pathogenesis. Bcl2, a key player in apoptosis, has been shown to undergo phosphorylation, which can impact its anti-apoptotic function (Ruvolo et al., 1998). Levels of bcl-2 were significantly increased upon pSer26Aβ treatment, wherein the other variants did not induce a significant change (Fig. **26C**). It has been demonstrated that the phosphorylation of bcl-2 can inhibit apoptosis (Kutuk & Letai, 2008), while dephosphorylation of bcl-2 at Ser87 has been shown to potentiate apoptosis (Liu et al., 2010). These experiments selectively showed increase in the expression of bcl-2 phosphorylated at serine 87 upon treatment with npAβ and pSer26Aβ (Fig. **26D**), wherein no changes were detected with respect to bcl-2 phosphorylated at serine 70 (data not shown). Activation of caspases ensures that cellular components are degraded in a controlled manner during apoptosis (Harvey and Kumar 1998). As shown in Fig. **26E-G**, both pAβ peptides, particularly pSer8Aβ, significantly increased the expression of pro-caspase-1, cleaved caspases-1 and -3, as compared to npAβ or control cells. These observations implicate the role of pAβ species in disparate processes of apoptosis and inflammation. IL-1β, which can promote apoptosis, is significantly increased with all Aβ variants with pSer8Aβ having strongest effect (Fig. **26H**). Also, TNFα , a considerable part of an apoptotic cascade showed a slight but significant increase in levels in pSer8Aβ, and pSer26Aβ treated cells (Fig. **26I**).

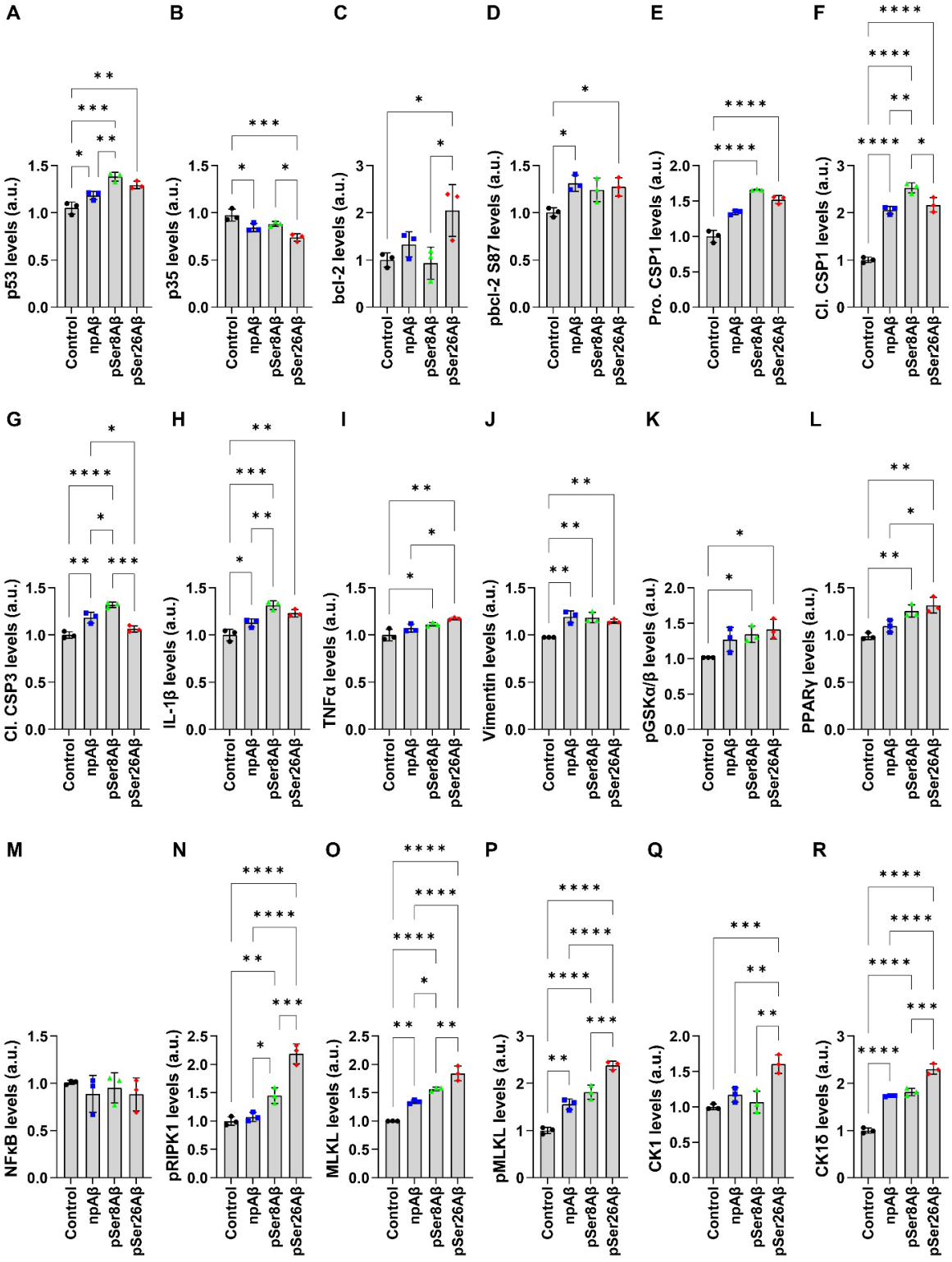

Fig. 26: pAβ differentially modulates cell death-associated pathways. A-R. Quantification of western immunoblot data of different proteins associated with apoptosis or necroptosis mediated cell death pathways from SH-SY5Y cells treated without (control) or with indicated Aβ variants (1 μM, 24 h) for. Values represent mean ± S.E.M.; n = 6, N

= 3. * $p < 0.05$; ** $p < 0.01$; *** $p < 0.001$; **** $p < 0.0001$; n.s. $p \geq 0.05$, not significant (One-way ANOVA, GraphPad Prism).

Treatment with either Aβ variants increased the expression of vimentin (Fig. **26J**), involved with caspases during apoptosis (Byun et al. 2001). pSer8Aβ and pSer26Aβ increased the expression of phosphorylated glycogen synthase kinase-3 beta (pGSK-3β, Fig. **26K**), a critical component in apoptosis along with regulation of a wide range of cellular functions. Treatment with npAβ did not induce a statistically significant effect. Similar effects of the different Aβ variants were observed for PPARγ (Fig. **26L**). However, NFκB levels were not significantly changed by either Aβ variant (Fig. **26M**). The necrosome complex, composed of phosphorylated proteins pRIPK1, pRIPK3, and pMLKL, is associated with neuronal loss in AD (Imbimbo et al., 2020; Schoor et al., 2020; Ré et al., 2014). Furthermore, the pMLKL is considered a marker for necroptosis, and its translocation to the plasma membrane is crucial for the execution of necroptosis (Wyczanska & Lange-Sperandio, 2020; Koper et al., 2019). The expression of both pRIPK1 as well as pMLKL, is increased in the presence of all Aβ variants, but pSer26Aβ had the strongest effect (Fig. **26N-P**). The role of CK1 in Wnt signaling suggests its potential involvement in regulating cell death pathways (Orrenius et al., 2003). Furthermore, CK1 has been linked to the regulation of key proteins involved in cell death pathways, such as p53 and MDM2, highlighting its potential impact on the control of cell fate. Here, the level of CK1 was significantly increased upon treatment with pSer26Aβ (Fig. **26Q**). Additionally, all Aβ species increased the expression of CK1 isoform δ, in particular, pSer26Aβ showed the strongest effect.

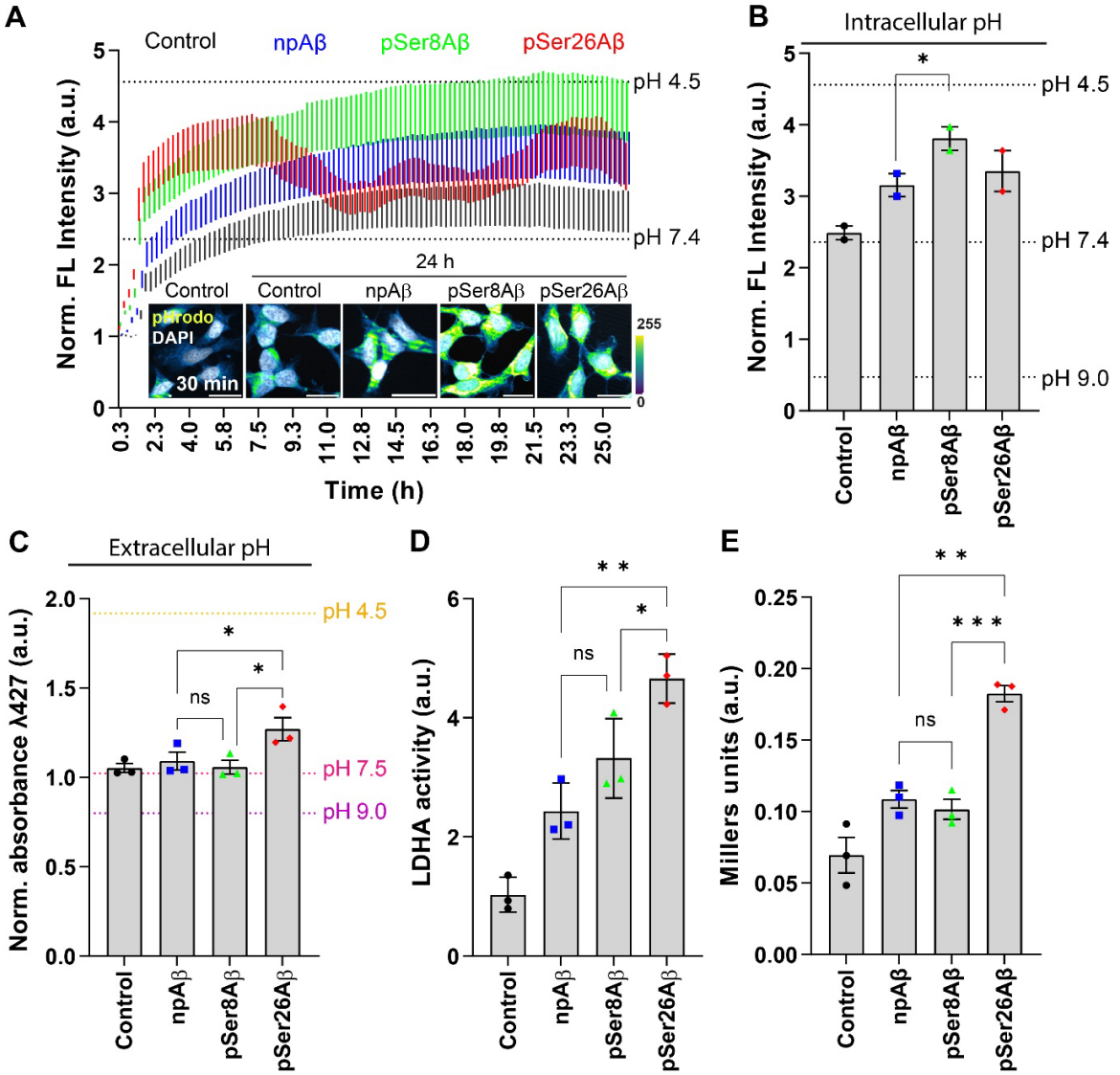

Fig. 27: Phosphorylation of Aβ differentially alters intracellular and extracellular pH dependent on lysosomal acidification. A-B. SH-SY5Y cells loaded with pHrodo red dye were treated in absence (control) or presence of indicated Aβ variants (1 μM, 24 h). Time-dependent change in the pHrodo dye fluorescence intensity was analyzed using a multi-well plate reader (λ_{Em} 590 nm), at regular intervals for 26 h. Readings were normalized to initial time point (0 h). Dotted line indicates the values of control cells with standard modulated pH, respectively. Readings are representative of two independent experiments. Inset depicts microscopy images of cells co-stained with DAPI (*gray*). Scale bar, 10 μm. Bar plot (**B**) showing change in fluorescence intensity of the pHrodo dye depict changed in intracellular pH (pH_i) in SH-SY5Y cells treated with different Aβ variants. Readings were normalized to initial time point (0 h) and values represent mean ± S.D.; n = 6, N = 2. **C**. Treatment media containing phenol red of SH-SY5Y cells treated with 1μM of Aβ variants, 24 h, were analyzed for the change in extracellular pH on a multi-well plate reader (λ_{abs} 427 nm). Dotted line indicates the standard values of culture media with standard modulated pH, respectively. Values represent mean ± S.E.M.; n = 12, N = 3. **D**. LDHA levels in cell lysates and treatment media of SH-SY5Y cells (control or 1 μM Aβ variants, 24 h) were analyzed via western immunoblotting. LDHA activity was computed

by analyzing the ratio of LDHA secreted in the supernatant *wrt* cell lysates, respectively. Values represent mean ± S.E.M.; n = 9, N = 3. **E**. SH-SY5Y cells treated without (control) or with different Aβ variants (1 μM, 24 h), were lysed and incubated with a fluorogenic substrate sensitive to β-galactosidase specific activity. Bar plots represent quantified values of cellular β-galactosidase specific activity (Miller's units) analyzed in a multi-well plate reader and quantified. Values represent mean ± S.E.M.; n = 9, N = 3. * $p < 0.05$; ** $p < 0.01$; *** $p < 0.001$; **** $p < 0.0001$; n.s. $p \geq 0.05$, not significant (One-way ANOVA, GraphPad Prism).

Another important aspect of regulated cell death is acidification of the intracellular milieu (Lagadic-Gossmann et al. 2004). Thus, the change in intracellular pH (pH_i) in SH-SY5Y cells loaded with pHrodo dye, was examined. First, pH modulators were used to establish standard pH values for comparison during the experiment. Aβ species induced differential effects on pH_i as compared control cells (Fig. **27A-B**). After 24 h, the pSer8Aβ-induced intracellular acidification is significantly strongest as compared to npAβ, but similar to that induced by pSer26Aβ. Notably, pSer26Aβ induced a steep increase in fluorescence intensity at the initial phase of the treatment, but then pH_i fluctuated over the time course. Such fluctuations were not observed with the other Aβ variants. These, and the previous observations with pSer26Aβ induced lysosomal acidification (Fig. **17**) prompted us to examine the possibility of leakage of lysosome-associated contents into extracellular space. Thus, conditioned media (containing phenol red as a pH indicator), were examined (Fig. **27C**), which were significantly acidified in the presence of pSer26Aβ as compared to other conditions. Moreover, lysosomes are involved in several types of cell death, including apoptosis and necroptosis (Yang et al., 2018). Additionally, lysosomal dysfunction and protease release have been implicated in a coordinated series of events that lead to necrotic cell death, highlighting the significance of lysosomes in this process (Prince et al., 2008). Lysosome regulated necrotic cell death could be one of the features contributing substantially to the case of pSer26Aβ induced cell death. Cells treated with pSer26Aβ showed significantly elevated levels of extracellular lactate dehydrogenase A (LDHA) and cellular β-galactosidase (β-gal) activity, indicating augmented expression of lysosomal proteolytic enzymes (Fig. **27G-H**). Results from cell supernatants/treatment media were comparable and did not show statistically significant differences.

Taken together, although the differences in effect sizes caused by the different Aβ species are relatively subtle, the combined data suggest that pSer8Aβ more potently induces apoptotic cell death, while pSer26Aβ induced cell damage also showed characteristics of

necroptosis. The present data indicate a phosphorylation-state specific effects of Aβ variants on distinct cell death pathways. Phosphorylation-site and state dependent differential modulation of cell death pathways could be a potential downstream effect of the previously discussed modulation of proteolytic degradation pathways and organelle dysfunction.

3.4. Neuron-to-microglia transfer of Aβ variants

3.4.1. Phosphorylation-state dependent accumulation of pAβ in microglia

Neurons are believed to be the major source of Aβ in brains. Secreted Aβ species are known to interact with and activate microglia resulting in neuroinflammation which facilitates neurodegeneration (Frigerio et al. 2021; Mandrekar et al. 2009; Leng and Edison 2021). pAβ variants and nmAβ species were examined via immunohistochemistry in the APP-PSEN1delE9 transgenic mouse model that was crossed with CX_3CR1-GFP transgenic mice to specifically label microglia (Tab. **1**, Fig. **28A-E** and Fig. **11A-E**).

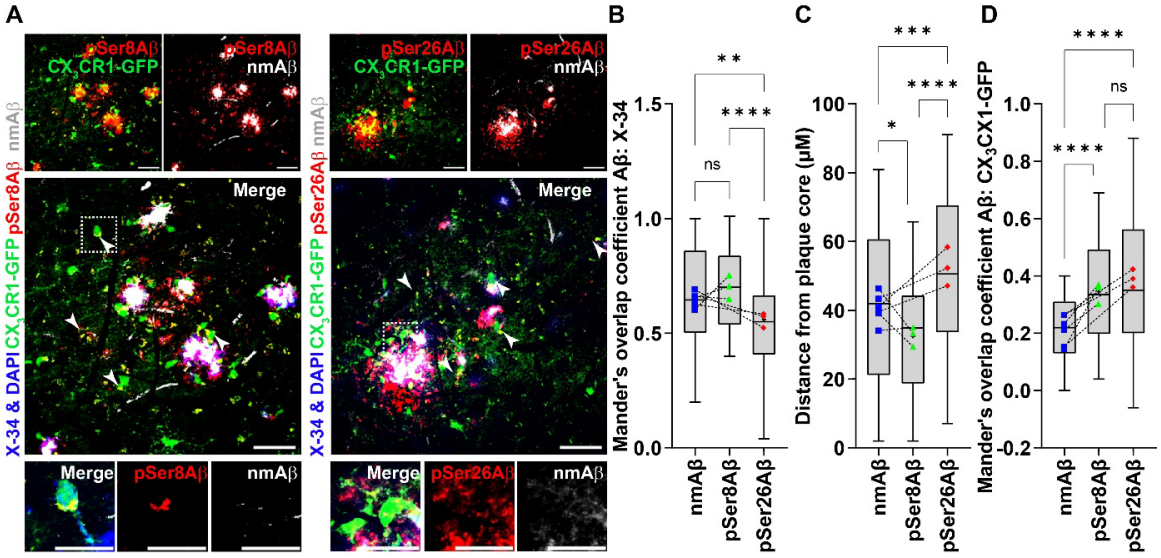

Fig. 28: Differential deposition of pAβ species within microglia in APP-PSEN1 transgenic mice. A-D. Immunohistochemistry (**A**) depicting differential intra and extracellular deposition of pSer8Aβ (1E4E11, *red*) and pSer26Aβ (5H11C10, *red*) compared to nmAβ (7H3D6, *gray*) in brain sections of APP-PSEN1delE9xCX_3CR1-GFP transgenic mouse cortex (14.2 m, female). Scale bar: 50 µm; zoomed panels, 10 µm. White arrowheads indicate colocalized punctate staining between red and gray channels in CX_3CR1-GFP positive microglia. Box plot (**B**) depicting Mander's coefficient of overlap between nmAβ (*A, gray channel*; *B, blue data points*), pSer8Aβ (*A, red channel*; *B, green data points*) and pSer26Aβ (*A, red channel*; *B, red data points*) with X-34 (plaque core, *blue channel*). Box plot quantification (**C**) shows association of nmAβ, pSer8Aβ and

pSer26Aβ species with Aβ plaque pathology. Distance from the plaque core was measured using Fiji ImageJ concentric circle processing module. Box plot (**D**) depicting Mander's coefficient of overlap between nmAβ (*blue data points*), pSer8Aβ (*green data points*) and pSer26Aβ (*red data points*) with respect to CX_3CR1-GFP positive microglia (*green channel*), respectively. Box plots depict the overall distribution of data, and each data point represents average values from an individual mouse, (B, C, n = ~100 cortical plaques), N = 3 transgenic mice. * $p < 0.05$; ** $p < 0.01$; *** $p < 0.001$; **** $p < 0.0001$; n.s. $p \geq 0.05$, not significant (One-way ANOVA, GraphPad Prism). Characterization of wild type (WT) and APP-PSEN1delE9xCX_3CR1-GFP transgenic mouse brain lysates, Aβ ELISA analyses in sucrose, SDS and FA fractions, along with antibody control staining are provided in Ext. Fig. **11**. SH-SY5Y and SIMA9 co-culture experiments have been enumerated in Ext Fig. **12**.

Similar to previous observations (Fig. **10A-D**), individual phosphorylated Aβ species *(red channels*, Fig. **28A**) showed differential deposition when compared to nmAβ (*gray channels*, Fig. **28A**) or to X-34 stained total fibrillar Aβ species (*blue channels*, Fig. **28A**). pSer8Aβ and nmAβ species are localized within the core of extracellular plaques containing X-34 positive fibrillar Aβ (Fig. **28B, C**). pSer26Aβ was rather detected around the plaque core with significantly lower colocalization with X-34. Interestingly, analyses of Mander's overlap coefficient revealed increased accumulation of both pAβ species within GFP positive microglia (Fig. **28D**). Thus, along with differential extracellular plaque-associated deposition, phosphorylated Aβ show increased accumulation within microglia. APP-PSEN1delE9xCX_3CR1-GFP mouse brains were further subjected to differential extraction and individual Aβ species detected by ELISA (Tab. **3b** and Ext. Fig. **11F**). Highest levels of total Aβ ($Aβ_{1-x}$) were detected in the FA soluble fraction containing plaque associated fibrillar material. Consistent with the accumulation of pSer8Aβ in the plaque core, this species was also abundant in the FA soluble fraction (Tab. **3b** and Ext. Fig. **11F**). Levels of Ser26Aβ were overall lower in sucrose, SDS and FA fraction. pSer8Aβ showed enrichment in the SDS (~2.3-fold) and FA fraction (~2.5-fold) as compared to the sucrose fraction, whereas pSer26Aβ species were enriched in sucrose soluble fractions (1.3-fold) compared to the SDS fractions, respectively.

3.4.2. Characterization of SH-SY5Y-APP_{Sw} stable transgenic cell lines

To investigate potential transfer of neuron-derived Aβ to microglia, SIMA9 (spontaneously immortalised primary microglia (Nagamoto-Combs et al. 2014)) were co-cultured with SH-SY5Y cells pre-treated with Aβ peptides, the Aβ content was examined via ICC (Ext. Fig.

12). Microglial cells showed association with all neuron derived Aβ variants. Levels of intracellular npAβ in both SH-SY5Y and SIMA9 cells were lower, which could be a result of increased metabolism/degradation of the peptide. On the other hand, levels of intracellular pAβ species were significantly higher in both cell types. In this experiment, observations for the pAβ variants were comparable to npAβ$_{42}$ treated conditions. Although this experiment showed differential uptake and clearance of Aβ peptides, the experiment had severe limitations. One major limitation is the amount of neuron-associated Aβ prior to microglial co-culture, e.g., the different amounts of the phosphorylation-state variants in neurons resulting from differential uptake or degradation of the species. This warranted the use of transgenic cell lines that over-express APP and secrete Aβ in extracellular media.

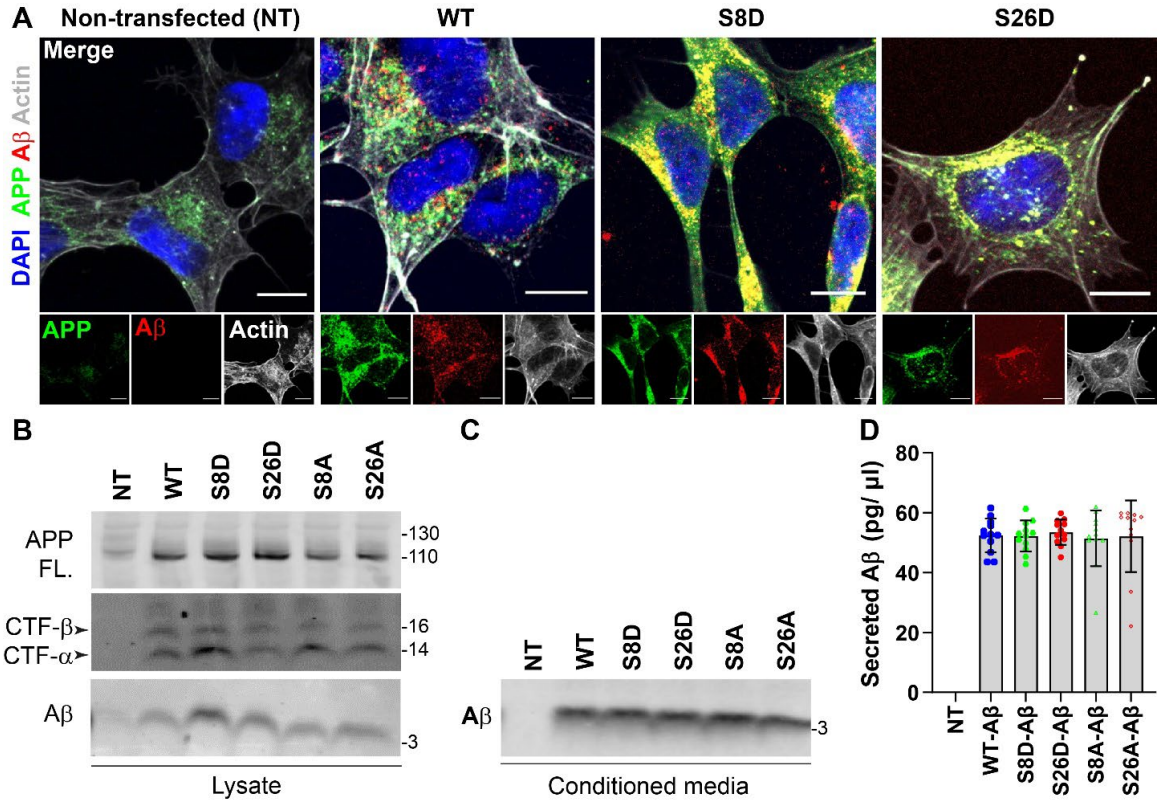

Fig. 29: Characterization of SH-SY5Y-APPSw transgenic cell lines. A-B. SH-SY5Y cells stably expressing wild type (WT-APPSw/Aβ), and pseudo-phosphorylated or non-phosphorylated versions (S8D/S8A- APPSw/Aβ and S26D/S26A- APPSw/Aβ) of amyloid precursor protein (APP695-Swedish mutation) were generated. Non-transfected (NT) cells contained mock DNA. Immunocytochemistry depicting the expression of APP and Aβ in SH-SY5Y-APP$_{Sw}$ cells (stable); stained with C-terminal specific APP antibody-140 and Aβ antibody 82E1, respectively. Cells were co-stained to visualize the nuclei (DAPI, *blue*) and cell membranes (phalloidin, *gray*), respectively. **C-D**. Western immunoblotting

analyses of cell lysates (**C**) showing expression of full-length APP, APP-CTFs and intracellular accumulated Aβ, non-transfected cells (NT) were used as control. Cell culture medium of the SH-SY5Y-APP_{Sw} transgenic cell lines was replaced with serum-free medium for secretion of Aβ for 24 h. Conditioned media was subjected to TCA precipitation and analyzed via WB (**D**). C-terminal specific APP antibody-140 antibody was used for detection of FL-APP and CTFs. Anti-$Aβ_{1-x}$ 82E1 antibody was used for detection of Aβ. **E.** Aβ levels in the conditioned media was also examined via indirect ELISA, normalized to the total cell amount and volume of the supernatant. Anti-Aβ 4G8 antibody was used as detection antibody. Values represent Mean ± S. E. M., N = 4, n = 12, * $p < 0.05$; ** $p < 0.01$; *** $p < 0.001$; **** $p < 0.0001$; n.s. $p \geq 0.05$, not significant (One-way ANOVA, GraphPad Prism)**.** All data and analyses depicted herewith is representative from four independent experiments consisting of three technical replicates. Stable cells were evaluated from different passage numbers and varying freeze thaw cycles. Additional ELISA characterization of $Aβ_{1-x}$, $Aβ_{x-40}$ and $Aβ_{x-42}$ and control experiments have been enumerated in Ext Fig. **13**.

Thus, SH-SY5Y-APP_{Sw} transgenic cells stably expressing wild type (WT- APP_{Sw}/Aβ), pseudo-phosphorylated and non-phosphorylatable versions (S8D/S8A- APP_{Sw}/Aβ and S26D/S26A- APP_{Sw}/Aβ) of amyloid precursor protein (APP695) with a Swedish mutation; were generated. The Swedish mutation (K595N-M596L) of amyloid precursor protein (APP_{Sw}) increases cleavage of cellular APP by β-secretase (BACE1), and thereby augment Aβ production (Mullan et al. 1992). SH-SY5Y-APP_{Sw} transgenic cells and conditioned media were examined for the expression of APP-FL, CTFs and Aβ using APP- and Aβ-specific antibodies via immunocytochemistry (Fig. **29A**), WB (Fig. **29B-C**) and ELISA (Fig. **29D** and Ext. Fig. **13**), respectively. SH-SY5Y-APP_{Sw} cells showed intracellular expression of APP, as well as APP-CTFs and Aβ. APP-full length, APP-CTF and Aβ was observed intravesicular compartments. In particular, the observed punctate staining in S8D-APP_{Sw}/Aβ and S26D-APP_{Sw}/Aβ variants, could be attributed to the vesicular accumulation/ trafficking deficits observed in the presence of pAβ / DAβ species. Serum free conditioned media contained secreted Aβ along with soluble APPα/β species (Ext. Fig. **13E**), further validating the transgenic cell culture model. Importantly, the mutations at the phosphorylation sites within the Aβ domain of APP did not significantly affect secreted and cellular Aβ levels. Additionally, treatment of the cells with β-secretase, γ-secretase modulators, shows a significant decrement in the levels of secreted Aβ content by ELISA (Ext. Fig. **13D).**

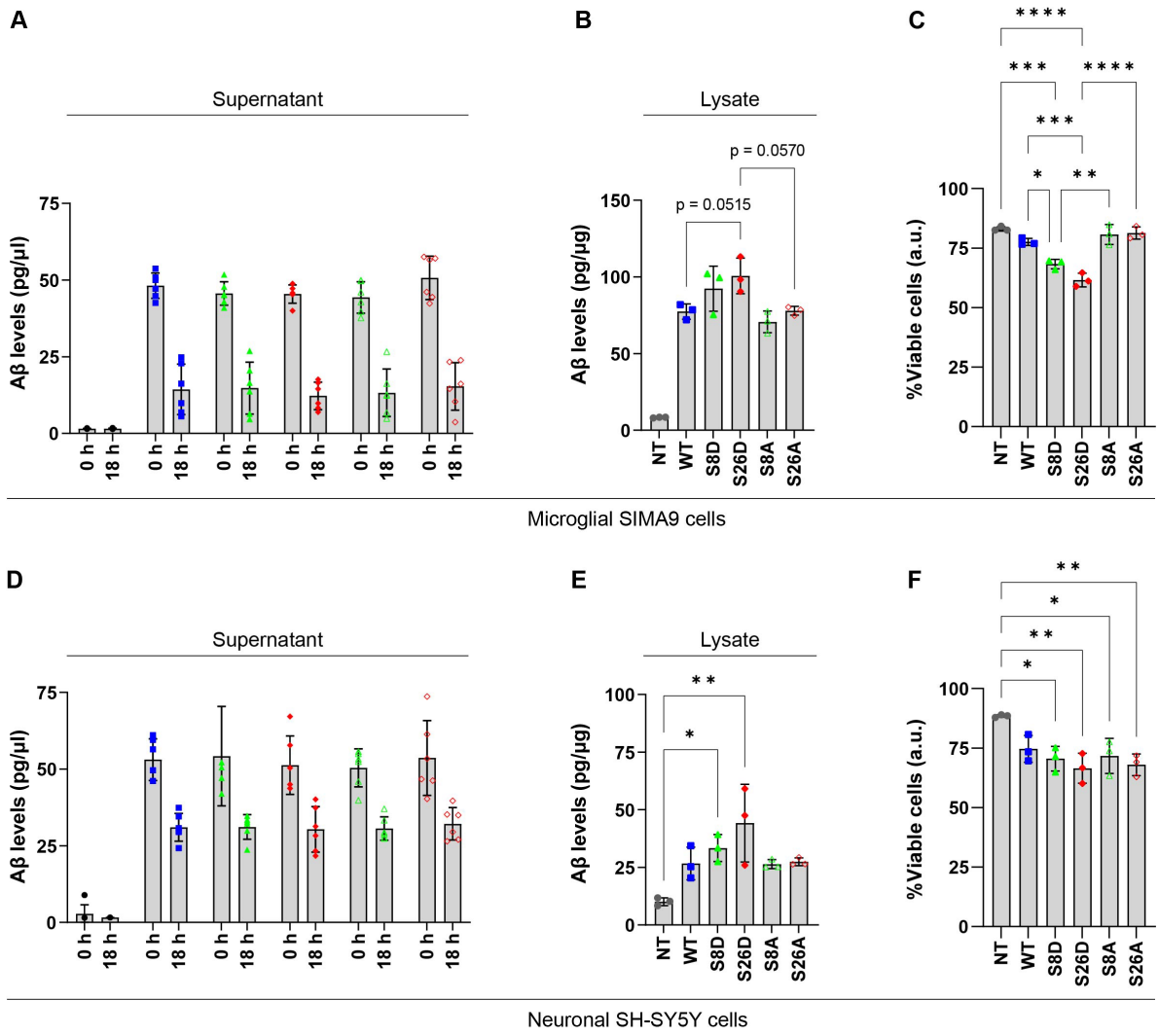

Fig. 30: Neuron-associated-DAβ uptake and cytotoxicity on neighboring cell types. A, B, D, E. Cell culture medium of SH-SY5Y-APP$_{Sw}$ cell variants was replaced with serum-free medium for secretion of Aβ for 24 h. Microglial (SIMA9, **A-C**) and neuronal (SH-SY5Y, **D-F**) cells were exposed to the SH-SY5Y-APP$_{Sw}$ cell conditioned media for 18 h. Aβ content in the conditioned media (pre-treatment - 0 and after treatment - 18 h; **A, D**) and cell lysates (**B, E**) were examined via indirect ELISA. Readings were normalized to total cell protein levels and expressed as pg/µl (supernatant) or pg/µg (cell lysate), respectively. Anti-Aβ antibody 82E1 was used for detection of Aβ. Values represent Mean ± S. E. M., n = 6, N = 3, (Two-way ANOVA, GraphPad Prism). **C, F.** Cell viability of microglial (SIMA9, **C**) and neuronal (SH-SY5Y, **F**) cells treated with SH-SY5Y-APP$_{Sw}$ cell conditioned media for 18 h, was evaluated using Presto Blue cell viability reagent. Values were normalized to control untreated cells with respective growth media. Values represent Mean ± S. E. M., n = 9, N = 3, (One-way ANOVA, GraphPad Prism). * $p < 0.05$; ** $p < 0.01$; *** $p < 0.001$; **** $p < 0.0001$; n.s. $p \geq 0.05$, not significant.

Serine to aspartic acid (S→D) substitutions can mimic phosphorylation, while serine to alanine substitutions (S→A) APP$_{Sw}$/Aβ conditions were also generated and characterised

to compare the effect of site- and state- specific Aβ phosphorylation to eliminate any artefacts resulting from differential APP processing. Non-phosphorylatable S→A APP_{Sw}/Aβ variants showed comparable and similar effects to that of the WT-APP_{Sw}/Aβ variant. Furthermore, comparable results were obtained when cell lysates and conditioned media were examined for APP-FL, CTFs and Aβ levels, respectively, across different cell passage numbers and freeze-thaw cycles, depicting stable APP expression (Ext. Fig. **13**).

3.4.3. Cell-to-cell transfer of DAβ species

Cell-to-cell transfer of Aβ can be mediated by several processes (Armingol et al. 2021). To characterize the neuron-to-microglia or neuron-to-neuron transfer of Aβ, respectively, conditioned media of the different APP transgenic SY5Y cells were transferred to, SIMA9 and neuroblastoma SH-SY5Ycells, respectively (Domert et al. 2014). ELISA of Aβ in media showed that exposure to SIMA9 cells resulted in a strong decrease in Aβ levels after 18 h (Fig. **30A**). Aβ levels in the conditioned media also decreased upon incubation with SH-SY5Y cells, but to a lower extent as compared to SIMA9 cells (Fig. **30D**). Almost three-fold increase in the cell-associated Aβ levels were detected in SIMA9 cells when compared to SH-SY5Y cells. The levels of cell-associated DAβ variants were significantly higher (Fig. **30E**) in SH-SY5Y cells. A similar trend was also seen with microglial cells, but the values were beyond the set limits of statistical significance (Fig. **30B**). Exposure to conditioned media containing the pseudo-phosphorylated DAβ variants impaired cell viability, with S26D Aβ containing media having strongest effect. Media containing WT Aβ or the S8A or S26A Aβ variants had no significant effect on viability of SIMA9 cells (Fig. **30C, F**). The differences in S8D Aβ, and particularly S26D Aβ, induced cytotoxicity in SIMA9 cells were statistically significant to non-modified WT Aβ species. Although a similar trend was also seen for the viability of SH-SY5Y cells, the differences were statistically significant only to the NT condition. The data showed that Aβ present in SH-SY5Y-APP_{Sw} cell conditioned media associates with microglial as well as neuron-like cells, wherein microglial cells showed higher intracellular accumulation probably due to phagocytosis, leading to Aβ induced cytotoxicity. A small fraction of Aβ species can be associated with exosomes (Sardar Sinha et al. 2018) that could contribute to propagation of Aβ pathology and the pathogenesis of AD (Rajendran et al. 2006; Xu et al. 2018; Sardar Sinha et al. 2018; Perez-Gonzalez et al. 2012).

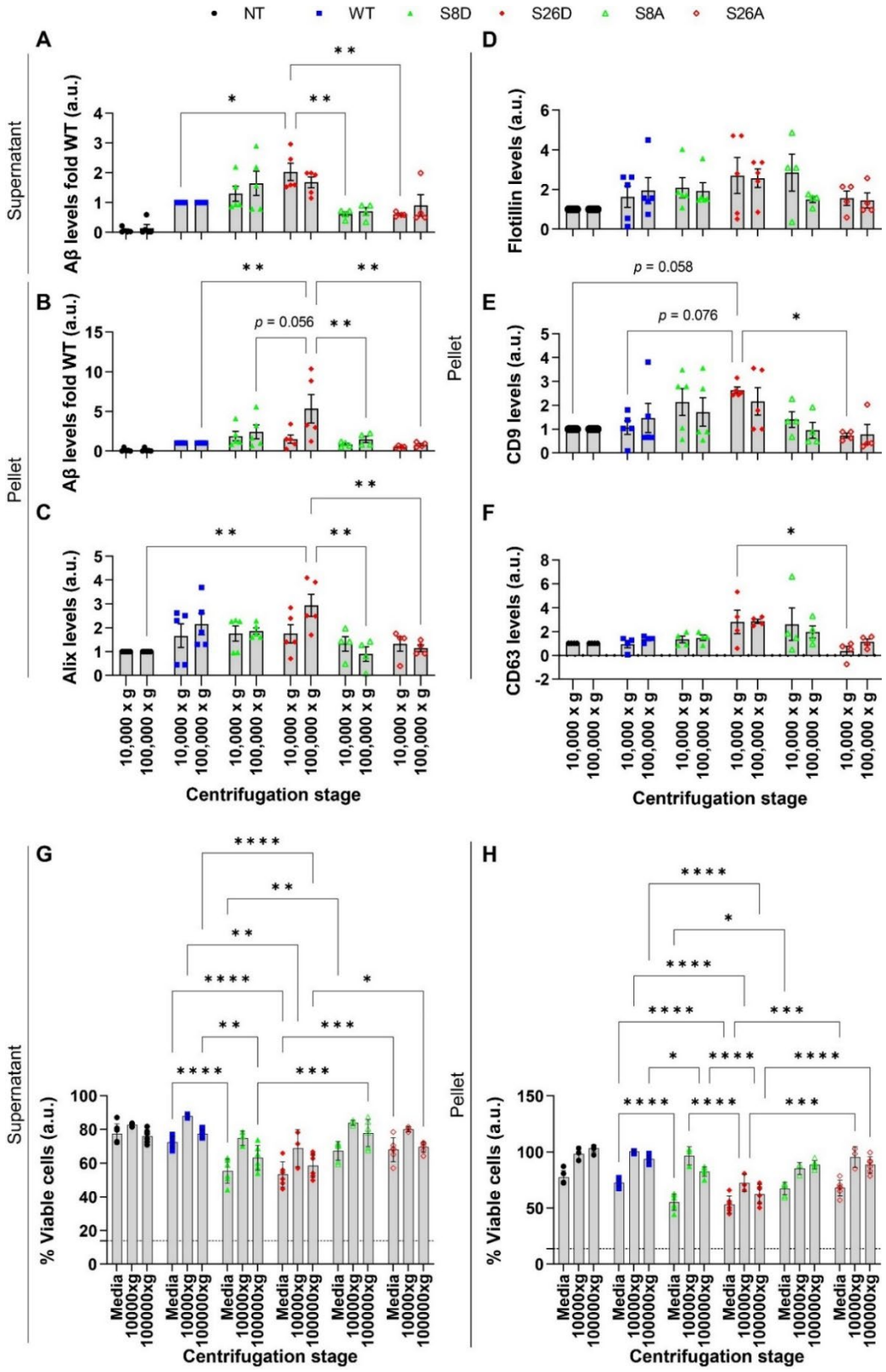

Fig. 31: Exosomal mediated neuron-to-microglia Aβ transfer is associated with S26D Aβ associated cytotoxicity. Cell culture medium of SH-SY5Y-APP$_{Sw}$ cell variants was replaced with serum-free medium for secretion of Aβ for 24 h. Conditioned media was

further subjected to differential centrifugation steps to enrich crude exosomes at 10,000 *g* and 100,000 *g* fractions. **A-F.** Densitometric analyses of western immunoblotting of Aβ content and different exosomal markers isolated via differential centrifugation of the conditioned media from APPSw stable cells. Bar plots depicting relative expression of Aβ in supernatant fraction (**A**) and pellet fraction (**B**). Exosomal markers like Alix/AIP1 (**C**), Flotillin-1 (**D**), tetraspanin proteins, CD9 (**E**) and CD63 (**F**) in 10,000 *g* and 100,000 *g* pellet fractions, respectively. Readings were normalised to either WT Aβ (A-B) or NT (C-F) and depicted as fold change respectively. Values represent Mean ± S. E. M., n = 6, N = 3, (Two-way ANOVA, GraphPad Prism). **G-H.** Supernatant and pellet fractions post-differential centrifugation at 300 *g* (media), 10,000 *g* and 100,000 g; were further used to treat microglial SIMA9 cells for 18 h. Cell viability was then evaluated using Presto Blue cell viability reagent. Readings were normalized to untreated cell control and depicted as percent change number of viable cells. Values represent Mean ± S. E. M., n = 6, N = 2, (One-way ANOVA, GraphPad Prism). * $p < 0.05$; ** $p < 0.01$; *** $p < 0.001$; **** $p < 0.0001$; n.s. $p \geq 0.05$, not significant. Cytotoxicity evaluation of SH-SY5Y cells treated with differentially fractionated conditioned media has been depicted in Ext. Fig. **14**.

Here, the potential involvement of exosomes in secretion and uptake of Aβ species in this cell models was examined (Sharma et al. 2013; Pegtel et al. 2014). Exosomes were enriched from conditioned media by differential centrifugation and characterised for the expression of exosome-associated proteins and Aβ content (Fig. **31A-B**). Notably, S26D Aβ is selectively enriched in exosomal fractions, wherein exosome-associated proteins such as Alix/AIP1, FLOT-1, tetraspanin proteins, CD9 and CD63 are also detected (Fig. **31C-F**). Exosome enriched fractions from WT-APP_{Sw} and in particular S26D-APP_{Sw} cells, showed increased levels of lysosomal membrane proteins (LAMP-1, Ext. Fig. **14A**), potentially indicating mechanisms involving lyso-exocytosis (Buratta et al. 2020), a process of secreting lysosomal material into the extracellular milieu. Indeed, pSer26Aβ (and npAβ to a minor extent) induced lysosomal defects in cells were previously demonstrated (Fig **14**, **17**).

SIMA9 or SH-SY5Y cells treated with exosome enriched fractions (100,000 *g* pellet) showed that both DAβ species (S26D Aβ > S8D Aβ) exerted higher cytotoxicity (Fig. **31G-H** and Ext. Fig. **14B-C**). For a complete comparative analyses, exosome depleted (100,000 *g* supernatant) and 10,000 *g* fractions (supernatant and pellet) were also used as treatment conditions. When comparing the different variants with respect to an independent traction, S26D Aβ present in the exosome-enriched fractions induce

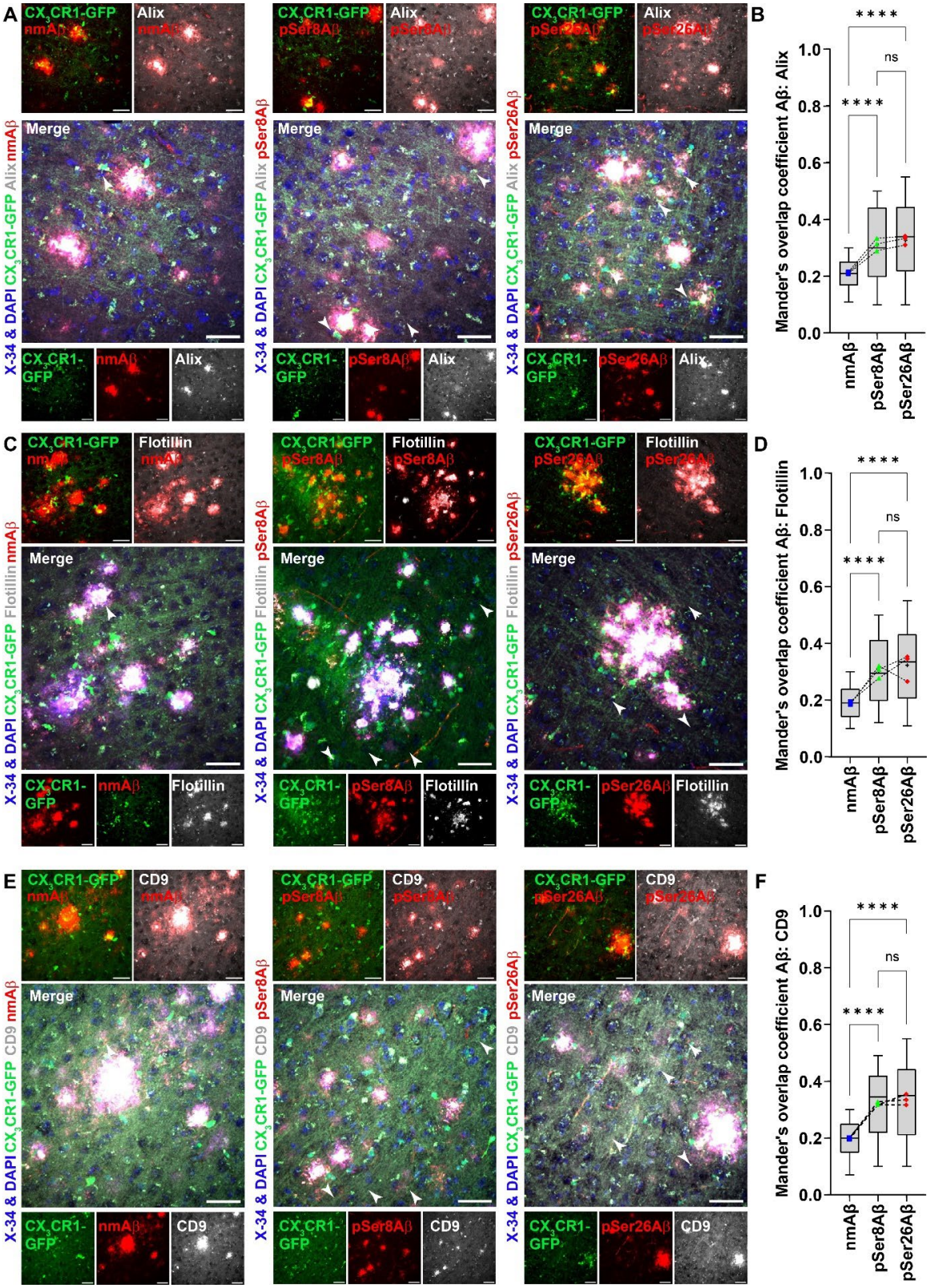

Fig. 32: Association of pAβ with exosomal marker proteins in APP/PS1 transgenic mice. A-F. Immunohistochemical staining (**A, C, E**) depicting colocalization of Aβ species in brain sections of APP-PSEN1delE9xCX_3CR1-GFP transgenic mouse cortex (12.2 m, A

or 14.2 m, C, E female) stained with different phosphorylation state specific Aβ antibodies (nmAβ- 7H3D6, pSer8Aβ- 1E4E11 and pSer26Aβ- 5H11C10; *red channels respectively*) along with antibody against Alix (*gray,* **A**), Flotillin-1 (*gray,* **C**) or CD9 (*gray,* **E**). DAPI + X-34 were used to stain nuclei and plaque core (*blue*), respectively. Scale bar: 50 µm. White arrowheads indicate colocalized punctate staining between red and gray channels in CX_3CR1-GFP positive microglia. Box plot (**B, D**) depicting Mander's coefficient of overlap between red channels (npAβ, *blue*; pSer8Aβ, *green* and pSer26Aβ, *red data points*) with respect to gray channels (Alix, **B**, Flotillin-1, **D** and CD9, **F**), quantified within CX_3CR1-GFP positive microglia, respectively. Box plot depicts the overall distribution of data, and each data point represents average values from an individual mouse, N = 3 transgenic mice. * $p < 0.05$; ** $p < 0.01$; *** $p < 0.001$; **** $p < 0.0001$; n.s. $p \geq 0.05$, not significant (One-way ANOVA, GraphPad Prism).

significantly higher cytotoxicity as compared to other conditions. Previously published reports showed that exosome-associated proteins were found to accumulate in the plaques of AD patient brains (Rajendran et al. 2006). Immunohistochemical analyses of APP-PSEN1delE9xCX_3CR1-GFP transgenic mice (Fig. **32**) with phosphorylation state specific Aβ antibodies, indeed showed the presence of exosomal proteins such as Alix, FLOT-1 and CD9 in extracellular plaque pathology. Along with extracellular plaque decoration, these protein/markers also colocalized with pAβ species within GFP positive microglia (*Mander's overlap coefficients*, Fig. **32B, D, F**). Taken together, along with the uptake of extracellular pools of Aβ (non-exosome associated), exosome mediated transfer of neuronally derived pAβ species may play a role as they have shown to have an effect on microglial (or neuronal) cells. Additionally, immunohistochemical observations support previous inferences, that exosome associated phosphorylated Aβ peptides, especially pSer26Aβ, interact with neighboring microglial cells. These inferences suggest that understating and dissecting the key mechanisms and differences could help to elucidate the contribution of pAβ pathology and microglial dysfunction in AD.

3.4.4. Differential effects of Aβ variants on microglial cells

Microglial response to Aβ is arguably the major source of cytokines contributing to neuroinflammation in AD (Heneka et al. 2015; Boon et al. 2018; Leng and Edison 2021). To examine the effect of phosphorylation state of Aβ in microglial associated inflammation pathways, the levels of pro-inflammatory markers IL-1β, TNFα and anti-inflammatory markers IL-10, IL-4 upon exposure of SIMA9 microglial cells to SH-SY5Y-APP_{Sw} cell conditioned media, were analyzed (Fig. **33A-D**).

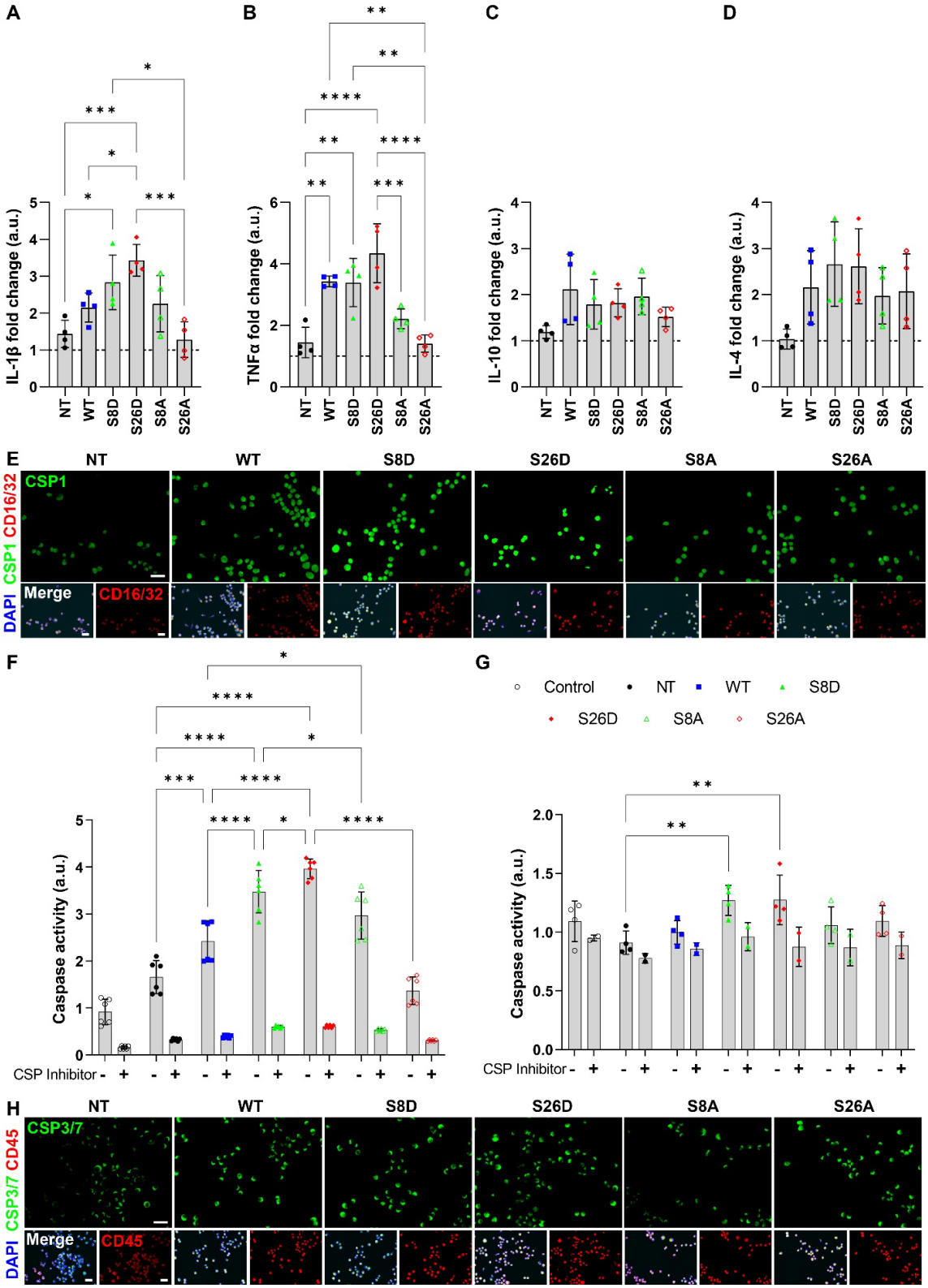

Fig. 33: Aβ transfer during neuron-to-microglia cross talk induces inflammatory response in microglial SIMA9 cells. A-D. SIMA9 cells were treated with SH-SY5Y-APP$_{Sw}$ cell conditioned media for 18 h. After treatment, pro-inflammatory markers IL-1β (**A**), TNFα (**B**) and anti-inflammatory markers IL-10 (**C**), IL-4 (**D**) were analyzed using in-

house ELISA method. Readings were normalized initial values before culturing with SIMA9 cells and then with respect to control untreated cells (*dotted line*) and represented as fold-change *wrt* control. Values represent Mean ± S. E. M., A-B, n = 12, N = 4; C-D, n = 8, N = 4, (One-way ANOVA, GraphPad Prism). **E.** Microscopy images depicting the Caspase-1 activity (*green channel*) in SIMA9 cells treated with SH-SY5Y-APP$_{Sw}$ cell conditioned media for 18 h. After treatment, SIMA9 cells loaded with Caspase-1 specific fluorescent substrate (*green channel, above panel*), co-stained with CD16/32 (*red channel*) and DAPI (*blue channel*) to visualize the nuclei. Merged and red channel image has been shown below. Images are representative of two independent experiments. **F, G.** SIMA9 cells after treatment with conditioned media from APPSw stable cells for 18 h (**F**) or APPSw stable cells themselves (**G**) were lysed in caspase assay buffers and were treated with fluorogenic substrate to measure the caspase 1, 4 and 5 specific activities. 10μM vYAD was used as an internal control to inhibit caspase activity. Readings were normalized to untreated cells (control); and depicted as fold change *wrt* control cells. Values represent mean ± S.E.M.; F, n = 22, N = 6; G, n = 12, N = 4; (Two-way ANOVA, GraphPad Prism). **H.** Microscopy images depicting the Caspase-3/7 activity (*green channel*) in SIMA9 cells treated with SH-SY5Y-APP$_{Sw}$ cell conditioned media for 18 h. After treatment, SIMA9 cells loaded with Caspase-3/7 specific fluorescent substrate (*green channel, above panel*), co-stained with CD45 (*red channel*) and DAPI (*blue channel*) to visualize the nuclei. Merged and red channel image has been shown below. Results are representative of two independent experiments. * $p < 0.05$; ** $p < 0.01$; *** $p < 0.001$; **** $p < 0.0001$; n.s. $p \geq 0.05$, not significant. Additional controls experiment with synthetic Aβ peptide treatment on SIMA9 cells have been summarized in Ext Fig. **15**.

An increase in the levels of pro-inflammatory markers is seen with WT (non-significant) and DAβ conditioned media (significant), but S26D Aβ showed the strongest effect. Analysis of the conditioned media from SH-SY5Y-APP$_{Sw}$ cells before the transfer to microglial cells also revealed significant differences in TNFα, IL-10 and IL-4 levels, specifically for DAβ secreting cell variants (Ext. Fig. **15E-H**). It is important to note that these changes were smaller as compared to that detected upon additional incubation of microglial cells. Also, to negate these differences, the readings for after treatment in microglial cells were normalised to the initial levels in each condition. Subsequently, anti-inflammatory markers IL-4 and IL-10 in conditioned media upon incubation with SIMA-9 cells were not significantly different but tended to be higher in Aβ containing media. An increasing trend in the expression of anti- inflammatory markers in all SY5Y-APP$_{Sw}$ cell conditioned media is observed, but the effects are not statistically significant when incubated with microglial cells. A similar trend and comparable results were also obtained when with SIMA9 and SH-SY5Y cells were treated with synthetic Aβ phosphorylation-state specific variants, respectively (Ext. Fig. **15A-D**).

The maturation and secretion of pro-inflammatory cytokines such as IL-1β is triggered by maturation of caspases. Thus, SIMA9 cells exposed to SH-SY5Y-APP_{Sw} cell conditioned media were examined for their intrinsic caspase activities by fluorescence microscopy (CSP1, Fig. **33E**; CSP3/7, Fig. **33H**). WT Aβ conditioned media significantly augmented CSP1 activity of microglial cells, but treatment with DAβ conditioned media showed even higher significant elevation as compared to other tested conditions (Fig. **33E** -CSP1, WT: 1.48 ± 0.24; S8D: 2.08 ± 0.31; S26D: 2.11 ± 0.47; fold change *wrt* control). Also, CSP-1, 4 and 5 sensitive fluorogenic substrate exposed to respective SIMA9 cell lysates in presence and absence of CSP inhibitors showed significantly augmented caspase activity in DAβ treatment conditions (Fig. **33F**). When comparing the DAβ variants together, S26D Aβ showed the strongest effect. In comparison to the microglial caspase activation capacity of the respective conditioned media, SH-SY5Y-APP_{Sw} cell lysates also showed lower but significant activity with both DAβ cell variants (Fig. **33G**). Activation of caspase 3/7 (CSP3/7, Fig. **33H**) demonstrates the ability of Aβ conditioned media, particularly the DAβ, to induce apoptosis mediated microglial cell death. Here, the effects induced by S8D Aβ were higher as compared to S26D Aβ, but the differences are not statistically significant (Fig. **33H** -CSP3/7, WT: 1.24 ± 0.14; S8D: 1.87 ± 0.25; S26D: 1.78 ± 0.21; fold change *wrt* control). Additionally, CD16/32 and CD45 as a marker to examine the activation of microglia in response to external stimuli (here Aβ) was also co-stained. In comparison to the controls and WT Aβ conditioned media, both the DAβ variants showed the strongest effect, but no significant differences were observed between the individual phosphorylation-state specific variants. In summary, exposure to SH-SY5Y-APPSw cell conditioned media caused caspase activation in SIMA9 cells, wherein both DAβ variants displayed strongest effects.

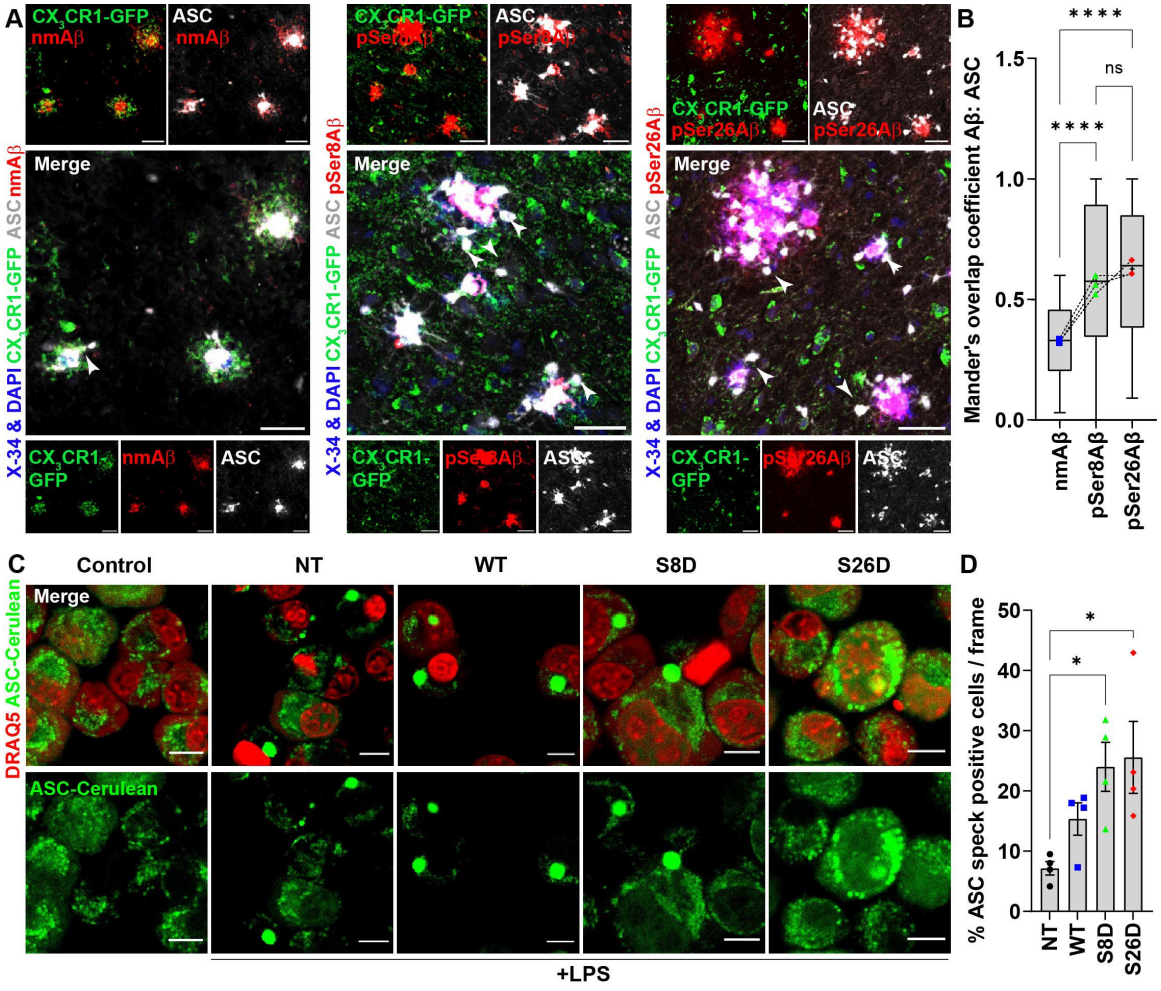

Fig. 34: Differential deposition of pAβ with apoptosis-associated speck-like protein (ASC) and inflammatory response in APP-PSEN1delE9-CX3CX1-GFP transgenic mouse model. A-B. Immunohistochemical staining (**A**) depicting colocalization of Aβ species in brain sections of APP-PSEN1delE9xCX$_3$CR1-GFP transgenic mouse cortex (14.2 m, female) stained with different phosphorylation state specific Aβ antibodies (nmAβ- 7H3D6, pSer8Aβ- 1E4E11 and pSer26Aβ- 5H11C10; *red channels respectively*) along with antibody against apoptosis-associated speck-like protein containing CARD - N-terminal ASC- AL177 (ASC, *gray,* **A**) along with DAPI + X-34 to stain nuclei and plaque core (*blue*), respectively. Scale bar: 50 µm. White arrowheads indicate colocalized punctate staining between red and gray channels in CX$_3$CR1-GFP positive microglia. Box plot (**B**) depicting Mander's coefficient of overlap between red channels (npAβ, *blue*; pSer8Aβ, *green* and pSer26Aβ, *red data points*) with respect to gray channels (ASC), quantified within CX$_3$CR1-GFP positive microglia, respectively. Box plot depicts the overall distribution of data, and each data point represents average values from an individual mouse, N = 3 transgenic mice. **C-D.** Immunocytochemical analyses (**C**) of SIMA9 cells expressing ASC-Cerulean reporter construct treated with SH-SY5Y-APP$_{Sw}$ cell conditioned media for 18 h in the presence of lipopolysaccharides (LPS: 2.5 ng/µl-priming; 100 ng/µl-positive control, 18 h). . Control represents untreated cells. After treatment, cells were co-stained to visualize the nucleus (DRAQ5, *red*). Scale bar, 10 µm. Green channel has been shown in the lower panel. Bar plot (**D**) depicts ASC speck occurrence per frame

was quantified by analyzing the number ASC specks to the number of cells per frame. Values represent mean ± S.E.M.; n = 4, N = 2. * $p < 0.05$; ** $p < 0.01$; *** $p < 0.001$; **** $p < 0.0001$; n.s. $p \geq 0.05$, not significant (One-way ANOVA, GraphPad Prism). Additional controls experiment in absence of LPS or with synthetic Aβ peptide treatment on have been depicted in Ext Fig. **16**.

Several recent reports indicate that the assembly of the multi-protein complex known as the NOD, LRR, and pyrin-domain containing 3 (NLRP3) inflammasome in microglia results in the formation of apoptosis spec-like protein containing a CARD (ASC) “specks” (Barczuk et al. 2022; Hulse and Bhaskar 2022), that promote seeding and spreading of Aβ pathology in mouse models of AD (Venegas et al. 2017). Thus, the colocalization of pAβ species with ASC proteins within GFP positive microglia of APP-PSEN1delE9xCX_3CR1-GFP transgenic mice, was examined (Fig. **34A-B**). Mander’s coefficient of overlap depicted increased colocalization of pSer8Aβ and pSer26Aβ species and ASC proteins in GFP positive microglia, as compared to nmAβ species. Next, ASC spec formation was analyzed in SIMA9 cells expressing ASC-Cerulean reporter (Stutz et al. 2013) upon incubation with SH-SY5Y-APP_{Sw} cell conditioned media. ASC-Cerulean expressing SIMA9 cells were microscopically examined for their propensity to form ASC “speck” as a readout for inflammasome activation (Fig. **34C-D** and Ext Fig. **16A**). Initial experiments with only conditioned media showed no significant effects of WT-, DAβ containing media with respect to untreated or NT controls. Thus, cells were primed with low concentration of LPS (2.5 ng). Priming with LPS augmented relative occurrence of ASC speck formation, but significantly increased in the presence of Aβ containing conditioned media, in particular the DAβ variants (Ext. Fig. **16A**). Similar effects on SIMA9 reporter cell line were caused by synthetic Aβ phosphorylation-state variants (Ext. Fig. **16B**), although the effects were less statistically significant. These observations indicate that, in comparison to the non-phosphorylated Aβ peptides, DAβ peptides augment microglial caspase activation and contribute to microglial induced neuroinflammation. Furthermore, inflammasome activation as well as ASC speck formation, could contribute to/ or additionally nucleate new Aβ plaques, thus amplifying DAβ-associated pathology in AD.

4. Discussion

4.1. Interaction of soluble oligomeric assemblies of phosphorylated Aβ with cellular membranes increases its cytotoxicity

Aggregation of Aβ plays an important role in the pathophysiology and the progression of AD (Bharadwaj et al. 2009; Penke et al. 2017; Finder and Glockshuber 2007; Rijal Upadhaya et al. 2014). npAβ upon aggregation showed the classical appearance of β-sheet rich fibrillar aggregates which were insoluble in nature (Fig. **6A-B**; **7A**, **D**; **8A**, **D**, **G**, **J**, **K**; Ext. Fig. **1A**). Evaluating the cytotoxic potentials of aggregated and non-aggregated species showed that npAβ peptide in monomeric/soluble form or lower molecular weight aggregates (e.g. dimers, trimers, etc.) as well as intermediate weight oligomeric species exert slightly higher toxicity as compared to the npAβ insoluble aggregated (higher molecular weight) fibrillar counterpart (Fig. **6D**, **7G**). These observations fall in line with previously published reports that suggest soluble intermediate oligomers, rather than fully formed fibrils, may be responsible for Aβ induced toxicity (Kayed et al. 2004; Sengupta et al. 2016; Walsh and Selkoe 2007; Salahuddin et al. 2016; Cecchi and Stefani 2013; Tay et al. 2013).

Phosphorylation is an important type of post-translation modification of a peptide or protein, which has been shown to change their intrinsic biophysical properties (Csizmok and Forman-Kay 2018). Phosphorylation of proteins, particularly tau and Aβ, plays a crucial role in the pathogenesis of AD (Chung 2009). The first part of this thesis delves into how phosphorylation alters Aβ oligomerization, the interaction with cellular membranes, and the potential effects on toxicity in cell culture models. Phosphorylation of serine residue 8 (pSer8Aβ) or 26 (pSer26Aβ) differentially affects the aggregation of Aβ (Rezaei-Ghaleh et al. 2016a; Kumar et al. 2011; Kumar et al. 2016). When compared with npAβ, phosphorylation at serine residue 8 augments aggregation propensity and results in the formation of β-sheet rich high molecular weight assemblies (Fig. **6A-C**; Ext. Fig. **1-2**; Kumar et al. 2011). Higher molecular weight aggregates formed by pSer8Aβ are oligomeric in nature and show enhanced solubility with respect to npAβ peptide (Fig. **7**-**8**; Ext. Fig. **2**). This feature could contribute to the detrimental impact on cell viability when compared with npAβ species, respectively (Fig. **6**-**7**; Ext. Fig. **2**; Kumar et al. 2011; Kumar

and Walter 2011). On the other hand, pSer26Aβ which preferentially only forms soluble oligomeric species (intermediate molecular weight as compared to fibrillar npAβ and soluble HMW oligomeric pSer8Aβ; Fig. **6**-**8**; Ext. Fig. **1**-**2**), showed maximum cytotoxicity in cell culture models (Kumar et al. 2016). A clear correlation was seen in the changes of intracellular Ca^{2+} flux measured in cells treated with either pre-aggregated or non-aggregated Aβ species, wherein phosphorylated Aβ peptides have significantly higher impact on disrupting cellular homeostasis (Fig. **6E-G**). Thus, it would be safe to assume that a balance between the solubility and aggregation of Aβ peptide is crucial for triggering cellular dysfunction. It could be hypothesized that the presence of a phosphoryl group within the Aβ peptide sequence, plausibly modulates their folding landscape, which in turn alters their aggregation states/propensity, and increases their solubility, subsequently impacting cell viability.

Numerous studies have demonstrated that Aβ species, in particular the soluble oligomeric (AβO) have a detrimental effect on cellular membranes (Ferreira et al. 2007; Bharadwaj et al. 2018; Zaretsky and Zaretskaia 2021a; Andreasen et al. 2015; Gibson Wood et al. 2003; Kakio et al. 2004; Niu et al. 2018; Teixeira et al. 2012). AβO species have been shown to disrupt the integrity and functionality of neuronal membranes, leading to synaptic dysfunction and neuronal loss (Pigino et al. 2009; Arbel-Ornath et al. 2017; Klein 2006; Lacor et al. 2004; Li and Selkoe 2020; Selkoe 2008b; Shankar et al. 2007; Takahashi et al. 2004; Tomiyama et al. 2010). The interaction of Aβ with lipid entities is a dynamic process which facilitates its attachment to cellular membranes and its subsequent internalization. The β-sheet conformation of Aβ, its interaction with cholesterol, and its ability to form pores in neuronal membranes could contribute to Aβ-induced neurotoxicity (Wang et al. 2022; Andreasen et al. 2015; Di Scala et al. 2014; Friedman et al. 2009). It could be hypothesized that along with increased oligomerization propensity of pAβ, the phosphoryl-moiety present in pAβ species provides an additional feature for their interaction with phospholipids, gangliosides, and cholesterol as well as receptors or proteins within the cell membrane leaflet. Furthermore, these interactions could lead to membrane destabilization and disruption of different membrane-associated processes. Studies have shown that Aβ aggregates interact preferentially with cholesterol and ganglioside-containing raft-like membranes. On the other hand, different lipids play a role

in altering the conformational transition of Aβ, modulating the aggregation process (Fabiani and Antollini 2019; Friedman et al. 2009; Lai and McLaurin 2010; Matsuzaki 2007; Niu et al. 2018). Additional studies using advanced computational simulation models to fully understand the effect of phosphorylation and its differential interaction with the lipid bilayer and its specific components would be required to understand their complex interplay. In both, non-aggregated and aggregated state, the pAβ variants showed increased interaction with cellular membranes (Fig. **9**, **10**). Since pAβ peptides preferentially forms soluble oligomeric assemblies during aggregation, this characteristic could facilitate their interaction with membrane-associated lipids and proteins, augmenting their internalization within cells. Thus, the increased cytotoxicity exerted by pAβ species could be dependent on their increased solubility (Fig. **6D**, **G**; **7G**, **H**, **I**; **9A-C**).

The internalization of Aβ species into cells is a complex process that involves various mechanisms, including and receptor-mediated endocytic uptake. Cholesterol present within the plasma membrane has been previously shown to facilitate the interaction of oligomeric Aβ species at the membrane surface, and accelerate intracellular uptake via receptor mediated endocytosis (Di Scala et al. 2014; Gibson Wood et al. 2003; Rodal et al. 1999; Refolo et al. 2001; Sponne et al. 2004). As seen before, exogenously added pre-aggregated or non-aggregated DAβ species showed higher intracellular accumulation than npAβ (Fig. **9D-G**). When the relative levels of cholesterol in the plasma membrane are pharmacologically lowered by β-MCD, the levels of intracellular DAβ were reduced, especially for the aggregated forms. It is also important to note that along with lowering the levels of membrane cholesterol, the treatment with β-MCD could also affect the membrane bound Aβ pools, which would need further investigation. In a "dock-lock" mechanism, described by (Esler et al. 2000), the interaction between Aβ and membrane lipids occurs in two phases. In the first phase, called "dock", wherein Aβ (substrate) binds relatively fast and reversibly to cholesterol/membrane lipids (template). In the second "lock" phase, the bound Aβ becomes irreversibly associated with the bound lipid. This reversible-dock and/or irreversible-lock interplay of DAβ with cholesterol could be different as compared to WT Aβ which could be one potential explanation for the differences observed between their respective aggregated and non-aggregated forms. Additionally, cholesterol is also known to partition into lipid rafts (specialized membrane microdomains

enriched in cholesterol and sphingolipids), and has been shown to facilitate the uptake of Aβ species (Cordy et al. 2006; Hoshino et al. 2013; Kayed et al. 2004). Additional reports have also shown that within the Aβ peptide sequence, there are preferential lipid binding sites (Wang et al. 2022; Hoshino et al. 2013; Verdier et al. 2004). Notably, Ser-8 and Ser-26 are localized within/around the ganglioside and cholesterol binding domains, respectively (Fig. **3**). These data and previously published reports suggest that intracellular uptake of extracellular npAβ pools is primarily facilitated by cholesterol (Fig. **9D-H**). On the other hand, while cholesterol seems to play a role in internalization of pAβ species, the data suggest that other membrane components may interact with pAβ species and facilitate their uptake. Additional experiments to modulate the membrane lipid and protein composition could be designed to further address the involvement specific components of the plasma membrane that mediate the interaction and internalization of different Aβ species. In conclusion, Aβ showed a phosphorylation-state specific effect on aggregation behavior in influencing its solubility and oligomerization propensity which increased membrane interactions, impacting cell viability, and suggesting a pivotal role in AD progression.

4.2. Intraneuronal pAβ species impacts cell homeostasis mechanisms

Intraneuronal Aβ accumulation correlates well with neuronal dysfunction and neurodegeneration, and could contribute to cellular Aβ propagation and Aβ plaque formation (Gowrishankar et al. 2015; Lee et al. 2022; Pasternak et al. 2004; Sharoar et al. 2019; van Acker et al. 2019). The next aspect of this thesis with transgenic mouse brains and neuronal cell culture models revealed the phosphorylation-state specific intraneuronal sorting of Aβ species (Fig. **10-15**, Ext. Fig. **3-6**). In particular, the data depicts the impact of phosphorylation-state of Aβ on vesicular localization (Fig. **11-15**, Ext. Fig. **5-6**), autophagic and endo-lysosomal pathways (Fig. **15-19**, Ext. Fig. **6-7**), Ubiquitin proteasomal machinery (Fig. **20-21**), ER stress (Fig. **22**), mitochondrial dysfunction (Fig. **23**, Ext. Fig. **8**), and oxidative stress (Fig. **23M-N**) linking neuronal dysfunction in the pathogenesis of AD. Besides the deposition of Aβ in extracellular plaques, intraneuronal Aβ accumulation could also play important roles in neuronal dysfunction during the pathogenesis of AD (Billings et al. 2005; Brewer et al. 2020; Gouras et al. 2005; Gouras et al. 2000; Takahashi et al. 2002; Wirths and Bayer 2012). Here, differential intraneuronal

localization of non-modified and phosphorylated Aβ species in APP-PSEN1 transgenic mouse model, were identified (Fig. **10A-D**, Tab. **2**, **3a**). As shown previously, pSer8Aβ was prominent in the fibrillar core of extracellular Aβ plaques (Kumar et al. 2013; Kumar et al. 2011; Kumar et al. 2020b; Kumar et al. 2018), while pSer26Aβ was detected diffusely associated with extracellular plaques (Kumar et al. 2016; Joshi et al. 2021a). More importantly, using a specific mouse model with YFP-labeled forebrain neurons, both phosphorylated Aβ species showed augmented intraneuronal localization as compared to the non-modified Aβ species. Additionally, studies with cultured neurons demonstrated that both phosphorylated Aβ species showed higher association with neuronal membranes as well as intraneuronal accumulation, as compared to npAβ (Fig. **10E-I**). In transgenic animal models, it has been observed that intraneuronal pSer8Aβ accumulation occurs before the formation of plaques (Ashby et al. 2015; Kumar et al. 2013; Kumar et al. 2018). This finding suggests that intraneuronal pAβ may play a significant role in the early stages of AD pathology. However, it also remains to be determined whether the differential accumulation of phosphorylated Aβ species in brain neurons *in vivo* results from neuronal uptake of already phosphorylated extracellular Aβ species or from intracellular generation and phosphorylation of Aβ (Kapadia et al. 2024).

Our previous results showed that phosphorylation at Ser8 promotes formation of soluble fibrillar assemblies, while phosphorylation at Ser26 stabilizes oligomeric assemblies (Fig. **6-8**, Kumar et al. 2011; Kumar et al. 2016). ELISA analyses of pAβ species in fractionated transgenic mouse brain samples showed enrichment of the pAβ within the sucrose-soluble and SDS-associated membrane-rich fractions as compared to the npAβ species (Ext. Fig. **3F**; **11F**, Tab. **3a-b**). Similarly, fractionated cultured neurons pre-treated with Aβ peptides showed augmented intraneuronal accumulation and differential compartmentalization of the pAβ species within membrane-rich, soluble, and insoluble cytosolic fractions (Fig. **10K**; Ext. Fig. **4**). Although, monomeric Aβ was added to neuronal cultures, western blot analyses indicated formation of pAβ aggregates during the course of the experiments (Ext. Fig. **4E**). Thus, not only the introduction of negative charges by phosphorylation of monomeric Aβ, but also differential aggregation could underlie the distinct association with neuronal membranes, vesicular distribution, and the functional effects of the Aβ phosphorylation-state variants (Kapadia et al. 2024).

Neuronal autophagy and the endo-lysosomal pathway play an important roles in the intracellular trafficking and accumulation of Aβ (Colacurcio et al. 2018; Karaca et al. 2014; Lee et al. 2022; Marshall et al. 2020; Nilsson and Saido 2014; Nixon et al. 2000; Pasternak et al. 2004; Tamboli et al. 2011; Wang et al. 2018). In both, transgenic mouse brains and cultured neurons, localization of pAβ species in distinct autophagic and endo-lysosomal compartments is seen (Fig. **11-15**, Ext. Fig. **5-6**; Kapadia et al. 2024). While pSer8Aβ showed higher colocalization in LC3 positive autophagic vesicles, pSer26Aβ was enriched in late endosomal and lysosomal compartments, including autolysosomes. Once internalized by primary neurons into early endosomal compartments, pSer26Aβ is efficiently targeted to late endosomal and lysosomal compartments, while pSer8Aβ predominantly accumulates within early endosomal and autophagosomal structures. Thus, the phosphorylation state could modulate the accumulation of Aβ in distinct intraneuronal vesicular compartments. However, the exact intracellular routes and the involvement of distinct autophagy dependent and independent vesicular compartments in the sorting of phosphorylated Aβ species need to be characterized in more detail, e.g., by live cell imaging with fluorescent Aβ species and high-resolution microscopy techniques. For example, it is possible that fractions of internalized Aβ variants, in particular of pSer26Aβ, could be transported in the endocytic pathway to lysosomes without initial involvement of autophagic vesicles. Such analyses could also provide further insight into the exact effects of distinct Aβ species in vesicular trafficking. Previous studies indicated that APP and APP C-terminal fragments can be targeted to endo-lysosomal and autophagic compartments and then processed to intravesicular Aβ (Cataldo et al. 2004; Glabe 2001; Karaca et al. 2014; LaFerla et al. 2007; Nixon 2017; Nixon and Yang 2011; Sannerud et al. 2016; Tamboli et al. 2011; Tien et al. 2016). Whether the pool of Aβ generated inside of vesicles can undergo phosphorylation remains to be investigated (Kapadia et al. 2024).

The differential sorting of Aβ phosphorylation-state variants was associated with distinct effects on autophagic and endo-lysosomal functions, and neuronal viability (Fig. **15-19**, Ext. Fig. **6-7**; Kapadia et al. 2024). The accumulation of internalized pSer8Aβ in endosomal or autophagosomal vesicles could impair efficient delivery of cargo or vesicular fusion with lysosomes as suggested from results with the mCherry-GFP-LC3 probe. Here,

pSer8Aβ increased the number mCherry^{+}GFP^{+} vesicles but decreased the number of mCherry^{+}GFP^{-} vesicles. This is indicative for increased formation and/or accumulation of autophagic vesicles, but decreased delivery to acidic lysosomal compartments. In contrast, pSer26Aβ had no significant effect on the number of mCherry^{+}GFP^{+} positive vesicles, but strongly increased the number of mCherry^{+}GFP^{-} vesicles, indicating efficient delivery of the construct to lysosomes during autophagic flux. Interestingly, the data also indicates that particularly pSer26Aβ, and to a lesser extent probably also npAβ and pSer8Aβ, could promote lysosomal biogenesis and augment intracellular accumulation of lysosomes. However, it remains to be determined in more detail whether the minor alterations in pH upon incubation with pSer26Aβ observed in this study translate to functional alterations or rather indicate a response to Aβ induced impairment of lysosomal function. Indeed, the accumulation of ubiquitinylated proteins and p62 suggests lysosomal failure upon persistent exposure to pSer26Aβ, associated with impairment of neuronal viability. Although pSer8Aβ was not efficiently targeted to lysosomes, this species also exerted comparable neurotoxicity. Here, the accumulation of pSer8Aβ in autophagic vesicles might impair vesicular transport and fusion with lysosomes, as supported by the accumulation of LC3 positive vesicles, and autophagic protein substrates, including p62 and ubiquitinylated proteins (Kapadia et al. 2024)

The UPS is responsible for identifying and degrading intracellular proteins (Nandi et al. 2006), and disruption of the UPS has been implicated AD (Ciechanover and Schwartz 1998; Hong et al. 2014; Upadhya and Hegde 2007). Studies have demonstrated that intraneuronal Aβ accumulation can lead to impairment of the UPS and subsequent accumulation of ubiquitinated proteins. In transgenic mouse models, impaired proteasome activity has been observed, which correlates with the detection of intraneuronal Aβ oligomers (Upadhya and Hegde 2007; Hegde et al. 2019). The data showed association between intraneuronal pAβ and poly-ubiquitinylated proteins within plaque pathology in APP-PSEN1 transgenic mice as well as intracellular accumulation in cultured primary cortical neurons (Fig. **20**). pAβ species differentially augment proteasomal activity as compared to their non-phosphorylated counterpart (Fig. **21**). The data showed subtle but significant differences between the substrate based proteolytic activities induced by pAβ peptides. Additional experiments to specifically dissect their impact on the different

proteasome-dependent and independent proteolytic activity have to be studied in detail. The increased activity of UPS induced by pAβ and npAβ species, can lead to the intracellular accumulation of misfolded proteins, including Aβ itself, and additionally contribute to neuronal dyshomeostasis. As discussed extensively in literature, the autophagy-endo-lysosomal and UPS are closely related to maintain cellular homeostasis. The interlinked dysfunction of both systems has been previously implicated in AD (Zhang et al. 2017; Ding et al. 2007; Korolchuk et al. 2010; Ji and Kwon 2017; Cao et al. 2019; Sjödin et al. 2019). These studies demonstrate a link between intraneuronal pAβ and npAβ accumulation to UPS dysfunction and impaired autophagy in AD. The results show that exposure of individual Aβ species to primary cultured neurons and their intraneuronal accumulation cause aberrations within subcellular and vesicular processing.

Additionally, with respect to the dysregulation in ALP and UPS, other modes of Aβ induced neurotoxicity like perturbation of plasma membrane integrity or rupture of vesicular membranes and Ca^{2+} dysregulation could also contribute to the impairment of neuronal viability (Ditaranto et al. 2001; Lee et al. 2022; Umeda et al. 2011; Zaretsky and Zaretskaia 2021; Zaretsky et al. 2021). Intraneuronal Aβ was described in different mouse models (Bayer and Wirths 2010; Cruz et al. 2006; Eimer and Vassar 2013; Knobloch et al. 2007; LaFerla et al. 2007; Takahashi et al. 2017) and thus, it will be interesting to also analyze age-dependent vesicular distribution and sorting of phosphorylated Aβ species in other transgenic mouse models in the future. Together, this part of the study demonstrates the complexity of functional effects caused by intraneuronal accumulation of distinct Aβ variants on autophagy, endo-lysosomal and the proteasomal system. It is interesting to note that disturbance of autophagy, endo-lysosomal and/or UPS function in AD pathogenesis could also involve Aβ independent mechanisms. These could include presenilin proteins (PSEN) dependent regulation of lysosomal pH, release of Ca^{2+} from lysosomes that facilitate fusion with late endosomes or autophagosomes, and transcriptional regulation of lysosomal biogenesis. Also, loss of PSEN resulting in accumulation of autophagic and endo-lysosomal compartments could also alter Aβ production and degradation (Coen et al. 2012; Neely et al. 2011; Zhang et al. 2012). Thus, several Aβ-dependent and -independent mechanisms could contribute to the impairment

of endo-lysosomal and autophagy related systems, and it will be important to further dissect their relative contribution to the pathogenesis of AD (Kapadia et al. 2024).

The ER unfolded protein response (UPR) is a cellular response aimed at restoring cellular homeostasis by increasing the production of ER chaperones and activating ER-associated protein degradation (ERAD). ERAD is responsible for disposing of misfolded proteins and preventing their accumulation in the ER (Hwang and Qi 2018; Meusser et al. 2005; Nishikawa et al. 2005). Intraneuronal accumulation of Aβ species has been implicated in the alteration of ER-associated proteins. Aβ oligomers potentially induce endosomal/lysosomal leakage along with induction of ER stress and mitochondrial dysfunction, ultimately leading to cell death (Umeda et al. 2011; Zaretsky et al. 2022; Yang et al. 1998). Additional studies have also suggested a role of intraneuronal Aβ species in altering ER homeostasis (ER regulated stress response) and disrupting cellular processes (Li et al. 2015; Endres and Reinhardt 2013; Penke et al. 2017; Penke et al. 2012). The presence of intraneuronal Aβ, specifically pAβ species, has differential impact on proteins involved in maintaining and regulating ER function such as IRE1, PERK, and ATF-6 proteins (Fig. **22**). This in turn, can lead to induction of ER stress response (Uddin et al. 2021), activate UPR (Chen et al. 2015) and impact mitochondrial homeostasis (Ferreiro et al. 2012; Hedskog et al. 2013).

It has already been shown that intraneuronal Aβ species can induce mitochondrial dysfunction observed in AD (Hirai et al. 2001; Moreira et al. 2010; Picone et al. 2014; Santos et al. 2010). Here, pSer26Aβ showed a significant impact on chaperones involved in mitochondrial protein homeostasis (heat shock protein families Hsp70 and HSP90) as well as on mitochondrial membrane potential and susceptibility (Fig. **23**; Ext. Fig. **8**). Mitochondrial dysfunction and oxidative stress are closely linked to the presence of intraneuronal Aβ species (Calvo-Rodriguez and Bacskai 2021; Butterfield and Boyd-Kimball 2020). PINK1 and Parkin play critical roles in maintaining mitochondrial homeostasis and quality control (Rüb et al. 2017), which are significantly increased in the presence of intraneuronal pAβ species. Loss of functional mitochondria ultimately leads to increased oxidative stress which in turn further exacerbates the neurodegenerative process in AD (Zhou et al. 2023; Du et al. 2017). This cascade of events and its contribution to synaptic loss and neurodegeneration needs to be critically evaluated to

identify therapeutic approaches targeting mitochondrial dysfunction and oxidative stress in AD. Furthermore, as seen earlier, pAβ species exhibit varying effects on autophagy, endo-lysosomal processes, and ubiquitin-proteasomal machinery, as well as on endoplasmic reticulum (ER) stress responses as well as disrupt ER-mitochondria cross talk.

To summarize, the combined data indicate a phosphorylation-state specific impact of Aβ species on neuronal viability, detailing their differential effects on intraneuronal trafficking and sorting within vesicular compartments, and alteration of organelle homeostasis. These results highlighted the association between pAβ variants and neuronal dyshomeostasis, including disruptions in autophagy, endo-lysosomal pathways (Kapadia et al. 2024), ubiquitin-proteasomal machinery, unfolded protein response, mitochondrial dysfunction, and oxidative stress in AD pathophysiology. Since recent evidence supports a critical role of intraneuronal Aβ accumulation in the formation of extracellular plaques (Bayer and Wirths 2014; Cataldo et al. 2004; Gouras et al. 2005; LaFerla et al. 2007; Lee et al. 2022; Takahashi et al. 2017), it will also be interesting to dissect the relative contribution of intraneuronal phosphorylated Aβ species to the generation of extracellular plaque pathology in the future.

4.3. Phosphorylation-state dependent effects of Aβ on differentially regulating cell-death pathways

While both intra- and extracellular Aβ deposits can affect neuronal viability (Kayed and Lasagna-Reeves 2013; Sengupta et al. 2016), the specific molecular mechanisms by which intraneuronal pAβ peptides exert their effects are not yet fully understood. Studies with transgenic mouse as well as cell culture models showed that intraneuronal accumulation of Aβ species correlated with caspase activation, suggesting neuron loss through apoptosis (Behl 2000; Eimer and Vassar 2013; Yang et al. 2008; Bamberger and Landreth 2002; LaFerla et al. 2007; LaFerla et al. 1997). Additionally, studies have shown that Aβ oligomers can function as apoptotic substrates for various receptors, including CD36, scavenger receptors, CD47, alpha(6)beta(1)-integrin, the serpin-enzyme complex receptor (SEC-R), and the insulin receptor (Bamberger et al., 2003; Verdier et al., 2004) and can directly or indirectly activate the intrinsic apoptotic pathway (Islam et al. 2017;

Malaplate-Armand et al. 2006). These findings suggest that intraneuronal Aβ can induce apoptosis in neurons. In addition to apoptosis, intraneuronal Aβ accumulation has also been associated with necrotic cell death (Tanaka et al. 2020). Taken together, these findings indicate that intraneuronal Aβ can trigger both apoptotic and necrotic cell death pathways in neurons (Mangalmurti and Lukens 2022; Carter and Lippa 2001). As seen in these studies, Aβ showed a phosphorylation-state dependent accumulation within neurons as well as differential modulation of organelle homeostasis mechanisms (Fig. **24-27**; Ext. Fig. **9-10**). Primarily, intraneuronal pSer26Aβ showed increased colocalization with CK1δ, pRIPK1 and pMLKL, which are markers used to denote necroptosis and/or necrotic cell death. It is interesting to note that, in human AD brains, protein kinase CK1 isoforms were found in granulovacuolar degeneration (GVD) compartments (Kurdi and Alghamdi 2020; Andrés-Benito et al. 2023) that also contain pSer26Aβ, and *in vitro* experiments demonstrated phosphorylation of Aβ by CK1 activity (Kumar et al. 2016). On the other hand, neurons showing the presence of intracellular pSer8Aβ also showed presence of phosphatidylserine (detected by AnnV) as a marker for apoptosis. These observations were complemented by *in vitro* experiments, wherein cells treated with either pAβ, showed preferential activation of either apoptotic or necrotic cell death pathway. Examining these observations, along with previously published reports indicating that the buildup of intraneuronal Aβ within multivesicular bodies (MVBs) or GVD bodies is linked to synaptic pathology, it is possible for Aβ species to occur or be transferred to, or within, distant neuronal subcellular compartments. The localization of intraneuronal Aβ within different neuronal or subcellular compartments may influence the type of cell death pathway. These observations could be further attributed to either caspase-dependent or -independent pathways, mitochondria induced apoptotic dysfunction as well as potential metabolic changes in cells.

The interplay between autophagy and apoptosis is complex and involves bidirectional regulation, wherein the dysregulation of autophagy in the presence of Aβ has been linked to the activation of apoptotic pathways (Mukhopadhyay et al., 2014). It could be hypothesized that in the intraneuronal presence of pSer8Aβ within autophagic vesicles, plausibly induces apoptosis. Also, accumulation of intraneuronal Aβ (npAβ, in particular pSer26Aβ) can lead to impairment of the autophagy-lysosome system including auto-

lysosomal leakage, ultimately promoting necrotic cell death. This suggests that lysosomal and autophagy dysfunction play a role in regulating both major cell death pathways (Fig. **27**). The preferential activation of necrotic cell death upon pSer26Aβ treatment, could result from the acidification of intracellular (cytosolic) or lysosomal pH, and significant increase in LDHA (Lactate Dehydrogenase A) and β-gal (β-galactosidase) activity. Thus, phosphorylated-state dependent dysregulation of homeostasis mechanisms could disrupt intracellular clearance of Aβ as well as other cargo, leading to its accumulation. This in turn could activate either necrotic or apoptotic cell death pathways. Although it is quite difficult to attribute a specific regulated cell death mechanism to either of the phosphorylated Aβ peptides, it could be safe to state that pSer8Aβ induced toxicity showed characteristics of apoptotic, while pSer26Aβ, more necroptotic cell death. In conclusion, the phosphorylation state of Aβ differentially affects autophagy and lysosome functions as well as different modes of cell death.

4.3.1. Effect of mimicking the phosphorylation state by amino acid substitution

The main motivation of using SY5Y-APP$_{Sw}$ transgenic cell lines generating pseudo-phosphorylated or non-phosphorylatable Aβ variants was to avoid influences of kinases and phosphatases in co-culture and exosome-transfer experiments (Fig. **24**, Ext. Fig **13**). Examination of SH-SY5Y-APP$_{Sw}$ transgenic cell lines showed that there is a slight effect of Serine to Aspartate substitutions (secreted sAPPα/β levels in the supernatant, Ext. Fig. **13E**). However, these effects were not statistically significant when compared across different experimental readings and cell passage states, and might be attributed to minor differences in the processing of APP. However, it is important to note that so far there is no indication that phosphorylation (at Ser8 or Ser26) occur within the APP sequence. Similar to the effects of phosphorylation at Ser 8, aspartic acid replacement of serine residue at position 8 (synthetic peptide) showed increased effects on its solubility. The aggregation and solubility behavior between the Ser 26 versions (S26D-Aβ and pSer26Aβ) were comparable. It is also interesting to note that intracellular DAβ was localized within different vesicular compartments. In particular, S8D-Aβ was enriched within autophagosomes and S26D-Aβ within perinuclear lysosomal compartments, thereby validating this approach to mimic phosphorylated Aβ for functional studies with cultured cells.

4.4. Relationship between pAβ and microglia in AD pathology

The last aspect of this study highlights a phosphorylation-state dependent impact on exosome mediated propagation of Aβ, cell viability and microglial inflammation in AD. Similar to the approach with APP-PSEN1delE9xThy1-YFP transgenic model to study intraneuronal Aβ, an APP-PSEN1delE9xCX$_3$CR1-GFP, wherein the CX$_3$CR1$^+$ microglia were labelled with GFP, to specifically investigate the association of different Aβ species with microglia *in vivo*, was used(Fig. **28**, Ext. Fig. **11**, Tab. **2-3b**). As already observed with the APP-PSEN1delE9xThy1-YFP model, differential localization of non-modified and phosphorylated Aβ species within the plaque pathology was detected. As shown previously, pSer8Aβ was detected prominently in the fibrillar core, while pSer26Aβ diffusely associated with extracellular plaques (Fig. **28**). Notably, both phosphorylated Aβ species showed augmented accumulation within microglia as compared to the non-modified Aβ species, which falls in line to previous observations showing increased intracellular accumulation of pAβ species in transgenic mouse models (Joshi et al. 2021a; Kumar et al. 2020a; Kumar et al. 2020b). These observations suggest potential contribution of pAβ in triggering microglial inflammation in the early stages of AD pathology, which needs to be examined further. Additionally, this opens new avenues of research to understand and compare the relative contribution of microglia associated phosphorylated Aβ species to that of neuronal pAβ to the generation of extracellular plaque pathology in the future.

Microglial cells play a crucial role in the clearance of Aβ, and their dysfunction or loss may contribute to the progression of AD (Block et al. 2007; Frigerio et al. 2021; Lee and Landreth 2010; Leng and Edison 2021). In-house generated and characterized APP$_{Sw}$ transgenic cell lines to study the interplay between neuron-microglia and Aβ, were employed. A phosphorylation-state dependent effect on intracellular accumulation as well as cell viability was observed when conditioned media containing respective secreted DAβ species were transferred to microglia (Fig. **30**). Here, both DAβ variants were internalized more efficiently and had stronger detrimental effects on cell viability as compared to npAβ. These observations again support the fact that the cytotoxic potential of DAβ species is related to the intracellular accumulation of these peptides, partly because they have increased solubility and membrane interaction. Thus, it will be interesting to investigate

genetic risk factors such as the TREM2, APOE, PLCγ2, ACE which have been implicated in altering microglial phagocytic capacity, in future (McQuade and Blurton-Jones 2019; Morgan et al. 2005; Leng and Edison 2021; Hodges et al. 2021; D'Andrea et al. 2004) Another interesting aspect would be to understand the effect of phosphorylation state of Aβ in altering microglial function and its contribution to plaque pathology (Joshi et al. 2021b; Joshi et al. 2021a).

Here, one specific pool of extracellularly secreted Aβ, i.e., Aβ species associated with exosomes; was focused on detail. Exosomes have been found to play a role in the intercellular transfer of misfolded proteins, such as Aβ and tau in AD (Sardar Sinha et al. 2018; Rajendran et al. 2006; Malm et al. 2016). Additionally, their role in the transfer of functional microRNAs and their potential modulation of cognitive function in AD models has also been highlighted. To examine this, exosomes secreted by APP_{Sw} transgenic cell lines were enriched and examined (Fig. **31**; Ext. Fig. **14**).

Interestingly, an important mechanism of cellular clearance is the lysosomal exocytosis, a process favoring secretion of lysosomal content upon lysosome fusion with plasma membrane (Buratta et al. 2020). An increase in the levels of lysosomal protein LAMP-1 within the exosome enriched pellet fraction secreted by S26D APP_{Sw} cells as well as WT APP_{Sw} cells was detected (Ext. Fig. **14A**). Taking insights from earlier observations showing the lysosomal accumulation of pSer26Aβ peptide (Fig. **13-15**), it could be hypothesized that pSer26Aβ-induced defects within the lysosomal pathway may play a key role in regulating exosomal secretion or lyso-exocytosis (Buratta et al. 2020) of pSer26Aβ/S26D-Aβ species.

When exposed to the media containing enriched exosomes, a significant decrement in microglial viability was seen in the case of DAβ variants (S26D-Aβ > S8D-Aβ). Indeed, higher levels of both DAβ variants were detected in exosome-enriched fractions as well as the supernatant. Although the differences could be attributed to an Aβ concentration dependent effect on toxicity, the relative comparison here does show a phosphorylation-state dependent effect of Aβ as compared to the non-phosphorylated counterpart. These observations are quite interesting since exosome-associated proteins localize with Aβ peptides within Aβ plaques as detected via immunohistochemistry (Fig. **32**). Thus,

additional studies on how these small vesicular compartments contribute to plaque pathology would be interesting. Accumulation of dysfunctional microglia around the plaque additionally adds a layer of complexity to plague pathology most observed in AD cases. One primary goal would be to elucidate the relative contribution of the exosome-associated pAβ pools to the extracellular (free form) in triggering microglial dysfunction and neuroinflammation.

Neuroinflammation, characterized by glial activation, is one of the major neuropathological features of AD, along with Aβ plaque deposition, neurofibrillary tangles, and neuronal loss (Boon et al. 2018; Heneka et al. 2015; Leng and Edison 2021; Streit et al. 2004). Microglial activation is a characteristic feature of AD brain pathology. Treatment of DAβ containing conditioned media from SH-SY5Y-APP$_{Sw}$ cell lines showed a strong activation of pro-inflammatory response in microglia as well as activation of caspases (Fig. **33**, Ext. Fig. **15**). In the trajectory of AD, there is an early and late peak in microglial activation (Fan et al. 2017). Initially, there is a microglial activation in the prodromal stage of AD, attempting to clear the Aβ. However, this activation eventually fails to clear Aβ deposits, and there is a progressive increase in pro-inflammatory microglial activation during the later stages of the disease. Immunohistochemical studies from previously published reports showed that pAβ accumulation is seen in early stages of different transgenic animal models (Kumar et al. 2018; Kumar et al. 2011; Kumar and Walter 2011; Kumar et al. 2013). However, human studies rather indicate deposition of pSer8Aβ in clinical/late phase of AD (Kumar et al. 2011; Kumar et al, 2013, Kumar et al, 2020). Furthermore, it would be interesting to dissect the role of pAβ in early stage of microglial activation in future. Additionally, it would also be interesting to elucidate its contribution to chronic neuroinflammation observed toward the end of the disease.

Studies have shown that Aβ has the capacity to activate the NLRP3-ASC inflammasome, leading to caspase-1 activation and the release of pro-inflammatory cytokines (Barczuk et al. 2022; Hanslik and Ulland 2020; Hulse and Bhaskar 2022; van Zeller et al. 2021). These studies showed a phosphorylation-state dependent effect on induction of pro-inflammatory factors, caspase and inflammasome activation (Fig. **33**, Ext. Fig. **15**). Both phosphorylated variants, particularly pSer26Aβ, showed stronger effects as compared to the non-phosphorylated counterpart. ASC specks play a role in the propagation of

inflammation and can induce caspase-1 activation in recipient cells (Hulse and Bhaskar 2022). Preliminary results showed that there is a phosphorylation-state dependent effect of Aβ on ASC speck formation (Fig. **34**, Ext. Fig. **16**). pSer8Aβ induced (on average) formation of a single speck per cell, wherein pSer26Aβ induced clustering of smaller ASC aggregates. Previous reports showed that microglia-derived ASC specks cross-seed Aβ aggregation (Venegas et al. 2017). They have also been shown to bind to Aβ and increase the formation of Aβ oligomers and aggregates, acting as an inflammation-driven cross-seed for Aβ pathology (Friker et al. 2020; Hulse and Bhaskar 2022). This finding highlights the role of ASC specks in the propagation and amplification of Aβ pathology in the brain, which needs to be thoroughly investigated in the context of pAβ *in vitro* and *in vivo*. Additionally, ASC specks have been found to act as prion-like aggregates, propagating inflammation and contributing to the pathogenesis of various autoimmune diseases (Franklin et al. 2014; Hulse and Bhaskar 2022), which add an additional level of complexity in the relationship between pAβ and microglial inflammation. Additionally, the interplay between microglia and Aβ pathology is further influenced by genetic risk factors, wherein, TREM2 and APOE have been extensively studied (Shi and Holtzman 2018; Wolfe et al. 2018; Li et al. 2023; Lefterov et al. 2023). Lastly, in addition to microglial activation, astrocyte activation is also involved in AD pathology (Kumar et al. 2023; Rostami et al. 2021). Thus, it would be important to also dissect the effect of phosphorylated Aβ species even further in the context of astroglia-neuron interactions.

Thus, these studies showed that uptake of exosome- and non-exosome- associated pAβ by microglia has an influence on inflammation, plaque formation, and cellular viability, which could play a crucial role in early AD stages by potentially altering microglial function and homeostasis.

Supplementary data

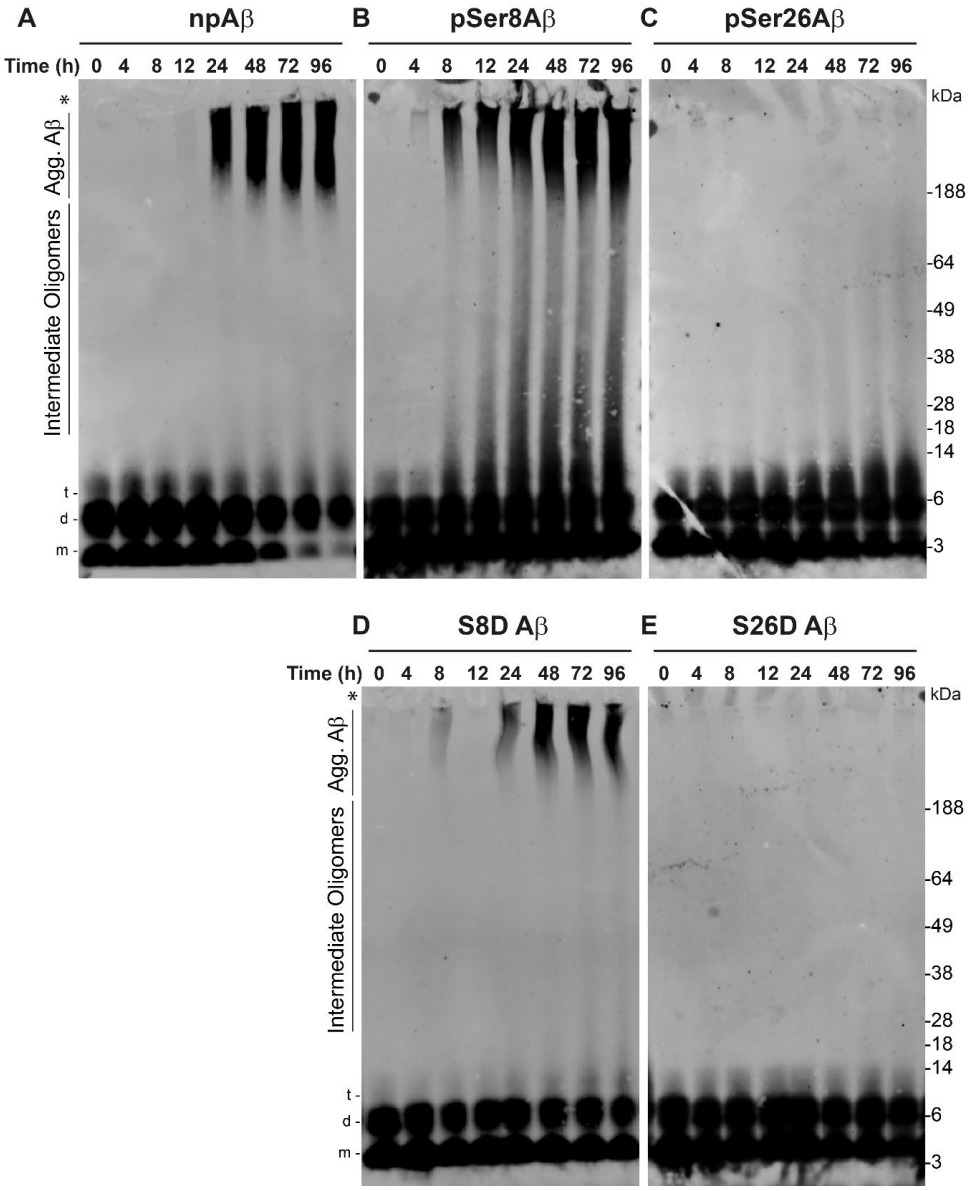

Ext. Fig. 1: A-E. Western immunoblotting showing differential aggregated states of non-phosphorylated npAβ (**A**), phosphorylated Aβ (pSer8Aβ, **B**; pSer26Aβ, **C**) and pseudo-phosphorylated Aβ (S8D Aβ, **D**; S26D Aβ, **E**) peptides aggregated at respective time points, analyzed via SDS-PAGE. Aβ species were detected with anti-Aβ antibody 82E1. *m,* monomer*; d,* dimer*; t,* trimer*; Agg.,* aggregated*; Int. oligomers,* Intermediate-weight oligomers*;* * fibrils.

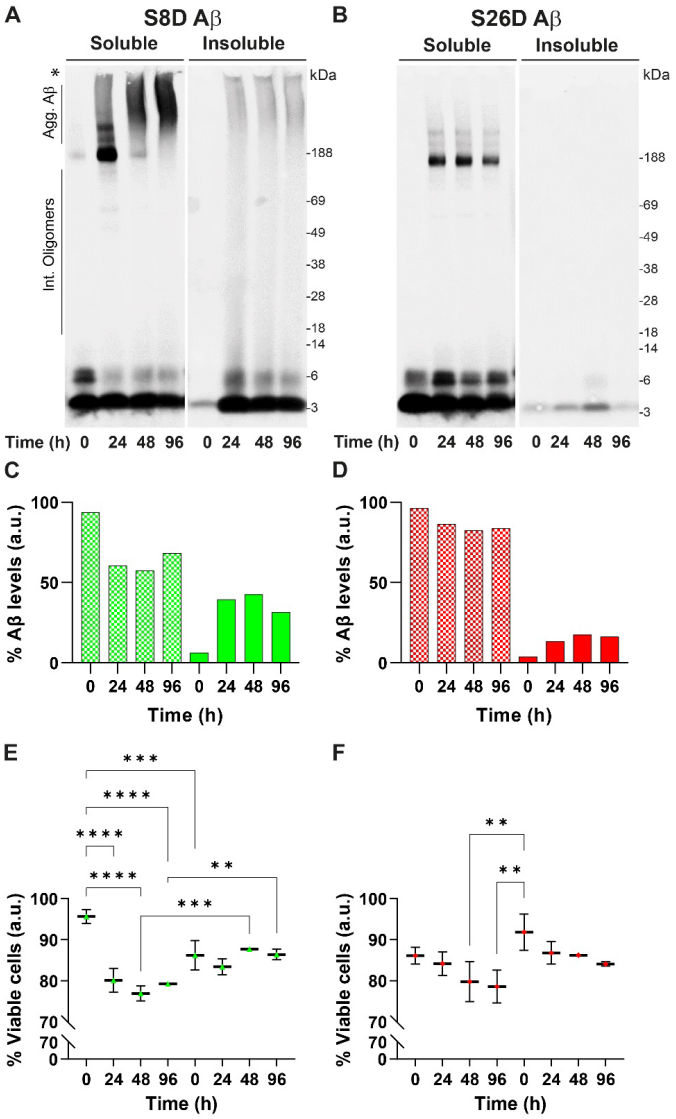

Ext. Fig. 2: A-B. Aβ aggregated for different time points were subjected to fractionation into soluble (*supernatant*) and insoluble (*pellet*) fractions and were analyzed by SDS-PAGE. Immunoblots depicting soluble and insoluble fractionated aggregated species of S8D Aβ (**A**) and S26D Aβ (**B**). Aβ species were detected with anti-Aβ antibody 82E1. *m,* monomer*; d,* dimer*; t,* trimer*; Agg.,* aggregated*; Int. oligomers,* Intermediate-weight oligomers*;* * fibrils **C-D.** Bar plots showing densitometric quantification of the Aβ signal intensities in the soluble and insoluble fractions of S8D Aβ (**C**) and S26D Aβ (**D**) variants, at indicated time points, respectively. Values were computed using ImageJ gel quantification module. Values were normalised to total signals in both soluble and insoluble fraction and depicted as percent Aβ levels in respective fractions. Data depicted herewith is representative of two independent experiments. **E-F.** Scatter plots showing the percentage viability of SH-SY5Y cells treated with the soluble and insoluble fractions of S8D Aβ (**E**) and S26D Aβ (**F**) variants, at indicated time points, respectively. Cell viability is evaluated using Presto-Blue assay. Readings were normalised to control untreated cells and presented as percent change in viable cells *wrt* control. Values represents the mean ± S.D; n = 3, N = 3. * $p < 0.05$; ** $p < 0.01$; *** $p < 0.001$; **** $p < 0.0001$; n.s. $p \geq 0.05$, not significant (One-way ANOVA, GraphPad Prism).

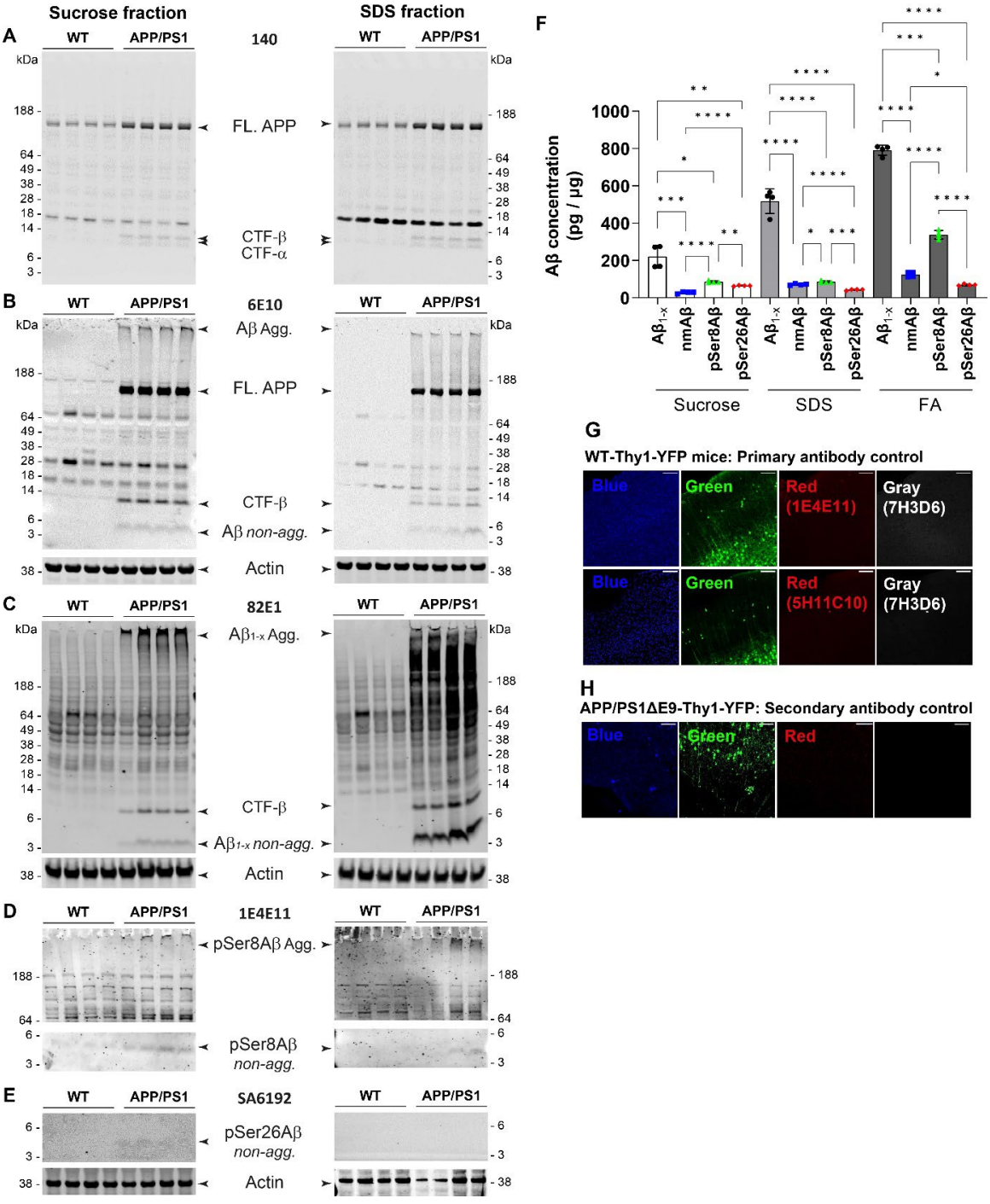

Ext. Fig. 3: A-E. Western immunoblotting analyses of sucrose soluble and SDS soluble fractions of wild type WTxThy1-YFP and transgenic APP-PSEN1delE9xThy1-YFP mouse brains (Tab. **1**, mouse ID 1-8). APP and APP derivatives were detected in parallel with polyclonal antibody 140 recognizing the C-terminus of APP and monoclonal antibody 6E10 recognizing an N-terminal epitope of the Aβ domain. Primary antibodies 140 (**A**) and 6E10 (**B**) were detected by anti-rabbit IR-680 conjugated and anti-mouse conjugated IR-800 secondary antibodies, respectively, using LiCOR fluorescence imaging. Aβ species and APP β-CTF were detected with anti-Aβ antibody 82E1 (**C**). This antibody recognizes a neoepitope generated by β-secretase mediated cleavage of APP, and thus, does not

recognize FL APP. pAβ species were independently detected with in house generated 1E4E11 (pSer8Aβ, **D**) and SA6192 (pSer26Aβ, **E**) antibodies, respectively. Actin was used as loading control respectively. **F**. Bar plots depicting the quantification of Aβ levels (pg/µg) in sucrose, SDS and formic acid (FA) soluble fractions by ELISA using phosphorylation state specific antibodies, respectively. Values represent mean ± S.D., from four different mouse brains per cohort, from two independent experiments, n = 4 mice, N = 2. * $p < 0.05$; ** $p < 0.01$; *** $p < 0.001$; **** $p < 0.0001$; n.s. $p \geq 0.05$, not significant (Two-way ANOVA, GraphPad Prism). **G.** Representative images for primary antibody controls, depicting the cortical regions of WTxThy1-YFP non-transgenic mouse stained for pSer8Aβ (1E4E11, *red*) or pSer26Aβ (5H11C10, *red*), along with nmAβ (7H3D6, *gray*) and DAPI + X-34 (nuclei + plaque core, *blue*). Scale bar, 100 µm. **H.** Representative images for secondary antibody controls; depicting the cortical regions of APP-PSEN1delE9xThy1-YFP transgenic mouse stained with donkey anti-mouse IgG - Alexa Fluor™ 647 (*red*) and donkey anti-rat IgG - Alexa Fluor™ 647 (*gray*) along with DAPI + X-34 (nuclei + plaque core, *blue*). Scale bar, 100 µm. Figure adapted from Kapadia et al. 2024.

Ext. Fig. 4 (legend): A-D. Bar plots depicting the quantification of Aβ concentration by ELISA in different cellular fractions (**A, B**) and in treatment media (**C, D**) of primary cortical neurons (**A, C**) and SH-SY5Y neuroblastoma cells (**B, D**). Aβ species were captured with either phosphorylation state specific antibodies (**A**); npAβ (7H3D6); pSer8Aβ (1E4E11); pSer26Aβ (5H11C10) or generic Aβ (82E1, **B-D**) antibodies, respectively. Bound Aβ detected with either Aβ detection antibodies (**A**, 82E1-Biotin and **B-D**, 4G8-Biotin), respectively. Values represent mean ± S.D., n = 9, N = 3. * $p < 0.05$; ** $p < 0.01$; *** $p < 0.001$; **** $p < 0.0001$; n.s. $p \geq 0.05$, not significant (A-B, Two-way ANOVA; C-D, One-way ANOVA, GraphPad Prism). **E.** NuPAGE and western immunoblot analyses of different cellular fractions of primary cortical neurons treated with the indicated Aβ variants (500 nM, 4 h); Aβ detected with anti-Aβ (82E1) antibody. *Above panel (higher contrast).* Figure adapted from Kapadia et al. 2024.

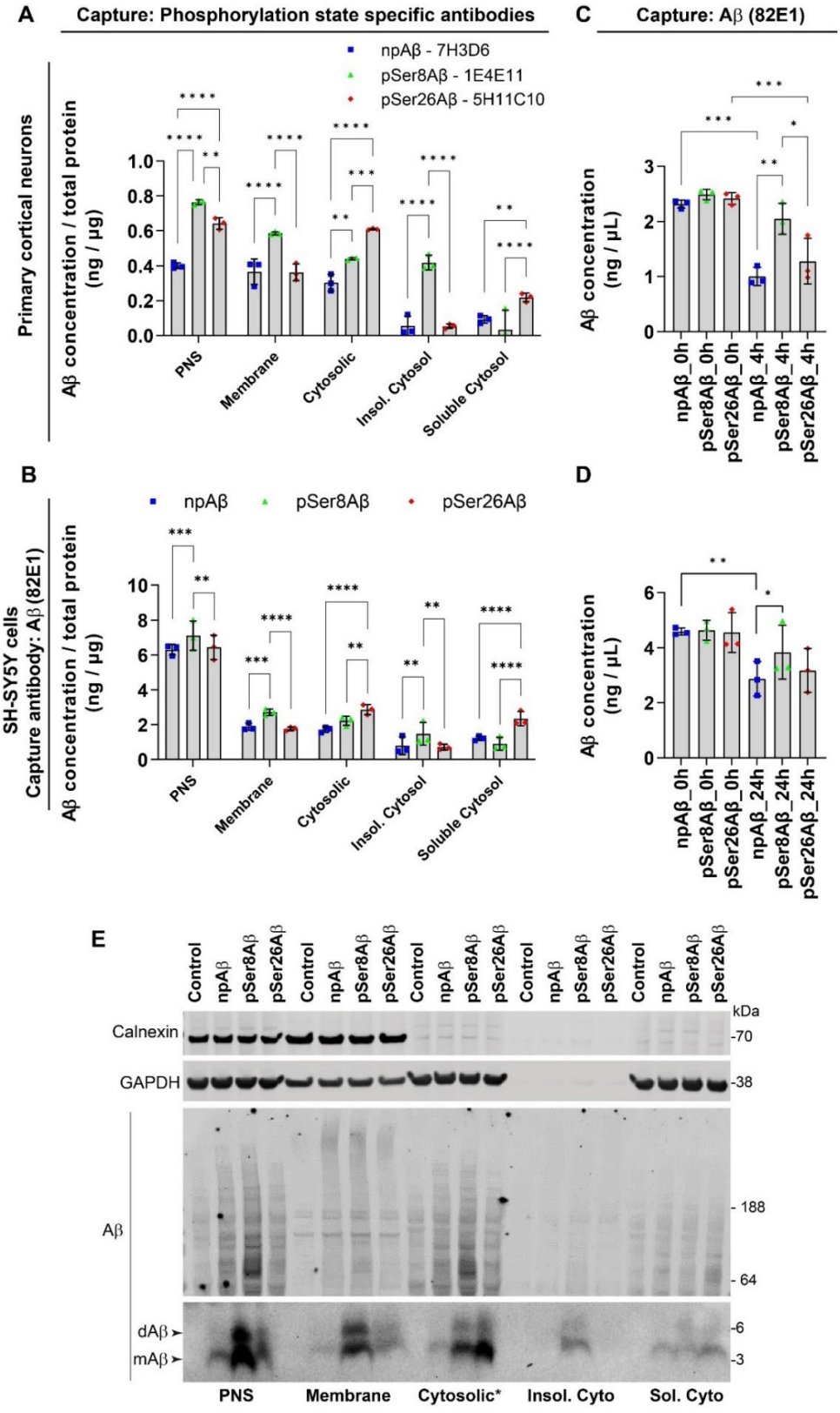
A
Capture: Phosphorylation state specific antibodies
npAβ - 7H3D6
pSer8Aβ - 1E4E11
pSer26Aβ - 5H11C10
Primary cortical neurons
Aβ concentration / total protein (ng / µg)
PNS
Membrane
Cytosolic
Insol. Cytosol
Soluble Cytosol
C
Capture: Aβ (82E1)
Aβ concentration (ng / µL)
npAβ_0h
pSer8Aβ_0h
pSer26Aβ_0h
npAβ_4h
pSer8Aβ_4h
pSer26Aβ_4h
B
npAβ
pSer8Aβ
pSer26Aβ
SH-SY5Y cells
Capture antibody: Aβ (82E1)
Aβ concentration / total protein (ng / µg)
D
Aβ concentration (ng / µL)
npAβ_24h
pSer8Aβ_24h
pSer26Aβ_24h
E
Control
npAβ
pSer8Aβ
pSer26Aβ
kDa
Calnexin
GAPDH
Aβ
dAβ
mAβ
-70
-38
-188
-64
-6
-3
PNS
Membrane
Cytosolic*
Insol. Cyto
Sol. Cyto

Ext. Fig. 4:

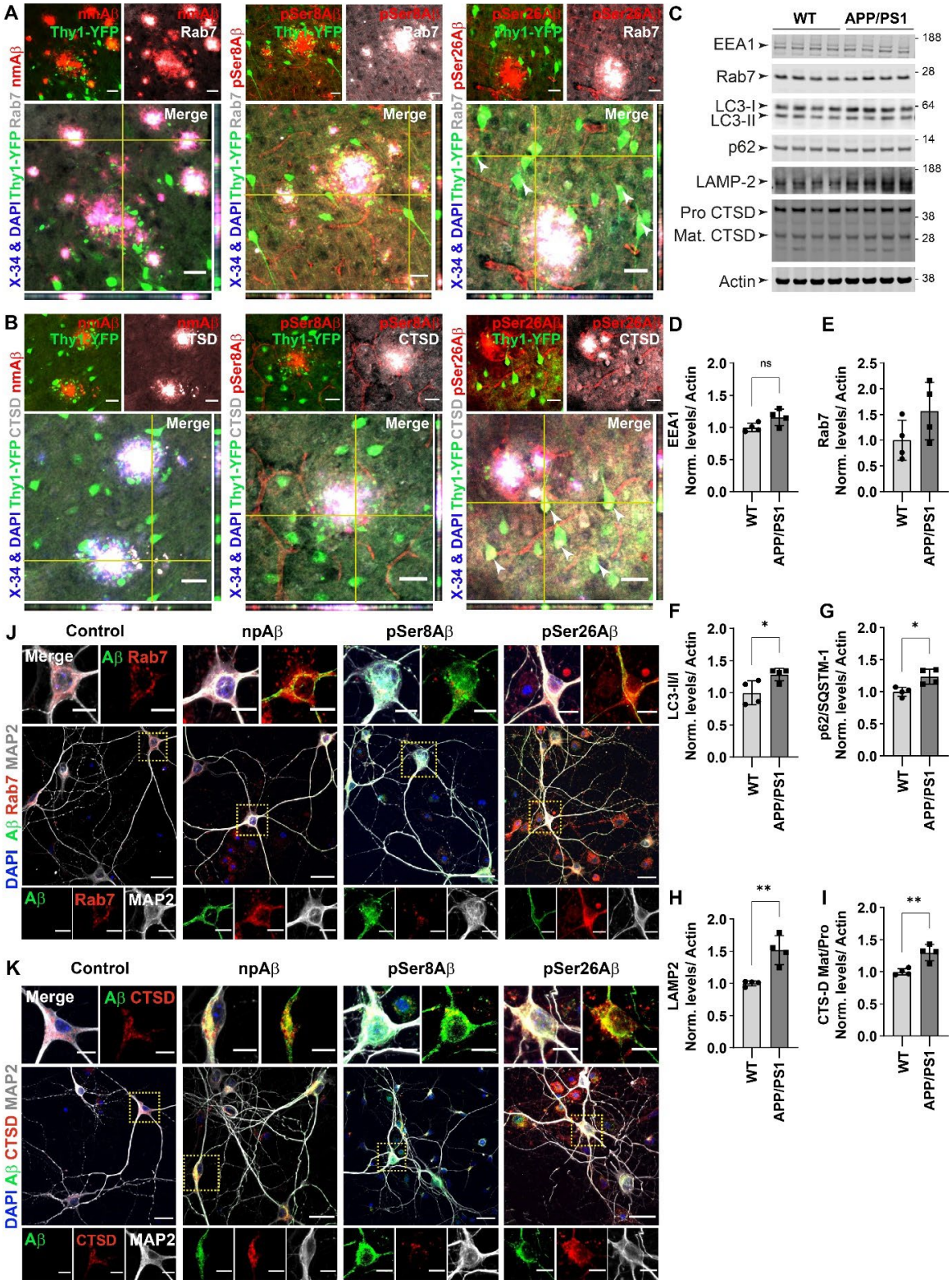

Ext. Fig. 5: A, B. Immunohistochemical staining of late endosomal protein RAB7 (**A**, *gray channel*) and luminal protease Cathepsin D (CTSD, **B**, *gray*) along with different phosphorylation state specific Aβ antibodies (nmAβ: 7H3D6; pSer8Aβ: 1E4E11 and pSer26Aβ: 5H11C10, *red channels respectively*) in brain sections of APP-PSEN1delE9xThy1-YFP transgenic mouse cortex. Blue channel depicts staining of nuclei

and fibrillar Aβ with DAPI and X-34, respectively. Scale bar: 50 μm. White arrowheads indicate colocalized punctate staining between red and gray channels in Thy1-YFP positive neurons. **C-I.** Western Immunoblotting (**C**) and densitometric quantification of early endosomes, EEA1 (**D**), late endosomes, RAB7 (**E**); autophagic vesicle markers, LC3-II/I (**F**), p62/SQSTM-1 (**G**); lysosomes, LAMP-2 (**H**) and active cathepsin-D, CST-D mature/pro (**I**). Actin depicts the amount of loaded protein per well. A total of four different mouse brains per cohort were loaded in different wells and analyzed as independent samples per condition. N = 4. * $p < 0.05$; ** $p < 0.01$; *** $p < 0.001$; **** $p < 0.0001$; n.s. $p \geq 0.05$, not significant (Student's *t*-test, GraphPad Prism). **J, K.** Primary cortical neurons were incubated with the indicated Aβ variants (500 nM, 4 h) and co-stained with antibodies against the microtubule-associated protein (MAP2 neuronal marker, *gray*), Aβ (82E1, *green*) and RAB7 (**J**, *red*) and CTSD (**K**, *red*). Nuclei were additionally stained with DAPI (*blue*). Scale bar, 10 μm. Dotted boxes indicate the region zoomed in the merged panels (*above*) and individual channels (*below*). Figure adapted from Kapadia et al. 2024.

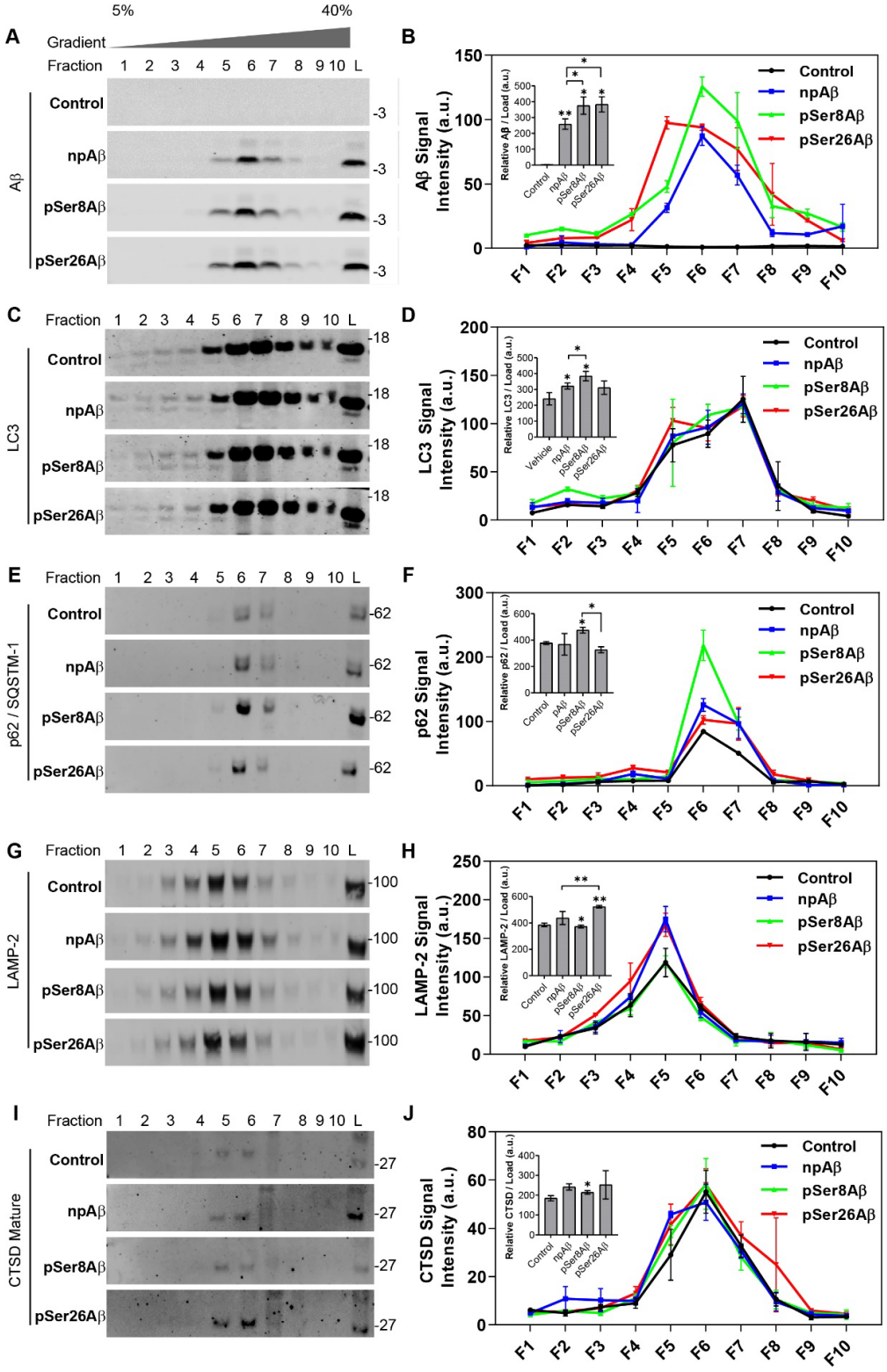

Ext. Fig. 6: A, C, E, G, I. SH-SY5Y cells were treated without (control) or with Aβ variants (1 µM, 24 h) and subjected to subcellular fractionation by density gradient centrifugation. Western immunoblotting was used to detect the density dependent fractionation of Aβ (**A**); LC3-I and II (**C**); p62/SQSTM-1 (**E**); LAMP-2 (**G**) and mature CTSD (**I**). L, protein load. Results are representative of two independent experiments. **B, D, F, H, J.** Line plots

represent quantification of signals for Aβ (**B**); LC3 (**D**); p62/SQSTM-1 (**F**); LAMP-2 (**H**) and mature CTSD (**J**); per fraction; total load (inset, bar plots) indicates the total protein load before fractionation. Values represent mean ± S.E.M.; n = 4, N = 2. * $p < 0.05$; ** $p < 0.01$; *** $p < 0.001$; **** $p < 0.0001$; n.s. $p \geq 0.05$, not significant (One-way ANOVA, GraphPad Prism).

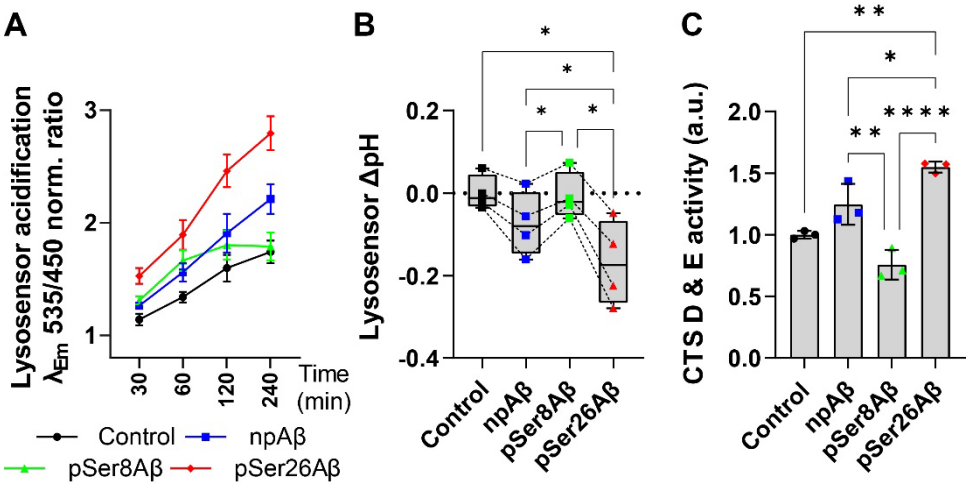

Ext. Fig. 7: A-B. Primary cortical neurons loaded with lysosensor-dextran complex were treated without or with the indicated Aβ variants (500 nM, 4 h). **A**. Line plots represent time-dependent lysosomal acidification from the cell lysates. SH-SY5Y cells (50 μM lysosensor + 500 nM Aβ variants) were analyzed in a multi-well plate reader at the mentioned time points. Readings were normalized to cells incubated only with the lysosensor. Fluorescence emission intensities were measured at λ_{Ex} 380 nm and ratio at λ_{Em} 535, and 450 nm was computed. Values were normalized to control cells and presented as mean ± S.E.M.; n = 12, N = 4. Box plot (**B**) Change in lysosensor pH (ΔpH) was quantified using the formula $\Delta pH = pH_{final}$ (control/Aβ, t = 4 h) − $pH_{initial}$ (control, t = 0 h). Box plot depicts the overall distribution of data, and each data point represents average values from an independent experiment; n = 12, N = 4, (Repeated measures one-way ANOVA, GraphPad Prism). **C.** Primary cortical neurons treated with Aβ variants (500 nM, 4 h) or without (control) were examined for cathepsin-D & E activity (per μg of total cellular protein) using a CTS D & E cleavable fluorogenic substrate. Readings were normalized to control cells; values represent mean ± S.D.; n = 6, N = 3. * $p < 0.05$; ** $p < 0.01$; *** $p < 0.001$; **** $p < 0.0001$; n.s. $p \geq 0.05$, not significant (One-way ANOVA, GraphPad Prism). Figure adapted from Kapadia et al. 2024.

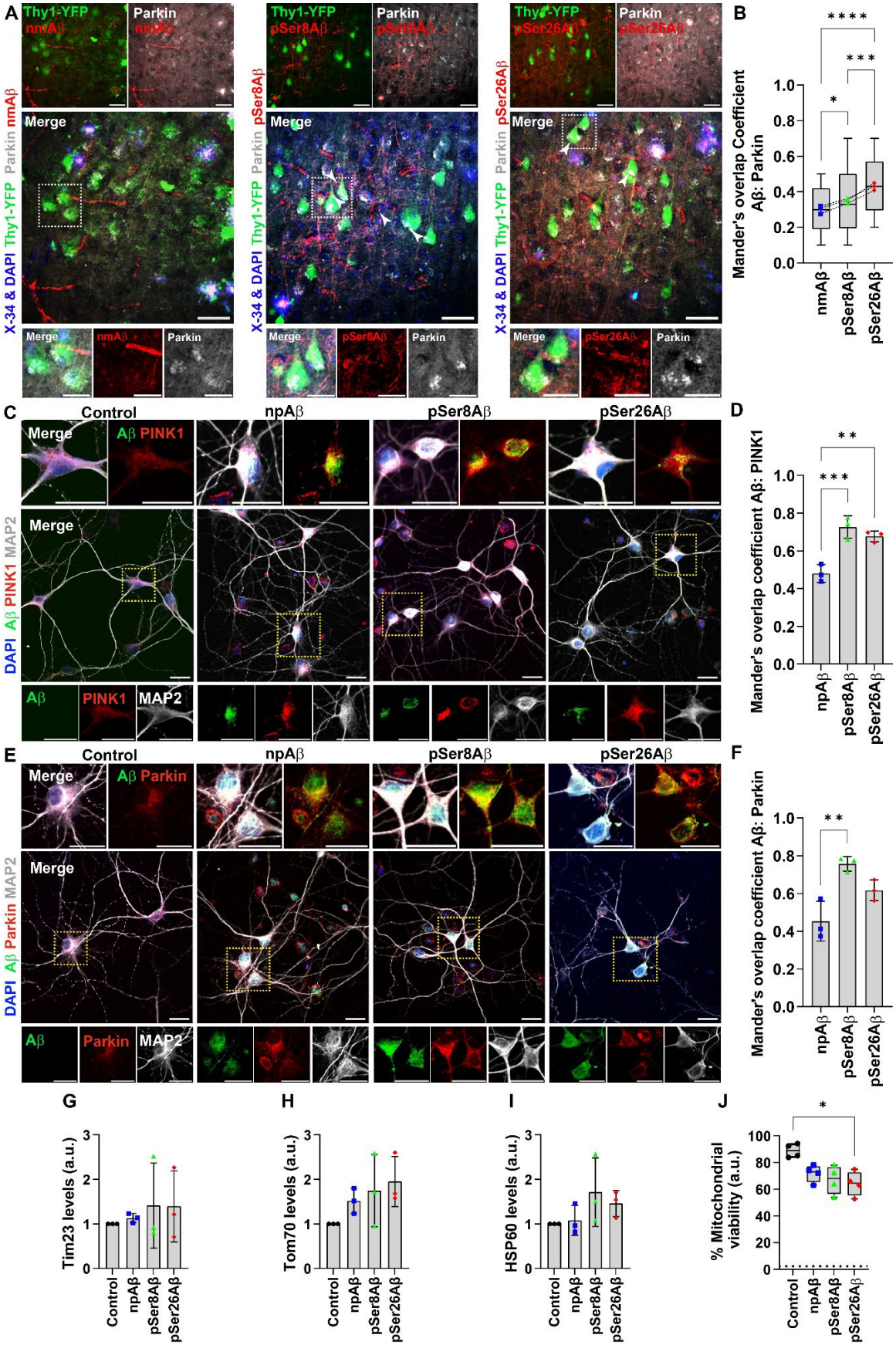
A
Thy1-YFP nmAβ
Parkin nmAβ
Merge
X-34 & DAPI Thy1-YFP Parkin nmAβ
Merge nmAβ Parkin
Thy1-YFP pSer8Aβ
Parkin pSer8Aβ
X-34 & DAPI Thy1-YFP Parkin pSer8Aβ
Merge pSer8Aβ Parkin
Thy1-YFP pSer26Aβ
Parkin pSer26Aβ
X-34 & DAPI Thy1-YFP Parkin pSer26Aβ
Merge pSer26Aβ Parkin
B
Mander's overlap Coefficient Aβ: Parkin
nmAβ
pSer8Aβ
pSer26Aβ
C
Control
npAβ
pSer8Aβ
pSer26Aβ
Merge Aβ PINK1
DAPI Aβ PINK1 MAP2
Aβ PINK1 MAP2
D
Mander's overlap coefficient Aβ: PINK1
E
Merge Aβ Parkin
DAPI Aβ Parkin MAP2
Aβ Parkin MAP2
F
Mander's overlap coefficient Aβ: Parkin
G
Tim23 levels (a.u.)
H
Tom70 levels (a.u.)
I
HSP60 levels (a.u.)
J
% Mitochondrial viability (a.u.)

Ext. Fig. 8: A-B. Immunohistochemical staining (**A**) depicting intraneuronal colocalization of Aβ species in brain sections of APP-PSEN1delE9xThy1-YFP transgenic mouse cortex (7.3 m, female) stained with different phosphorylation state specific Aβ antibodies (nmAβ- 7H3D6, pSer8Aβ- 1E4E11 and pSer26Aβ- 5H11C10; *red channels respectively*) along with antibody against mitochondrial marker protein, Parkin (*gray*) and DAPI + X-34 (nuclei and plaque core, *blue*). Scale bar: 50 μm; zoomed panels, 10 μm. White arrowheads indicate colocalized punctate staining between red and gray channels in Thy1-YFP positive neurons. Box plot (**B**) depicting Mander's coefficient of overlap between red channels (npAβ, *blue*; pSer8Aβ, *green* and pSer26Aβ, *red data points*) with respect to gray channels (Parkin), quantified within Thy1-YFP positive neurons respectively. Box plot depicts the overall distribution of data, and each data point represents average values from an individual mouse, N = 3 transgenic mice. **C-F**. Immunocytochemistry of primary cortical neurons were incubated without (control) or with the indicated Aβ variants (500 nM, 4 h) and co-stained with antibodies against the microtubule-associated protein 2 (MAP2, *gray*), Aβ (82E1, *green*) and PINK1 (**C**, *red*) or Parkin (**E**, *red*). Nuclei were stained with DAPI (*blue*). Scale bar, 10 μm. Dotted boxes indicate the regions zoomed in the merged panels (*above*) and individual channels (*below*). Bar plots depicting Mander's overlap coefficients between Aβ (*green channel*) with PINK1 (**D**) and Parkin (**F**) (*respective red channels*), analyzed by the Fiji ImageJ colocalization processing module. Values represent mean ± S.D.; n = 6, N = 3. **G-I.** Quantification of western immunoblot data of mitochondrial proteins from SH-SY5Y cells upon treatment without (control) or with the indicated Aβ variants (1 μM, 24 h). Values represent mean ± S.E.M.; n = 6, N = 3. **J.** Box plot depicting percent mitochondrial viability of SH-SY5Y cells treated with Aβ variants (1.11 μM, 24 h) or without (control) in presence of glucose containing media, examined using a Mitochondrial ToxGlo™ assay kit. Readings were normalized to untreated cells (growth medium) and represented as percent control; individual points depict the average values from each individual experiment; n = 8, N = 4. * $p < 0.05$; ** $p < 0.01$; *** $p < 0.001$; **** $p < 0.0001$; n.s. $p \geq 0.05$, not significant (One-way ANOVA, GraphPad Prism).

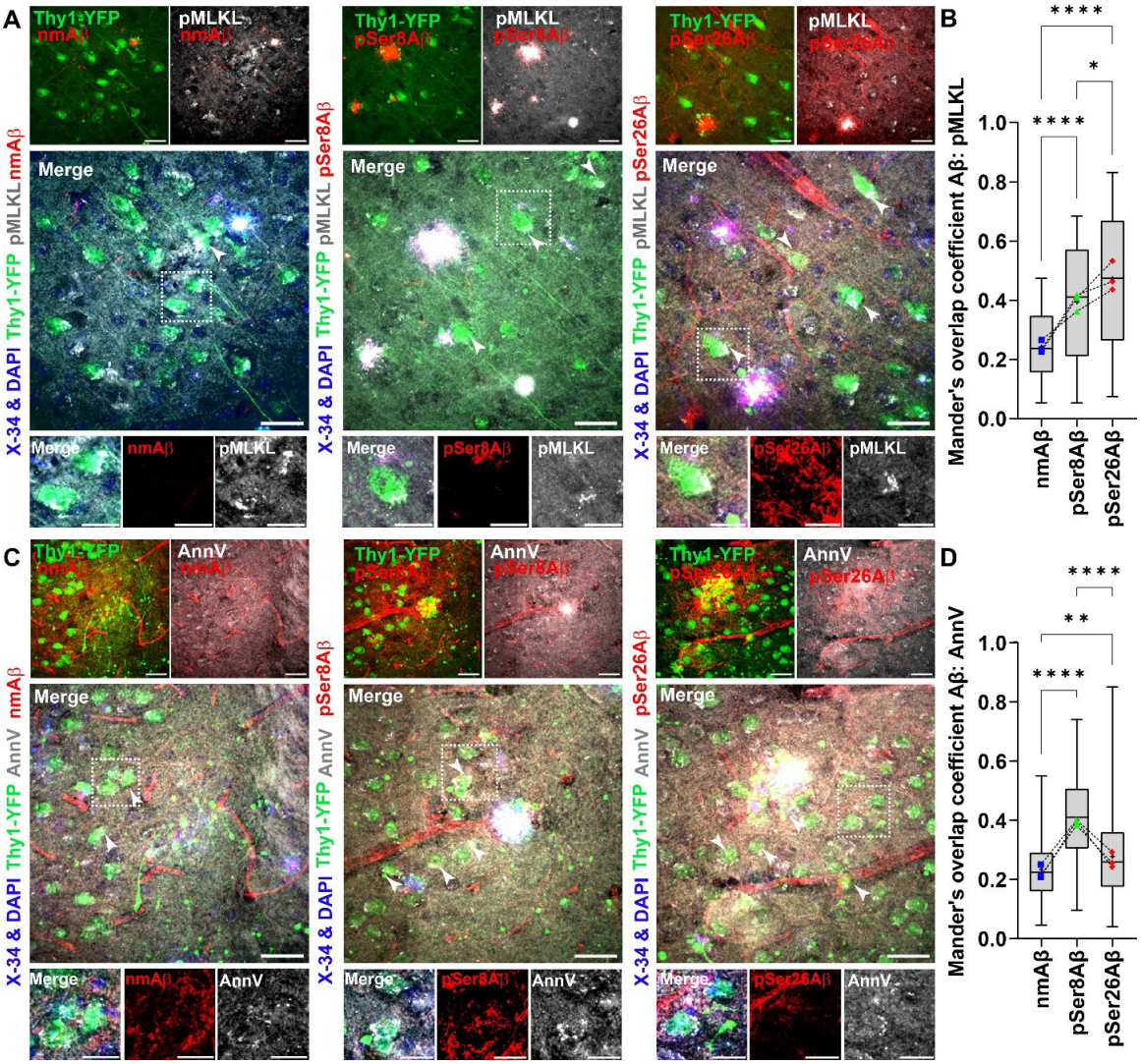

Ext. Fig. 9: A-D. Immunohistochemical staining depicting intraneuronal colocalization of Aβ species in brain sections of APP-PSEN1delE9xThy1-YFP transgenic mouse cortex (7.3 m, female) stained with different phosphorylation state specific Aβ antibodies (nmAβ- 7H3D6, pSer8Aβ- 1E4E11 and pSer26Aβ- 5H11C10; *red channels respectively*) along with antibody against phosphorylated- mixed lineage kinase domain-like protein, p-MLKL (*gray,* **A**) and AnnexinV, AnnV (*gray,* **C**) and. DAPI + X-34 were used to stain nuclei and plaque core (*blue*), respectively. Scale bar: 50 µm; zoomed panels, 10 µm. White arrowheads indicate colocalized punctate staining between red and gray channels in Thy1-YFP positive neurons. Box plot depicting Mander's coefficient of overlap between red channels (npAβ, *blue*; pSer8Aβ, *green* and pSer26Aβ, *red data points*) with respect to gray channels (p-MLKL, **B** and AnnV, **D**), quantified within Thy1-YFP positive neurons respectively. Box plot depicts the overall distribution of data, and each data point represents average values from an individual mouse, N = 3 transgenic mice. Values represent mean ± S.E.M. * $p < 0.05$; ** $p < 0.01$; *** $p < 0.001$; **** $p < 0.0001$; n.s. $p \geq 0.05$, not significant (One-way ANOVA, GraphPad Prism).

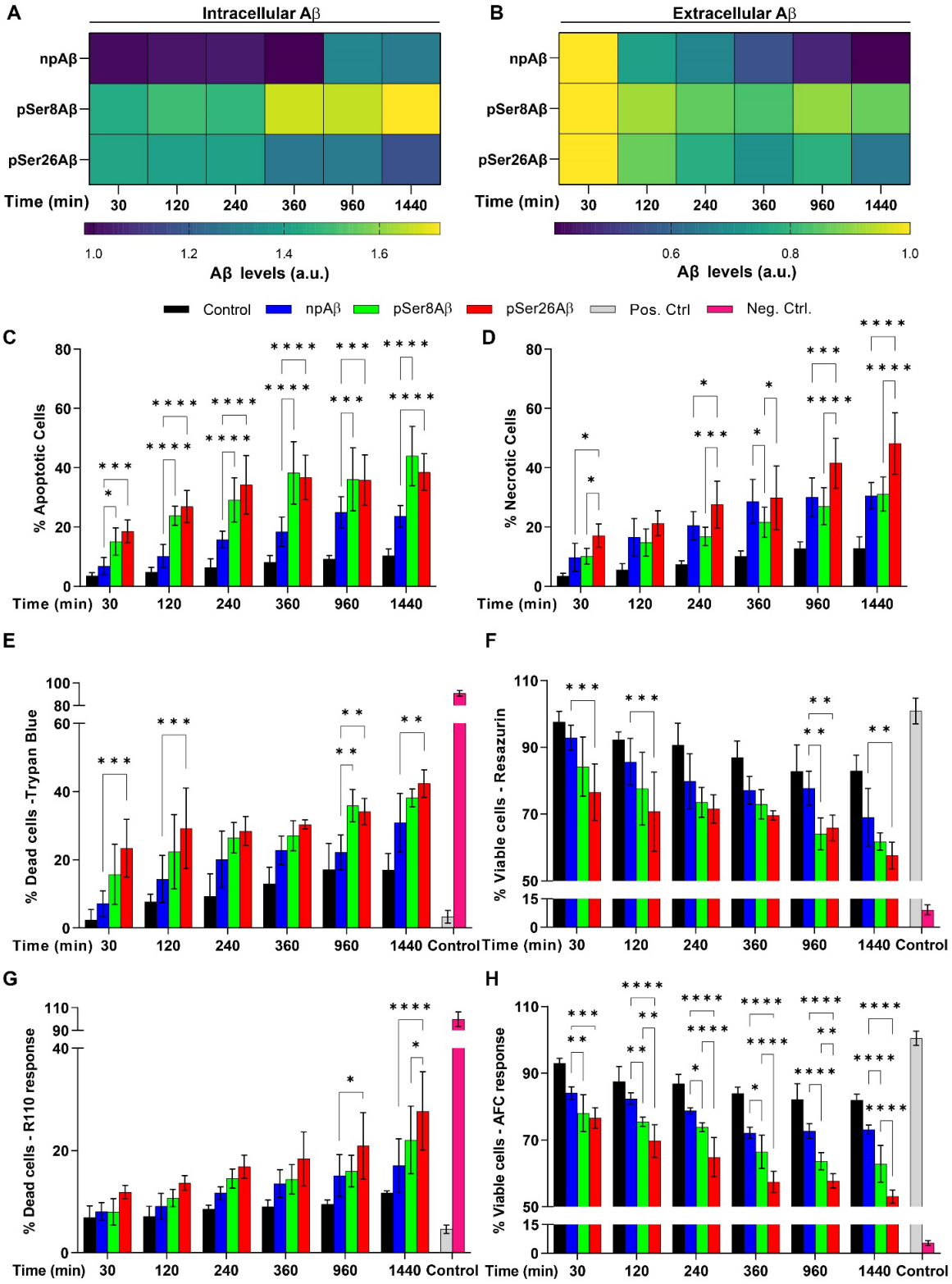

Ext. Fig. 10: A-B. Time dependent quantification of amount of Aβ internalized by the cells (**A**) and Aβ remaining in the treatment media after treatment time (**B**), quantified using indirect ELISA of cell lysates and treatment media respectively. Aβ antibody 82E1 was used to detect Aβ. Readings were normalized to the total protein content and the respective volume of cell supernatant used. Values are depicted as fold increase to the

npAβ content at 30 min of treatment time, respectively. **C-D**. Time dependent quantification of percent apoptotic (stained with AnnV, **C**) or necrotic (stained with PI, **D**) cell death induced by Aβ in SH-SY5Y cells. Readings have been normalised to untreated cells treated with normal growth media (positive control) and represented as percent change. Cells treated with methanol for 10 min were used as dead cell control. Readings were normalized to control cells; values represent mean ± S.D.; n = 6, N = 3. **E-H.** Time dependent quantitative analyses of percent dead (**E, G**) and percent viable (**F, H**) cells analyzed using different cytotoxicity assays using SH-SY5Y cells treated with 1 μM of Aβ variants for the mentioned time points. Readings were normalized to control cells; values represent mean ± S.D.; n = 6, N = 3. * $p < 0.05$; ** $p < 0.01$; *** $p < 0.001$; **** $p < 0.0001$; n.s. $p \geq 0.05$, not significant (Two-way ANOVA, GraphPad Prism).

Ext. Fig. 11 *(legend continued)***:** respectively. Values represent mean ± S.D., from four different mouse brains per cohort, from two independent experiments, n = 4 mice, N = 2. * $p < 0.05$; ** $p < 0.01$; *** $p < 0.001$; **** $p < 0.0001$; n.s. $p \geq 0.05$, not significant (Two-way ANOVA, GraphPad Prism). **G.** Representative images for primary antibody controls, depicting the cortical regions of WTxCX_3CR1-GFP non-transgenic mouse stained for pSer8Aβ (1E4E11, *red*) or pSer26Aβ (5H11C10, *red*), along with nmAβ (7H3D6, *gray*) and DAPI + X-34 (nuclei + plaque core, *blue*). Scale bar, 100 μm. **H.** Representative images for secondary antibody controls; depicting the cortical regions of APP-PSEN1delE9xCX_3CR1-GFP transgenic mouse stained with donkey anti-mouse IgG - Alexa Fluor™ 647 (*red*) and donkey anti-rat IgG - Alexa Fluor™ 647 (*gray*) along with DAPI + X-34 (nuclei + plaque core, *blue*). Scale bar, 50 μm.

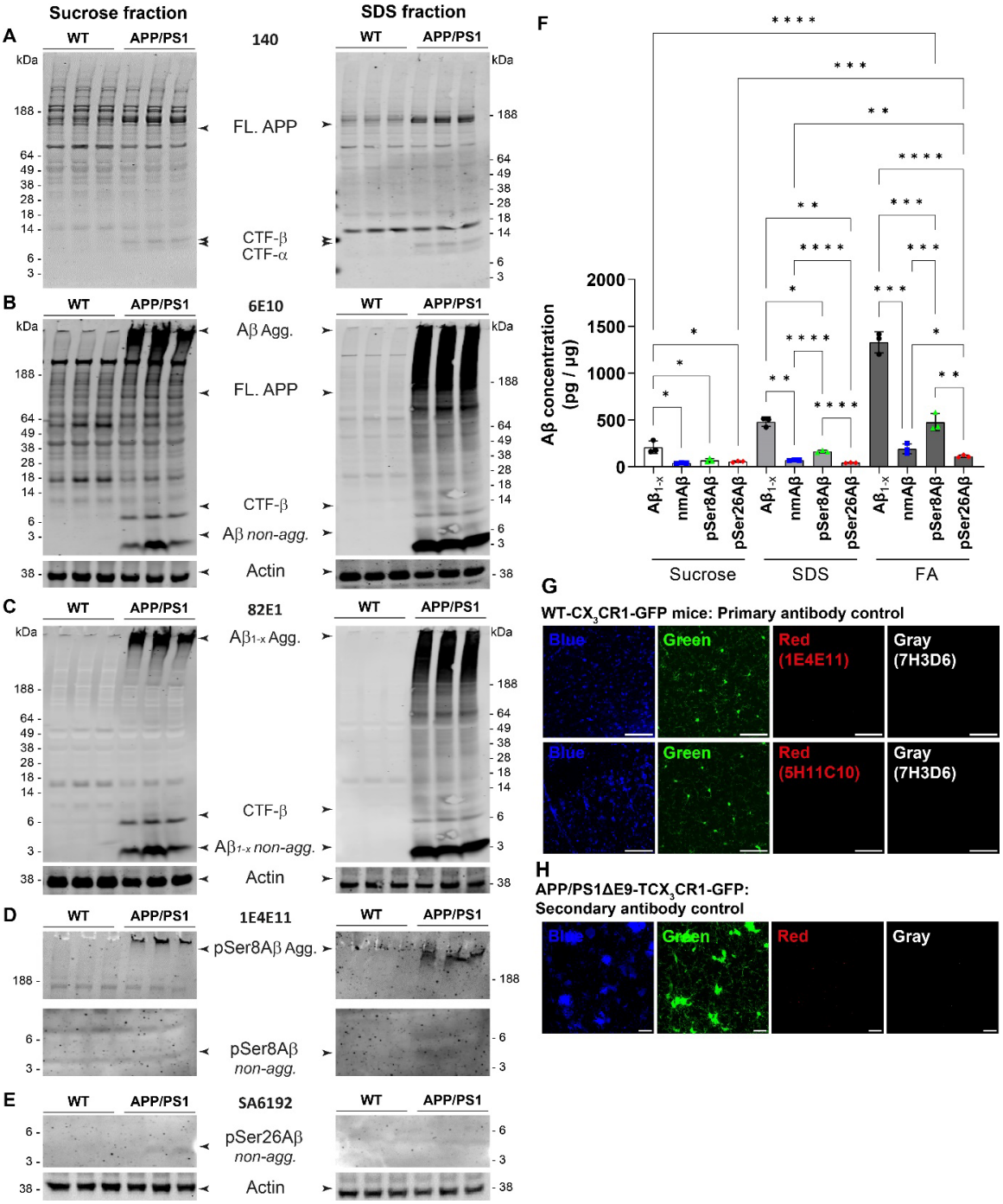

Ext. Fig. 11: A-E. Western immunoblotting analyses of sucrose soluble and SDS soluble fractions of wild type WTxCX3CR1-GFP and transgenic APP-PSEN1delE9xCX3CR1-GFP mouse brains (Tab. **1**, mouse ID 9-14). APP and APP derivatives were detected in parallel primary antibodies 140 (**A**) and 6E10 (**B**), respectively, using LiCOR fluorescence imaging. Aβ species and APP β-CTF were detected with anti-Aβ antibody 82E1 (**C**). pAβ species were independently detected with in house generated 1E4E11 (pSer8Aβ, **D**) and SA6192 (pSer26Aβ, **E**) antibodies, respectively. Actin was used as loading control respectively. **F**. Bar plots depicting the quantification of Aβ levels (pg/µg) in sucrose, SDS and FA soluble fractions by ELISA using phosphorylation state specific antibodies,

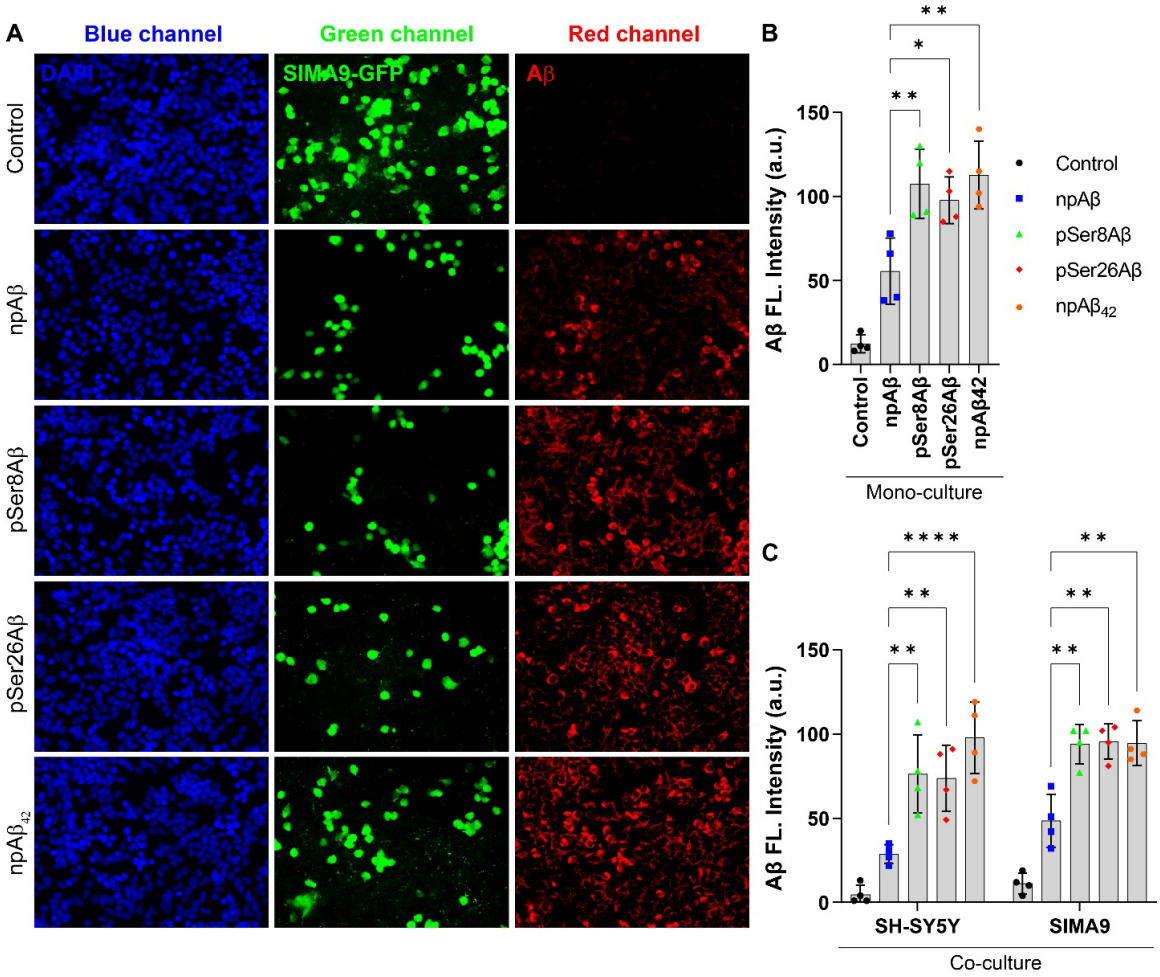

Ext. Fig. 12: A-C. SH-SY5Y cells pre-treated with synthetic Aβ variants (1 µM, 6h) were co-cultured with GFP tagged microglial SIMA9 cells for 18 h. Co-cultured cells were stained with anti-Aβ antibody 82E1 and analyzed via immunocytochemistry (**A**). Data is representative of two independent experiments. Bar plots depicting average values of absolute fluorescence intensities in the green channel (Aβ signals) in SH-SY5Y cells (monoculture, **B** and co-culture, **C**) and microglial SIMA9 cells (co-culture, **C**), analyzed by immunocytochemistry. Values represent mean ± S.D.; n = 4, N = 2. * $p < 0.05$; ** $p < 0.01$; *** $p < 0.001$; **** $p < 0.0001$; n.s. $p \geq 0.05$, not significant (One-way ANOVA, GraphPad Prism).

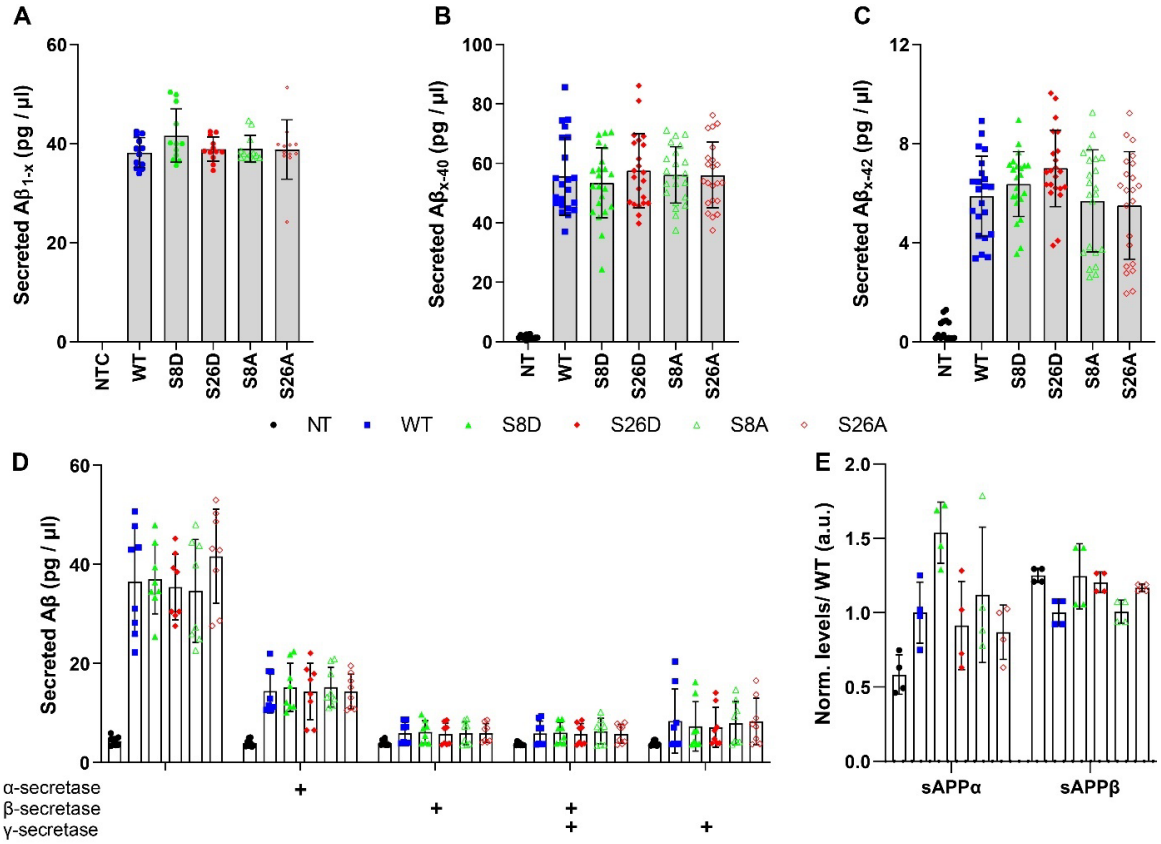

Ext. Fig. 13: A-C. Cell culture medium of the SH-SY5Y-APP$_{Sw}$ cells was replaced with serum-free medium for secretion of Aβ for 24 h. Conditioned media was subjected indirect ELISA analyses using different epitope specific Aβ or sAPP antibodies. **A.** Anti-Aβ$_{1-x}$ antibody 82E1 was used for detection of Aβ, n = 12, N = 4. **B**. Anti-Aβ$_{x-40}$ BAP-29 (in house generated) antibody was used for detection of Aβ$_{x-40}$, n = 16, N = 4. **C**. Anti-Aβ$_{x-42}$ BAP-15 (in house generated) antibody was used for detection of Aβ$_{x-42}$, n = 16, N = 4. **D.** SH-SY5Y-APP$_{Sw}$ transgenic cells were either treated without or with α-secretase, β-secretase, γ-secretase and β + γ secretase together, respectively, as indicated; and evaluated for Aβ content using Aβ antibody 82E1. n = 8, N = 4. **E.** Anti-sAPPα and sAPPβ (in house generated) antibodies were used to detect sAPP species in the conditioned media, n = 4, N = 2. In all experiments readings were normalized to the total cell protein content and volume of the supernatant. Values represent Mean ± S. E. M; * $p < 0.05$; ** $p < 0.01$; *** $p < 0.001$; **** $p < 0.0001$; n.s. $p \geq 0.05$, not significant (One-way ANOVA, GraphPad Prism). All data and analyses depicted herewith is representative from four independent experiments consisting of three technical replicates. Stable cells were evaluated from different passage numbers and varying freeze thaw cycles.

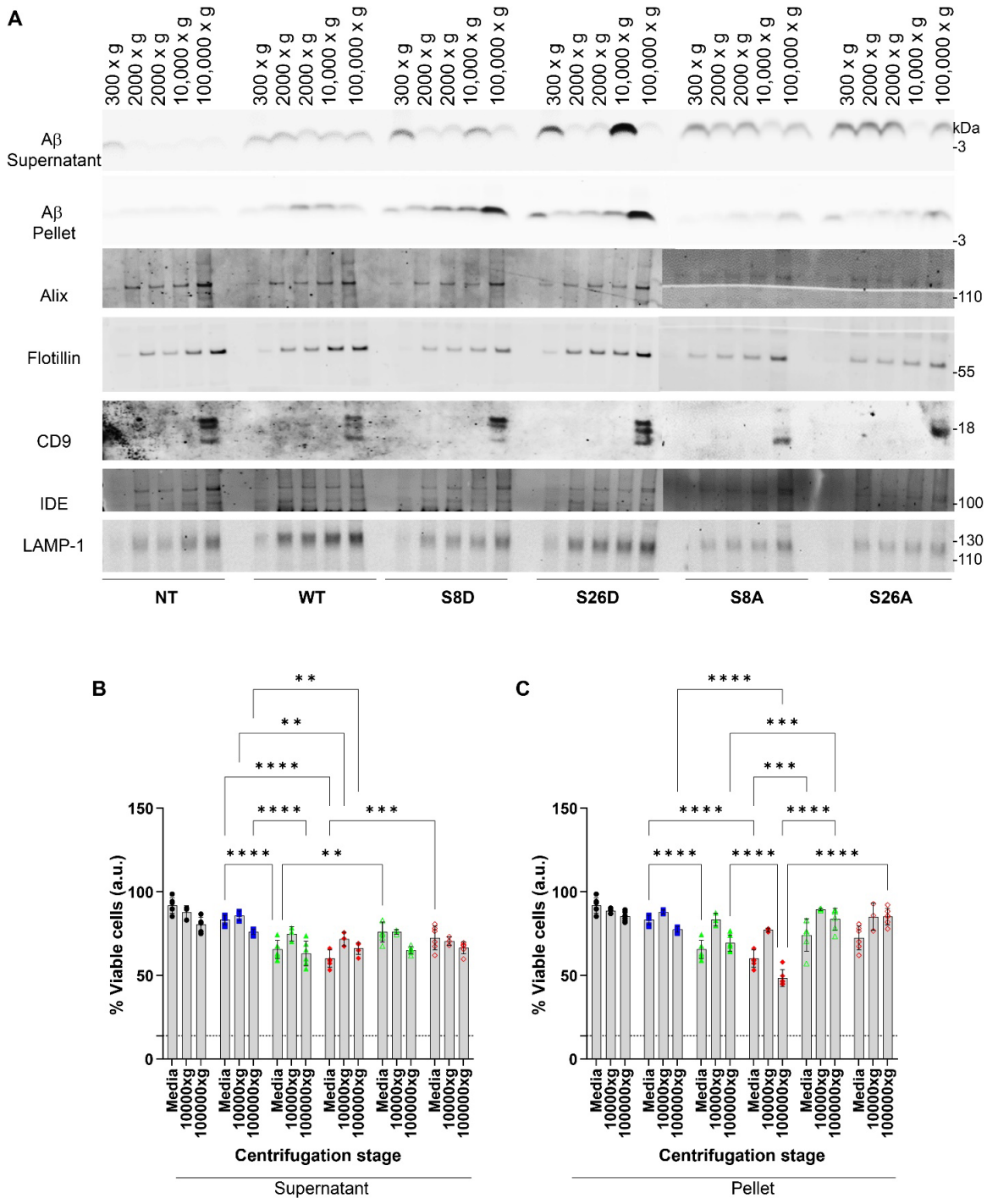

Ext. Fig. 14: A. Cell culture medium of SH-SY5Y-APP$_{Sw}$ cells was replaced with serum-free medium for secretion of Aβ for 24 h. Conditioned media was further subjected to differential centrifugation steps (*indicated*) to enrich crude exosomes at 10,000 *g* and 100,000 *g* fractions. Western immunoblotting of Aβ in supernatant and pellet fraction. Exosomal markers like Alix/AIP1, Flotillin-1, CD9, along with insulin degrading enzyme (IDE) and LAMP-1 were detected in differentially centrifuged pellet fractions, respectively. data is representative of three independent experiments. **B-C.** Supernatant (**B**) and pellet (**C**) fractions post-differential centrifugation at 300 *g* (media), 10,000 *g* and 100,000 g;

were further used to treat neuronal SH-SY5Y cells for 18 h. Cell viability was then evaluated using Presto Blue cell viability reagent. Readings were normalized to untreated cell control and depicted as percent change number of viable cells. Values represent Mean ± S. E. M., n = 4, N = 2; * $p < 0.05$; ** $p < 0.01$; *** $p < 0.001$; **** $p < 0.0001$; n.s. $p \geq 0.05$, not significant (One-way ANOVA, GraphPad Prism).

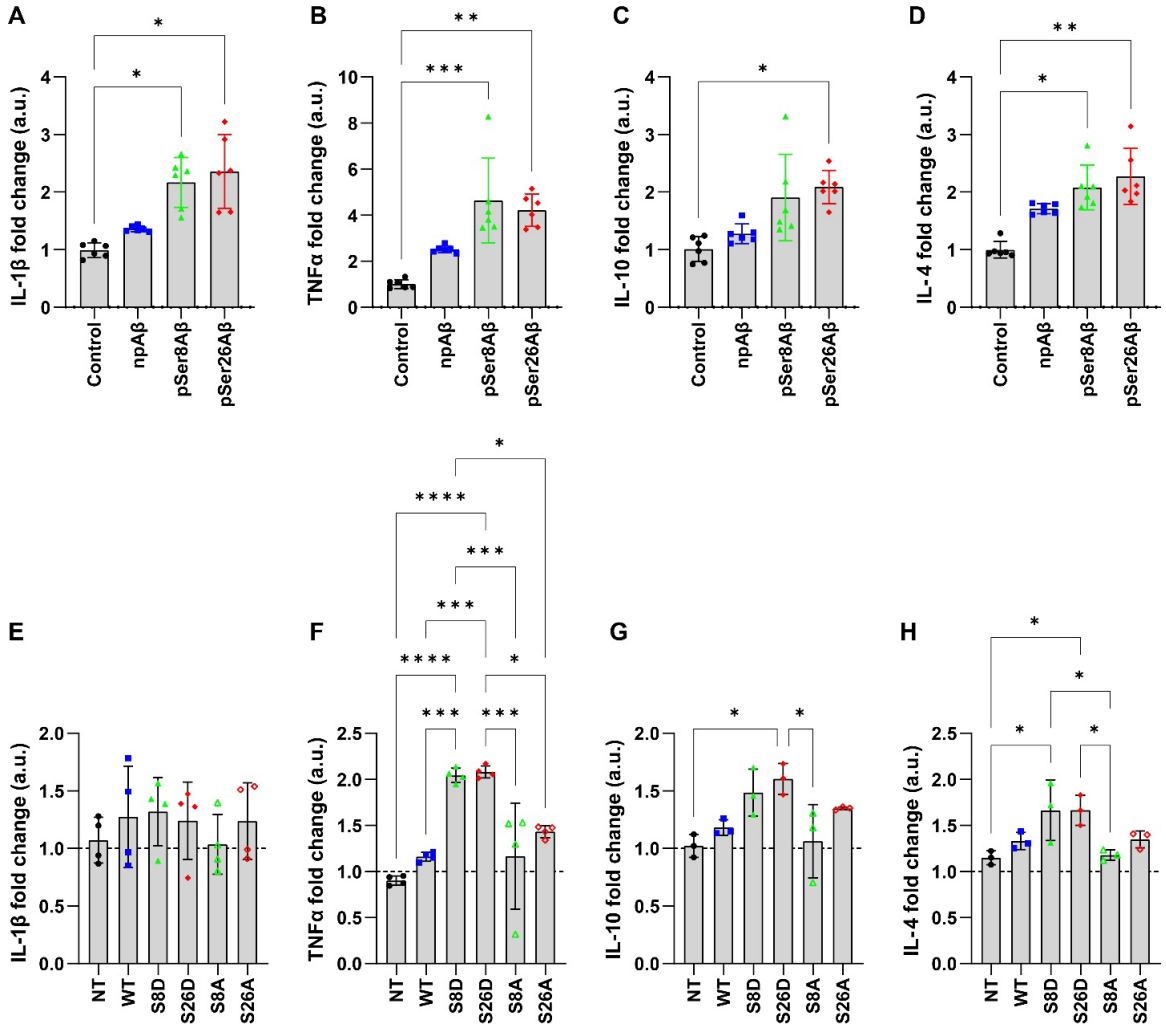

Ext. Fig. 15: SIMA9 cells (**A-D**) were treated without (control) or with Aβ variants (1μM, 24 h) and levels of pro-inflammatory markers IL-1β (**A**), TNFα (**B**) and anti-inflammatory markers IL-10 (**C**), IL-4 (**D**) using in-house ELISA method, were analyzed. Values represent Mean ± S. E. M., n = 18, N = 6. SH-SY5Y-APP$_{Sw}$ cells (**E-H**) used for conditioning serum free medium for 24 h, were analyzed for different inflammation markers using respective ELISA systems. Values represent Mean ± S. E. M., n = 8, N = 4 (E-F); n = 6, N = 3 (G-H). All readings were normalized to control untreated cells and represented as fold-change *wrt* control. * $p < 0.05$; ** $p < 0.01$; *** $p < 0.001$; **** $p < 0.0001$; n.s. $p \geq 0.05$, not significant (One-way ANOVA, GraphPad Prism).

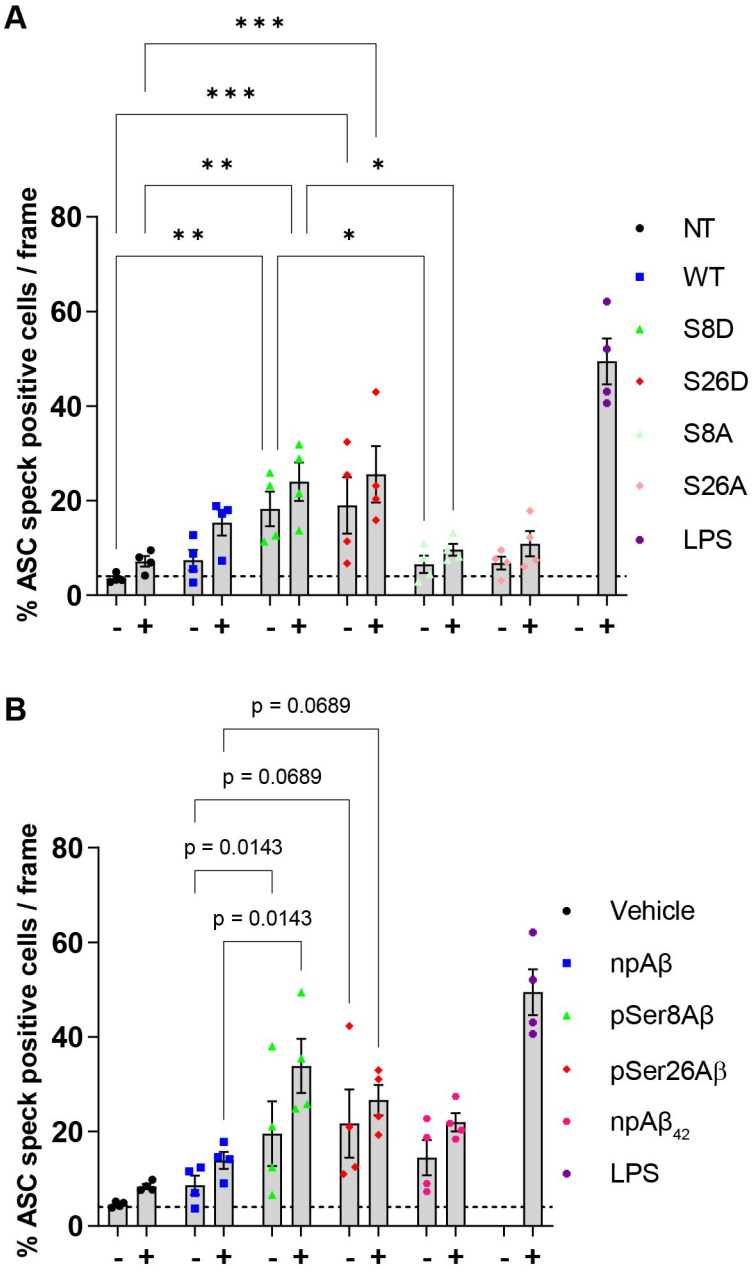

Ext. Fig. 16: A. SIMA9 cells expressing ASC-Cerulean reporter construct treated with 24 h SH-SY5Y-APP$_{Sw}$ cell conditioned media for 18 h, in the presence or absence of lipopolysaccharides (LPS: 2.5 ng/µl-priming; 100 ng/µl-positive control, 18 h). **B.** SIMA9 cells were treated with different Aβ variants (1 µM, 24 h) in the presence or absence of LPS. Control represents untreated cells (*dotted line*). ASC speck formation occurrence per frame was quantified by analyzing the number ASC specks to the number of cells per frame. Values represent mean ± S.E.M.; n = 4, N = 2. * $p < 0.05$; ** $p < 0.01$; *** $p < 0.001$; **** $p < 0.0001$; n.s. $p \geq 0.05$, not significant (Two-way ANOVA, GraphPad Prism).

Scheme 1: Workflow representation for preparation of different cellular protein fractions analyzed in this work.

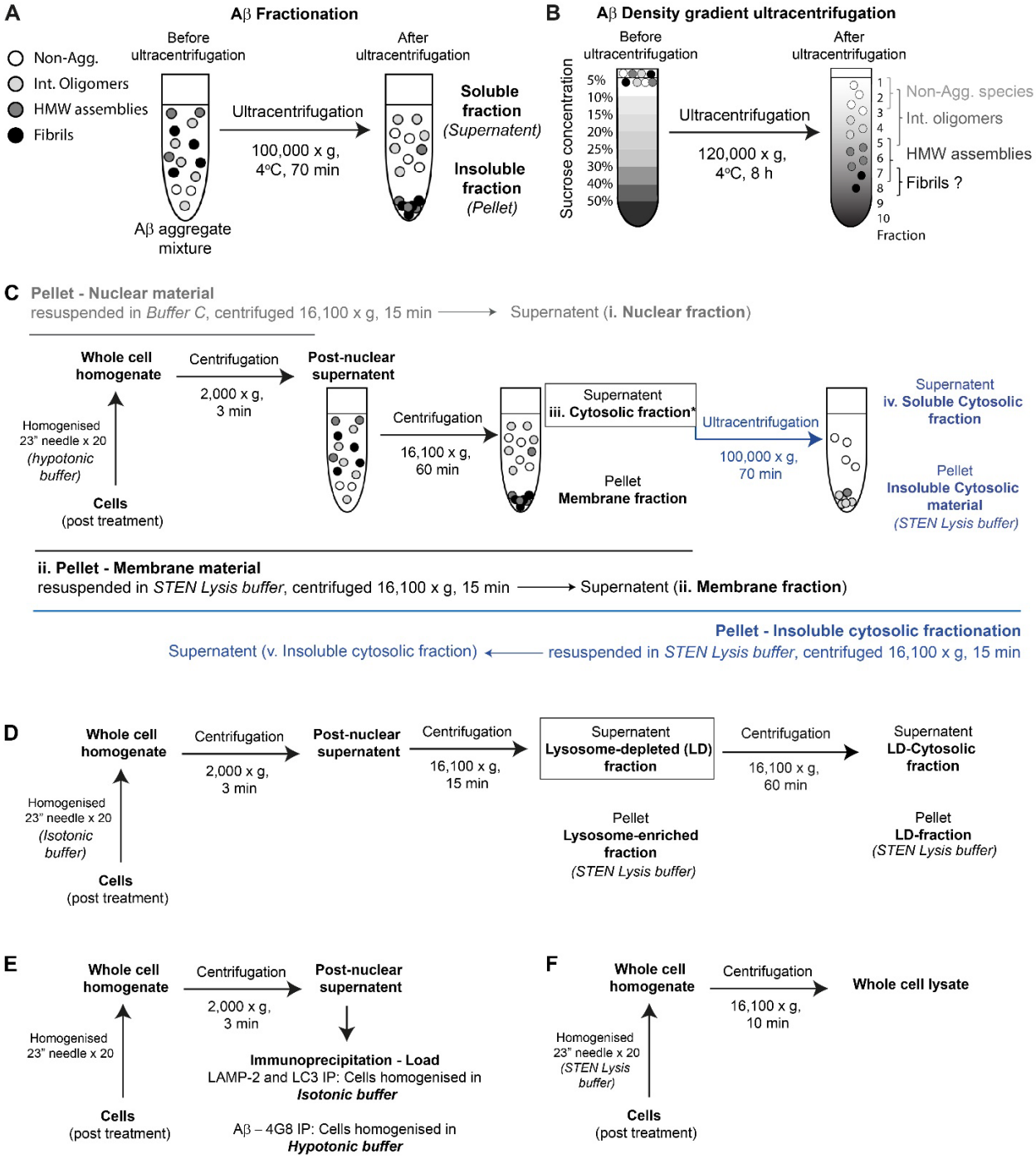

Tab. 3: Quantification of Aβ levels in sucrose, SDS or formic acid (FA) soluble fractions by ELISA.

a. **WTxThy1-YFP and APP-PSEN1delE9xThy1-YFP mice** (n = 4 mice)

Aβ species	**Aβ concentration (pg / µg)**					
	Sucrose		**SDS**		**FA**	
	WT	**APP-PSEN1delE 9xThy1-YFP**	**WT**	**APP-PSEN1delE 9xThy1-YFP**	**WT**	**APP-PSEN1delE 9xThy1-YFP**
$Aβ_{1-x}$	0 ± 3.4	220.4 ± 61.8	0 ± 11	517.6 ± 72.3	0.8 ± 41.3	790.6 ± 93.5
nmAβ	0 ± 2.3	28 ± 4.8	0 ± 1.6	71.4 ± 4.5	0.3 ± 5.2	124.1 ± 18.2
pSer8Aβ	0 ± 6.8	85.8 ± 9.2	0 ± 2.5	162.6 ± 8.4	0.6 ± 10.1	338 ± 39.3
pSer26Aβ	0 ± 5.7	64.5 ± 3.3	0 ± 0.6	42.9 ± 4	0.2 ± 2.6	69.3± 11.2

b. **WTxCX$_3$CR1-GFP and APP-PSEN1delE9xCX$_3$CR1-GFP mice** (n = 3 mice)

Aβ species	**Aβ concentration (pg / µg)**					
	Sucrose		**SDS**		**FA**	
	WT	**APP-PSEN1delE 9xCX$_3$CR1-GFP**	**WT**	**APP-PSEN1delE 9xCX$_3$CR1-GFP**	**WT**	**APP-PSEN1delE 9xCX$_3$CR1-GFP**
$Aβ_{1-x}$	0.7 ± 4.8	208.8 ± 65.5	1.3 ± 6.1	480.9 ± 123.3	33.3 ± 12.7	1328.9 ± 154.6
nmAβ	0 ± 1.6	39.3 ± 2.9	1.2 ± 1.1	70.4 ± 2.8	6 ± 4.6	191.7 ± 48.5
pSer8Aβ	0 ± 3.4	68.7 ± 21.8	0.6 ± 2.4	162.1 ± 12.5	20.7 ± 6.2	474.3 ± 86.9
pSer26Aβ	0 ± 1	54.9 ± 9.1	1.3 ± 1	42.8 ± 3.7	8.3 ± 13.4	112.2 ± 13.5

Aβ species in different fractions were captured with either generic anti-$Aβ_{1-x}$ (82E1); anti-nmAβ (7H3D6); phosphorylation state specific antibodies; anti-pSer8Aβ (1E4E11) and anti-pSer26Aβ (5H11C10), respectively. Bound Aβ was detected with biotin conjugated anti-Aβ (4G8) detection antibody. Raw values were normalised to respective WTxCX$_3$CR1-GFP mouse brain fractions and values represent mean ± S.D, from four different mouse brains per cohort, from two independent experiments, N = 2.

Tab. 4: Levels of different marker proteins in autophagy and endo-lysosomal pathway analyzed by SDS-PAGE and immunoblotting of membrane and cytosolic* fractions from primary cortical neurons.

	Control	**npAβ**	**pSer8Aβ**	**pSer26Aβ**
EEA1*	1 ± 0.05	1.22 ± 0.15	1.65 ± 0.21	1.28 ± 0.12
Rab5*	1 ± 0.02	1.08 ± 0.07	1.26 ± 0.09	1.47 ± 0.11
Rab7*	1 ± 0.09	1.1 ± 0.08	0.95 ± 0.17	1.25 ± 0.12
Rab11*	1 ± 0.05	1.47 ± 0.22	1.75 ± 0.29	1.89 ± 0.06
LAMP2	1 ± 0.04	1.16 ± 0.08	0.97 ± 0.06	1.23 ± 0.07
CTSD Mature*	1 ± 0.03	1.08 ± 0.07	0.94 ± 0.09	1.46 ± 0.11
CTSD Pro*	1 ± 0.02	0.99 ± 0.06	0.99 ± 0.04	1.19 ± 0.05
Atg14	1 ± 0.06	1.27 ± 0.08	1.17 ± 0.05	1.58 ± 0.17
ULK1/atg1	1 ± 0.06	1.37 ± 0.35	0.88 ± 0.22	1.74 ± 0.36
UBQ*	1 ± 0.08	1.36 ± 0.19	1.62 ± 0.14	2.11 ± 0.4
Atg5	1 ± 0.05	1.08 ± 0.11	1.18 ± 0.1	1.31 ± 0.11
Atg5/12	1 ± 0.04	1.04 ± 0.09	1.18 ± 0.2	1.43 ± 0.23
Atg12*	1 ± 0.09	1.07 ± 0.18	1.14 ± 0.29	1.35 ± 0.34
Atg3	1 ± 0.04	1.23 ± 0.21	1.23 ± 0.38	1.38 ± 0.32
LC3-I	1 ± 0.04	1.37 ± 0.06	1.43 ± 0.15	1.45 ± 0.12
LC3-II	1 ± 0.06	1.48 ± 0.06	1.95 ± 0.14	1.42 ± 0.2
p62*	1 ± 0.04	1.19 ± 0.02	1.49 ± 0.06	1.41 ± 0.08

Primary cortical neurons were treated without (control) or with different Aβ variants (500 nM, 4 h) were subjected to membrane and cytosolic* fractionation. All raw values were normalised to Actin/GAPDH as loading controls and presented as fold change *wrt* control cells, values represent mean ± S.E.M.; n = 6, N = 3.

5. Abstract

Progressive accumulation of Aβ aggregates as extracellular plaques is a characteristic hallmark of AD. Alternative processing of APP and/or further peptidic cleavages, results in the generation of Aβ peptides with various lengths. In addition, multiple post-translationally modified Aβ variants have also been reported. Extracellular Aβ can be phosphorylated by secreted and cell-surface localized protein kinases, and phosphorylated Aβ (pAβ) peptides showed differential aggregation characteristics and exert higher cytotoxicity compared to the non-phosphorylated variant (npAβ). pAβ species also exhibit differential deposition in transgenic mouse models and human AD brains.

The research in this PhD project was focused on elucidating the molecular and cellular mechanisms that contribute to pAβ-associated neurotoxicity.

Primarily, the effect of phosphorylation on Aβ oligomerization properties was analyzed. The data indicate that Aβ phosphorylated at serine residue 8 (pSer8Aβ) formed higher molecular weight soluble oligomeric species. On the other hand, phosphorylation at serine residue 26 (pSer26Aβ), resulted in the formation of low and intermediate weight soluble oligomers. This behavior was completely different when compared to the insoluble fibrillar species formed by npAβ peptides. Importantly, pAβ variants exerted increased neurotoxicity as compared to the npAβ peptides.

Secondly, the impact of phosphorylation-state specific Aβ variants on neuronal autophagy and the endo-lysosomal pathway (ALP) as well as ubiquitin proteasomal systems (UPS), were investigated. The relation of pAβ species with respect to neuronal proteostasis (ALP and UPS) in an APP-PSEN1 transgenic AD mouse models, and as well as *in vitro* cell culture and primary neuronal models was examined. The results demonstrate that phosphorylation-state dependent intraneuronal accumulation and vesicular sorting of Aβ resulted in differential effects on the functioning of ALP, UPS, endoplasmic reticulum (ER) stress response, and mitochondria, suggesting a role in their contribution to neurotoxicity.

Lastly, the role of pAβ species in triggering microglia-associated neuroinflammation was investigated. The difference in deposition and accumulation of pAβ species in the context of microglial neuroinflammatory parameters was demonstrated in an APP-PSEN1 transgenic AD mouse model along with microglia cell culture models. The results show a

phosphorylation-state dependent differential effect on microglial Aβ uptake, homeostatic function as well as inflammasome activation.

Taken together, the combined results support important roles of pAβ species in molecular and cellular mechanisms that could contribute to neurodegenerative and neuroinflammatory processes in the pathogenesis of AD.

6. List of figures

7. List of tables

8. References

2023 Alzheimer's disease facts and figures. Alzheimer's & Dementia 2023; 19(4): 1598–695

Adams CJ, Kopp MC, Larburu N, Nowak PR, Ali MMU. Structure and Molecular Mechanism of ER Stress Signaling by the Unfolded Protein Response Signal Activator IRE1. Front Mol Biosci 2019; 6: 11

Aits S, Jäättelä M, Nylandsted J. Methods for the quantification of lysosomal membrane permeabilization: a hallmark of lysosomal cell death. Methods Cell Biol 2015; 126: 261–85

Albakova Z, Mangasarova Y, Albakov A, Gorenkova L. HSP70 and HSP90 in Cancer: Cytosolic, Endoplasmic Reticulum and Mitochondrial Chaperones of Tumorigenesis. Front Oncol 2022; 12: 829520

Aleksis R, Oleskovs F, Jaudzems K, Pahnke J, Biverstål H. Structural studies of amyloid-β peptides: Unlocking the mechanism of aggregation and the associated toxicity. Biochimie 2017; 140: 176–92

Alu A, Han X, Ma X, Wu M, Wei Y, Wei X. The role of lysosome in regulated necrosis. Acta Pharm Sin B 2020; 10(10): 1880–903

Andreasen M, Lorenzen N, Otzen D. Interactions between misfolded protein oligomers and membranes: A central topic in neurodegenerative diseases? Biochim Biophys Acta 2015; 1848(9): 1897–907

Andrade-Guerrero J, Santiago-Balmaseda A, Jeronimo-Aguilar P, Vargas-Rodríguez I, Cadena-Suárez AR, Sánchez-Garibay C, Pozo-Molina G, Méndez-Catalá CF, Cardenas-Aguayo MD, Diaz-Cintra S, Pacheco-Herrero M. Alzheimer’s Disease: An Updated Overview of Its Genetics. Int J Mol Sci 2023; 24(4): 3754.

Andrés-Benito P, Carmona M, Pirla MJ, Torrejón-Escribano B, Del Rio JA, Ferrer I. Dysregulated Protein Phosphorylation as Main Contributor of Granulovacuolar Degeneration at the First Stages of Neurofibrillary Tangles Pathology. Neurosci 2023; 518: 119–40

Arbel-Ornath M, Hudry E, Boivin JR, et al. Soluble oligomeric amyloid-β induces calcium dyshomeostasis that precedes synapse loss in the living mouse brain. Mol Neurodegener 2017; 12(1): 27

Ashby EL, Miners JS, Kumar S, Walter J, Love S, Kehoe PG. Investigation of Aβ phosphorylated at serine 8 (pAβ) in Alzheimer's disease, dementia with Lewy bodies and vascular dementia. Neuropathol Appl Neurobiol 2015; 41(4): 428–44

Asher DM, Belay E, Bigio E, et al. Risk of Transmissibility From Neurodegenerative Disease-Associated Proteins: Experimental Knowns and Unknowns. J Neuropathol Exp Neurol 2020; 79(11): 1141–6

Atwood CS, Martins RN, Smith MA, Perry G. Senile plaque composition and posttranslational modification of amyloid-β peptide and associated proteins. Peptides 2002; 23(7): 1343–50

Babaei P. NMDA and AMPA receptors dysregulation in Alzheimer's disease. European J Pharmacol 2021; 908: 174310

Bamberger ME, Landreth GE. Inflammation, apoptosis, and Alzheimer's disease. J Neurosci 2002; 8(3): 276–83

Barczuk J, Siwecka N, Lusa W, Rozpędek-Kamińska W, Kucharska E, Majsterek I. Targeting NLRP3-Mediated Neuroinflammation in Alzheimer's Disease Treatment. Int J Mol Sci 2022; 23(16)

Bates KA, Verdile G, Li Q-X, et al. Clearance mechanisms of Alzheimer's amyloid-beta peptide: implications for therapeutic design and diagnostic tests. Mol Psychiatry 2009; 14(5): 469–86

Bayer TA, Wirths O. Focusing the amyloid cascade hypothesis on N-truncated Abeta peptides as drug targets against Alzheimer's disease. Acta Neuropathol 2014; 127(6): 787–801

Bayer TA, Wirths O. Intracellular accumulation of amyloid-Beta - a predictor for synaptic dysfunction and neuron loss in Alzheimer's disease. Front Aging Neurosci 2010; 2: 8

Becker-Pauly C, Pietrzik CU. The Metalloprotease Meprin β Is an Alternative β-Secretase of APP. Front Mol Neurosci 2016; 9: 159

Behl C. Apoptosis and Alzheimer's disease. J Neu Trans 2000; 107(11): 1325–44

Bell RD, Sagare AP, Friedman AE, et al. Transport pathways for clearance of human Alzheimer's amyloid beta-peptide and apolipoproteins E and J in the mouse central nervous system. J Cerebral blood flow & metab. 2007; 27(5): 909–18

Bellenguez C, Grenier-Boley B, Lambert J-C. Genetics of Alzheimer's disease: where we are, and where we are going. Curr Opin Neurobiol. 2020; 61: 40–8

Benjamin Yang. A united disease theory brings two groups of Alzheimer’s disease researchers together. Discovery Medicine 2009.

Benyair R, Eisenberg-Lerner A, Merbl Y. Maintaining Golgi Homeostasis: A Balancing Act of Two Proteolytic Pathways. Cells 2022; 11(5): 780

Bharadwaj P, Solomon T, Malajczuk CJ, et al. Role of the cell membrane interface in modulating production and uptake of Alzheimer's beta amyloid protein. Biochim Biophys Acta Biomembr 2018; 1860(9): 1639–51

Bharadwaj PR, Dubey AK, Masters CL, Martins RN, Macreadie IG. Abeta aggregation and possible implications in Alzheimer's disease pathogenesis. J Cel Mol Med 2009; 13(3): 412–21

Billings LM, Oddo S, Green KN, McGaugh JL, LaFerla FM. Intraneuronal Abeta causes the onset of early Alzheimer's disease-related cognitive deficits in transgenic mice. Neuron 2005; 45(5): 675–88

Block ML, Zecca L, Hong J-S. Microglia-mediated neurotoxicity: uncovering the molecular mechanisms. Nat Rev Neurosci 2007; 8(1): 57–69

Boon BDC, Hoozemans JJM, Lopuhaä B, et al. Neuroinflammation is increased in the parietal cortex of atypical Alzheimer's disease. J Neuroinflam 2018; 15(1): 170

Braithwaite SP, Stock JB, Lombroso PJ, Nairn AC. Protein phosphatases and Alzheimer's disease. Prog Mol Biol Transl Sci 2012; 106: 343–79

Brewer GJ, Herrera RA, Philipp S, Sosna J, Reyes-Ruiz JM, Glabe CG. Age-Related Intraneuronal Aggregation of Amyloid-β in Endosomes, Mitochondria, Autophagosomes, and Lysosomes. J Alzheimers Dis 2020; 73(1): 229–46

Brier MR, Thomas JB, Ances BM. Network dysfunction in Alzheimer's disease: refining the disconnection hypothesis. Brain Conn 2014; 4(5): 299–311

Brockhaus M, Grünberg J, Röhrig S, et al. Caspase-mediated cleavage is not required for the activity of presenilins in amyloidogenesis and NOTCH signaling. Neuro Rep 1998; 9(7): 1481–6

Broncel M, Falenski JA, Wagner SC, Hackenberger CPR, Koksch B. How post-translational modifications influence amyloid formation: a systematic study of phosphorylation and glycosylation in model peptides. Chemistry 2010; 16(26): 7881–8

Buratta S, Tancini B, Sagini K, et al. Lysosomal Exocytosis, Exosome Release and Secretory Autophagy: The Autophagic- and Endo-Lysosomal Systems Go Extracellular. Int J Mol Sci 2020; 21(7)

Busche MA, Hyman BT. Synergy between amyloid-β and tau in Alzheimer's disease. Nat Neurosci 2020; 23(10): 1183–93

Butterfield DA, Boyd-Kimball D. Mitochondrial Oxidative and Nitrosative Stress and Alzheimer Disease. Antioxidants 2020; 9(9): 818

Byun Y, Chen F, Chang R, Trivedi M, Green KJ, Cryns VL. Caspase cleavage of vimentin disrupts intermediate filaments and promotes apoptosis. Cell Death Differ 2001; 8(5): 443–50

Calvo-Rodriguez M, Bacskai BJ. Mitochondria and Calcium in Alzheimer's Disease: From Cell Signaling to Neuronal Cell Death. Trends in Neurosci 2021; 44(2): 136–51

Cao J, Zhong MB, Toro CA, Zhang L, Cai D. Endo-lysosomal pathway and ubiquitin-proteasome system dysfunction in Alzheimer's disease pathogenesis. Neurosci Lett 2019; 703: 68–78

Capetillo-Zarate E, Gracia L, Tampellini D, Gouras GK. Intraneuronal Aβ accumulation, amyloid plaques, and synapse pathology in Alzheimer's disease. Neurodegener Dis 2012; 10(1-4): 56–9

Cardoso SM, Santana I, Swerdlow RH, Oliveira CR. Mitochondria dysfunction of Alzheimer's disease cybrids enhances Abeta toxicity. J Neurochem 2004; 89(6): 1417–26

Carter DB. The Interaction of Amyloid-β with ApoE. Alz Dis 2005; 255–72.

Carter J, Lippa CF. Beta-amyloid, neuronal death and Alzheimer's disease. Curr Mol Med 2001;1(6):733-7.

Cataldo AM, Nixon RA. Enzymatically active lysosomal proteases are associated with amyloid deposits in Alzheimer brain. Proc Natl Acad Sci USA 1990; 87(10): 3861–5

Cataldo AM, Petanceska S, Terio NB, et al. Abeta localization in abnormal endosomes: association with earliest Abeta elevations in AD and Down syndrome. Neurobiol Aging 2004; 25(10): 1263–72

Cecchi C, Stefani M. The amyloid-cell membrane system. The interplay between the biophysical features of oligomers/fibrils and cell membrane defines amyloid toxicity. Biophys Chem 2013; 182: 30–43

Cenini G, Rüb C, Bruderek M, Voos W. Amyloid β-peptides interfere with mitochondrial preprotein import competence by a coaggregation process. Mol Biol Cell 2016; 27(21): 3257–72

Ceyzériat K, Zilli T, Millet P, Frisoni GB, Garibotto V, Tournier BB. Learning from the Past: A Review of Clinical Trials Targeting Amyloid, Tau and Neuroinflammation in Alzheimer's Disease. Curr Alzheimer Res 2020; 17(2): 112–25

Cheignon C, Tomas M, Bonnefont-Rousselot D, Faller P, Hureau C, Collin F. Oxidative stress and the amyloid beta peptide in Alzheimer's disease. Redox Biol 2018; 14: 450–64

Chen G-F, Xu T-H, Yan Y, et al. Amyloid beta: structure, biology and structure-based therapeutic development. Acta Pharmacol Sin 2017; 38(9): 1205–35

Chen JJ, Genereux JC, Wiseman RL. Endoplasmic reticulum quality control and systemic amyloid disease: Impacting protein stability from the inside out. IUBMB Life 2015; 67(6): 404–13

Chow VW, Mattson MP, Wong PC, Gleichmann M. An overview of APP processing enzymes and products. Neuromol Med 2010; 12(1): 1–12

Chung S-H. Aberrant phosphorylation in the pathogenesis of Alzheimer's disease. BMB Rep 2009; 42(8): 467–74

Ciechanover A, Schwartz AL. The ubiquitin-proteasome pathway: the complexity and myriad functions of proteins death. Proc Natl Acad Sci USA 1998; 95(6): 2727–30

Cirrito JR, Kang J-E, Lee J, et al. Endocytosis is required for synaptic activity-dependent release of amyloid-beta in vivo. Neuron 2008; 58(1): 42–51

Cleary JP, Walsh DM, Hofmeister JJ, et al. Natural oligomers of the amyloid-beta protein specifically disrupt cognitive function. Nat Neurosci 2005; 8(1): 79–84

Cline EN, Bicca MA, Viola KL, Klein WL. The Amyloid-β Oligomer Hypothesis: Beginning of the Third Decade. J Alzheimers Dis 2018; 64(s1): S567-S610

Colacurcio DJ, Pensalfini A, Jiang Y, Nixon RA. Dysfunction of autophagy and endosomal-lysosomal pathways: Roles in pathogenesis of Down syndrome and Alzheimer's Disease. Free Radic Biol Med 2018; 114: 40–51

Cordy JM, Hooper NM, Turner AJ. The involvement of lipid rafts in Alzheimer's disease. Mol Membr Biol 2006; 23(1): 111–22

Cotman CW, Su JH. Mechanisms of neuronal death in Alzheimer's disease. Brain Pathol 1996; 6(4): 493–506

Csizmok V, Forman-Kay JD. Complex regulatory mechanisms mediated by the interplay of multiple post-translational modifications. Curr Opin Struct Biol 2018; 48: 58–67

Cuello AC, Canneva F. Impact of intracellular beta-amyloid in transgenic animals and cell models. Neurodegener Dis 2008; 5(3-4): 146–8

Cuello AC. Intracellular and extracellular Abeta, a tale of two neuropathologies. Brain Pathol 2005; 15(1): 66–71

Cummings JL, Morstorf T, Zhong K. Alzheimer's disease drug-development pipeline: few candidates, frequent failures. Alzheimers Res Ther 2014; 6(4): 37

Dana D, Garcia J, Bhuiyan AI, et al. Cell penetrable, clickable and tagless activity-based probe of human cathepsin L. Bioorg Chem 2019; 85: 505–14

D'Andrea MR, Cole GM, Ard MD. The microglial phagocytic role with specific plaque types in the Alzheimer disease brain. Neurobiol Aging 2004; 25(5): 675–83

Denton D, Xu T, Kumar S. Autophagy as a pro-death pathway. Immunol Cell Biol 2015; 93(1): 35–42

Di Scala C, Chahinian H, Yahi N, Garmy N, Fantini J. Interaction of Alzheimer's β-amyloid peptides with cholesterol: mechanistic insights into amyloid pore formation. Biochem 2014; 53(28): 4489–502

Dickson TC, King CE, McCormack GH, Vickers JC. Neurochemical diversity of dystrophic neurites in the early and late stages of Alzheimer's disease. Exp Neurol 1999; 156(1): 100–10

Ding W-X, Ni H-M, Gao W, et al. Linking of autophagy to ubiquitin-proteasome system is important for the regulation of endoplasmic reticulum stress and cell viability. The Amer J Pathol 2007; 171(2): 513–24

Domert J, Rao SB, Agholme L, et al. Spreading of amyloid-β peptides via neuritic cell-to-cell transfer is dependent on insufficient cellular clearance. Neurobiol of Dis 2014; 65: 82–92

Domínguez-Prieto M, Velasco A, Tabernero A, Medina JM. Endocytosis and Transcytosis of Amyloid-β Peptides by Astrocytes: A Possible Mechanism for Amyloid-β Clearance in Alzheimer's Disease. J Alz Dis 2018; 65(4): 1109–24

Dong S, Duan Y, Hu Y, Zhao Z. Advances in the pathogenesis of Alzheimer's disease: a re-evaluation of amyloid cascade hypothesis. Transl Neurodegener 2012; 1(1): 18

Du F, Yu Q, Yan S, et al. PINK1 signalling rescues amyloid pathology and mitochondrial dysfunction in Alzheimer's disease. Brain 2017; 140(12): 3233–51

Du H, Guo L, Yan S, Sosunov AA, McKhann GM, Yan SS. Early deficits in synaptic mitochondria in an Alzheimer's disease mouse model. Proc Natl Acad Sci 2010; 107(43): 18670–5

Edgar JR, Willén K, Gouras GK, Futter CE. ESCRTs regulate amyloid precursor protein sorting in multivesicular bodies and intracellular amyloid-β accumulation. J Cell Sci 2015; 128(14): 2520–8

Eimer WA, Vassar R. Neuron loss in the 5XFAD mouse model of Alzheimer's disease correlates with intraneuronal Aβ42 accumulation and Caspase-3 activation. Mol Neurodegener 2013; 8(1): 2

Eisele YS, Duyckaerts C. Propagation of Aß pathology: hypotheses, discoveries, and yet unresolved questions from experimental and human brain studies. Acta Neuropathol 2016; 131(1): 5–25

Endres K, Reinhardt S. ER-stress in Alzheimer's disease: turning the scale? Am J Neurodegener Dis 2013; 2(4): 247–65

Esler WP, Stimson ER, Jennings JM, et al. Alzheimer's disease amyloid propagation by a template-dependent dock-lock mechanism. Biochem 2000; 39(21): 6288–95

Esparza TJ, Wildburger NC, Jiang H, et al. Soluble Amyloid-beta Aggregates from Human Alzheimer's Disease Brains. Sci Rep 2016; 6: 38187

Fabiani C, Antollini SS. Alzheimer's Disease as a Membrane Disorder: Spatial Cross-Talk Among Beta-Amyloid Peptides, Nicotinic Acetylcholine Receptors and Lipid Rafts. Front Cell Neurosci 2019; 13: 309

Faller P, Hureau C, Berthoumieu O. Role of metal ions in the self-assembly of the Alzheimer's amyloid-β peptide. Inorg Chem 2013; 52(21): 12193–206

Fan Z, Brooks DJ, Okello A, Edison P. An early and late peak in microglial activation in Alzheimer's disease trajectory. Brain 2017; 140(3): 792–803

Ferreira ST, Vieira MNN, Felice FG de. Soluble protein oligomers as emerging toxins in Alzheimer's and other amyloid diseases. IUBMB Life 2007; 59(4-5): 332–45

Ferreiro E, Baldeiras I, Ferreira IL, et al. Mitochondrial- and endoplasmic reticulum-associated oxidative stress in Alzheimer's disease: from pathogenesis to biomarkers. Int J Cell Biol 2012; 2012: 735206

Finder VH, Glockshuber R. Amyloid-beta aggregation. Neurodegener Dis 2007; 4(1): 13–27

Finder VH. Alzheimer's disease: a general introduction and pathomechanism. J Alz Dis 2010; 22 Suppl 3: 5–19

Finkbeiner S. The Autophagy Lysosomal Pathway and Neurodegeneration. Cold Spring Harb Perspect Biol 2020; 12(3): a033993

Fossati S, Ghiso J, Rostagno A. Insights into caspase-mediated apoptotic pathways induced by amyloid-β in cerebral microvascular endothelial cells. Neurodegener Dis 2012; 10(1-4): 324–8

Francis PT, Palmer AM, Snape M, Wilcock GK. The cholinergic hypothesis of Alzheimer's disease: a review of progress. J Neurol Neurosurg Psychiatry 1999; 66(2): 137–47

Franklin BS, Bossaller L, Nardo D de, et al. The adaptor ASC has extracellular and 'prionoid' activities that propagate inflammation. Nat Immunol 2014; 15(8): 727–37

Frere S, Slutsky I. Alzheimer's Disease: From Firing Instability to Homeostasis Network Collapse. Neuron 2018; 97(1): 32–58

Friedman R, Pellarin R, Caflisch A. Amyloid aggregation on lipid bilayers and its impact on membrane permeability. J Mol Biol 2009; 387(2): 407–15

Frigerio I, Boon BDC, Lin C-P, et al. Amyloid-β, p-tau and reactive microglia are pathological correlates of MRI cortical atrophy in Alzheimer's disease. Brain Commun 2021; 3(4): fcab281

Friker LL, Scheiblich H, Hochheiser IV, et al. β-Amyloid Clustering around ASC Fibrils Boosts Its Toxicity in Microglia. Cell Rep 2020; 30(11): 3743-3754.e6

Frisoni GB. Complexity is the simple truth about Alzheimer's disease. Lancet Neurol 2023; 22(9): 776–8

Ganley IG, Du Lam H, Wang J, Ding X, Chen S, Jiang X. ULK1.ATG13.FIP200 complex mediates mTOR signaling and is essential for autophagy. J Biol Chem 2009; 284(18): 12297–305

Gerakis Y, Hetz C. Emerging roles of ER stress in the etiology and pathogenesis of Alzheimer's disease. FEBS J 2018; 285(6): 995–1011

Gibson Wood W, Eckert GP, Igbavboa U, Müller WE. Amyloid beta-protein interactions with membranes and cholesterol: causes or casualties of Alzheimer's disease. Biochimica et Biophysica Acta (BBA) - Biomembranes 2003; 1610(2): 281–90

Glabe C. Intracellular Mechanisms of Amyloid Accumulation and Pathogenesis in Alzheimer's Disease. J Mol Neurosci 2001; 17(2): 137–45

Glebov K, Löchner M, Jabs R, et al. Serotonin stimulates secretion of exosomes from microglia cells. Glia 2015; 63(4): 626–34

Gong C-X, Liu F, Grundke-Iqbal I, Iqbal K. Dysregulation of protein phosphorylation/dephosphorylation in Alzheimer's disease: a therapeutic target. J Biomed Biotechnol 2006; 2006(3): 31825

González-Polo R-A, Boya P, Pauleau A-L, et al. The apoptosis/autophagy paradox: autophagic vacuolization before apoptotic death. J Cell Sci 2005; 118(Pt 14): 3091–102

Goudarzi S, Hosseini A, Abdollahi M, Haghi-Aminjan H. Insights Into Parkin-Mediated Mitophagy in Alzheimer's Disease: A Systematic Review. Front. Aging Neurosci. 2021; 13: 674071

Gouras GK, Almeida CG, Takahashi RH. Intraneuronal Abeta accumulation and origin of plaques in Alzheimer's disease. Neurobiol Aging 2005; 26(9): 1235–44

Gouras GK, Olsson TT, Hansson O. β-Amyloid peptides and amyloid plaques in Alzheimer's disease. Neurotherapeutics 2015; 12(1): 3–11

Gouras GK, Tampellini D, Takahashi RH, Capetillo-Zarate E. Intraneuronal beta-amyloid accumulation and synapse pathology in Alzheimer's disease. Acta Neuropathol 2010; 119(5): 523–41

Gouras GK, Tsai J, Naslund J, et al. Intraneuronal Aβ42 Accumulation in Human Brain. The Amer J Pathol 2000; 156(1): 15–20

Gowrishankar S, Yuan P, Wu Y, et al. Massive accumulation of luminal protease-deficient axonal lysosomes at Alzheimer's disease amyloid plaques. Proc Natl Acad Sci 2015; 112(28): E3699-708

Graham JM. Isolation of lysosomes from tissues and cells by differential and density gradient centrifugation. Curr Protoc Cell Biol 2001; Chapter 3: Unit 3.6

Guérin R, Arseneault G, Dumont S, Rokeach LA. Calnexin is involved in apoptosis induced by endoplasmic reticulum stress in the fission yeast. Mol Biol Cell 2008; 19(10): 4404–20

Guerrero-Muñoz MJ, Castillo-Carranza DL, Kayed R. Therapeutic approaches against common structural features of toxic oligomers shared by multiple amyloidogenic proteins. Biochem Pharmacol 2014; 88(4): 468–78

Haass C, Kaether C, Thinakaran G, Sisodia S. Trafficking and proteolytic processing of APP. Cold Spring Harb Perspect Med 2012; 2(5): a006270

Haass C, Selkoe D. If amyloid drives Alzheimer disease, why have anti-amyloid therapies not yet slowed cognitive decline? PLOS Biol 2022; 20(7): e3001694

Haass C, Selkoe DJ. Cellular processing of beta-amyloid precursor protein and the genesis of amyloid beta-peptide. Cell 1993; 75(6): 1039–42

Hampel H, Hardy J, Blennow K, et al. The Amyloid-β Pathway in Alzheimer's Disease. Mol Psychiatry 2021; 26(10): 5481–503

Hanslik KL, Ulland TK. The Role of Microglia and the Nlrp3 Inflammasome in Alzheimer's Disease. Front. Neurol. 2020; 11: 570711

Hardy J, Selkoe DJ. The amyloid hypothesis of Alzheimer's disease: progress and problems on the road to therapeutics. Science 2002; 297(5580): 353–6

Hardy JA, Higgins GA. Alzheimer's disease: the amyloid cascade hypothesis. Science 1992; 256(5054): 184–5

Harris JR, Fahrenholz F, editors. Alzheimer's disease: Cellular and molecular aspects of amyloid [beta] New York: Springer; 2005.

Harvey NL, Kumar S. The role of caspases in apoptosis. Adv Biochem Eng Biotechnol 1998; 62: 107–28

Hedskog L, Pinho CM, Filadi R, et al. Modulation of the endoplasmic reticulum-mitochondria interface in Alzheimer's disease and related models. Proc Natl Acad Sci 2013; 110(19): 7916–21

Hegde AN, Smith SG, Duke LM, Pourquoi A, Vaz S. Perturbations of Ubiquitin-Proteasome-Mediated Proteolysis in Aging and Alzheimer's Disease. Front. Aging Neurosci. 2019; 11: 324

Heneka MT, Carson MJ, El Khoury J, et al. Neuroinflammation in Alzheimer's disease. Lancet Neurol 2015; 14(4): 388–405

Heras-Sandoval D, Pérez-Rojas JM, Hernández-Damián J, Pedraza-Chaverri J. The role of PI3K/AKT/mTOR pathway in the modulation of autophagy and the clearance of protein aggregates in neurodegeneration. Cell Signal 2014; 26(12): 2694–701

Herrup K. The case for rejecting the amyloid cascade hypothesis. Nat Neurosci 2015; 18(6): 794–9

Hirai K, Aliev G, Nunomura A, et al. Mitochondrial abnormalities in Alzheimer's disease. J. Neurosci. 2001; 21(9): 3017–23

Hodges AK, Piers TM, Collier D, Cousins O, Pocock JM. Pathways linking Alzheimer’s disease risk genes expressed highly in microglia. Neuroimmunol and Neuroinflam 2021; 8: 245–68.

Hong L, Huang H-C, Jiang Z-F. Relationship between amyloid-beta and the ubiquitin-proteasome system in Alzheimer's disease. Neurol Res 2014; 36(3): 276–82

Hoshino T, Mahmood MI, Mori K, Matsuzaki K. Binding and aggregation mechanism of amyloid β-peptides onto the GM1 ganglioside-containing lipid membrane. J Phys Chem B 2013; 117(27): 8085–94

Hu H, Tian M, Ding C, Yu S. The C/EBP Homologous Protein (CHOP) Transcription Factor Functions in Endoplasmic Reticulum Stress-Induced Apoptosis and Microbial Infection. Front Immunol 2018; 9: 3083

Huang L-K, Chao S-P, Hu C-J. Clinical trials of new drugs for Alzheimer disease. J Biomed Sci 2020; 27(1): 18

Hulse J, Bhaskar K. Crosstalk Between the NLRP3 Inflammasome/ASC Speck and Amyloid Protein Aggregates Drives Disease Progression in Alzheimer's and Parkinson's Disease. Front. Mol. Neurosci. 2022; 15: 805169

Hunter S, Brayne C. Understanding the roles of mutations in the amyloid precursor protein in Alzheimer disease. Mol Psychiatry 2018; 23(1): 81–93

Hwang J, Qi L. Quality Control in the Endoplasmic Reticulum: Crosstalk between ERAD and UPR pathways. Trend Biochem Sci 2018; 43(8): 593–605

Hyman BT, Phelps CH, Beach TG, et al. National Institute on Aging-Alzheimer's Association guidelines for the neuropathologic assessment of Alzheimer's disease. Alz & Dement 2012; 8(1): 1–13

Hyman BT. Amyloid-dependent and amyloid-independent stages of Alzheimer disease. Arch Neurol 2011; 68(8): 1062–4

Islam MI, Sharoar MG, Ryu E-K, Park I-S. Limited activation of the intrinsic apoptotic pathway plays a main role in amyloid-β-induced apoptosis without eliciting the activation of the extrinsic apoptotic pathway. Int J Mol Med 2017; 40(6): 1971–82

Jack CR, Therneau TM, Weigand SD, et al. Prevalence of Biologically vs Clinically Defined Alzheimer Spectrum Entities Using the National Institute on Aging-Alzheimer's Association Research Framework. JAMA Neurol 2019; 76(10): 1174–83

Ji CH, Kwon YT. Crosstalk and Interplay between the Ubiquitin-Proteasome System and Autophagy. Mol Cells 2017; 40(7): 441–9

Johnson DE, Ostrowski P, Jaumouillé V, Grinstein S. The position of lysosomes within the cell determines their luminal pH. J Cell Biol 2016; 212(6): 677–92

Jongbloed W, Bruggink KA, Kester MI, et al. Amyloid-β oligomers relate to cognitive decline in Alzheimer's disease. J Alz Dis 2015; 45(1): 35–43

Joshi P, Riffel F, Kumar S, et al. TREM2 modulates differential deposition of modified and non-modified Aβ species in extracellular plaques and intraneuronal deposits. Acta Neuropathol Commun 2021; 9(1): 168

Joshi P, Riffel F, Satoh K, et al. Differential interaction with TREM2 modulates microglial uptake of modified Aβ species. Glia 2021; 69(12): 2917–32

Jucker M, Walker LC. Self-propagation of pathogenic protein aggregates in neurodegenerative diseases. Nature 2013; 501(7465): 45–51

Kaizuka T, Morishita H, Hama Y, et al. An Autophagic Flux Probe that Releases an Internal Control. Mol Cell 2016; 64(4): 835–49

Kakio A, Yano Y, Takai D, et al. Interaction between amyloid beta-protein aggregates and membranes. J Pept Sci 2004; 10(10): 612–21

Kamenetz F, Tomita T, Hsieh H, et al. APP processing and synaptic function. Neuron 2003; 37(6): 925–37

Kametani F, Hasegawa M. Reconsideration of Amyloid Hypothesis and Tau Hypothesis in Alzheimer's Disease. Front Neurosci 2018; 12: 25

Kanekiyo T, Cirrito JR, Liu C-C, et al. Neuronal clearance of amyloid-β by endocytic receptor LRP1. J Neurosci 2013; 33(49): 19276–83

Kang J, Lemaire HG, Unterbeck A, et al. The precursor of Alzheimer's disease amyloid A4 protein resembles a cell-surface receptor. Nature 1987; 325(6106): 733–6

Kapadia A, Theil S, Opitz S, et al. Phosphorylation-state dependent intraneuronal sorting of Aβ differentially impairs autophagy and the endo-lysosomal system. Autophagy 2024; 20(1): 166–87

Karran E, Mercken M, Strooper B de. The amyloid cascade hypothesis for Alzheimer's disease: an appraisal for the development of therapeutics. Nat Rev Drug Discov 2011; 10(9): 698–712

Karran E, Strooper B de. The amyloid cascade hypothesis: are we poised for success or failure? Journal of Neurochemistry 2016; 139 Suppl 2: 237–52

Kavčič N, Pegan K, Turk B. Lysosomes in programmed cell death pathways: from initiators to amplifiers. Biol Chem 2017; 398(3): 289–301

Kayed R, Lasagna-Reeves CA. Molecular mechanisms of amyloid oligomers toxicity. JAD 2013; 33 Suppl 1(s1): S67-78

Kayed R, Sokolov Y, Edmonds B, et al. Permeabilization of lipid bilayers is a common conformation-dependent activity of soluble amyloid oligomers in protein misfolding diseases. J Biol Chem 2004; 279(45): 46363–6

Kimpe L de, van Haastert ES, Kaminari A, et al. Intracellular accumulation of aggregated pyroglutamate amyloid beta: convergence of aging and Aβ pathology at the lysosome. Age (Dordr) 2013; 35(3): 673–87

Kisselev AF, Goldberg AL. Monitoring activity and inhibition of 26S proteasomes with fluorogenic peptide substrates. Methods in Enzymology 2005; 398: 364–78

Klein W. Targeting small Aβ oligomers: the solution to an Alzheimer's disease conundrum? Trend Neurosci 2001; 24(4): 219–24

Klein WL. Synaptic targeting by A beta oligomers (ADDLS) as a basis for memory loss in early Alzheimer's disease. Alzheimers Dement 2006; 2(1): 43–55

Klionsky DJ, Abdel-Aziz AK, Abdelfatah S, et al. Guidelines for the use and interpretation of assays for monitoring autophagy. Autophagy 2021; 17(1): 1–382

Konstantoulea K, Guerreiro P, Ramakers M, et al. Heterotypic Amyloid β interactions facilitate amyloid assembly and modify amyloid structure. EMBO J 2022; 41(2): e108591

Korolchuk VI, Menzies FM, Rubinsztein DC. Mechanisms of cross-talk between the ubiquitin-proteasome and autophagy-lysosome systems. FEBS Lett 2010; 584(7): 1393–8

Kroemer G, Jäättelä M. Lysosomes and autophagy in cell death control. Nat Rev Cancer 2005; 5(11): 886–97

Kumar A, Fontana IC, Nordberg A. Reactive astrogliosis: A friend or foe in the pathogenesis of Alzheimer's disease. J Neurochem 2023; 164(3): 309–24

Kumar S, Frost JL, Cotman CW, et al. Deposition of phosphorylated amyloid-β in brains of aged nonhuman primates and canines. Brain Pathol 2018; 28(3): 427–30

Kumar S, Kapadia A, Theil S, et al. Novel Phosphorylation-State Specific Antibodies Reveal Differential Deposition of Ser26 Phosphorylated Aβ Species in a Mouse Model of Alzheimer's Disease. Front Mol Neurosci 2020; 13: 619639

Kumar S, Lemere CA, Walter J. Phosphorylated Aβ peptides in human Down syndrome brain and different Alzheimer's-like mouse models. Acta Neuropathol Commun 2020; 8(1): 118

Kumar S, Rezaei-Ghaleh N, Terwel D, et al. Extracellular phosphorylation of the amyloid β-peptide promotes formation of toxic aggregates during the pathogenesis of Alzheimer's disease. EMBO J 2011; 30(11): 2255–65

Kumar S, Singh S, Hinze D, et al. Phosphorylation of amyloid-β peptide at serine 8 attenuates its clearance via insulin-degrading and angiotensin-converting enzymes. J Biol Chem 2012; 287(11): 8641–51

Kumar S, Walter J. Phosphorylation of amyloid beta (Aβ) peptides - a trigger for formation of toxic aggregates in Alzheimer's disease. Aging 2011; 3(8): 803–12

Kumar S, Wirths O, Stüber K, et al. Phosphorylation of the amyloid β-peptide at Ser26 stabilizes oligomeric assembly and increases neurotoxicity. Acta Neuropathol 2016; 131(4): 525–37

Kumar S, Wirths O, Theil S, Gerth J, Bayer TA, Walter J. Early intraneuronal accumulation and increased aggregation of phosphorylated Abeta in a mouse model of Alzheimer's disease. Acta Neuropathol 2013; 125(5): 699–709

Kummer MP, Heneka MT. Truncated and modified amyloid-beta species. Alz Res Therapy 2014; 6(3): 28

Kurdi M, Alghamdi B. Is granulovacuolar degeneration an essential pathological component of Alzheimer's disease? A review of the pathogenesis and histochemistry of old studies. Neuropathol 2020; 58(4): 277–86

La Torre JC de. The vascular hypothesis of Alzheimer's disease: bench to bedside and beyond. Neurodegener Dis 2010; 7(1-3): 116–21

Lacor PN, Buniel MC, Chang L, et al. Synaptic targeting by Alzheimer's-related amyloid beta oligomers. J Neurosci 2004; 24(45): 10191–200

LaFerla FM, Green KN, Oddo S. Intracellular amyloid-beta in Alzheimer's disease. Nat Rev Neurosci 2007; 8(7): 499–509

LaFerla FM, Troncoso JC, Strickland DK, Kawas CH, Jay G. Neuronal cell death in Alzheimer's disease correlates with apoE uptake and intracellular Abeta stabilization. J Clin Invest 1997; 100(2): 310–20

Lagadic-Gossmann D, Huc L, Lecureur V. Alterations of intracellular pH homeostasis in apoptosis: origins and roles. Cell Death Differ 2004; 11(9): 953–61

Lai AY, McLaurin J. Mechanisms of amyloid-Beta Peptide uptake by neurons: the role of lipid rafts and lipid raft-associated proteins. Int J Alzheimers Dis 2010; 2011: 548380

Lambert J-C, Amouyel P. Genetics of Alzheimer's disease: new evidences for an old hypothesis? Curr Opin Gen Dev 2011; 21(3): 295–301

Lambert MP, Barlow AK, Chromy BA, et al. Diffusible, nonfibrillar ligands derived from Abeta1-42 are potent central nervous system neurotoxins. Proc Natl Acad Sci USA 1998; 95(11): 6448–53

Lane CA, Hardy J, Schott JM. Alzheimer's disease. Eur J Neurol 2018; 25(1): 59–70

Langui D, Girardot N, El Hachimi KH, et al. Subcellular Topography of Neuronal Aβ Peptide in APPxPS1 Transgenic Mice. The Amer J Pathol 2004; 165(5): 1465–77

Leclerc E, Sturchler E, Vetter SW, Heizmann CW. Crosstalk between calcium, amyloid beta and the receptor for advanced glycation endproducts in Alzheimer's disease. Rev Neurosci 2009; 20(2): 95–110

Lee CYD, Landreth GE. The role of microglia in amyloid clearance from the AD brain. J Neural Transm 2010; 117(8): 949–60

Lefterov I, Fitz NF, Lu Y, Koldamova R. APOEε4 and risk of Alzheimer's disease - time to move forward. Front Neurosci 2023; 17: 1195724

Leng F, Edison P. Neuroinflammation and microglial activation in Alzheimer disease: where do we go from here? Nat Rev Neurol 2021; 17(3): 157–72

Leong YQ, Ng KY, Chye SM, Ling APK, Koh RY. Mechanisms of action of amyloid-beta and its precursor protein in neuronal cell death. Metab Brain Dis 2020; 35(1): 11–30

Li J-Q, Yu J-T, Jiang T, Tan L. Endoplasmic reticulum dysfunction in Alzheimer's disease. Mol Neurobiol 2015; 51(1): 383–95

Li M, Chen L, Lee DHS, Yu L-C, Zhang Y. The role of intracellular amyloid beta in Alzheimer's disease. Prog Neurobiol 2007; 83(3): 131–9

Li S, Selkoe DJ. A mechanistic hypothesis for the impairment of synaptic plasticity by soluble Aβ oligomers from Alzheimer's brain. J Neurochem 2020; 154(6): 583–97

Li X, Donowitz M. Fractionation of subcellular membrane vesicles of epithelial and non-epithelial cells by OptiPrep™ density gradient ultracentrifugation. Methods Mol Biol 2014; 1174: 85–99

Li X, Ospitalieri S, Robberechts T, et al. Seeding, maturation and propagation of amyloid β-peptide aggregates in Alzheimer's disease. Brain 2022; 145(10): 3558–70

Li Y, Xu H, Wang H, Yang K, Luan J, Wang S. TREM2: Potential therapeutic targeting of microglia for Alzheimer's disease. Biomed Pharmacother 2023; 165: 115218

Li Y, Zhao X, Hu Y, et al. Age-associated decline in Nrf2 signaling and associated mtDNA damage may be involved in the degeneration of the auditory cortex: Implications for central presbycusis. Int J Mol Med 2018; 42(6): 3371–85

Lin H, Bhatia R, Lal R. Amyloid beta protein forms ion channels: implications for Alzheimer's disease pathophysiology. FASEB J 2001; 15(13): 2433–44

Liu ML, Hong ST. Early phase of amyloid beta42-induced cytotoxicity in neuronal cells is associated with vacuole formation and enhancement of exocytosis. Exp Mol Med 2005; 37(6): 559–66

Lopez Salon M, Pasquini L, Besio Moreno M, Pasquini JM, Soto E. Relationship between beta-amyloid degradation and the 26S proteasome in neural cells. Exp Neurol 2003; 180(2): 131–43

Maccioni RB, Farías G, Morales I, Navarrete L. The revitalized tau hypothesis on Alzheimer's disease. Arch Med Res 2010; 41(3): 226–31

Majd S, Power JH, Grantham HJM. Neuronal response in Alzheimer's and Parkinson's disease: the effect of toxic proteins on intracellular pathways. BMC Neurosci 2015; 16(1): 69

Majdi A, Sadigh-Eteghad S, Rahigh Aghsan S, et al. Amyloid-β, tau, and the cholinergic system in Alzheimer's disease: seeking direction in a tangle of clues. Rev Neurosci 2020; 31(4): 391–413

Malaplate-Armand C, Florent-Béchard S, Youssef I, et al. Soluble oligomers of amyloid-beta peptide induce neuronal apoptosis by activating a cPLA2-dependent sphingomyelinase-ceramide pathway. Neurobiol Dis 2006; 23(1): 178–89

Malik BR, Maddison DC, Smith GA, Peters OM. Autophagic and endo-lysosomal dysfunction in neurodegenerative disease. Mol Brain 2019; 12(1): 100

Malito E, Hulse RE, Tang W-J. Amyloid beta-degrading cryptidases: insulin degrading enzyme, presequence peptidase, and neprilysin. Cell Mol Life Sci 2008; 65(16): 2574–85

Malm T, Loppi S, Kanninen KM. Exosomes in Alzheimer's disease. Neurochem Int 2016; 97: 193–9

Mandrekar S, Jiang Q, Lee CYD, Koenigsknecht-Talboo J, Holtzman DM, Landreth GE. Microglia mediate the clearance of soluble Abeta through fluid phase macropinocytosis. J Neurosci 2009; 29(13): 4252–62

Mangalmurti A, Lukens JR. How neurons die in Alzheimer's disease: Implications for neuroinflammation. Curr Opin Neurobiol 2022; 75: 102575

Marcello E, Epis R, Saraceno C, Di Luca M. Synaptic Dysfunction in Alzheimer’s Disease. In: Synaptic Plasticity. Springer, Vienna 2012; 573–601.

Markesbery WR. Oxidative stress hypothesis in Alzheimer's disease. Free Rad Biol Med 1997; 23(1): 134–47

Marshall KE, Vadukul DM, Staras K, Serpell LC. Misfolded amyloid-β-42 impairs the endosomal-lysosomal pathway. Cell Mol Life Sci 2020; 77(23): 5031–43

Matsuzaki K. Aβ-ganglioside interactions in the pathogenesis of Alzheimer's disease. Biochim Biophys Acta Biomembr 2020; 1862(8): 183233

Matsuzaki K. Physicochemical interactions of amyloid beta-peptide with lipid bilayers. Biochim Biophys Acta 2007; 1768(8): 1935–42

Mauvezin C, Neufeld TP. Bafilomycin A1 disrupts autophagic flux by inhibiting both V-ATPase-dependent acidification and Ca-P60A/SERCA-dependent autophagosome-lysosome fusion. Autophagy 2015; 11(8): 1437–8

McQuade A, Blurton-Jones M. Microglia in Alzheimer's Disease: Exploring How Genetics and Phenotype Influence Risk. J Mol Biol 2019; 431(9): 1805–17

Mecocci P, MacGarvey U, Beal MF. Oxidative damage to mitochondrial DNA is increased in Alzheimer's disease. Ann Neurol 1994; 36(5): 747–51

Menon S, Sengupta N. Influence of crowding and surfaces on protein amyloidogenesis: A thermo-kinetic perspective. Biochim Biophys Acta Proteins Proteom 2019; 1867(10): 941–53

Meusser B, Hirsch C, Jarosch E, Sommer T. ERAD: the long road to destruction. Nat Cell Biol 2005; 7(8): 766–72

Milton NGN. Phosphorylated Amyloid-β: the Toxic Intermediate in Alzheimer's Disease Neurodegeneration. In: Harris JR, Fahrenholz F, editors. Alzheimer's disease: Cellular and molecular aspects of amyloid [beta] New York: Springer 2005; 381–402.

Milton NGN. Phosphorylation of amyloid-β at the serine 26 residue by human cdc2 kinase. Neuroreport 2001; 12(17): 3839

Mohamed A, Posse de Chaves E. Aβ internalization by neurons and glia. Int J Alzheimers Dis 2011; 2011: 127984

Mohandas E, Rajmohan V, Raghunath B. Neurobiology of Alzheimer's disease. Indian J Psychiatry 2009; 51(1): 55–61

Moravec RA, O'Brien MA, Daily WJ, Scurria MA, Bernad L, Riss TL. Cell-based bioluminescent assays for all three proteasome activities in a homogeneous format. Anal Biochem 2009; 387(2): 294–302

Moreira PI, Carvalho C, Zhu X, Smith MA, Perry G. Mitochondrial dysfunction is a trigger of Alzheimer's disease pathophysiology. Biochim Biophys Acta 2010; 1802(1): 2–10

Morgan D, Gordon MN, Tan J, Wilcock D, Rojiani AM. Dynamic complexity of the microglial activation response in transgenic models of amyloid deposition: implications for Alzheimer therapeutics. J Neuropathol Exp Neurol 2005; 64(9): 743–53

Mosser S, Gerber H, Fraering PC. Identification of truncated C-terminal fragments of the Alzheimer's disease amyloid protein precursor derived from sequential proteolytic pathways. J Neurochem 2021; 156(6): 943–56

Mudher A, Lovestone S. Alzheimer's disease-do tauists and baptists finally shake hands? Trends Neurosci 2002; 25(1): 22–6

Mullan M, Crawford F, Axelman K, et al. A pathogenic mutation for probable Alzheimer's disease in the APP gene at the N-terminus of beta-amyloid. Nat Genet 1992; 1(5): 345–7

Murphy MP, LeVine H. Alzheimer's disease and the amyloid-beta peptide. J Alz Dis 2010; 19(1): 311–23

Nagamoto-Combs K, Kulas J, Combs CK. A novel cell line from spontaneously immortalized murine microglia. J Neurosci Methods 2014; 233: 187–98

Nagele R, D'Andrea M, Anderson W, Wang H-Y. Intracellular accumulation of β-amyloid1–42 in neurons is facilitated by the α7 nicotinic acetylcholine receptor in Alzheimer's disease. Neurosci 2002; 110(2): 199–211

Nagele RG, Wegiel J, Venkataraman V, Imaki H, Wang K-C, Wegiel J. Contribution of glial cells to the development of amyloid plaques in Alzheimer's disease. Neurobiol of Aging 2004; 25(5): 663–74

Nandi D, Tahiliani P, Kumar A, Chandu D. The ubiquitin-proteasome system. J Biosci 2006; 31(1): 137–55

Napolitano G, Esposito A, Choi H, et al. mTOR-dependent phosphorylation controls TFEB nuclear export. Nat Commun 2018; 9(1): 3312

N'Diaye E-N, Kajihara KK, Hsieh I, Morisaki H, Debnath J, Brown EJ. PLIC proteins or ubiquilins regulate autophagy-dependent cell survival during nutrient starvation. EMBO Rep 2009; 10(2): 173–9

Nestler EJ, Greengard P. Protein phosphorylation in the brain. Nature 1983; 305(5935): 583–8

Nilsson P, Loganathan K, Sekiguchi M, et al. Aβ secretion and plaque formation depend on autophagy. Cell Rep 2013; 5(1): 61–9

Nishikawa S, Brodsky JL, Nakatsukasa K. Roles of molecular chaperones in endoplasmic reticulum (ER) quality control and ER-associated degradation (ERAD). J Biochem 2005; 137(5): 551–5

Niu Z, Zhang Z, Zhao W, Yang J. Interactions between amyloid β peptide and lipid membranes. Biochim Biophys Acta Biomembr 2018; 1860(9): 1663–9

Nixon RA, Mathews PM, Cataldo AM. The neuronal endosomal-lysosomal system in Alzheimer's disease. J Alz Dis 2001; 3(1): 97–107

Nixon RA, Wegiel J, Kumar A, et al. Extensive involvement of autophagy in Alzheimer disease: an immuno-electron microscopy study. J Neuropathol Exp Neurol 2005; 64(2): 113–22

Nixon RA, Yang D-S. Autophagy failure in Alzheimer's disease--locating the primary defect. Neurobiol Dis 2011; 43(1): 38–45

Nixon RA. Amyloid precursor protein and endosomal-lysosomal dysfunction in Alzheimer's disease: inseparable partners in a multifactorial disease. FASEB J 2017; 31(7): 2729–43

Nixon RA. Autophagy, amyloidogenesis and Alzheimer disease. J Cell Sci 2007; 120(Pt 23): 4081–91

Noda NN, Fujioka Y. Atg1 family kinases in autophagy initiation. Cell Mol Life Sci 2015; 72(16): 3083–96

Ntsapi C, Lumkwana D, Swart C, Du Toit A, Loos B. New Insights Into Autophagy Dysfunction Related to Amyloid Beta Toxicity and Neuropathology in Alzheimer's Disease. Int Rev Cell Mol Biol 2018; 336: 321–61

O'Brien M, Moehring D, Muñoz-Planillo R, et al. A bioluminescent caspase-1 activity assay rapidly monitors inflammasome activation in cells. J Immunol Methods 2017; 447: 1–13

Oddo S, Caccamo A, Smith IF, Green KN, LaFerla FM. A dynamic relationship between intracellular and extracellular pools of Abeta. The Amer J Pathol 2006; 168(1): 184–94

Ogawa M, Tsukuda M, Yamaguchi T, et al. Ganglioside-mediated aggregation of amyloid β-proteins (Aβ): comparison between Aβ-(1-42) and Aβ-(1-40). J Neurochem 2011; 116(5): 851–7

Oh S, Hong HS, Hwang E, et al. Amyloid peptide attenuates the proteasome activity in neuronal cells. Mech Ageing Dev 2005; 126(12): 1292–9

Okazawa H. Intracellular amyloid hypothesis for ultra-early phase pathology of Alzheimer's disease. Neuropathol 2021; 41(2): 93–8

Oliveira J, Costa M, Almeida MSC de, Da Cruz E Silva OAB, Henriques AG. Protein Phosphorylation is a Key Mechanism in Alzheimer's Disease. J Alz Dis 2017; 58(4): 953–78

Omtri RS, Thompson KJ, Tang X, et al. Differential Effects of Alzheimer's Disease Aβ40 and 42 on Endocytosis and Intraneuronal Trafficking. Neurosci 2018; 373: 159–68

Onyango IG, Khan SM. Oxidative stress, mitochondrial dysfunction, and stress signaling in Alzheimer's disease. Curr Alz Res 2006; 3(4): 339-49.

Orr ME, Oddo S. Autophagic/lysosomal dysfunction in Alzheimer's disease. Alz Res Ther 2013; 5(5): 53

Pacheco-Quinto J, Eckman EA. Endothelin-converting enzymes degrade intracellular β-amyloid produced within the endosomal/lysosomal pathway and autophagosomes. J Biol Chem 2013; 288(8): 5606–15

Pande M, Srivastava R. Molecular and clinical insights into protein misfolding and associated amyloidosis. Eur J Med Chem 2019; 184: 111753

Pasternak SH, Callahan JW, Mahuran DJ. The role of the endosomal/lysosomal system in amyloid-beta production and the pathophysiology of Alzheimer's disease: reexamining the spatial paradox from a lysosomal perspective. J Alz Dis 2004; 6(1): 53–65

Pattingre S, Tassa A, Qu X, et al. Bcl-2 antiapoptotic proteins inhibit Beclin 1-dependent autophagy. Cell 2005; 122(6): 927–39

Pegtel DM, Peferoen L, Amor S. Extracellular vesicles as modulators of cell-to-cell communication in the healthy and diseased brain. Philos Trans R Soc Lond B Biol Sci 2014; 369(1652)

Penke B, Bogár F, Fülöp L. β-Amyloid and the Pathomechanisms of Alzheimer's Disease: A Comprehensive View. Molecules 2017; 22(10): 1692

Penke B, Tóth AM, Földi I, Szűcs M, Janáky T. Intraneuronal β-amyloid and its interactions with proteins and subcellular organelles. Electrophoresis 2012; 33(24): 3608–16

Perez-Gonzalez R, Gauthier SA, Kumar A, Levy E. The exosome secretory pathway transports amyloid precursor protein carboxyl-terminal fragments from the cell into the brain extracellular space. J Biol Chem 2012; 287(51): 43108–15

Perluigi M, Barone E, Di Domenico F, Butterfield DA. Aberrant protein phosphorylation in Alzheimer disease brain disturbs pro-survival and cell death pathways. Biochim Biophys Acta 2016; 1862(10): 1871–82

Pflanzner T, Janko MC, André-Dohmen B, et al. LRP1 mediates bidirectional transcytosis of amyloid-β across the blood-brain barrier. Neurobiol Aging 2011; 32(12): 2323.e1-11

Picone P, Nuzzo D, Caruana L, Scafidi V, Di Carlo M. Mitochondrial dysfunction: different routes to Alzheimer's disease therapy. Ox Med Cell Longevity 2014; 2014: 780179

Pigino G, Morfini G, Atagi Y, et al. Disruption of fast axonal transport is a pathogenic mechanism for intraneuronal amyloid beta. Proc Natl Acad Sci 2009; 106(14): 5907–12

Pimplikar SW. Reassessing the amyloid cascade hypothesis of Alzheimer's disease. The Int J Biochem Cell Biol 2009; 41(6): 1261–8

Pithadia AS, Lim MH. Metal-associated amyloid-β species in Alzheimer's disease. Curr Op Chem Biol 2012; 16(1-2): 67–73

Praticò D. Oxidative stress hypothesis in Alzheimer's disease: a reappraisal. Trends Pharmacol Sci 2008; 29(12): 609–15

Rajendran L, Honsho M, Zahn TR, et al. Alzheimer's disease beta-amyloid peptides are released in association with exosomes. Proc Natl Acad Sci USA 2006; 103(30): 11172–7

Razani E, Pourbagheri-Sigaroodi A, Safaroghli-Azar A, Zoghi A, Shanaki-Bavarsad M, Bashash D. The PI3K/Akt signaling axis in Alzheimer's disease: a valuable target to stimulate or suppress? Cell Stress and Chaperones 2021; 26(6): 871–87

Refolo LM, Pappolla MA, LaFrancois J, et al. A cholesterol-lowering drug reduces beta-amyloid pathology in a transgenic mouse model of Alzheimer's disease. Neurobiol Dis 2001; 8(5): 890–9

Rezaei-Ghaleh N, Amininasab M, Kumar S, Walter J, Zweckstetter M. Phosphorylation modifies the molecular stability of β-amyloid deposits. Nat Commun 2016; 7: 11359

Rezaei-Ghaleh N, Kumar S, Walter J, Zweckstetter M. Phosphorylation Interferes with Maturation of Amyloid-β Fibrillar Structure in the N Terminus. J Biol Chem 2016; 291(31): 16059–67

Rijal Upadhaya A, Kosterin I, Kumar S, et al. Biochemical stages of amyloid-β peptide aggregation and accumulation in the human brain and their association with symptomatic and pathologically preclinical Alzheimer's disease. Brain 2014; 137(Pt 3): 887–903

Roberts BR, Ryan TM, Bush AI, Masters CL, Duce JA. The role of metallobiology and amyloid-β peptides in Alzheimer's disease. J Neurochem 2012; 120(1): 149–66

Rodal SK, Skretting G, Garred O, Vilhardt F, van Deurs B, Sandvig K. Extraction of cholesterol with methyl-beta-cyclodextrin perturbs formation of clathrin-coated endocytic vesicles. Mol Biol Cell 1999; 10(4): 961–74

Roher AE, Kokjohn TA, Clarke SG, et al. APP/Aβ structural diversity and Alzheimer's disease pathogenesis. Neurochem Int 2017; 110: 1–13

Roos TT, Garcia MG, Martinsson I, et al. Neuronal spreading and plaque induction of intracellular Aβ and its disruption of Aβ homeostasis. Acta Neuropathol 2021; 142(4): 669–87

Rosenblum WI. Why Alzheimer trials fail: removing soluble oligomeric beta amyloid is essential, inconsistent, and difficult. Neurobiol Aging 2014; 35(5): 969–74

Rostami J, Mothes T, Kolahdouzan M, et al. Crosstalk between astrocytes and microglia results in increased degradation of α-synuclein and amyloid-β aggregates. J Neuroinflam 2021; 18(1): 124

Rüb C, Wilkening A, Voos W. Mitochondrial quality control by the Pink1/Parkin system. Cell Tissue Res 2017; 367(1): 111–23

Saito T, Suemoto T, Brouwers N, et al. Potent amyloidogenicity and pathogenicity of Aβ43. Nat Neurosci 2011; 14(8): 1023–32

Salahuddin P, Fatima MT, Abdelhameed AS, Nusrat S, Khan RH. Structure of amyloid oligomers and their mechanisms of toxicities: Targeting amyloid oligomers using novel therapeutic approaches. Eur J Med Chem 2016; 114: 41–58

Salminen A, Ojala J, Suuronen T, Kaarniranta K, Kauppinen A. Amyloid-beta oligomers set fire to inflammasomes and induce Alzheimer's pathology. J Cell Mol Med 2008; 12(6A): 2255–62

Santos RX, Correia SC, Wang X, et al. A synergistic dysfunction of mitochondrial fission/fusion dynamics and mitophagy in Alzheimer's disease. J Alz Dis 2010; 20(2): S401-12

Sardar Sinha M, Ansell-Schultz A, Civitelli L, et al. Alzheimer's disease pathology propagation by exosomes containing toxic amyloid-beta oligomers. Acta Neuropathol 2018; 136(1): 41–56

Savelieff MG, Lee S, Liu Y, Lim MH. Untangling amyloid-β, tau, and metals in Alzheimer's disease. ACS Chem Biol 2013; 8(5): 856–65

Schaefer J, Jovanovic G, Kotta-Loizou I, Buck M. Single-step method for β-galactosidase assays in Escherichia coli using a 96-well microplate reader. Anal Biochem 2016; 503: 56–7

Scheltens P, Strooper B de, Kivipelto M, et al. Alzheimer's disease. Lancet 2021; 397(10284): 1577–90

Schneider A, Schulz-Schaeffer W, Hartmann T, Schulz JB, Simons M. Cholesterol depletion reduces aggregation of amyloid-beta peptide in hippocampal neurons. Neurobiol Dis 2006; 23(3): 573–7

Selkoe DJ, Hardy J. The amyloid hypothesis of Alzheimer's disease at 25 years. EMBO Mol Med 2016; 8(6): 595–608

Selkoe DJ. Cell biology of the amyloid beta-protein precursor and the mechanism of Alzheimer's disease. Annu Rev Cell Biol 1994; 10(1): 373–403

Selkoe DJ. Soluble oligomers of the amyloid beta-protein impair synaptic plasticity and behavior. Behav Brain Research 2008; 192(1): 106–13

Selkoe DJ. The molecular pathology of Alzheimer's disease. Neuron 1991; 6(4): 487–98

Sengoku R. Aging and Alzheimer's disease pathology. Neuropathol 2020; 40(1): 22–9

Sengupta U, Nilson AN, Kayed R. The Role of Amyloid-β Oligomers in Toxicity, Propagation, and Immunotherapy. EBioMedicine 2016; 6: 42–9

Shah A, Kishore U, Shastri A. Complement System in Alzheimer's Disease. Int J Mol Sci 2021; 22(24)

Shah SZA, Zhao D, Hussain T, Yang L. The Role of Unfolded Protein Response and Mitogen-Activated Protein Kinase Signaling in Neurodegenerative Diseases with Special Focus on Prion Diseases. Front Aging Neurosci 2017; 9: 120

Shankar GM, Bloodgood BL, Townsend M, Walsh DM, Selkoe DJ, Sabatini BL. Natural oligomers of the Alzheimer amyloid-beta protein induce reversible synapse loss by modulating an NMDA-type glutamate receptor-dependent signaling pathway. J Neurosci 2007; 27(11): 2866–75

Sharma P, Schiapparelli L, Cline HT. Exosomes function in cell-cell communication during brain circuit development. Curr Op Neurobiol 2013; 23(6): 997–1004

Sharoar MG, Hu X, Ma X-M, Zhu X, Yan R. Sequential formation of different layers of dystrophic neurites in Alzheimer's brains. Mol Psychiatry 2019; 24(9): 1369–82

Shea D, Daggett V. Amyloid-β Oligomers: Multiple Moving Targets. Biophysica 2022; 2(2): 91–110

Sheng M, Sabatini BL, Südhof TC. Synapses and Alzheimer's disease. Cold Spring Harb Perspect Biol 2012; 4(5): a005777

Shi J-M, Li H-Y, Liu H, et al. N-terminal Domain of Amyloid-β Impacts Fibrillation and Neurotoxicity. ACS Omega 2022; 7(43): 38847–55

Shi Y, Holtzman DM. Interplay between innate immunity and Alzheimer disease: APOE and TREM2 in the spotlight. Nat Rev Immunol 2018; 18(12): 759–72

Shinohara M, Tachibana M, Kanekiyo T, Bu G. Role of LRP1 in the pathogenesis of Alzheimer's disease: evidence from clinical and preclinical studies. J Lipid Res 2017; 58(7): 1267–81

Shirwany NA, Payette D, Xie J, Guo Q. The amyloid beta ion channel hypothesis of Alzheimer's disease. Neuropsych Dis Treat 2007; 3(5): 597–612

Shoji M, Hirai S, Yamaguchi H, Harigaya Y, Kawarabayashi T. Amyloid β-protein precursor accumulates in dystrophic neurites of senile plaques in Alzheimer-type dementia. Brain Research 1990; 512(1): 164–8

Sjödin S, Brinkmalm G, Öhrfelt A, et al. Endo-lysosomal proteins and ubiquitin CSF concentrations in Alzheimer's and Parkinson's disease. Alz Res Therapy 2019; 11(1): 82

Sontag J-M, Wasek B, Taleski G, et al. Altered protein phosphatase 2A methylation and Tau phosphorylation in the young and aged brain of methylenetetrahydrofolate reductase (MTHFR) deficient mice. Front Aging Neurosci. 2014; 6: 214

Soreghan B, Kosmoski J, Glabe C. Surfactant properties of Alzheimer's A beta peptides and the mechanism of amyloid aggregation. J Biol Chem 1994; 269(46): 28551–4

Spires-Jones TL, Hyman BT. The intersection of amyloid beta and tau at synapses in Alzheimer's disease. Neuron 2014; 82(4): 756–71

Sponne I, Fifre A, Koziel V, Oster T, Olivier J-L, Pillot T. Membrane cholesterol interferes with neuronal apoptosis induced by soluble oligomers but not fibrils of amyloid-beta peptide. FASEB J 2004; 18(7): 836–8

Stefani M. Biochemical and biophysical features of both oligomer/fibril and cell membrane in amyloid cytotoxicity. FEBS J 2010; 277(22): 4602–13

Stefani M. Structural features and cytotoxicity of amyloid oligomers: implications in Alzheimer's disease and other diseases with amyloid deposits. Prog Neurobiol 2012; 99(3): 226–45

Streit WJ, Mrak RE, Griffin WST. Microglia and neuroinflammation: a pathological perspective. J Neuroinflam 2004; 1(1): 14

Stutz A, Horvath GL, Monks BG, Latz E. ASC speck formation as a readout for inflammasome activation. Methods Mol Biol 2013; 1040: 91–101

Takahashi RH, Almeida CG, Kearney PF, et al. Oligomerization of Alzheimer's beta-amyloid within processes and synapses of cultured neurons and brain. J Neurosci 2004; 24(14): 3592–9

Takahashi RH, Milner TA, Li F, et al. Intraneuronal Alzheimer Aβ42 Accumulates in Multivesicular Bodies and Is Associated with Synaptic Pathology. The Amer J Pathol 2002; 161(5): 1869–79

Takahashi RH, Nagao T, Gouras GK. Plaque formation and the intraneuronal accumulation of β-amyloid in Alzheimer's disease. Pathol Int 2017; 67(4): 185–93

Takashima A. Amyloid-beta, tau, and dementia. J Alz Dis 2009; 17(4): 729–36

Tamboli IY, Barth E, Christian L, et al. Statins promote the degradation of extracellular amyloid {beta}-peptide by microglia via stimulation of exosome-associated insulin-degrading enzyme (IDE) secretion. J Biol Chem 2010; 285(48): 37405–14

Tanaka H, Homma H, Fujita K, et al. YAP-dependent necrosis occurs in early stages of Alzheimer's disease and regulates mouse model pathology. Nat Commun 2020; 11(1): 507

Tarasoff-Conway JM, Carare RO, Osorio RS, et al. Clearance systems in the brain-implications for Alzheimer disease. Nat Rev Neurol 2015; 11(8): 457–70

Tay WM, Huang D, Rosenberry TL, Paravastu AK. The Alzheimer's amyloid-β(1-42) peptide forms off-pathway oligomers and fibrils that are distinguished structurally by intermolecular organization. J Mol Biol 2013; 425(14): 2494–508

Teixeira V, Feio MJ, Bastos M. Role of lipids in the interaction of antimicrobial peptides with membranes. Prog Lipid Res 2012; 51(2): 149–77

Terakawa MS, Lin Y, Kinoshita M, et al. Impact of membrane curvature on amyloid aggregation. Biochim Biophys Acta Biomembr 2018; 1860(9): 1741–64

Tien NT, Karaca I, Tamboli IY, Walter J. Trehalose Alters Subcellular Trafficking and the Metabolism of the Alzheimer-associated Amyloid Precursor Protein. J Biol Chem 2016; 291(20): 10528–40

Tomic JL, Pensalfini A, Head E, Glabe CG. Soluble fibrillar oligomer levels are elevated in Alzheimer's disease brain and correlate with cognitive dysfunction. Neurobiol Dis 2009; 35(3): 352–8

Tomiyama T, Matsuyama S, Iso H, et al. A mouse model of amyloid beta oligomers: their contribution to synaptic alteration, abnormal tau phosphorylation, glial activation, and neuronal loss in vivo. J Neurosci 2010; 30(14): 4845–56

Tõugu V, Tiiman A, Palumaa P. Interactions of Zn(II) and Cu(II) ions with Alzheimer's amyloid-beta peptide. Metal ion binding, contribution to fibrillization and toxicity. Metallomics. 2011; 3(3): 250–61

Trojanowski JQ. Tauists, Baptists, Syners, Apostates, and new data. Ann Neurol. 2002; 52(3): 263–5

Tseng BP, Green KN, Chan JL, Blurton-Jones M, LaFerla FM. Abeta inhibits the proteasome and enhances amyloid and tau accumulation. Neurobiol Aging 2008; 29(11): 1607–18

Uddin MS, Yu WS, Lim LW. Exploring ER stress response in cellular aging and neuroinflammation in Alzheimer's disease. Ageing Res Rev 2021; 70: 101417

Umeda T, Tomiyama T, Sakama N, et al. Intraneuronal amyloid β oligomers cause cell death via endoplasmic reticulum stress, endosomal/lysosomal leakage, and mitochondrial dysfunction in vivo. J Neurosci Res 2011; 89(7): 1031–42

Upadhya SC, Hegde AN. Role of the ubiquitin proteasome system in Alzheimer's disease. BMC Biochem 2007; 8(1): S12

Uranga RM, Salvador GA. Unraveling the Burden of Iron in Neurodegeneration: Intersections with Amyloid Beta Peptide Pathology. Oxidative Medicine and Cellular Longevity 2018; 18: 285-341

Vadukul DM, Maina M, Franklin H, Nardecchia A, Serpell LC, Marshall KE. Internalisation and toxicity of amyloid-β 1-42 are influenced by its conformation and assembly state rather than size. FEBS Letters 2020; 594(21): 3490–503

van Zeller M, Dias D, Sebastião AM, Valente CA. NLRP3 Inflammasome: A Starring Role in Amyloid-β- and Tau-Driven Pathological Events in Alzheimer's Disease. J Alz Dis 2021; 83(3): 939–61

Venegas C, Kumar S, Franklin BS, et al. Microglia-derived ASC specks cross-seed amyloid-β in Alzheimer's disease. Nature 2017; 552(7685): 355–61

Verbeek MM, Otte-Höller I, Fransen JAM, Waal RMW de. Accumulation of the amyloid-beta precursor protein in multivesicular body-like organelles. J Histochem Cytochem 2002; 50(5): 681–90

Verdier Y, Zarándi M, Penke B. Amyloid beta-peptide interactions with neuronal and glial cell plasma membrane: binding sites and implications for Alzheimer's disease. J Pept Sci 2004; 10(5): 229–48

Vickers JC, Dickson TC, Adlard PA, Saunders HL, King CE, McCormack G. The cause of neuronal degeneration in Alzheimer's disease. Prog Neurobiol 2000; 60(2): 139–65

Vilchez D, Saez I, Dillin A. The role of protein clearance mechanisms in organismal ageing and age-related diseases. Nat Commun 2014; 5(1): 5659

Viola KL, Klein WL. Amyloid β oligomers in Alzheimer's disease pathogenesis, treatment, and diagnosis. Acta Neuropathol 2015; 129(2): 183–206

Walaas SI, Greengard P. Protein phosphorylation and neuronal function. Pharmacol Rev 1991; 43(3): 299–349

Walsh DM, Selkoe DJ. A beta oligomers - a decade of discovery. Journal of Neurochemistry 2007; 101(5): 1172–84

Walsh DM, Selkoe DJ. Amyloid β-protein and beyond: the path forward in Alzheimer's disease. Curr Opin Neurobiol 2020; 61: 116–24

Wang C, Telpoukhovskaia MA, Bahr BA, Chen X, Gan L. Endo-lysosomal dysfunction: a converging mechanism in neurodegenerative diseases. Curr Opin Neurobiol 2018; 48: 52–8

Wang K, Shao X, Cai W. Binding Models of Aβ42 Peptide with Membranes Explored by Molecular Simulations. J Chem Infor Model 2022; 62(24): 6482–93

Wang M, Wey S, Zhang Y, Ye R, Lee AS. Role of the unfolded protein response regulator GRP78/BiP in development, cancer, and neurological disorders. Antioxid Redox Signal 2009; 11(9): 2307–16

Wang W, Zhao F, Ma X, Perry G, Zhu X. Mitochondria dysfunction in the pathogenesis of Alzheimer's disease: recent advances. Mol Neurodegener 2020; 15(1): 30

Wegiel J, Imaki H, Wang K-C, et al. Origin and turnover of microglial cells in fibrillar plaques of APPsw transgenic mice. Acta Neuropathol 2003; 105(4): 393–402

Wegiel J, Wang KC, Imaki H, et al. The role of microglial cells and astrocytes in fibrillar plaque evolution in transgenic APP(SW) mice. Neurobiol Aging 2001; 22(1): 49–61

Wen J, Fang F, Guo S-H, et al. Amyloid β-Derived Diffusible Ligands (ADDLs) Induce Abnormal Autophagy Associated with Aβ Aggregation Degree. J Mol Neurosci 2018; 64(2): 162–74

Wildsmith KR, Holley M, Savage JC, Skerrett R, Landreth GE. Evidence for impaired amyloid β clearance in Alzheimer's disease. Alz Res Therapy 2013; 5(4): 33

Williams TL, Serpell LC. Membrane and surface interactions of Alzheimer's Aβ peptide--insights into the mechanism of cytotoxicity. FEBS J 2011; 278(20): 3905–17

Wirths O, Bayer TA. Intraneuronal Aβ accumulation and neurodegeneration: lessons from transgenic models. Life Sci 2012; 91(23-24): 1148–52

Wolfe CM, Fitz NF, Nam KN, Lefterov I, Koldamova R. The Role of APOE and TREM2 in Alzheimer's Disease-Current Understanding and Perspectives. Int J Mol Sci 2018; 20(1): 81

Wolfe KJ, Cyr DM. Amyloid in neurodegenerative diseases: friend or foe? Sem Cell & Dev Biol 2011; 22(5): 476–81

Wong P-M, Puente C, Ganley IG, Jiang X. The ULK1 complex: sensing nutrient signals for autophagy activation. Autophagy 2013; 9(2): 124–37

Wu F, Yao PJ. Clathrin-mediated endocytosis and Alzheimer's disease: an update. Ageing Res Rev 2009; 8(3): 147–9

Wu T, Lin D, Cheng Y, et al. Amyloid Cascade Hypothesis for the Treatment of Alzheimer's Disease: Progress and Challenges. Aging Dis 2022; 13(6): 1745–58

Xiao Q, Yan P, Ma X, et al. Neuronal-Targeted TFEB Accelerates Lysosomal Degradation of APP, Reducing Aβ Generation and Amyloid Plaque Pathogenesis. J Neurosci 2015; 35(35): 12137–51

Xu J, Camfield R, Gorski SM. The interplay between exosomes and autophagy - partners in crime. J Cell Sci 2018; 131(15)

Yamazaki T, Koo EH, Selkoe DJ. Trafficking of cell-surface amyloid beta-protein precursor. II. Endocytosis, recycling and lysosomal targeting detected by immunolocalization. J Cell Sci 1996; 109(5): 999–1008

Yang AJ, Chandswangbhuvana D, Margol L, Glabe CG. Loss of endosomal/lysosomal membrane impermeability is an early event in amyloid A?1-42 pathogenesis. J Neurosci Res 1998; 52(6): 691–8

Yang D-S, Kumar A, Stavrides P, et al. Neuronal apoptosis and autophagy cross talk in aging PS/APP mice, a model of Alzheimer's disease. The Amer J Pathol 2008; 173(3): 665–81

Yankner BA. Mechanisms of neuronal degeneration in Alzheimer's disease. Neuron 1996; 16(5): 921–32

Yasuda Y, Kageyama T, Akamine A, et al. Characterization of new fluorogenic substrates for the rapid and sensitive assay of cathepsin E and cathepsin D. J Biochem 1999; 125(6): 1137–43

Zadka Ł, Sochocka M, Hachiya N, et al. Endocytosis and Alzheimer's disease. GeroScience 2023: 1–15

Zaretsky DV, Zaretskaia MV, Molkov YI. Membrane channel hypothesis of lysosomal permeabilization by beta-amyloid. Neurosci Lett 2022; 770: 136338

Zaretsky DV, Zaretskaia MV. Intracellular ion changes induced by the exposure to beta-amyloid can be explained by the formation of channels in the lysosomal membranes. Biochim Biophys Acta Mol Cell Res 2021; 1869(1): 119145

Zaretsky DV, Zaretskaia MV. Mini-review: Amyloid degradation toxicity hypothesis of Alzheimer's disease. Neurosci Lett 2021; 756: 135959

Zhang H, Ma Q, Zhang Y-W, Xu H. Proteolytic processing of Alzheimer's β-amyloid precursor protein. Journal of Neurochemistry 2012; 120(1): 9–21

Zhang J, Wang J, Wong YK, et al. Docetaxel enhances lysosomal function through TFEB activation. Cell Death Dis 2018; 9(6): 614

Zhang L, Trushin S, Christensen TA, et al. Altered brain energetics induces mitochondrial fission arrest in Alzheimer's Disease. Sci Rep 2016; 6(1): 18725

Zhang Y, Chen X, Zhao Y, Ponnusamy M, Liu Y. The role of ubiquitin proteasomal system and autophagy-lysosome pathway in Alzheimer's disease. Rev Neurosci 2017; 28(8): 861–8

Zhao Z, Sagare AP, Ma Q, et al. Central role for PICALM in amyloid-β blood-brain barrier transcytosis and clearance. Nat Neurosci 2015; 18(7): 978–87

Zheng H, Koo EH. The amyloid precursor protein: beyond amyloid. Mol Neurodegener 2006; 1(1): 5

Zheng L, Cedazo-Minguez A, Hallbeck M, Jerhammar F, Marcusson J, Terman A. Intracellular distribution of amyloid beta peptide and its relationship to the lysosomal system. Transl Neurodegener 2012; 1(1): 19

Zhou T-Y, Ma R-X, Li J, et al. Review of PINK1-Parkin-mediated mitochondrial autophagy in Alzheimer's disease. Eur J Pharmacol 2023; 959: 176057

Zlokovic BV, Martel CL, Matsubara E, et al. Glycoprotein 330/megalin: probable role in receptor-mediated transport of apolipoprotein J alone and in a complex with Alzheimer disease amyloid beta at the blood-brain and blood-cerebrospinal fluid barriers. Proc Natl Acad Sci USA 1996; 93(9): 4229–34

Zlokovic BV. Clearing amyloid through the blood-brain barrier. J Neurochem 2004; 89(4): 807–11

9. Acknowledgements

This important milestone of PhD has been possible because of my supervisor who believed in me, Prof. Jochen Walter. I would like to thank him for his belief in me and providing me the opportunity to take this step ahead in the field of Alzheimer's. I would like to express my indebtedness to him for his unfailing interest, constructive encouragement, continual and prompt support throughout my research period. His suggestions will remain as an inexhaustible source of scientific learning throughout my life. I heartily thank him for everything he has done for me throughout my tenure and in future days to come. I could not have imagined having a better supervisor for my PhD studies.

'If you can dream about it, don't stop working for it'- Mihir P. Khambete.

It is to this motivational line that I would dedicate my journey till date and all my future endeavors for Alzheimer's disease. The love for AD fueled during my second year and constructive impetus received from Prof. Rahul Jain, Prof. Mariam. S. Degani and now Prof. Anne-Sophie Hafner helped shape it into a beautiful thing which I will cherish and nurture for years to come. I am happy to have the constant guidance and support from Mihir and Siddhisha in my life.

This PhD journey would not have been the same, if not, for the constant support and encouragement of my two important pillars in the lab - Sandra Theil and Dr. Marietta Fabiano. Words fail to express the love, affection and respect I have for them. You both have been supportive and a source of never-ending enthusiasm throughout. I would also like to express my sincere thanks to thoughtful discussions with Dr. Naoto Oikawa, Thomas Bajaj, and Prof. Neil Gassen. I would like to express my gratitude towards lab members and colleagues from both, Walter and Wullner lab. I would like to express my thanks to Dr. Sathish Kumar for procuring the AFI funding and discussion during the initial year of my PhD tenure. Although the time together was challenging, I did learn something. With respect to aid and assistance with the projects completed during my PhD tenure - I would like to thank T. Bajaj and Dr. N. Gassen (University Clinic Bonn), and Dr. J. Höhfeld (University of Bonn) for sharing GFP-LC3-LC3Δ-RFP and mCherry-GFP-LC3B reporter cDNA constructs, scientific discussions, and result interpretation. I would also like to thank

D. Puchta-Stromberg and Prof. Voos for their assistance in doing the mitochondrial experiments, antibodies, and scientific discussions. The transgenic animals were provided by Dr. Nadia Villacampa and Prof. Micheal Heneka, and we greatly appreciate their support in this case. The monoclonal antibodies H4B4 and ABL-93c developed by J.T. August was obtained from the Developmental Studies Hybridoma Bank, created by the NICHD of the NIH and maintained at the University of Iowa, Department of Biology, Iowa City, IA 52242. We also thank the Microscopy Core Facility, in particular Lydia Maus and Pia Stausberg, of the Medical Faculty at the University of Bonn for providing support and instrumentation funded by the Deutsche Forschungsgemeinschaft, Project Number: 388169927 (Confocal microscope) and 388171357 (Electron microscope). Last but not the least, I would like to thank BIGS Neuroscience, Young German Neuroscience society, University of Bonn, and University Hospital Bonn for the different experience I had during my PhD tenure.

I dedicate this work to my parents and grandparents who have always worked and prayed for me. They have always hoped that I would succeed in all my endeavors. My family has been my constructive pillars of supportive strength and have always stood by me in good and bad times. Their belief in me has always been my motivation to excel. I dedicate all the successful endeavors to the dreams of my beloved mother. Love you Mom, Dad, Mayur and now, Khaled Trabelsi! Special mention to SOFRA Cologne (SOFRA Queer Migrants e. V. now) for the love and support in providing a home away from home!

Finally, I thank God for making me capable enough to fulfil all my goals and be successful in all that I undertook. I bow before him for his limitless love and countless blessings.

10. Publications and patent

- **Kapadia, A.**, Theil, S., Opitz, S., Villacampa, N., Beckert, H., Schoch, S., Heneka, M.T., Kumar, S. and Walter, J. 2024. Phosphorylation-state dependent intraneuronal sorting of Aβ differentially impairs autophagy and the endo-lysosomal system. *Autophagy*, 20(1), p166-187. DOI: 10.1080/15548627.2023.2252300 *(part of this thesis)*
- Kundu, R.*, Mondal, S.*, **Kapadia, A.***, Banerjee, A.A.*, Kucherak, O.A., Klymchenko, A.S., Koushika, S.P., Venkatramani, R., Vaidya, V.A. and Datta, A. (2024) A Cell-Permeable Fluorescent Probe Reveals Temporally Diverse PI (4, 5) P2 Dynamics Evoked by Distinct GPCR Agonists in Neurons. *bioRxiv*, pp.2024-06. (*equal contribution) DOI: 10.1101/2024.06.17.599302
- Das, S.*, **Kapadia, A.***, Pal, S., & Datta, A. (2021) Spatio-Temporal Autophagy Tracking with a Cell-Permeable, Water-Soluble, Peptide-Based, Autophagic Vesicle-Targeted Sensor. *ACS Sensors*, 6, 2252-2260. (*equal contribution) DOI: 10.1021/acssensors.1c00191
- Sharma, K.K., Ravi, R., Maurya, I.K., **Kapadia, A.**, Khan, S.I., Kumar, V., Tikoo, K. and Jain, R. (2021) Modified histidine containing amphipathic ultrashort antifungal peptide, His [2-p-(n-butyl) phenyl]-Trp-Arg-OMe exhibits potent anticryptococcal activity. *Eur. J. Med. Chem.*, 223, p.113635. DOI: 10.1016/j.ejmech.2021.113635
- **Kapadia, A.**, Sharma, K. K., Maurya, I. K., Singh, V., Khullar, M., Jain, R. (2020) Structural and Mechanistic Insights into the Inhibition of Amyloid-β Aggregation by Aβ39-42 Fragment Derived Synthetic Peptides. *Eur. J. Med. Chem.*, 212, 113-126. DOI: 10.1016/j.ejmech.2020.113126
- **Kapadia, A.**, Patel, A., Sharma, K. K., Maurya, I. K., Singh, V., Khullar, M., Jain, R. (2020) Effect of C-terminus amidation of Aβ 39–42 fragment derived peptides as potential inhibitors of Aβ aggregation. *RSC Advances*, 10 (45), 27137-27151. DOI: 10.1039/d0ra04788k
- Kumar, S., **Kapadia, A.**, Theil, S., Joshi, P., Riffel, F., Heneka, M. T., Walter, J. (2020) Novel phosphorylation-state specific antibodies reveal differential deposition of Ser26 phosphorylated Aβ species in a mouse model of Alzheimer's disease. *Front. Mol. Neurosci.*, 13, 257. DOI: 10.3389/fnmol.2020.619639

- Khambete, M.P., Khare, L.P., **Kapadia, A.B.** and Degani, M.S. (2020) Exploring the potential of pyrazoline containing molecules as Aβ aggregation inhibitors in Alzheimer's disease. Drug Metabolism and Personalized Therapy, 35(3), p.20190031. DOI: 10.1515/dmpt-2019-0031
- Jain, R.; **Kapadia, A.**; Patel A. (2018) Synthetic β-sheet breaker tetrapeptides having inhibitory activity against amyloid β-aggregation. *IN Patent App.* 201811011680.